THE UNIVERSITY *of* EDINBURGH

Rare strange to down quark transitions from lattice quantum chromodynamics

Raoul Hodgson

Doctor of Philosophy
The University of Edinburgh
June 2023

ABSTRACT

In the search for new physics beyond the Standard Model (SM) of particle physics, one promising set of probes are rare decays, due to the possibility of large contributions from new physics relative to their SM prediction. Two examples of such processes are the long distance dominated flavour-changing neutral current decays $K^+ \to \pi^+\ell^+\ell^-$ and $\Sigma^+ \to p\ell^+\ell^-$, referred to as the rare kaon and rare hyperon decays respectively. These processes contain the transition of a strange quark into a down quark which can only occur at loop level within the SM, however tree level contributions could exist from physics beyond the SM. Currently, the only known method for making *ab initio* calculations of low energy hadronic quantities such as these, is through the use of Lattice Quantum Chromodynamics (LQCD) where correlation functions are computed numerically via Monte Carlo methods on a discrete, finite and Euclidean space-time lattice.

Work from this PhD has contributed to a calculation of the rare kaon decay at physical pion mass. We then investigate an alternative method utilising directly integrated correlation functions in an attempt to reduce the large computational cost of this and similar calculations.

In addition, we present work extending the existing theoretical framework for computing the rare kaon decay using LQCD to the rare hyperon decay, including the handling of exponentially growing intermediate states and the correction of power-like finite volume effects. We also present the current status of the first exploratory calculation of the form factors of this decay with unphysically heavy pions and $2+1$ flavours of domain wall fermions.

In order to perform this work, multiple developments have been made to the Grid and Hadrons C++ libraries, which are open-source tools for performing large scale lattice field theory calculations on both CPU and GPU based machines.

LAY SUMMARY

The Standard Model (SM) of Particle Physics is the theory that currently best describes the universe at a subatomic level. It is known, however, to not be a complete description of the universe as it fails to include the gravitational interaction, as well as not being able to explain the domination of matter over antimatter that is observed in the universe. In almost all direct measurements of subatomic interactions, the results have been statistically consistent with the theoretical predictions of the SM, and the few that are not in good agreement have not yet reached a confidence level necessary to be classified as evidence for New Physics (NP) beyond the SM. One of the key goals of the particle physics community is to improve both the experimental observations and theoretical predictions in order to achieve this threshold for a discovery of NP.

One such type of observation is how often certain particles decay into collections of other particles. Amongst others, some promising processes to investigate are the so-called rare kaon and rare hyperon decays, $K^+ \to \pi^+\ell^+\ell^-$ and $\Sigma^+ \to p\ell^+\ell^-$ respectively. These decays have been observed by several particle physics experiments, and measurements are currently being improved by the NA64 and LHCb experiments located at the CERN particle accelerator facility.

In addition to improvements in the experimental measurements, the theoretical predictions must also be improved if any NP is to be discovered in these decays. Currently, these predictions are only calculable using pen-and-paper techniques with certain approximations made. However, these approximations leads to large uncertainties in the predictions, that limit our ability to identify any NP.

In the past several decades, huge advances in computing power have been made which allow for an alternative method known as Lattice Quantum Field Theory (LQFT) in which calculations are performed numerically on large-scale supercomputers. In this thesis, we describe the how calculations of these rare processes can be performed using LQFT, and present the latest developments towards making improved SM predictions of these decays.

DECLARATION

I declare that this thesis was composed by myself, that the work contained herein is my own except where explicitly stated otherwise in the text, and that this work has not been submitted for any other degree or professional qualification except as specified.

Parts of this work have been published in [1] and [2].

(*Raoul Hodgson, June 2023*)

ACKNOWLEDGEMENTS

First I must express my deepest gratitude to my supervisors Antonin Portelli and Vera Gülpers for all their guidance throughout the PhD, and for providing me the freedom to explore my research interests. Without you none of this would be possible.

In addition, I would like to thank the whole lattice group here in Edinburgh for their assistance and contributions, especially to Felix Erben who put in much of the technical groundwork for the project.

A special thanks should go to Alessandro Lupo and Nelson Lachini for the invaluable discussions we've had throughout the PhD. Without these conversations I wouldn't be half the scientist I am today.

Of course, many thanks to all the members of office 4301 over the years for providing an excellent environment, and more importantly their friendship. I should especially thank William Lindved for his wonderfully distracting thoughts during the thesis writing process, without which I would have submitted significantly earlier.

Finally, I must thanks all of my family and friends, without whom I would not be where I am today.

CONTENTS

INTRODUCTION

The rare kaon and rare hyperon decays, $K^+ \to \pi^+\ell^+\ell^-$ and $\Sigma^+ \to p\ell^+\ell^-$ respectively with $\ell = e, \mu$, are Flavor Changing Neutral Current (FCNC) processes in which a strange quark transitions into a down quark. These processes are highly suppressed within the Standard Model (SM) since it does not include any interactions that allow FCNCs at tree-level, and therefore they can only occur at loop level. The rarity of these decays makes them, amongst other processes, ideal probes in the search for New Physics (NP) beyond the SM.

With recent improvements to the branching fraction measurements of these decays by the NA64 and LHCb experiments, and further improvements expected to come in the future, the large uncertainties from existing theoretical predictions are the limiting factor in the search for NP in these decays. With Lattice Quantum Chromodynamics (LQCD) being the only known systematically improvable *ab initio* method for calculating low energy hadronic processes, it is the the ideal tool for making predictions of these processes. In this thesis, we present direct computations of both the rare kaon and rare hyperon decays using LQCD, and investigate potential methodological improvements for these calculations.

The structure of this thesis is as follows. Chapters 1 and 2 provide a description of the broader framework, and specific methods utilised throughout this work. A brief overview of the SM is given in chapter 1, separated into Quantum Chromodynamics (QCD) (section 1.1) and Electroweak sector (section 1.2). Chapter 2 then describes the method of LQCD which allows for non-perturbative calculations of QCD processes to be computed numerically.

Chapter 3, discusses the experimental and theoretical status of the rare kaon decay, $K^+ \to \pi^+\ell^+\ell^-$, and describes the existing framework for calculating this decay on the lattice. The first calculation of this decay on the lattice directly at physical pion mass is then presented, and the challenges involved in future improvements are

identified.

In chapter 4, the use of directly integrated correlation functions is discussed, in which the time coordinate of an operator is integrated/summed over all time via sequential inversions of the Dirac operator. This can be used to reduce the measurement costs of many calculations, and so far has only be used in the context of degenerate initial and final states. We discuss the applicability of this method to systems where this degeneracy is broken. In addition, we show how this method can be applied to the rare kaon decay, although in a restrictive kinematic setup, and a numerical study is performed to demonstrate the validity and cost reduction of this method.

The theoretical framework for extracting the rare kaon decay on the lattice is then extended in chapter 5 to allow for calculations of the baryonic equivalent, rare hyperon decay $\Sigma^+ \to p\ell^+\ell^-$. While there are many similarities between these decays, the extra spin degrees of freedom of the baryons, as well as the qualitatively different spectrum of baryonic states, introduce modifications to the methods that are described in detail. These modifications include the handling of residual intermediate state time dependence, extending the so-called "scalar-shift" method to baryonic systems, and the removal of the power-like finite-volume corrections from on-shell intermediate states.

Chapter 6 presents the first exploratory calculation of the rare hyperon decay on the lattice using the framework from chapter 5. This calculation is performed at unphysically heavy pion mass to act as a proof of concept calculation where the practicality of the methods can be evaluated. In addition, we identify challenges that must be addressed before this calculation can be performed at the physical point.

Finally, chapter 7 concludes this thesis with a summary of the work presented, as well as the outlook for further research on these topics.

CHAPTER

ONE

THE STANDARD MODEL AND THE SEARCH FOR NEW PHYSICS

The SM of particle physics is currently the best model for describing the subatomic world. Using the framework of Quantum Field Theory (QFT), it combines the strong and weak nuclear forces, and electromagnetism into a single theory. While there is an overwhelming abundance of experimental verifications of the SM, it is not a complete theory of everything, as it does not include (and is incompatible with) the theory of General Relativity (GR) which describes the universe at astronomical scales.

Aside from the inconsistency between the SM and GR, the SM also fails to explain the observed matter-antimatter asymmetry of the universe, and provides no candidates for dark matter which accounts for a large portion of the content of the universe. In addition, there are several experimental observations that are in tension with predictions of the SM. These are anomalies that are statistically unlikely to be random chance, but nonetheless have not yet achieved the community decided threshold to be classed as a discovery of NP beyond the SM.

For these reasons, a key goal of the particle physics community at the present time is to find, and confirm, these anomalies as they provide the smoking gun that can lead us to a new theory beyond the SM. In order to confirm the existence of an anomaly, both an experimental observation and a SM prediction must be made, and a discrepancy between the two must pass some statistically significant threshold.

As a result of the amazing predictive power of the SM, any NP must necessarily have very subtle effects on any observation. For this reason, there are two major approaches to searches for Beyond the Standard Model (BSM) physics:

- Searches for small deviations in high frequency processes, using high precision measurements.
- Searches for large relative deviations in rare/forbidden processes.

The former utilises ever improving statistical precision to find tiny deviations from the SM predictions, for example in the muon magnetic moment $(g-2)_\mu$, and Cabibbo–Kobayashi–Maskawa (CKM) matrix unitarity tests. The latter looks for signals that are rare or forbidden within the SM, where deviations resulting from NP can have a large relative influence that can be observed with significantly less precision. In this thesis, we focus on making SM predictions of rare decays for use in this latter approach.

The SM is a quantum theory based on the gauge group

$$\mathrm{SU}(3)_c \times \mathrm{SU}(2)_L \times \mathrm{U}(1)_Y \tag{1.1}$$

where the subscript c indicates the color group that describes the strong nuclear force, L and Y indicate the left-handed and hypercharge sectors that describe the electroweak interactions. We shall discuss these two separately in the following sections.

1.1 Quantum Chromodynamics

QCD is the theory of the strong nuclear force which describes the spectrum and interactions of the hadronic particles. These hadrons can be separated into the mesons (π, K, ϕ, ρ, ...) and the baryons (p, Σ, Λ, Ω, ...), which are all described by the $\mathrm{SU}(3)_c$ part of the SM gauge group.

The fundamental quantum fields of this theory are the N_f flavours of quarks, q_f, and gluons $G_{a,\mu}$, with a Lagrangian given by

$$\mathcal{L} = -\frac{1}{4g^2} G_{a,\mu\nu} G^{a,\mu\nu} + \sum_{f=1}^{N_f} \bar{q}_f \left(i\gamma_\mu D^\mu - m_f \right) q_f \,, \tag{1.2}$$

where $D_\mu = \partial_\mu - iG_{a,\mu}T^a$, T^a are the generators of the SU(3) group, g is the (bare) QCD coupling, m_f is the (bare) mass of the quark flavour f, and the gluonic field strength tensor is given by

$$G_{\mu\nu} = i[D_\mu, D_\nu] = \partial_\mu G_\nu - \partial_\nu G_\mu - i[G_\mu, G_\nu] = G_{a,\mu\nu}T^a \,. \tag{1.3}$$

This Lagrangian is constructed such that it is invariant under local $\mathrm{SU}(3)_c$ transformations where the fields transform as

$$q(x) \to \Omega(x)q(x) \,, \tag{1.4}$$
$$\bar{q}(x) \to \bar{q}(x)\Omega^\dagger(x) \,, \tag{1.5}$$
$$G_\mu \to G_\mu - i\Omega(x)\partial_\mu\Omega^\dagger(x) \,, \tag{1.6}$$

where $\Omega(x) \in \mathrm{SU}(3)$. The Feynman vertices that arise from this Lagrangian are shown in fig. 1.1, where the first indicates the interaction of the quarks and gluons, and the remaining two diagrams are 3 and 4 gluon interactions that arise as a result of the non-abelian nature of the SU(3) group.

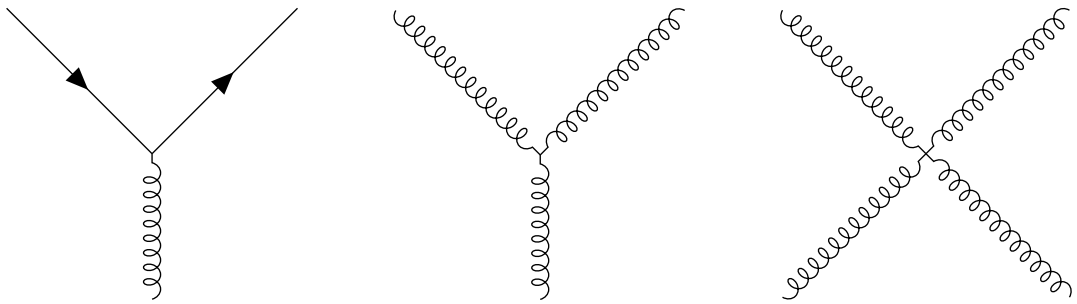

Figure 1.1 *Quark and gluon interaction vertices for continuum QCD.*

As with all quantum field theories, the parameters of the theory must undergo a renormalisation procedure which results in the running of the QCD coupling g and masses m_f. Most importantly for this discussion, the coupling, g, becomes a function of the renormalisation scale μ, and its behaviour is governed by the renormalisation group equation

$$\mu\frac{dg(\mu)}{d\mu} = \beta(g) \,, \tag{1.7}$$

where $\beta(g)$ is the beta-function. In perturbation theory, this beta-function at one

loop is given by

$$\beta(g) = -\left(11 - \frac{2N_f}{3}\right)\frac{g^3}{(4\pi)^2}\,, \tag{1.8}$$

and defining a quantity analogous to the fine structure constant ($\alpha_{\text{em}} = \frac{e^2}{4\pi}$), the solution to the renormalisation group equation gives

$$\alpha_s(\mu) = \frac{g^2(\mu)}{4\pi} = \frac{\alpha_s(\mu_0)}{1 + \frac{\alpha_s(\mu_0)}{4\pi}\left(11 - \frac{2N_f}{3}\right)\ln\left(\frac{\mu}{\mu_0}\right)}\,, \tag{1.9}$$

where μ_0 is some reference scale at which α_s can be measured. Figure 1.2 shows the running of the QCD coupling extracted from various experimental measurements, which shows a very good agreement with the theoretical scaling.

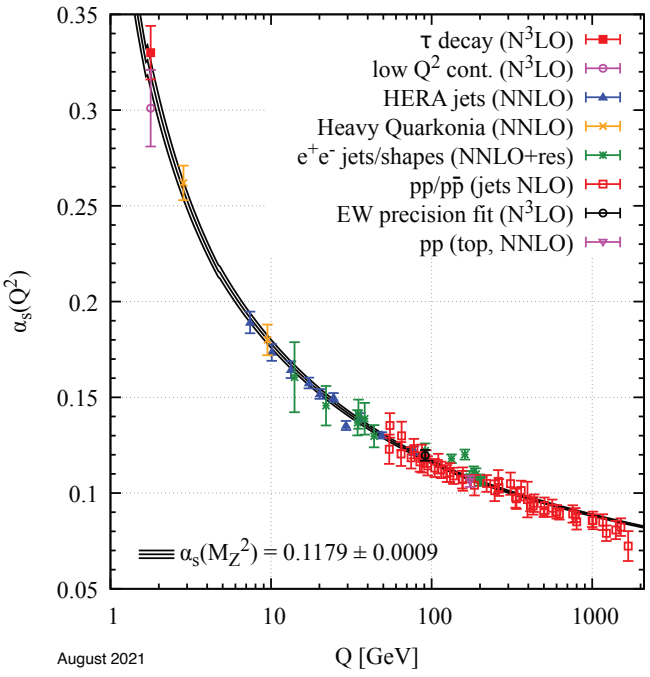

Figure 1.2 *Running of the QCD coupling. Figure reproduced from ref. [3].*

Within the SM, there are at most 6 flavours of quarks active in QCD (u, d, s, c, b, t), and therefore the factor $11 - \frac{2N_f}{3}$ will always be positive, causing $\alpha_s \to 0$ as the scale increases, known as asymptotic freedom where the quarks and gluons behave as free particles. Conversely, α_s increases as the scale decrease, resulting in the breakdown of the perturbative expansion below a certain scale known as the QCD scale $\Lambda_{\text{QCD}} \simeq 200 - 300\,\text{MeV}$ in the $\overline{\text{MS}}$ renormalisation scheme at 2 GeV. This makes non-perturbative methods such as LQCD crucial for calculations of hadronic quantities at low energies.

1.1.1 Chiral symmetry and its breaking

Chiral symmetry, and specifically its breaking, is hugely important for the phenomenology of low energy hadronic physics, and will cause issues when attempting to put fermions on the lattice in section 2.2.

In the continuum, the fermionic component of the Lagrangian for N_f massless fermions has the form

$$\mathcal{L}_F = \sum_{f=1}^{N_f} \bar{\psi}_f \, iD \, \psi_f \,, \tag{1.10}$$

where $D = \gamma^\mu D_\mu$. In the absence of a mass term, this Lagrangian separates into two terms corresponding to two non-directly interacting Weyl fermions

$$\mathcal{L}_F = \sum_f \left(\bar{\psi}_f^L \, iD \, \psi_f^L + \bar{\psi}_f^R \, iD \, \psi_f^R \right) \,, \tag{1.11}$$

where $\psi^{R,L} = P^{R,L}\psi$, and $P^{R,L} = \frac{1}{2}(1 \pm \gamma_5)$ are the right- and left-handed chiral projectors. It is clear that this Lagrangian is invariant under a global chiral transformation defined by the group

$$\mathrm{U}(N_f)_L \times \mathrm{U}(N_f)_R \tag{1.12}$$

where the fields transform as $\psi^{L,R} \to U^{L,R} \psi^{L,R}$ with $U^{R,L} \in \mathrm{U}(N_f)_{R,L}$ in the fundamental representation acting on the flavour space.

Explicit Symmetry Breaking

The simplest mechanism for breaking this chiral symmetry is to add a term to the Lagrangian that breaks it explicitly. Introducing a mass term in which all flavours have the same mass m, the fermionic Lagrangian has the form

$$\mathcal{L}_F = \sum_f \bar{\psi}_f \left(iD - m \right) \psi_f \tag{1.13}$$

$$= \sum_f \left(\bar{\psi}_f^L \, iD \, \psi_f^L + \bar{\psi}_f^R \, iD \, \psi_f^R - m \, \bar{\psi}_f^L \psi_f^R - m \, \bar{\psi}_f^R \psi_f^L \right) \,, \tag{1.14}$$

which couples the different chiralities and breaks the symmetry. The Lagrangian is, however, still invariant to the vector subgroup $\mathrm{U}(1)_V \times \mathrm{SU}(N_f)_V$ where the left and right chiral fields transform in the same way, $\psi^{L,R} \to V\psi^{L,R}$ for

$V \in \mathrm{U}(1)_V \times \mathrm{SU}(N_f)_V$. The symmetries that are broken by the mass term are the axial symmetries, where the two chiralities transform opposite to one another, $\psi_L \to A\psi_L$ and $\psi_R \to A^{-1}\psi_R$ for $A \in \mathrm{U}(1)_A \times \mathrm{SU}(N_f)_A$. The elements of these two groups can be written as

$$V = e^{i\alpha_V^a T_a} \qquad \text{and} \qquad A = e^{i\alpha_A^a T_a \gamma_5}\,, \tag{1.15}$$

where α_V^a and α_A^a parametrise the transformations with generators T_a and $T_a\gamma_5$ respectively.

With just the vector flavour symmetry remaining after the addition of the universal mass term, this can be further broken by the introduction of a different mass for each flavour, as is realised in nature, giving the Lagrangian

$$\mathcal{L}_F = \sum_f \bar{\psi}_f \left(iD - m_f\right) \psi_f\,, \tag{1.16}$$

which now has only N_f independent U(1) symmetries corresponding to rephasing each flavour independently. By Noether's theorem, this gives a set of N_f conserved charges that are the flavour quantum number of type f. As a result baryon number is also conserved, which corresponds to the charge of the subgroup in which all the fields are rephased in the same way.

In the SM, there are 6 flavours of quarks all with different masses. However, at energies below Λ_{QCD}, only the lightest 3 of these remain active. So we shall only consider $N_f = 3$ in the discussion of chiral symmetry breaking in QCD.

Spontaneous Symmetry Breaking

Spontaneous symmetry breaking is a process where the equations of motion governing a system posses a symmetry, however, the ground state of that system is not symmetric. In the case of QFT, this corresponds to the Lagrangian having a symmetry transformation that the vacuum is not invariant under. This non-symmetric vacuum can be transformed into another equally valid, but distinct, vacuum. The Nambu-Goldstone theorem [4], says that for every generator that is broken spontaneously, there is an associated massless Goldstone boson.

It was shown in ref. [5] that, given some reasonable assumptions, a theory such as QCD with no θ-term cannot spontaneously break the vector symmetry $\mathrm{U}(N_f)_V$, otherwise it would be possible to construct massless particles from arbitrarily

massive quarks.

The axial symmetry, however, is not protected from breaking spontaneously. If the $\mathrm{U}(N_f)_A$ symmetry were respected by the vacuum, it can be shown that all particles would have a degenerate opposite parity partner, known as parity doubling. Table 1.1 shows the masses of the lowest positive and negative parity hadrons observed. It can be clearly seen that no parity doubling is observed, suggesting the axial symmetry must be broken.

J^P	Particle	Mass [MeV]	J^P	Particle	Mass [MeV]
	$f_0(500)$	500		π	140
0^+	$f_0(980)$	980	0^-	η	550
	$a_0(980)$	980		η'	960
$\frac{1}{2}^+$	N	940	$\frac{1}{2}^-$	$N(1535)$	1535
	$N(1440)$	1440		$N(1650)$	1650

Table 1.1 *List of the lightest experimentally measured particles in the positive and negative parity sectors for the unflavoured (pseudo)scalars and the baryons [6].*

The quantity that parametrises the spontaneous breaking of the axial symmetry is known as the chiral condensate, Σ,

$$\langle \bar{\psi}_f \psi_{f'} \rangle = \Sigma \, \delta_{ff'} \tag{1.17}$$

which is only non-zero if the axial symmetry is spontaneously broken. While this quantity is not experimentally measurable, it can be calculated from first principles on the lattice, giving the value $\Sigma = -(245(12)\,\mathrm{MeV})^3$ [7], which is significantly different from zero. From the Nambu-Goldstone theorem, we should expect the presence of N_f^2 massless bosons of negative parity from the total breaking of $U(N_f)_A$, however, no massless hadrons have been observed experimentally.

Since chiral symmetry is explicitly broken by a small mass term for these lightest quarks, the axial symmetry is not exact at the level of the Lagrangian. This small explicit breaking corresponds to the production of pseudo-Nambu-Goldstone bosons that have a small, but non-zero mass, which should of course go to zero as $m_f \to 0$.

In QCD, we would then expect the existence of 9 pseudoscalar mesons that are lighter than the rest of the hadronic spectrum. However, only 8 have been observed, the three pions, four kaons and the η meson. The next lightest is the η' which has nearly twice the mass of the η. This is to be expected if the group that is spontaneously broken is $\mathrm{SU}(N_f)_A$, with $N_f^2 - 1$ generators, instead of the full $\mathrm{U}(N_f)_A$.

The remaining $\mathrm{U}(1)_A$ axial symmetry is in fact broken by some other mechanism, known as anomalous symmetry breaking.

Anomalous symmetry breaking

In the following, we consider a theory with only a single massless quark ($N_f = 1$, $m_f = 0$) to describe the breaking of the residual $\mathrm{U}(1)_A$, without loss of generality.

The axial $U(1)_A$ transformation acts on the field as

$$\psi \to e^{i\alpha\gamma_5}\,\psi \qquad \text{and} \qquad \bar{\psi} \to \bar{\psi}\,e^{i\alpha\gamma_5} \tag{1.18}$$

which is a symmetry of the massless Lagrangian due to the anti-commutation relation $\{\gamma_\mu, \gamma_5\} = 0$, and is therefore a symmetry of the classical theory. However, for this symmetry to survive to the quantum theory it must not break during the quantisation procedure. If it does so, this is known as anomalous symmetry breaking. By considering the path integral approach to quantising the theory, we can gain insight by investigating the partition function of the quantum theory

$$Z = \int \mathcal{D}[G, \bar{\psi}, \psi]\, e^{iS[G,\bar{\psi},\psi]}\,, \tag{1.19}$$

where S is the full action, and G is the set of gluon fields. The action is invariant under the axial transformation, however, the fermionic measure $\mathcal{D}[\bar{\psi}, \psi]$ is not. Since both the field and conjugate field transform in the same way, it can be seen that

$$Z \to \int \mathcal{D}[G, \bar{\psi}, \psi]\, \det\!\left(e^{-i\alpha\gamma_5}\right)^2 e^{iS[G,\bar{\psi},\psi]}\,, \tag{1.20}$$

which can be evaluated using the identity $\det\left(e^X\right) = e^{\mathrm{Tr}[X]}$. The determinant then becomes

$$\det\left(e^{i\alpha\gamma_5}\right)^2 = e^{-i2\alpha\,\mathrm{Tr}[\gamma_5]}\,, \tag{1.21}$$

where $\mathrm{Tr}[\gamma_5]$ is a trace over the fermionic spectrum. Defining the eigenvalues of the Dirac operator λ corresponding to an eigenvector $|\lambda\rangle$, i.e. $D\,|\lambda\rangle = \lambda\,|\lambda\rangle$, then the trace is simply

$$\mathrm{Tr}[\gamma_5] = \sum_\lambda \langle\lambda|\,\gamma_5\,|\lambda\rangle\ . \tag{1.22}$$

Due to the anti-hermiticity of the Dirac operator, all of the eigenvalues λ are

imaginary. In addition, the anti-commutation $\{D, \gamma_5\} = 0$ results in the relation $(\lambda - \lambda^*) \langle\lambda| \gamma_5 |\lambda\rangle = 0$, and therefore, only values of $\lambda \in \mathbb{R}$ can have a non-zero value for $\langle\lambda| \gamma_5 |\lambda\rangle$. Therefore, only the zero-modes of the Dirac operator can contribute to the trace.

It can be shown that $[D, \gamma_5]||_{\lambda=0} = 0$, that is the Dirac operator and γ_5 commute when restricted to just the zero-mode subspace, and therefore both operators can be diagonalised simultaneously. The eigenvalues of γ_5 are simply ± 1 corresponding to the modes with positive or negative chirality. The trace therefore becomes

$$\mathrm{Tr}[\gamma_5] = n_+ - n_- \,, \tag{1.23}$$

where $n_\pm$ is the number of zero-modes of the Dirac operator with $\pm$ chirality. The values of $n_\pm$ are in general a function of the background gauge field, so the partition function then transforms as

$$Z = \int \mathcal{D}[G, \bar{\psi}, \psi] e^{-S[G,\bar{\psi},\psi]} \tag{1.24}$$

$$\to \int \mathcal{D}[G, \bar{\psi}, \psi] e^{-2i\alpha(n_+ - n_-)[G]} \, e^{-S[G,\bar{\psi},\psi]} \tag{1.25}$$

which is not invariant. Therefore the axial $U(1)_A$ symmetry must be anomalously broken, preventing it from breaking spontaneously, and preventing the η' from being a pseudo-Goldstone boson.

It is clear to see from our discussion, that the low energy spectrum of QCD involving the 3 lightest quarks has a rich connection with chiral symmetry and its breaking, which must be present in order to to make accurate predictions of the physical world. It shall be seen later that this is in fact problematic when discretising this theory on the lattice.

1.2 Electroweak physics

The electroweak sector of the SM is described by the $\mathrm{SU}(2)_L \times \mathrm{U}(1)_Y$ gauge group. The subscript L indicates this gauge symmetry applies to the left-handed chiral components described in the previous section, while the right handed particles don't participate in the transformation.

The matter particle content of the electroweak sector is described by the up-type quarks u, c, t, the down-type quarks d, s, b, the charged leptons e, μ, τ and the

neutral-leptons ν_e, ν_μ, ν_τ. These are arranged into the $\mathrm{SU}(2)_L$ doublets

$$Q_{1,L} = \begin{pmatrix} u_L \\ d_L \end{pmatrix} \quad , \quad Q_{2,L} = \begin{pmatrix} c_L \\ s_L \end{pmatrix} \quad , \quad Q_{3,L} = \begin{pmatrix} t_L \\ b_L \end{pmatrix} , \tag{1.26}$$

$$L_{1,L} = \begin{pmatrix} \nu_{e,L} \\ e_L \end{pmatrix} \quad , \quad L_{2,L} = \begin{pmatrix} \nu_{\mu,L} \\ \mu_L \end{pmatrix} \quad , \quad L_{3,L} = \begin{pmatrix} \nu_{\tau,L} \\ \tau_L \end{pmatrix} , \tag{1.27}$$

which transform as $Q_{i,L} \to UQ_{i,L}$ and $L_{i,L} \to UL_{i,L}$ for $U \in \mathrm{SU}(2)_L$. The singlets are

$$u_{i,R} = (u_R, c_R, t_R)_i \tag{1.28}$$

$$d_{i,R} = (d_R, s_R, b_R)_i \tag{1.29}$$

$$l_{i,R} = (e_R, \mu_R, \tau_R)_i \tag{1.30}$$

$$\nu_{i,R} = (\nu_{e,R}, \nu_{\mu,R}, \nu_{\tau,R})_i \, . \tag{1.31}$$

In addition, each of these fields has a hypercharge

$$Y(Q_L) = \frac{1}{6} \quad , \quad Y(L_L) = -\frac{1}{2} \tag{1.32}$$

$$Y(u_R) = \frac{2}{3} \quad , \quad Y(d_R) = -\frac{1}{3} \tag{1.33}$$

$$Y(l_R) = -1 \quad , \quad Y(\nu_R) = 0 \, . \tag{1.34}$$

These are then accompanied by the $\mathrm{SU}(2)_L$ gauge fields $W_\mu = W^1_\mu \sigma_1 + W^2_\mu \sigma_2 + W^3_\mu \sigma_3$ and the $\mathrm{U}(1)_Y$ gauge field B_μ. The Lagrangian for this theory is

$$\mathcal{L} = -\frac{1}{4} W^i_{\mu\nu} W^{\mu\nu}_i - \frac{1}{4} B_{\mu\nu} B^{\mu\nu} \tag{1.35}$$

$$+ \sum_F \bar{F}_L \left(i\gamma_\mu D^\mu_F \right) F_L + \sum_f \bar{f}_R \left(i\gamma_\mu D^\mu_f \right) f_R \tag{1.36}$$

where $F = Q, L$ and $f = u, d, l, \nu$. The covariant derivatives are given by

$$D_{F,\mu} = \partial_\mu - i g_w W_\mu - i g_y Y(F) B_\mu \tag{1.37}$$

$$D_{f,\mu} = \partial_\mu - i g_y Y(f) B_\mu \, . \tag{1.38}$$

The chiral nature of the $\mathrm{SU}(2)_L$ interaction prevents this Lagrangian from containing a naive mass term for the fermions or vector bosons. Since these term are not gauge invariant, all particles are naively predicted to be exactly massless. In practice however, the fermions and the weak vector bosons are observed to have non-zero masses. These can both be added to the theory in a gauge invariant way via the Higgs

mechanism [8, 9]. This mechanism includes an additional scalar $\mathrm{SU}(2)_L$ doublet field

$$\Phi = \begin{pmatrix} \phi_1 \\ \phi_2 \end{pmatrix} \tag{1.39}$$

that has a hypercharge $Y(\Phi) = \frac{1}{2}$, that has the Lagrangian

$$\mathcal{L}_\Phi = (D_\mu \Phi)^\dagger (D^\mu \Phi) - V(\Phi)\,, \tag{1.40}$$

with a quartic potential $V(\Phi) = -\mu^2 \Phi^\dagger\Phi + \lambda \left(\Phi^\dagger\Phi\right)^2$. The final part of the Lagrangian couples this scalar field to the left and right handed fermions via a Yukawa interaction

$$\mathcal{L}_Y = -\bar{Q}_L Y^u \Phi d_R - \bar{Q}_L Y^u \widetilde{\Phi} u_R - \bar{L}_L Y^l \Phi l_R - \bar{Q}_L Y^\nu \widetilde{\Phi} \nu_R + \text{h.c.} \tag{1.41}$$

where Y^f are 3×3 matrices of couplings, and $\widetilde{\Phi} = i\sigma_2 \Phi^*$ transforms in the same way as Φ under $\mathrm{SU}(2)_L$, but has the opposite hypercharge. In order for this scalar field to generate mass terms from these interactions, it needs to acquire a non-zero vacuum-expectation-value, which is done through the process of spontaneous symmetry breaking. In the event the scalar potential parameters satisfy

$$\mu^2 > 0 \quad \text{and} \quad \lambda > 0\,, \tag{1.42}$$

the potential is minimised when $\Phi^\dagger\Phi = \frac{v^2}{2}$, $v = \sqrt{\frac{\mu^2}{\lambda}}$. The value of this vacuum expectation that corresponds to our physically observed reality is

$$\Phi = \frac{1}{\sqrt{2}} \begin{pmatrix} 0 \\ v \end{pmatrix}. \tag{1.43}$$

Note that this vacuum is not invariant under $\mathrm{SU}(2) \times \mathrm{U}(1)_Y$, but only under the $\mathrm{U}(1)_{\text{em}}$ subgroup corresponding to electromagnetism. Therefore the $\mathrm{SU}(2)_L \times \mathrm{U}(1)_Y$ gauge group gets spontaneously broken down to $\mathrm{U}(1)_{\text{em}}$. Expanding the scalar field around this vacuum gives

$$\Phi = \frac{1}{\sqrt{2}} \begin{pmatrix} 0 \\ v + H \end{pmatrix} \tag{1.44}$$

where H is the Higgs field that has a zero vacuum expectation value. Writing the Lagrangian in terms of this new field H, it can be see that the vacuum expectation value gives rise to terms bilinear in the W_μ, B_μ and fermion fields. These mass

eigenstates correspond to the charged weak vector bosons

$$W_\mu^\pm = W^1 \pm iW^2\,, \tag{1.45}$$

and the neutral vector bosons

$$\begin{pmatrix} Z_\mu \\ A_\mu \end{pmatrix} = \begin{pmatrix} \cos\theta_w & \sin\theta_w \\ -\sin\theta_w & \cos\theta_w \end{pmatrix} \begin{pmatrix} W_\mu^3 \\ B_\mu \end{pmatrix} \tag{1.46}$$

where θ_w is the Weinberg angle $\sin\theta_w = \frac{g_y}{\sqrt{g_y^2+g_w^2}}$.

In addition, the flavour eigenstate quark fields get mixed into mass eigenstates by the CKM matrix V by

$$\begin{pmatrix} d' \\ s' \\ b' \end{pmatrix} = V \begin{pmatrix} d \\ s \\ b \end{pmatrix}\,. \tag{1.47}$$

It is this CKM matrix that is responsible for the mixing between the different generations of quarks when undergoing a charge current weak decay. Note that the neutral Z_μ and A_μ fields do not change quark flavour and therefore there are no FCNC iterations at tree-level within the SM. Instead this can only occur at loop level with charged W boson interactions.

4-quark Fermi Interaction

The experimentally measured masses of the weak vector bosons are

$$m_W \simeq 80\,\text{GeV} \quad \text{and} \quad m_Z \simeq 91\,\text{GeV}\,, \tag{1.48}$$

which are much heavier than the low energy scales involved in the hadronic processes of interest here. The flavour changing processes of particular relevance to the rare kaon and hyperon decays are shown in fig. 1.3.

The momentum space W-boson propagator has the form

$$S_{\mu\nu}^W(q) = -i\frac{\eta_{\mu\nu} - \frac{q^\mu q^\nu}{m_W^2}}{q^2 - m_W^2} \simeq i\frac{\eta_{\mu\nu}}{m_W^2} \tag{1.49}$$

where the low momentum transfer limit $q_\mu \ll m_W$ is taken. In this limit, the propagator looks like a point-like 4-quark interaction in position space.

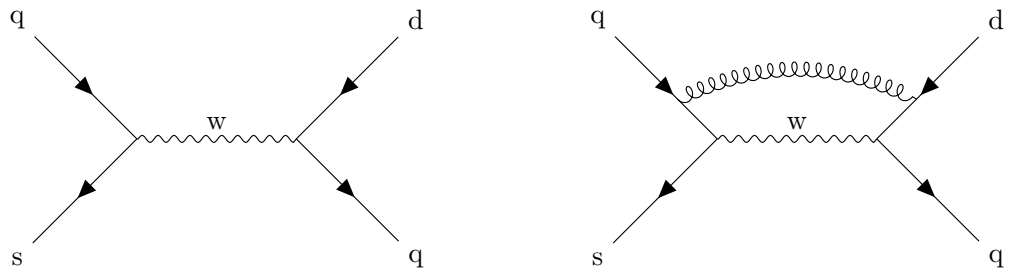

Figure 1.3 *Feynman diagrams for the $s \to d$ 4-quark interactions relevant for the rare kaon and hyperon decays within the SM.*

This is described in a systematic way as an effective field theory know as the Fermi-theory of weak interactions, and the corresponding vertices for fig. 1.3 are shown in fig. 1.4. Ref. [10] gives a detailed analysis of the relevant operators and Wilson coefficients for flavour changing decays in this effective field theory.

Figure 1.4 *Feynman diagrams for the $s \to d$ 4-quark interactions relevant for the rare kaon and hyperon decays within the Fermi effective theory.*

CHAPTER

TWO

LATTICE QCD

Due to the non-perturbative nature of QCD at low energies, it is important to have alternative methods of calculating quantities in this theory. One of these non-perturbative methods is the use of effective field theories. An effective field theory of QCD is Chiral Perturbation Theory (ChPT), in which the hadrons are the degrees of freedom rather than the quarks and gluons. This method has the benefit that many calculations can be performed perturbatively in some small scale, e.g. particle momenta and/or flavour symmetry breaking parameters, giving access to analytic forms of the results. However, these effective theories are generally non-renormalisable and therefore require additional inputs as higher orders are included.

Currently, the only known method of computing non-perturbative quantities in QCD directly, is through the use of Lattice Quantum Field Theory (LQFT). This allows one to perform non-perturbative calculations numerically, which requires discretising the theory to put it onto a computer.

The partition function of a theory, with field(s) ϕ, in real valued time is the path integral weighted by a phase factor dependent on the value of the action, S,

$$Z = \int \mathcal{D}[\phi] e^{iS[\phi]} \,, \tag{2.1}$$

which gives rise to a sign problem when performing the integrals numerically. It is therefore advantageous to perform a Wick rotation of the time variable taking $t \to -it$ which gives rise to a Euclidean space-time. The partition function this

then given by the path integral with a Euclidean action S_E as

$$Z = \int \mathcal{D}[\phi] e^{-S_E[\phi]}\,, \tag{2.2}$$

which can be interpreted as a statistical field theory that can be sampled via Monte Carlo methods where fields are drawn from a probability distribution

$$P[\phi] = \frac{1}{Z} e^{-S_E[\phi]}\,. \tag{2.3}$$

The physical information is extracted through correlation functions which are simply the expectation of certain operators

$$\Gamma_{\mathcal{O}} = \langle \mathcal{O}[\phi] \rangle = \frac{1}{Z} \int \mathcal{D}[\phi]\, \mathcal{O}[\phi] e^{-S_E[\phi]}\,. \tag{2.4}$$

If a series of N fields ϕ_i are draw following the probability distribution of eq. (2.3), the correlation function can then be estimated as

$$\Gamma_{\mathcal{O}} \simeq \frac{1}{N} \sum_{i=1}^{N} \mathcal{O}[\phi_i]\,, \tag{2.5}$$

and taking $N \to \infty$ recovers the exact correlator.

The relevant fields for the study of QCD on the lattice are the gauge link field, $U_\mu(x)$, and the quark fields $q(x), \bar{q}(x)$. Since the quark fields are fermionic, they are Grassmann valued fields and therefore cannot be sampled directly (without massive computational overhead). However, since the QCD action is quadratic in these fields, they can be integrated out exactly, leaving only the integral over the gauge links to be performed via Monte-Carlo methods, which we shall refer to as the gauge average.

2.1 Discretisation of QCD

In order to discretise a theory, we must define a discrete version of the field content of that theory, as well as the Lagrangian and all the operations therein. The discretisation of Euclidean space-time is done by simply considering all points separated by a distance a in each dimension which is referred to as the lattice spacing,

giving the (infinite) lattice

$$\Lambda = a\mathbb{Z}^4 \,. \tag{2.6}$$

When defining a discrete version of fields and operations, they should recover the continuum value when the continuum limit is taken, $a \to 0$. There are infinitely many discretisations that all give the correct continuum limit, however, often a simple choice arises. We shall describe this first with the simple case of a real scalar field ϕ with continuum action

$$S = \frac{1}{2}\int d^4x\, \phi(x)\left(-\partial_\mu\partial_\mu + m^2\right)\phi(x)\,. \tag{2.7}$$

The discretised scalar field can simply be taken to be the field evaluated at only sites on the lattice Λ, and the integral can be discretised by replacing it with the Riemann sum

$$\int d^4x \to a^4 \sum_{x\in\Lambda} \,. \tag{2.8}$$

The discretisation of the derivative is somewhat less obvious. The two simplest choices are the forward and backward single step finite difference

$$\delta^{\mathrm{f}}_\mu\phi(x) = \frac{\phi(x+a\hat{\mu}) - \phi(x)}{a} = \partial_\mu\phi(x) + \frac{a}{2}\partial^2_\mu\phi(x) + O(a^2) \tag{2.9}$$

$$\delta^{\mathrm{b}}_\mu\phi(x) = \frac{\phi(x) - \phi(x+a\hat{\mu})}{a} = \partial_\mu\phi(x) - \frac{a}{2}\partial^2_\mu\phi(x) + O(a^2) \tag{2.10}$$

where $\hat{\mu}$ is a unit vector in the direction μ. We can see that these derivatives give the continuum one up to $O(a)$ discretisation effects, however, they can be combined into the symmetric finite difference

$$\delta_\mu\phi(x) = \frac{1}{2}(\delta^{\mathrm{f}}_\mu + \delta^{\mathrm{b}}_\mu)\phi(x)\,, \tag{2.11}$$

which has discretisation effects of $O(a^2)$. One common choice to construct the second order derivative is from one forward and one backward finite difference

$$\delta^b_\mu\delta^f_\mu\phi(x) = \frac{\phi(x+\hat{\mu}) - 2\phi(x) + \phi(x-\hat{\mu})}{a^2}\,, \tag{2.12}$$

which gives a symmetric, nearest neighbour second derivative with discretisation effects at $\mathcal{O}(a^2)$. This gives us all the ingredients for the simple scalar field theory on the lattice. Fermions come with additional complications that will be discussed

in the next section.

The final type of field we will be interested in discretising are gauge fields. As we have seen in the previous chapter, the gauge fields are often described with non-compact vector fields $A_\mu(x)$ that are valued in the group algebra. In lattice field theory we instead generally use a compact, group valued parallel transporter field $U_\mu(x)$ known as a gauge link. Since it is the parallel transporter of the theory, this field can be considered as not living on the lattice site x, but instead living on the grid line joining two neighbouring sites x and $x + \hat{\mu}$. Importantly, under a gauge transformation, the matter fields transform as $\phi(x) \to \Omega(x)\phi(x)$, while for the gauge links

$$U_\mu(x) \to \Omega(x)U_\mu(x)\Omega^{-1}(x + \hat{\mu})\,, \tag{2.13}$$

which makes the combination $\phi^\dagger(x)U_\mu(x)\phi(x + \hat{\mu})$ a gauge invariant quantity. This allows us to define a gauge covariant symmetric derivative as

$$D_\mu\phi(x) = U_\mu(x)\phi(x + \hat{\mu}) - U_{-\mu}(x)\phi(x - \hat{\mu})\,. \tag{2.14}$$

With this new gauge field defined, it must also have a kinetic term in the action in order to be dynamical field. One such action that has the appropriate continuum limit is the Wilson gauge action [11] that is constructed from the plaquette

$$\begin{aligned} P_{\mu\nu}(x) =& U_\mu(x)U_\nu(x + \hat{\mu})U_{-\mu}(x + \hat{\mu} + \hat{\nu})U_{-\nu}(x + \hat{\nu}) && (2.15)\\ =& U_\mu(x)U_\nu(x + \hat{\mu})U_\mu(x + \hat{\nu})^\dagger U_\nu(x)^\dagger\,, && (2.16)\end{aligned}$$

where we have used the fact that $U_{-\mu}(x + \hat{\mu}) = U_\mu(x)^\dagger$. The gauge action is then given by

$$S_G = \frac{\beta}{N}\sum_{x\in\Lambda}\sum_{\mu>\nu}\mathrm{Re}\,\mathrm{Tr}[1 - P_{\mu\nu}]\,, \tag{2.17}$$

where N is the degree of the gauge group $\mathrm{SU}(N)$.

These important lattice objects and their relationship to the lattice are summarised in the schematic diagram fig. 2.1.

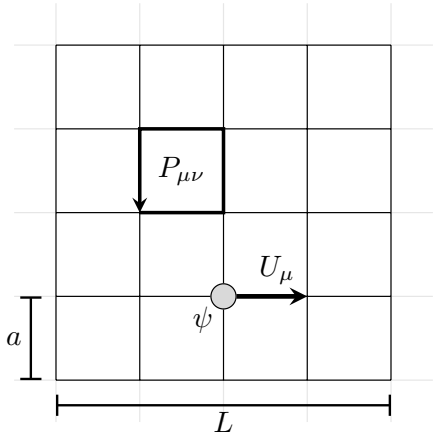

Figure 2.1 *Schematic of a lattice of size L with lattice spacing a. The matter field ψ lives on the sites, the gauge link U_μ connects neighbouring sites, and the plaquette $P_{\mu\nu}$ connects 4 nearest sites in the $\mu - \nu$ plane.*

2.2 Fermion doubling and chiral fermions

The continuum action for a Dirac fermion with bare mass m in Euclidean space-time is given by

$$S_{\mathrm{C}} = \int d^4x\, \bar{\psi}(x)\,[D + m]\,\psi(x)\,, \tag{2.18}$$

where D is the massless Dirac operator $D = \gamma_\mu D_\mu$ and D_μ is the gauge-covariant derivative, which in the free theory is simply given by $D_\mu = \partial_\mu$. The naive free fermion action on the lattice is then obtained by replacing the derivative with the symmetric finite difference (2.11),

$$S_{\mathrm{N}} = a^4 \sum_{x\in\Lambda} \bar{\psi}(x)\,[\delta + m]\,\psi(x)\,. \tag{2.19}$$

The massive Dirac operator for this action $D_N = \delta + m$ is easily diagonalised by plane wave solutions $e^{ip\cdot x}$ with corresponding eigenvalues

$$\lambda = m \pm \frac{i}{a}\sqrt{\sum_\mu \sin^2 ap_\mu}\,. \tag{2.20}$$

The poles in the propagator corresponding to physical particles occur when these the eigenvalues vanish, and therefore for a fixed spatial momentum $\boldsymbol{p}$, p_0 is given by

$$p_0 = \pm\, iE(\boldsymbol{p}), \frac{\pi}{a} \pm iE(\boldsymbol{p})\,, \tag{2.21}$$

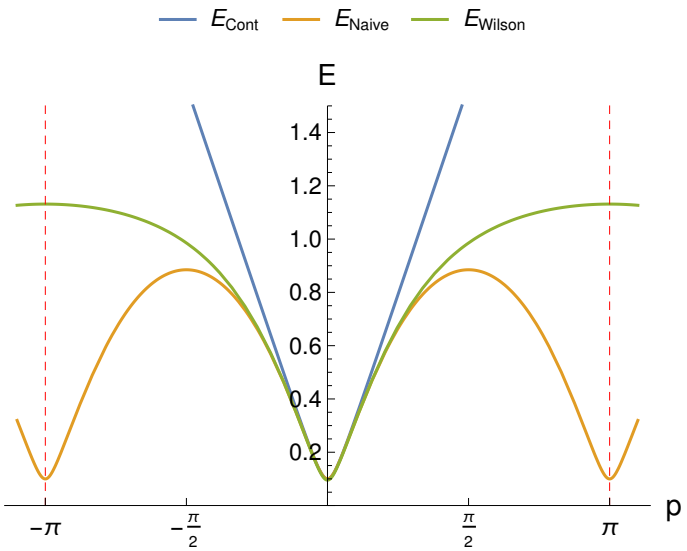

Figure 2.2 *Fermion dispersion relation for momentum* $\boldsymbol{p} = (p, 0, 0)$ *within the* 1^{st} *BZ* $(p \in (-\pi/a, \pi/a])$ *for continuum fermions, naive lattice fermions and Wilson fermions.*

where the real part of p_0 is restricted to the 1^{st} Brillouin zone (BZ) $(-\frac{\pi}{a}, \frac{\pi}{a}]$, and the dispersion relation is given by

$$E(\boldsymbol{p}) = \frac{1}{a}\sqrt{(am)^2 + \sum_i \sin^2 a\boldsymbol{p}_i}\,. \tag{2.22}$$

Taking the continuum limit $a \to 0$, the solutions $p_0 = \pm iE(\boldsymbol{p})$ recover the positive and negative energy particles. There are however two additional poles with $\text{Re}(p_0) = \frac{\pi}{a}$. These extra poles become infinitely far away from the origin in p_0 space as $a \to \infty$, however, they remain as light degrees of freedom and therefore do not decouple from the theory when the continuum limit is taken. Since the number of particles in the continuum theory has doubled, these extra particles are called the doublers.

In addition, looking at the lattice dispersion relation in eq. (2.22) that is depicted in fig. 2.2, it can be seen that the global minima corresponding to the rest energy of the particle is actually a set of 8 degenerate points $\boldsymbol{p} = (0,0,0), (\frac{\pi}{a}, 0, 0), ...(\frac{\pi}{a}, \frac{\pi}{a}, \frac{\pi}{a})$, which corresponds to a doubling of the particles in each spatial dimension. There are therefore 16 fermions in total generated by the naive fermion discretisation, while the target continuum theory contains only a single fermion.

While the doubling problem may seem somewhat innocuous, there are greater (and related) issues with this naive fermion discretisation. Unlike the continuum QCD discussed previously, this naive fermion discretisation does not suffer from the same anomalous breaking of the $\text{U}(1)_A$ axial symmetry. This is because, in the massless

limit, each doubler has an opposite chirality, and therefore $n_+ - n_- = 0$ in eq. (1.23) for all background gauge configurations. The lack of axial anomaly is a major issue since it cannot be recovered by taking the continuum limit, and therefore will not accurately reproduce the structure of the QCD spectrum.

An important result of the work in ref. [12] is the Nielsen–Ninomiya no-go theorem that states there are four desirable properties of a lattice fermion discretisation that cannot all be realised simultaneously.
These properties are:

1. The fermion action S is local.
2. The Dirac operator D has the correct continuum limit.
3. The theory is free from fermion doublers.
4. The massless Dirac operator possesses chiral symmetry $\{D, \gamma_5\} = 0$.

When constructing the naive fermion discretisation, we implicitly satisfied the no-go theorem by accepting the doublers into the theory. There are many alternatives to the naive discretisation to choose from, and the exact one used should be guided by the specific needs of the calculation being performed.

Generally, it is undesirable to give up either of the first two properties. The locality of the action is very beneficial for practical simulations at finite lattice spacing, and must be recovered in the continuum limit. Alternatively, it would be very problematic to give up the requirement that the Dirac operator obtained in the continuum is the correct one. Some commonly used discretisation give up the third property and accept the doublers (although usually not all 16 of them from the naive case). Finally, many of the most used actions instead give up chiral symmetry $\{D, \gamma_5\} \neq 0$.

Wilson Fermions

The original solution to the fermion doublers was proposed by Wilson in ref. [11], where the doublers can be given a mass that diverges as $a \to 0$, and therefore decouple from the theory in the continuum limit. In momentum space, this can be thought of as having a 4-momentum dependant mass

$$\widetilde{m}(p) = m + \frac{1}{a}\sum_{\mu}(1 - \cos ap_\mu) \tag{2.23}$$

which can be achieved by the inclusion of the Wilson term to the naive Dirac operator

$$D_{\mathrm{W}} = D_{\mathrm{N}} - \frac{a}{2}\sum_{\mu}\delta^{\mathrm{f}}_{\mu}\delta^{\mathrm{b}}_{\mu}\,. \tag{2.24}$$

It should be noted that since this Wilson term is effectively generating a mass-like term, it explicitly breaks chiral symmetry ($\{D_{\mathrm{W}}, \gamma_5\} \neq 0\}$) in order to satisfy the Nielsen–Ninomiya no-go theorem.

One very important consequence of this is that the quark mass is no longer protected from additive renormalisation. Therefore, in the interacting theory the chiral point ($m_\pi = 0$) no longer corresponds to zero bare mass $m_q = 0$. Instead, the bare quark mass must go through a tuning process to obtain the chiral point in the continuum. Chiral symmetry of the Dirac operator can greatly simplify operator mixing during renormalisation of higher-point vertices, as will be seen later in the case of the 4-quark effective Weak Hamiltonian. Because of this, the Wilson fermion action usually suffers from a more complicated renormalisation procedure than for chiral actions.

There exist improvements to Wilson fermions, such as the $O(a)$ improved Wilson-Clover fermions [13] and more recently stabilised Wilson-Clover fermions [14], but we shall not go into details of these actions here.

Other actions

A wide range of other fermion actions have been proposed since the inception of lattice field theory that attempt to circumnavigate the no-go theorem and incur the minimal side effects while satisfying the constraints. There are the "perfect fermion actions" which are constructed as a fixed point in the renormalisation group via a blocking procedure from the continuum theory [15]. In this way they preserve the chiral properties of the continuum theory, however the price they pay is that the lattice action is generally non-local and in practice is very difficult to perform computations.

Another approach is to accept the presence of the doublers, but reduce their number. This is done in the staggered formulation [16] where, in 4 dimensions, the number of fermions can be reduced from 16 down to 4 by a spin-diagonalisation procedure. Defining new fields ψ' and $\bar{\psi}'$ by

$$\psi(n) = \gamma_1^{n_1}\gamma_2^{n_2}\gamma_3^{n_3}\gamma_4^{n_4}\psi'(n) \qquad \text{and} \qquad \bar{\psi}(n) = \bar{\psi}'(n)\gamma_1^{n_1}\gamma_2^{n_2}\gamma_3^{n_3}\gamma_4^{n_4}\,, \tag{2.25}$$

it can be seen that the naive Dirac operator becomes diagonal in spinor space, giving 4 degenerate 1-component fields. The staggered action takes only one of these components, discarding the other 3. This also discards their associated doublers which takes the number of fermions down to just 4. One advantage is that the fermion fields no longer have spinor structure, and are therefore are a factor 4 smaller objects. The disadvantage is that the remaining doublers must be accounted for, which can be non-trivial.

Finally, one can give up the exact continuum chiral symmetry, and instead have a lattice analogue of chiral symmetry given by the Ginsparg-Wilson relation [17]

$$\{D, \gamma_5\} = aD\gamma_5 D\,, \tag{2.26}$$

which corresponds to a Dirac operator that is invariant under the modified axial transformation [18]

$$\psi \to e^{i\alpha\gamma_5(1-\frac{a}{2}D)}\psi \qquad \text{and} \qquad \bar{\psi} \to \bar{\psi}e^{i\alpha(1-\frac{a}{2}D)\gamma_5}\psi\,, \tag{2.27}$$

that tend to the original chiral transformation as $a \to 0$. It can be shown that any action satisfying eq. (2.26) has complex eigenvalues $\lambda = |\lambda|e^{i\phi}$ that satisfies $\cos\phi = \frac{a}{2}|\lambda|$, which is the equation of a circle centred on the real axis at $\frac{1}{a}$ with radius $\frac{1}{a}$. It is therefore clear that as $a \to 0$, this simply gives a set of eigenvalues on the imaginary axis, as is the case for the massless continuum Dirac operator.

The overlap formulation is one such solution to the Ginsparg-Wilson relation with a Dirac operator of the form

$$D_{\text{ov}} = \frac{1}{a}\big((1+m) + (1-m)\gamma_5\,\text{sgn}[H]\big) \tag{2.28}$$

where $H = \gamma_5 D$ is a hermitian kernel related to a γ_5-hermitian lattice Dirac operator D. The sign function acting on an operator is given by the spectral representation, where the function is applied to each of the eigenvalues of that operator. This is of course prohibitively expensive to compute exactly in a practical simulation, and therefore polynomial or rational approximations to this exact sign function are often used.

The simplest choice of kernel operator $H = \gamma_5 D_{\text{W}}(-M_0)$ is the Wilson Dirac operator with a negative mass $-M_0$. This is required since a strictly positive mass does not recreate the entire circle of eigenvalues, and in the free theory, $M_0 = 0$ has a zero mode of H for which the sign function is ill-defined.

The overlap action is very closely related to the domain wall fermion action which is heavily utilised in this work, and therefore we shall discuss this action in more detail.

2.2.1 Domain wall fermions

Kaplan's Formulation

The central concept of domain wall fermions is instead of considering a theory of chiral fermions in $2n$ ($n \in \mathbb{N}^+$) dimensions, we consider a non-chiral theory in $2n+1$ dimensions with some feature in this extra dimension that $2n$ dimensional chiral modes adhere to. In Kaplan's original formulation [19], the mass parameter of the fermion is promoted to a function of the position in this new dimension labelled s. In the continuum the Dirac operator has the form (for a 5D theory)

$$D_{5\mathrm{D}} = D_{4\mathrm{D}} + \gamma_5 \partial_s + m(s)\,, \tag{2.29}$$

where $D_{4\mathrm{D}}$ is the regular (massless) Dirac operator, and the $5D$ fields are $\Psi(x,s)$ and $\bar{\Psi}(x,s)$. The name domain wall comes from considering the mass function

$$m(s) = \begin{cases} m & \text{for} \quad s > 0 \\ -m & \text{for} \quad s < 0 \end{cases}\,, \tag{2.30}$$

that separates the space into two domains with mass of a different sign. The 4-dimensional chiral modes $P_{R,L}\psi(x)$ are then bound to the wall as their wavefunction has the form

$$\Psi(x,s) = [\alpha(s)P_R + \beta(s)P_L]\psi(x) \tag{2.31}$$

$$\alpha(s) = Ne^{-m|s|} \tag{2.32}$$

$$\beta(s) = N'e^{+m|s|}\,. \tag{2.33}$$

Clearly, for $m > 0$ with an infinite s extent, $\beta(s)$ in non-normalisable and therefore N' must be zero. For a finite s extent, however, this other chirality is normalisable, but will be exponentially suppressed at $s = 0$. This opposite chirality mode is instead predominantly bound to an anti-domain-wall that must be induced by the periodicity in the finite 5^{th} dimension.

Shamir Formulation

Inspired by Kaplan's formulation of domain wall fermions, Furman and Shamir developed a similar formulation that is advantageous for numerical simulations [20, 21]. The 5-dimensional Shamir domain wall Dirac operator takes the form

$$D_{\mathrm{DW}}(x,s|y,r) = D_{\parallel}(x|y)\delta_{s,r} + D_{\perp}(s|r)\delta_{x,y} \tag{2.34}$$

where there is a parallel component, $D_{\parallel}$, that only depends on the 4D position and is diagonal in the 5^{th} dimension, and a perpendicular component, $D_{\perp}$, that is diagonal in 4D space and is only dependent on the position in the 5^{th} dimension. These operators are given by

$$\begin{aligned}
D_{\parallel} =& D_{\mathrm{W}}(-M_5) + 1 && (2.35)\\
D_{\perp} =& -\left[P_L\delta_{s+1,r}(1-\delta_{s,L_s-1}) + P_R\delta_{s-1,r}(1-\delta_{s,0})\right] && (2.36)\\
&+ m(P_L\delta_{s,L_s}\delta_{1,r} + P_R\delta_{s,1}\delta_{L_s,r})\\
=& -\left[P_L\delta_{s+1,r} + P_R\delta_{s-1,r}\right] && (2.37)\\
&+ (m+1)\left(P_L\delta_{s,L_s}\delta_{1,r} + P_R\delta_{s,1}\delta_{L_s,r}\right) .
\end{aligned}$$

Note that $D_{\perp}$, as written in its second form, looks like a hopping term with periodic boundary conditions ($\Psi(x,L_s{+}1) = \Psi(x,1)$) plus a boundary term. Consequently, it can be seen that for $m=-1$, the full operator D_{DW} becomes simply a 5-dimensional Wilson fermion with mass $-M_5$.

It has been shown in ref. [22] (and in [23] for the more general forms discussed later) that with an appropriate change of field variables $\Psi(x,s) \to \chi(x,s)$, the Schur complement with respect to the $s=r=1$ component of D_{DW} gives the reduced operator for that component

$$D_{\chi} = -(1+T^{-L_s})\gamma_5\left[\frac{1+m}{2} + \frac{1-m}{2}\gamma_5\epsilon_{L_s}(H_T)\right] , \tag{2.38}$$

where $\epsilon_{L_s}(H_T) = \frac{T^{-L_s}-1}{T^{-L_s}+1}$, T is the transition matrix defined by $T^{-1} = \frac{1+H_T}{1-H_T}$, and

$$H_T = \gamma_5\frac{D_{\mathrm{W}}}{2+D_{\mathrm{W}}} \tag{2.39}$$

is the Shamir kernel. The Wilson Dirac operator $D_{\mathrm{W}} = D_{\mathrm{W}}(-M_5)$ is always evaluated at the negative mass parameter so we leave the argument implicit. It

can be seen that

$$\epsilon_{L_s}(x) = \tanh\big(L_s \tanh^{-1} x\big) \tag{2.40}$$

is the tanh approximation of the sign function. Note that this new operator D_χ is a purely 4D operator acting on a 4D field $\chi_1(x)$. Performing the path integral of the $\chi_1(x)$ field gives the fermionic determinant

$$\det\big(-(1+T^{-L_s})\gamma_5\big)\det\left(\frac{1+m}{2}+\frac{1-m}{2}\gamma_5\epsilon_{L_s}(H_T)\right), \tag{2.41}$$

where the first factor is independent of the mass m, and the second is an approximation to the overlap action with the kernel H_T and the sign function ϵ_{L_s}. Therefore, up to the extra non-trivial factor coming from the 5D theory, this is an approximation to the overlap Dirac operator, $\widetilde{D}_{\text{ov}}$. Notice that at $m = 1$ the overlap determinant goes to 1, giving only the determinant of the 5D artefacts. Therefore, these artefacts can be removed by introducing a 5D pseudofermion field, Φ, that obeys the domain wall operator with mass $m = 1$, known as the Pauli-Villars (PV) field. The partition function then has the form

$$\begin{aligned}
Z &= \int \mathcal{D}[U\Psi,\bar{\Psi},\Phi,\bar{\Phi}]\exp\big\{-S_g-\bar{\Psi}D_{\text{DW}}(m)\Psi-\bar{\Phi}D_{\text{DW}}(1)\Phi\big\} && (2.42)\\
&= \int \mathcal{D}[U]\frac{\det[D_{\text{DW}}(m)]}{\det[D_{\text{DW}}(1)]}\exp\{-S_g\} && (2.43)\\
&= \int \mathcal{D}[U]\frac{\det[D_{\chi}(m)]}{\det[D_{\chi}(1)]}\exp\{-S_g\} && (2.44)\\
&= \int \mathcal{D}[U]\det\Big[\widetilde{D}_{\text{ov}}(m)\Big]\exp\{-S_g\}\,. && (2.45)
\end{aligned}$$

It can be seen that the tanh approximation to the sign function becomes exact in the limit $L_s \to \infty$, corresponding to an infinite extent in the 5^{th} dimension, although any practical simulation is limited to a finite value of L_s. When evaluating the quality of this approximation, we must take into account the difference between the target and approximate function, but only over the range of eigenvalues of the kernel.

For the Shamir kernel with $M_5 = 1$ in the free theory, it can be seen that the maximum eigenvalues have a magnitude of 1. Figure 2.3 shows the tanh approximation to the sign function on the range $-1 \le x \le 1$ for several values of L_s, along with the relative error of that approximation. Of course the quality of the approximation used must be weighed against the computation cost of simulating a larger 5^{th} dimension.

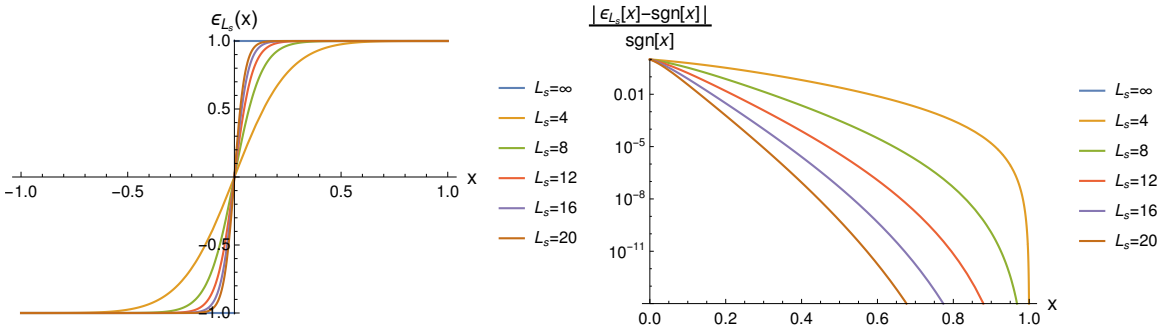

Figure 2.3 *Tanh approximation to the sign function for different L_s on the range $x \in [-1, 1]$ (left), and the relative error of these approximations (right).*

General Möbius Formulation

A generalised version of the Shamir setup is the Möbius domain wall formulation from Brower, Neff and Orginos [23–25]. It is designed in such a way as to construct a kernel operator that is a Möbius transformation of the Wilson-Dirac operator. The most general form available also allows this transformation to be dependent on the position in the 5^{th} dimension. The parallel part of the 5D domain wall operator $D_{\parallel}$ becomes

$$D_{\parallel}^{(s)} = \frac{b_s\, D_{\mathrm{W}} + 1}{1 - c_s\, D_{\mathrm{W}}}\,, \tag{2.46}$$

where two new sets of parameters have been introduced which are dependent on the position in the 5^{th} dimension s. It can be seen that the Shamir result is recovered when $b_s = 1$ and $c_s = 0$ for all s.

The effective overlap operator obtained here is given by

$$\widetilde{D}_{\mathrm{ov}} = \frac{1+m}{2} + \frac{1-m}{2}\gamma_5 \frac{\Pi_s(1+H_T^{(s)}) - \Pi_s(1-H_T^{(s)})}{\Pi_s(1+H_T^{(s)}) + \Pi_s(1-H_T^{(s)})}\,, \tag{2.47}$$

where the generalised Möbius kernel is

$$H_T^{(s)} = \gamma_5 \frac{(b_s + c_s) D_{\mathrm{W}}}{2 + (b_s - c_s) D_{\mathrm{W}}}\,, \tag{2.48}$$

which is a Möbius transformation, defined by the parameters b_s, c_s and M_5.

A few important limits of this general form should be discussed. As already observed, the Shamir kernel with a tanh approximation is given by $b_s = 1$ and $c_s = 0$. A similar limit is the scaled Shamir fermion with $b_s + c_s = \alpha$ and $b_s - c_s = 1$. The scaling

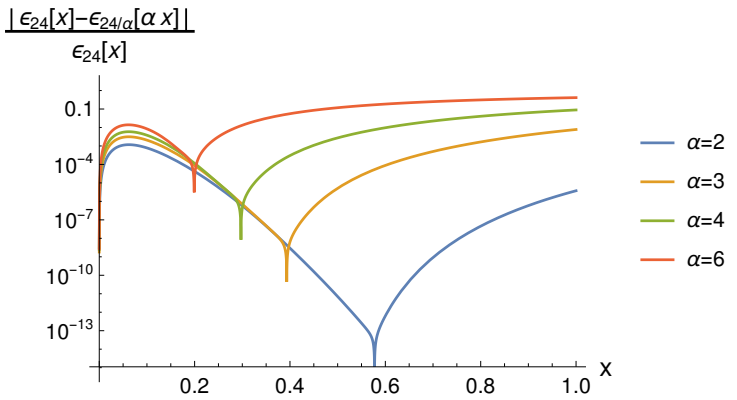

Figure 2.4 *Relative error of the scaled Shamir sign function compared to the Shamir sign function at* $L_s = 24$.

parameter α gives the same sign function approximation, but scales the argument by α. Note that since $\mathrm{sgn}(x) = \mathrm{sgn}(\alpha x)$ for all $\alpha > 0$, the Shamir and scaled Shamir actions are two approximations of the same overlap action. This scaling allows the optimal region of the tanh approximation to be applied over different parts of the spectrum of H_T. A reasonable approximation of this scaled sign function is

$$\epsilon_{L_s}(\alpha x) \simeq \epsilon_{\alpha L_s}(x)\,, \tag{2.49}$$

where the relative error is shown in fig. 2.4 for the case of $L_s = 24$. Since this approximation is relatively good, the scaled Shamir action can be thought of as allowing for the reduction of L_s by a factor of α compared to the standard Shamir action, significantly reducing the computational cost.

The final case relevant for this work is when $b_s - c_s = 1$ and $b_s + c_s = \frac{\alpha}{\omega_s}$. The approximation to the sign function then becomes

$$\mathrm{sgn}(\alpha x) \simeq \frac{\Pi_s(\omega_s + \alpha x) - \Pi_s(\omega_s - \alpha x)}{\Pi_s(\omega_s + \alpha x) + \Pi_s(\omega_s - \alpha x)}\,, \tag{2.50}$$

which is the Zolotarev rational approximation to the sign function with scaled argument. The values of ω_s and can be tuned to give a more evenly spread error than the tanh approximation, or to reduce the error in regions where the eigenvalue density of H_T is large.

Note that for this to be a real valued function, the ω_s must be real or come in complex conjugate pairs. This approximation is referred to as the zMöbius action. An example of this approximation with $L_s = 10$ for a target of an $L_s = 24$ scaled Shamir kernel ($\alpha = 2$), is shown in fig. 2.5, and other examples of this approximation are given in ref. [26].

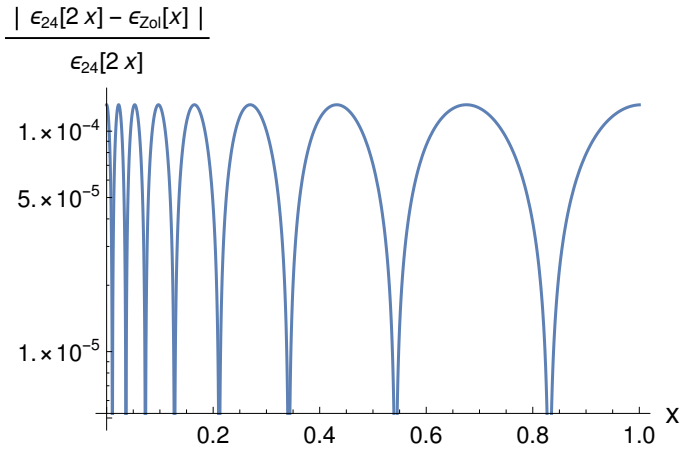

Figure 2.5 *Relative error of the Zolotarev approximation (with $L_s = 10$) to the scaled Shamir sign function.*

2.2.2 MADWF Algorithm

The Möbius Accelerated Domain Wall Fermion (MADWF) algorithm, as originally demonstrated in ref. [27], is a method of inverting the 5D domain wall Dirac operator approximately, using a different domain wall action that is cheaper to invert. We shall refer to the target of the approximation as the outer action, and the inner action as that used for the approximation. For example one might use this method to accelerate a Shamir (outer) action with $L_s = 24$, by solving a scaled Shamir (inner) action with $L_s = 12$ and scaling factor $\alpha = 2$. Neglecting any overhead from the MADWF algorithm, this would lead to a factor ~ 2 improvement in solve times.

The algorithm is entirely based around the domain wall - overlap correspondence, as discussed previously, where the inversion of both the outer and inner actions correspond to the same approximate 4D overlap linear system. Therefore the outer solve can be transformed into an inner solve and the solution can be transformed back. This is then iterated in a restarting defect correction process.

Consider a linear system with the outer domain wall 5D action of mass m, $D_{\mathrm{DW}}(m)$, and a source b

$$D_{\mathrm{DW}}(m)x = b\,. \tag{2.51}$$

By applying the transformation to the χ field alluded to earlier, this system is equivalent to

$$E_{\mathrm{DW}}(m)y = c\,, \tag{2.52}$$

where the new source, solution and operators are defined as

$$c = \mathcal{P}^{-1}D_{\mathrm{DW}}^{-1}(1)b \tag{2.53}$$

$$y = \mathcal{P}^{-1}x \tag{2.54}$$

$$E_{\mathrm{DW}}(m) = \mathcal{P}^{-1}D_{\mathrm{DW}}^{-1}(1)\,D_{\mathrm{DW}}(m)\mathcal{P}\,, \tag{2.55}$$

where $D_{\mathrm{DW}}(1)$ is the PV operator, and $\mathcal{P}_{sr} = P_L\delta_{s,r} + P_R\delta_{s+1(\mathrm{mod}\ L_s),r}$ is the chiral permutation operator in the 5^{th} dimension. The operator $E_{\mathrm{DW}}(m)$ has the form in

the 5^{th} dimension

$$E_{\mathrm{DW}} = \begin{pmatrix} D_{\mathrm{ov}} & 0 & 0 & \cdots & 0 \\ A_2 & 1 & 0 & \cdots & 0 \\ A_3 & 0 & 1 & \cdots & 0 \\ \vdots & & & \ddots & \\ A_{L_s} & 0 & 0 & \cdots & 1 \end{pmatrix} , \tag{2.56}$$

where D_{ov} is the approximate overlap operator corresponding to D_{DW}, and the A_s are additional operators related to D_{ov}, the form of which is not important for this discussion. The first element of the linear equation is simply given by

$$D_{\mathrm{ov}} y_1 = c_1 \, , \tag{2.57}$$

which is a 4D system, and the field c_1 can be simply extracted from c.

Considering a second domain wall operator D'_{DW} that, following the exact same procedure, has a corresponding overlap operator D'_{ov} that is tuned such that $D'_{\mathrm{ov}} \simeq D_{\mathrm{ov}}$. If we require that the effective overlap systems are approximately equivalent, i.e. $c_1 \simeq c'_1$, the source of the second system can be replaced by that from the original system

$$D'_{\mathrm{ov}} y'_1 = c_1 \, . \tag{2.58}$$

The domain wall - overlap correspondence can then be inverted by constructing the 5D boundary source

$$b' = D'_{\mathrm{DM}}(1) \mathcal{P} \left(c_1, 0, 0, \cdots\right)^T . \tag{2.59}$$

With the new source constructed, the inner 5D system

$$D'_{\mathrm{DW}}(m) x' = b' \tag{2.60}$$

can then be inverted using a standard Conjugate Gradient (CG) solver to acquire x'. Once this solution is found, it must be translated back to the outer domain wall system. This is done by constructing $y'_1 = (\mathcal{P}^{-1} x')_1$, and making the approximation $y_1 \simeq y'_1$. The full 5D y is obtained from the relation $y_{s>1} = c_s - A_s y_1$. It can be

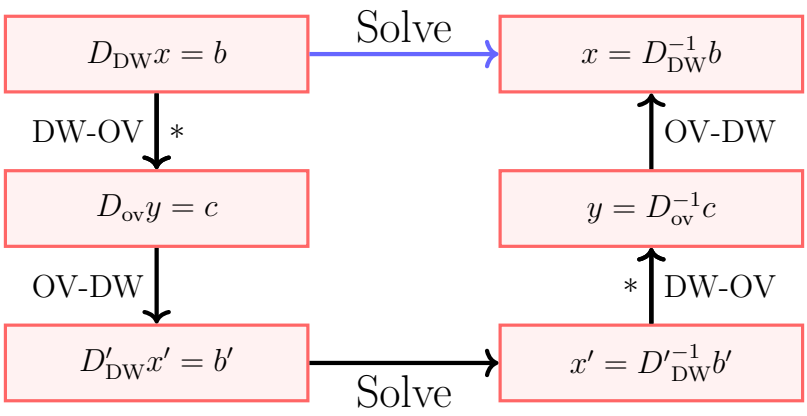

Figure 2.6 *Workflow of the MADWF solver (black) and the standard solver (blue). The outer operator is designated D_{DW} and the inner operator D'_{DW}. Steps are labelled with the domain wall - overlap correspondence (DW-OV) and its inverse (OV-DW). $*$ indicates step requiring a PV solve.*

seen from the form of $E_{\mathrm{DW}}(m)$ in eq. (2.56), that

$$\begin{aligned}\widetilde{y} =& E_{\mathrm{DW}}(m)(-y'_1, c_2, c_3, \cdots)^T && (2.61)\\ =& (-D_{\mathrm{ov}}y'_1, c_2 - A_2 y'_1, \cdots)^T && (2.62)\\ \simeq& (-D_{\mathrm{ov}}y_1, y_2, y_3, \cdots\cdots)^T\,, && (2.63)\end{aligned}$$

which gives us approximately the remaining elements of y. If $\mathbb{P}_s$ is a projector that selects only a single 5^{th} dimensional slice, then we can construct

$$y \simeq \mathbb{P}_1 y' + \sum_{s>1} \mathbb{P}_s \widetilde{y}\,, \tag{2.64}$$

which is trivially related to the final solution via $x = \mathcal{P}y$.

A schematic of the workflow of the MADWF solver is given in fig. 2.6. While this process may seem computationally quite simple, there are two steps that require the inversion of the PV operator $D_{\mathrm{DW}}(1)$, which is generally much cheaper than inverting $D_{\mathrm{DM}}(m)$ for lighter quarks, but can still add a significant overhead. The inner and outer actions, and solver tolerances must then be tuned in order to evaluate any improvements in time-to-solution.

For use in work performed during this PhD, the MADWF algorithm was implemented in the Hadrons codebase [28] as an additional solver module using a restarted defect correction. It grants users full access to the CG solver parameters of the inner, outer and PV steps to allow for maximum flexibility when performing tuning. In addition, there is the option to accelerate the inner solve with a guesser function such as a low-mode deflation step (see 2.4.2). Finally, the implementation accepts a

precision change between the outer and inner fields allowing for further acceleration.

The MADWF algorithm was used in the published works [1, 29], to accelerate a scaled Shamir outer solve with $L_s = 24$ and $\alpha = 2$, with a zMöbius inner solve with $L_s = 10$ and low-mode deflation with 2000 exact eigenvectors. The MADWF tuning was performed on the Tesseract supercomputer which is a CPU based machine located in the Edinburgh EPCC facility. Figure 2.7 shows the time-to-solution as a function of the inner solver residual for different choices of the PV residual, and for one choice where the PV and inner residual remain equal. It can be seen that the minimum is when the inner and PV residual both equal 10^{-4}, and is 8.8 times faster than without the MADWF algorithm.

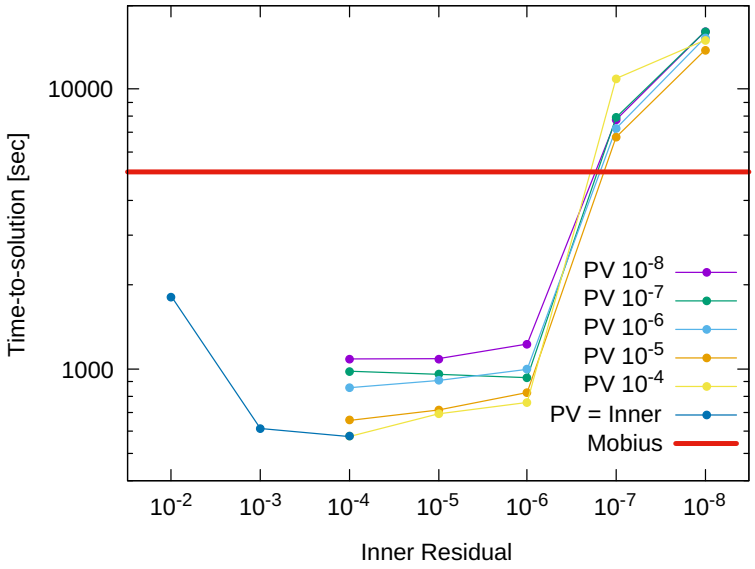

Figure 2.7 *MADWF solver solution time for light quarks on the C0 ensemble (see table 2.2) with an outer scaled Shamir action ($\alpha = 2$ and $L_s = 24$) and zMöbius inner action ($L_s = 10$ and 2000 eigenvector exact low-mode deflation). Shown is a scan over inner and PV solver stopping residual. The time taken for a standard scaled Shamir solve is shown for reference.*

It is unfortunate however, that the situation is different on GPU based machines. After a retuning for this new architecture, the MADWF solver only gives roughly a factor 2 speed-up over the standard Möbius solve. This is due to the fact that the inner low-mode deflation is significantly slower than on a CPU machine, and the optimisations that can be applied are not simple to propagate into the MADWF solver.

Particle	Flavour	J^P	I	I_3	Interpolator
p	uud		$\frac{1}{2}$	$\frac{1}{2}$	$\epsilon^{abc}(u_a^T\Gamma d_b)u_c$
n	ddu		$\frac{1}{2}$	$-\frac{1}{2}$	$\epsilon^{abc}(d_a^T\Gamma u_b)d_c$
Σ^+	uus		1	1	$\epsilon^{abc}(u_a^T\Gamma s_b)u_c$
Σ^0	uds	$\frac{1}{2}^+$	1	0	$\epsilon^{abc}\left((u_a^T\Gamma s_b)d_c + (d_a^T\Gamma s_b)u_c\right)$
Σ^-	dds		1	-1	$\epsilon^{abc}(d_a^T\Gamma s_b)d_c$
Λ	uds		0	0	$\epsilon^{abc}\left((u_a^T\Gamma d_b)s_c + (u_a^T\Gamma s_b)d_c - (d_a^T\Gamma s_b)u_c\right)$
Ξ^0	ssu		$\frac{1}{2}$	$\frac{1}{2}$	$\epsilon^{abc}(s_a^T\Gamma u_b)s_c$
Ξ^-	ssd		$\frac{1}{2}$	$-\frac{1}{2}$	$\epsilon^{abc}(s_a^T\Gamma d_b)s_c$
Ω^-	sss	$\frac{3}{2}^+$	0	0	$\epsilon^{abc}(s_a^T\Gamma_\mu s_b)s_c$

Table 2.1 *Baryon label, flavour structure, spin-parity(J^P), Isospin (I) and its third component (I_3), and lattice interpolator for the QCD stable octet and duplet baryons. $q \in \{u, d, s\}$ are quark fields with spinor structure and q^T are transposed fields. a, b, c are color indices and μ is a Lorentz index. For the spin-$\frac{1}{2}$ baryons the gamma structure is $\Gamma = C\gamma_5$, while for the spin-$\frac{3}{2}$ Ω baryon $\Gamma_\mu = C\gamma_\mu$, where $C = -\gamma_y\gamma_t$ is the charge conjugation operator*

2.3 Baryons on the Lattice

While the methodology of extracting baryonic quantities from the lattice is conceptually very similar to extracting mesonic observables, there are practical differences that are introduced by the additional spin degree of freedom.

The fundamental objects of interest on the lattice are correlation functions. The simplest is the 2-point correlation function

$$\Gamma^2(t, \boldsymbol{p}) = \sum_{\boldsymbol{x}} e^{i\boldsymbol{p}\cdot\boldsymbol{x}} \langle \psi(t, \boldsymbol{x})\bar{\psi}(0)\rangle \,, \tag{2.65}$$

where $\psi(x)$ is an interpolation operator that has the quantum numbers of the baryon of interest. One set of interpolators for the ground state baryons is given in table 2.1. The expectation value in eq. (2.65) corresponds to the spectral trace

$$\langle \psi(t, \boldsymbol{x})\bar{\psi}(0)\rangle = \mathrm{Tr}\left[e^{-HT}\psi(t, \boldsymbol{x})\bar{\psi}(0)\right] / \mathrm{Tr}\left[e^{-HT}\right] , \tag{2.66}$$

where H is the Hamiltonian operator, T is the temporal extent of the lattice, and the trace is given by

$$\mathrm{Tr}[\mathcal{O}] = \sum_n \sum_{\boldsymbol{p}} \mathcal{N}_{n,\boldsymbol{p}} \langle n, \boldsymbol{p}| \mathcal{O} |n, \boldsymbol{p}\rangle \,, \tag{2.67}$$

with the sum running over the states n, spatial momentum $\boldsymbol{p}$, and $\mathcal{N}_{n,\boldsymbol{p}} =$

$1/\langle n,\boldsymbol{p}|n,\boldsymbol{p}\rangle$ being the state normalisation. Similarly, the identity can we written

$$\mathbb{1} = \sum_{n}\sum_{\boldsymbol{p}} \mathcal{N}_{n,\boldsymbol{p}} \left|n,\boldsymbol{p}\right\rangle \left\langle n,\boldsymbol{p}\right| . \tag{2.68}$$

For this work we consider the normalisation $\langle n,\boldsymbol{p}|n,\boldsymbol{p}\rangle = 2E_n(\boldsymbol{p})$ where $E_n(\boldsymbol{p})$ is the energy of the state $|n,\boldsymbol{p}\rangle$. By inserting the identity in-between the two interpolators, and using the space-time translation property

$$\mathcal{O}(x) = e^{Ht}e^{i\boldsymbol{p}\cdot\boldsymbol{x}}\mathcal{O}(0)e^{-i\boldsymbol{p}\cdot\boldsymbol{x}}e^{-Ht} , \tag{2.69}$$

the spectral representation for the 2-point function is given by

$$\begin{aligned}\Gamma^2(t,\boldsymbol{p}) = \sum_{n,m}\sum_{\boldsymbol{k}} \mathcal{N}_{n,\boldsymbol{p}+\boldsymbol{k}}\mathcal{N}_{m,\boldsymbol{k}} \left\langle m,\boldsymbol{k}\right| \psi(0) \left|n,\boldsymbol{p}+\boldsymbol{k}\right\rangle \left\langle n,\boldsymbol{p}+\boldsymbol{k}\right| \bar{\psi}(0) \left|m,\boldsymbol{k}\right\rangle \\ \times e^{-E_m(\boldsymbol{k})(T-t)}e^{-E_n(\boldsymbol{p}+\boldsymbol{k})t} .\end{aligned} \tag{2.70}$$

Note that if using Domain-Wall Fermions, the quark propagator contains additional unphysical poles that can contribute negative eigenvalues of the transfer matrix e^{-H} for certain values of M_5 [30, 31]. This has the effect of introducing oscillatory contributions of the form $(-1)^t e^{-Et}$ to eq. (2.70) which can in principle be included in fits. Since these unphysical poles are at the level of the cuttoff, these oscillatory states generally have large masses and can therefore be considered as excited states that are relevant only at small times.

If the time, t, is very far from the end of the lattice $t \ll T$, this will suppress all states m apart from the lowest energy state, corresponding to the vacuum with $E_0 = 0$. Therefore the 2-point function can be taken to be

$$\Gamma^2(t \ll T,\boldsymbol{p}) = \sum_{n} \frac{\left\langle 0\right| \psi(0) \left|n,\boldsymbol{p}\right\rangle \left\langle n,\boldsymbol{p}\right| \bar{\psi}(0) \left|0\right\rangle}{2E_n(\boldsymbol{p})} e^{-E_n(\boldsymbol{p})t} , \tag{2.71}$$

and similarly if the time is far from the origin

$$\Gamma^2(t \gg 0,\boldsymbol{p}) = \sum_{n} \frac{\left\langle n,-\boldsymbol{p}\right| \psi(0) \left|0\right\rangle \left\langle 0\right| \bar{\psi}(0) \left|n,-\boldsymbol{p}\right\rangle}{2E_n(\boldsymbol{p})} e^{-E_n(\boldsymbol{p})(T-t)} . \tag{2.72}$$

So far this process is no different from mesonic systems, however, baryonic

interpolators are spinor objects, and therefore the overlap factors are given by

$$\langle 0|\,\psi(0)\,\big|n^+,s,\boldsymbol{p}\big\rangle = Z_n^+ u_s(\boldsymbol{p}) \tag{2.73}$$
$$\big\langle n^+,s,\boldsymbol{p}\big|\,\bar{\psi}(0)\,|0\rangle = (Z_n^+)^* \bar{u}_s(\boldsymbol{p}) \tag{2.74}$$
$$\langle 0|\,\bar{\psi}(0)\,\big|n^+,s,\boldsymbol{p}\big\rangle = Z_n^+ \bar{v}_s(\boldsymbol{p}) \tag{2.75}$$
$$\big\langle n^+,s,\boldsymbol{p}\big|\,\psi(0)\,|0\rangle = (Z_n^+)^* v_s(\boldsymbol{p})\,, \tag{2.76}$$

where the states have been given 2 additional labels to indicate they have positive parity, and spin projection s. $u_s(\boldsymbol{p})$ and $v_s(\boldsymbol{p})$ are the positive and negative energy spinors respectively. Similarly for the negative parity states

$$\langle 0|\,\psi(0)\,\big|n^-,s,\boldsymbol{p}\big\rangle = Z_n^- \gamma_5 u_s(\boldsymbol{p}) \tag{2.77}$$
$$\big\langle n^-,s,\boldsymbol{p}\big|\,\bar{\psi}(0)\,|0\rangle = (Z_n^-)^* \bar{u}_s(\boldsymbol{p})\gamma_5 \tag{2.78}$$
$$\langle 0|\,\bar{\psi}(0)\,\big|n^-,s,\boldsymbol{p}\big\rangle = Z_n^- \bar{v}_s(\boldsymbol{p})\gamma_5 \tag{2.79}$$
$$\big\langle n^-,s,\boldsymbol{p}\big|\,\psi(0)\,|0\rangle = (Z_n^-)^* \gamma_5 v_s(\boldsymbol{p})\,. \tag{2.80}$$

Since the sum over states includes the different spin projections and parities, and the spinor completeness relations are $\sum_s u_s(\boldsymbol{p})\bar{u}_s(\boldsymbol{p}) = i\not{p}+m$ and $\sum_s v_s(\boldsymbol{p})\bar{v}_s(\boldsymbol{p}) = -i\not{p}+m$, the spectral representation becomes

$$\begin{aligned}\Gamma^2(t,\boldsymbol{p}) = &\sum_{n^+} \frac{|Z_n^+|^2 m_n}{E_n^+(\boldsymbol{p})} \left(\mathbb{P}_n^+(\boldsymbol{p}) e^{-E_n^+(\boldsymbol{p})t} + \mathbb{P}_n^-(\boldsymbol{p}) e^{-E_n^+(\boldsymbol{p})(T-t)}\right) \\ &+ \sum_{n^-} \frac{|Z_n^-|^2 m_n}{E_n^-(\boldsymbol{p})} \left(\mathbb{P}_n^-(\boldsymbol{p}) e^{-E_n^-(\boldsymbol{p})t} + \mathbb{P}_n^+(\boldsymbol{p}) e^{-E_n^-(\boldsymbol{p})(T-t)}\right)\end{aligned} \tag{2.81}$$

where the projectors $\mathbb{P}^\pm(\boldsymbol{p}) = \frac{\mp i\not{p}+m}{2m}$, which at zero momentum are simply $\mathbb{P}^\pm(\boldsymbol{0}) = P^\pm = \frac{1}{2}(1 \pm \gamma_t)$. Taking the trace with P^+ gives

$$\frac{1}{2}\,\mathrm{Tr}\big[\Gamma^2(t,\boldsymbol{0})P^+\big] = \sum_{n^+} |Z_n^+|^2 e^{-E_n^+(\boldsymbol{0})t} + \sum_{n^-} |Z_n^-|^2 e^{-E_n^-(\boldsymbol{0})(T-t)}\,, \tag{2.82}$$

which isolates the positive parity baryon in the first half of the lattice, and the negative parity baryon in the second half.

Finally, in the limit of large time separations, the exponentials isolate only the ground states of these sums which correspond to the baryon of interest, and its negative parity partner propagating backwards from the boundary at T. If the time separation is not large enough, the ground state will not be properly isolated and the low lying excited states provide a non-negligible contribution. This is known as

excited state contamination, and is a large problem in the measurement of baryonic observables, where a usable signal is only observed for a early time windows. This is the signal-to-noise problem which is described in the next section.

2.3.1 Signal-to-noise Problem

It is observed in lattice simulations that baryonic correlation functions have a degradation of signal as the source-sink separation increases. This is contrary to what is observed in zero momentum pseudoscalar meson correlation functions, which maintain a constant relative signal throughout. A description of this degradation was originally given by Parisi [32] and Lepage [33], where the variance of the 2-point function is related to higher point correlation functions, and the contributing spectra are examined. We shall follow the same reasoning, but extend the argument to gain additional insight into the statistical behaviour of the correlators.

Consider an arbitrary interpolator $\mathcal{O}$ for a particle P, then the corresponding 2-point function is given by

$$\begin{aligned}\Gamma(t) =& \langle \mathcal{O}(t)\mathcal{O}^\dagger(0)\rangle && (2.83)\\ \simeq& \langle 0|\,\mathcal{O}\,|P\rangle\,\langle P|\,\mathcal{O}^\dagger\,|0\rangle\, e^{-E_P t}\,, && (2.84)\end{aligned}$$

where we have taken the ground state dominance for large t. The statistical noise associated with taking N measurements of the gauge average can be approximated (for large N) by

$$\sigma(t) \simeq \sqrt{\frac{\mathrm{Var}(t)}{N}} \tag{2.85}$$

where the variance is given by

$$\begin{aligned}\mathrm{Var}(t) =& \left\langle \left(\mathcal{O}(t)\mathcal{O}^\dagger(0) - \Gamma(t)\right)^\dagger \left(\mathcal{O}(t)\mathcal{O}^\dagger(0) - \Gamma(t)\right)\right\rangle && (2.86)\\ =& \langle \mathcal{O}(0)\mathcal{O}^\dagger(t)\mathcal{O}(t)\mathcal{O}^\dagger(0)\rangle - \Gamma^\dagger(t)\Gamma(t)\,, && (2.87)\end{aligned}$$

and is therefore described by the combination of a 4-point function and the original 2-point function. Interestingly this is a physical observable rather than an artefact of the Monte-Carlo sampling procedure, and therefore the properties of the uncertainty of our measurement can be reasoned about purely on physical grounds. Before doing

so, we shall extend the argument slightly by considering the covariance

$$\begin{aligned}\mathrm{Cov}(t,t') =& \left\langle \left(\mathcal{O}(t)\mathcal{O}^\dagger(0) - \Gamma(t)\right)^\dagger \left(\mathcal{O}(t')\mathcal{O}^\dagger(0) - \Gamma(t')\right)\right\rangle && (2.88)\\ =& \langle \mathcal{O}(0)\mathcal{O}^\dagger(t)\mathcal{O}(t')\mathcal{O}^\dagger(0)\rangle - \Gamma^\dagger(t)\Gamma(t')\,, && (2.89)\end{aligned}$$

of which the variance is simply the diagonal $\mathrm{Var}(t) = \mathrm{Cov}(t,t)$. The off-diagonal part gives rise to the statistical correlation between the different times of the correlator

$$\mathrm{Corr}(t,t') = \frac{\mathrm{Cov}(t,t')}{\sqrt{\mathrm{Var}(t)\mathrm{Var}(t')}} \tag{2.90}$$

such that $\mathrm{Corr}(t,t) = 1$. The spectral decomposition of the covariance for the time ordering $t' \gg t \gg 0$ has the form

$$\begin{aligned}\mathrm{Cov}(t,t') =& \langle \mathcal{O}(t')\mathcal{O}^\dagger(t)\mathcal{O}^\dagger(0)\mathcal{O}(0)\rangle - \Gamma^\dagger(t)\Gamma(t') && (2.91)\\ \simeq& \langle 0|\,\mathcal{O}\,|P\rangle\,\langle P|\,\mathcal{O}^\dagger\,|\ell\rangle\,\langle \ell|\,\mathcal{O}^\dagger\mathcal{O}\,|0\rangle\; e^{-m_\ell t}\, e^{-E_P(t'-t)}\\ & - \left|\langle 0|\,\mathcal{O}\,|P\rangle\,\langle P|\,\mathcal{O}^\dagger\,|0\rangle\right|^2\, e^{-2E_P\, t}\, e^{-E_P(t'-t)}\,. && (2.92)\end{aligned}$$

where the state ℓ is the lightest state that couples to the $\mathcal{O}^\dagger\mathcal{O}$ operator. Note that we can construct an unflavoured state $P\bar{P}$ from a P and it's antiparticle with zero back-to-back momentum. Therefore, ignoring any finite-volume energy shift, the lightest state should satisfy $m_\ell \leq 2m_P$, giving the dominant contribution to the covariance at large time separations

$$\mathrm{Cov}(t,t') \sim e^{-m_\ell\, t}\, e^{-E_P(t'-t)}\,, \tag{2.93}$$

and by the same reasoning, the variance goes like

$$\mathrm{Var}(t) \sim e^{-m_\ell t}\,. \tag{2.94}$$

The signal-to-noise ratio therefore behaves as

$$R_P(t) = \frac{\Gamma(t)}{\sigma(t)} \sim e^{-(E_P - \frac{m_\ell}{2})t}\,, \tag{2.95}$$

where we see that it decays exponentially in time with a scale defined by $(E_P - \frac{m_\ell}{2})^{-1}$. The correlation has the form

$$\mathrm{Corr}(t,t') \sim \frac{e^{-m_\ell\, t}\, e^{-E_P(t'-t)}}{e^{-m_\ell/2\,(t+t')}} = e^{-(E_P - \frac{m_\ell}{2})(t'-t)}\,. \tag{2.96}$$

As should be expected, for large enough t, t', the correlation is only a function

of the separation of the two points being compared. It is however less expected that this function has the same exponential decay rate as the signal-to-noise ratio $\mathrm{Corr}(t, t') \sim R_P(t - t')$.

We shall now examine some examples in iso-symmetric QCD at the physical point. If P is the pion, then the lightest unflavoured state that couples to 4 quarks is the $\pi\pi$ state, and therefore $m_\ell = 2m_\pi$. In this case the energy difference in the signal-to-noise ratio is $E_\pi - m_\pi$, which for a stationary pion gives a constant $R_\pi(t)$. Therefore the relative signal does not degrade in time. Alternatively, for a moving pion, $E_\pi > m_\pi$, and therefore $R_\pi(t)$ decays exponentially in time with the pion's kinetic energy, which is only a small exponential signal-to-noise problem unless the momentum is sufficiently large.

If we instead consider P to be a nucleon, the lightest unflavoured state for which $\langle \ell | \, \psi_N \bar{\psi}_N \, | 0 \rangle \neq 0$ is not the $N\bar{N}$ state, but instead can be a 3π state since there are 3 light quark-antiquark pairs. Therefore R_N decays with the energy difference $m_N - \frac{3}{2} m_\pi$, which is very large (~ 730MeV) at the physical point. With exactly the same reasoning for the other baryons, it is clear that baryonic correlation functions generally have a severe exponential signal-to-noise problem.

While baryonic observables suffer greatly from this signal-to-noise problem, there is one advantage we observe over the light pseudoscalar mesons. This is due to the fact that the correlation matrix behaves in the same way as the signal-to-noise ratio, and therefore is asymptotically constant for the light pseudoscalar mesons, while it decays exponentially for baryonic correlation functions.

A simplified model of the correlation matrix that only incorporates this asymptotic behaviour is given by

$$\mathrm{Corr}(t, t') = \delta_{tt'} + c \, e^{-m|t-t'|}(1 - \delta_{tt'}) \tag{2.97}$$

which has only two parameters, the coefficient c and the "mass" of the exponential decay $m = E_P - m_\ell/2$. Figure 2.8 shows the scaling of the condition number of this correlation matrix with its size, for a fixed coefficient $c = 0.5$ and a range of masses. In practice this is a measure of the difficulty of inverting this matrix during the fitting procedure. Of course, with only finitely many data samples, the estimation of this correlation matrix is noisy, and at some point the matrix inversion will become numerically unstable. We can see that the m parameter acts as a regulator on the condition number preventing the matrix from becoming arbitrarily ill-conditioned.

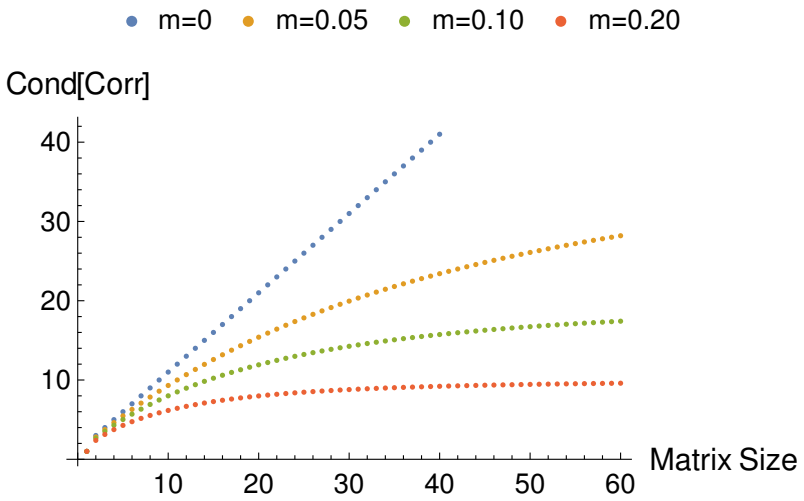

Figure 2.8 *Scaling of the condition number of the correlation matrix with the matrix size, using the model in eq. (2.97). The coefficient used is $c = 0.5$ and several mass parameters m are shown.*

Name	a^{-1} [MeV]	L [fm]	$N_L^3 \times N_T$	N_s	Action	m_π [MeV]	m_K [MeV]	Ref.
C0	1730(4)	5.5	$48^3 \times 96$	24	Möbius	139	499	[37]
C1	1785(5)	2.6	$24^3 \times 64$	16	Shamir	340	620	[37, 38]
C2	1785(5)	2.6	$24^3 \times 64$	16	Shamir	432	626	[37, 38]
M0	2359(7)	5.4	$64^3 \times 128$	12	Möbius	139	507	[37]

Table 2.2 *Details of the RBC-UKQCD domain wall fermion ensembles used in this work. The action lists the type of fermion action used, and all ensembles use the Iwaskai gauge action. The specific Möbius action used in the C0 and M0 ensembles are the scaled Shamir fermions with $\alpha = 2$.*

2.4 Simulating Lattice QCD

The software used throughout the work presented in this thesis are the open-source C++ libraries Grid [34, 35] and Hadrons [28]. Grid is a massively parallel software package that provides cross-platform functionality for performing large scale LQFT simulations. It provides many heavily optimised operations with support for CPU multithreading, multi-node MPI decomposition, SIMD vectorisation, SIMT and GPU acceleration. Hadrons is a workflow management library that packages commonly used Grid functionality into modules, manages object lifetimes, and provides module scheduling to minimise the peak memory requirements. It also provides support for resource monitoring and output file organisation via sqlite databases.

Several improvements and new functionalities required for the work presented in this thesis have been implemented in both of these libraries. This includes improvements to the baryon 2-point and 4-quark contractions, as well as the implementation of general baryonic quark bilinear 3-point function contractions, which have been critical to the measurements presented in chapter 6. In addition, the MADWF solver has been implemented in Hadrons to accelerate solves of domain wall fermion propagators with large L_s (see section 2.2.2). Finally, much work has been done to optimise low-mode deflation (see section 2.4.2) for use with GPU architectures, including the implementation of batch-deflation, local-coherence deflation and a batched multi-right-hand-side mixed precision solver.

All of the numerical results presented in this thesis are measured on the RBC-UKQCD ensembles with an Iwasaki gauge action [36] and various domain wall fermion actions. Table 2.2 shows some key details for these ensembles and gives the names by which they will be referred in this thesis.

2.4.1 Setting the Scale

In lattice simulations, all quantities are calculated in lattice units as dimensionless numbers, where the corresponding dimensionful quantity comes with an appropriate power of the lattice spacing a. Since a is not an input to the theory, it must be obtained by matching a lattice observable, X, to its desired physical value in the target theory. In the case where X has mass dimension 1

$$a = \frac{(aX)_{\text{lat}}}{X_{\text{phys}}} \,. \tag{2.98}$$

One commonly used observable is the mass of the Ω^- baryon since it has a clear experimental value with which to match. It does however suffer from an exponential signal-to-noise problem (see section 2.3.1) which makes fitting the effective mass problematic. In addition, it is relatively expensive to compute compared to purely gluonic observables, since it requires the computation of fermion propagators.

Lattice simulations of many quantities are now reaching sub-percent precision, and therefore need to include the effects of Quantum Electrodynamics (QED) and the mass difference of the up and down quarks. These effects are referred to as isospin breaking effects. In this section, we present the calculation of the Ω^- baryon mass with the full theory of QCD+QED. Since the Ω^- baryon consists of 3 strange quarks, the non-zero m_u-m_d mass difference only enters through disconnected diagrams which are not considered here. On the ensembles used, the strange quark is slightly mistuned away from its physical value by some amount δm_s, and therefore this mistuning must be corrected for in the calculation of the Ω^- mass.

Since the electric charge e and δm_s are small quantities, both effects can be included perturbatively. The next-to-leading order expansion of the Ω^- mass in these parameters is given by

$$m_\Omega^{\text{QED}} = m_\Omega|_0 + \frac{1}{2} q_s^2 e^2 \frac{\partial^2 m_\Omega}{\partial e^2}\bigg|_0 + \delta m_s \, \frac{\partial m_\Omega}{\partial m_s}\bigg|_0 + \mathcal{O}(e^4, \delta m_s^2) \,, \tag{2.99}$$

where the subscript 0 indicates the quantity is evaluated at $e = 0$ and $\delta m_s = 0$, called the simulation point, and the first order derivative $\frac{\partial m_\Omega}{\partial e}\big|_0 = 0$ has been used which is a result of the fact that the mass shift must be independent of the sign of the electric charge.

The zero momentum two-point function used to extract the Ω^- mass is given by

$$\Gamma_\Omega(t) = \frac{1}{4}\sum_i \sum_{\boldsymbol{x}} \mathrm{Tr}\left[\langle \psi^i_\Omega(t,\boldsymbol{x})\bar{\psi}^i_\Omega(0)\rangle P^+\right] , \tag{2.100}$$

where the operator $\bar{\psi}^\mu_\Omega(x) = \psi^{\mu\,\dagger}_\Omega(x)\gamma^0$ denotes the spin-3/2 interpolating operator for the Ω^- baryon, and the spatial direction i is summed over. The point source interpolator is given in table 2.1, and an alternative interpolator replaces the quark fields with Gaussian smeared fields

$$\tilde{s}(t,\boldsymbol{x}) = \sum_{\boldsymbol{y}} \exp\left[-(\boldsymbol{x}-\boldsymbol{y})^2/(2\sigma^2)\right] s(t,\boldsymbol{y}) , \tag{2.101}$$

with some width σ. Since this smearing is not gauge covariant, it requires gauge fixing of the QCD gauge configurations.

One feature of lattice baryon interpolating operators is that, on a torus, they couple to negative parity states propagating backward in time. As a consequence, assuming ground state dominance, the correlator has the form

$$\Gamma_\Omega(t) = |Z_\Omega|^2\, e^{-m_\Omega t} + |\bar{Z}_\Omega|^2\, e^{-\bar{\omega}_\Omega(T-t)} \tag{2.102}$$

where $\bar{\omega}_\Omega$ is the energy of the state with negative parity ground state. The operator-state overlaps for a state with spin projection $s \in \{\pm\frac{3}{2}, \pm\frac{1}{2}\}$ are defined by $Z_\Omega\, u^\mu_s = \langle 0|\, \psi^\mu_\Omega(0)\, |\Omega, s\rangle$ and $\bar{Z}_\Omega\, \gamma_5 u^\mu_s = \langle 0|\, \psi^\mu_\Omega(0)\, \big|\bar{\Omega}, s\big\rangle$, where u^μ_s is the positive energy solution to the spin-3/2 Rarita-Schwinger equation (see e.g. [39] for a recent review), and $|\Omega, s\rangle$ and $\big|\bar{\Omega}, s\big\rangle$ are states with positive and negative parity respectively. More details regarding spin-$\frac{3}{2}$ particle solutions are given in appendix D.

Since baryon correlators are significantly affected by an exponential signal-to-noise-ratio problem, we are restricted to early times $t \ll T/2$ where the backward propagating contributions are negligible, giving just

$$\Gamma_\Omega(t) = |Z_\Omega|^2\, e^{-m_\Omega t} , \tag{2.103}$$

which can be computed at the simulation point and fit to extract $m_\Omega|_0$.

Taking the derivatives of this correlator with respect to the e.m. coupling and the

strange quark mass, and taking the ratio with the original correlator, gives

$$\mathcal{R}^{\text{em}}_{\Omega}(t) = \frac{1}{\Gamma_\Omega(t)} \frac{\partial^2 \Gamma_\Omega(t)}{\partial e^2}\bigg|_0 = \frac{1}{|Z_\Omega|^2} \frac{\partial^2 |Z_\Omega|^2}{\partial e^2}\bigg|_0 - \frac{\partial^2 m_\Omega}{\partial e^2}\bigg|_0 t\,, \tag{2.104}$$

$$\mathcal{R}^{s}_{\Omega}(t) = \frac{1}{\Gamma_\Omega(t)} \frac{\partial \Gamma_\Omega(t)}{\partial m_s}\bigg|_0 = \frac{1}{|Z_\Omega|^2} \frac{\partial |Z_\Omega|^2}{\partial m_s}\bigg|_0 - \frac{\partial m_\Omega}{\partial m_s}\bigg|_0 t\,, \tag{2.105}$$

which are both linear in time, and can therefore be fit to a linear ansatz to extract the quantities of interest.

We begin by considering the Wick contractions for the iso-QCD correlator given in eq. (2.100), of which there are 6 contributions. These are shown diagrammatically in fig. 2.9. The color structure of these contractions is not represented in these diagrams.

For the QED corrections to this correlator, we require two insertions of the quark-photon interaction $iZ_V \sum_x \bar{s} \not{A} s$, where A_μ is a stochastically evaluated photon field in the QED$_L$ prescription and Z_V is the vector current renormalisation factor. This term corresponds to a photon propagator connecting the quark legs, as well as a quark-disconnected contribution that is omitted in this work. Taking for example diagram (a) in fig. 2.9, the corresponding QED corrections are shown in fig. 2.10 where (a), (b) and (c) are the exchange diagrams and (d), (e) and (f) are the self energy diagrams contributing to $\frac{\partial^2 \Gamma_\Omega(t)}{\partial e^2}$. Similarly, quark-mass corrections are given by the insertion of the scalar density $\sum_x \bar{s}s$. Again taking diagram (a) in fig. 2.9 as an example, the mass corrections are given by the diagrams in fig. 2.11, as well as a disconnected contribution that is also omitted.

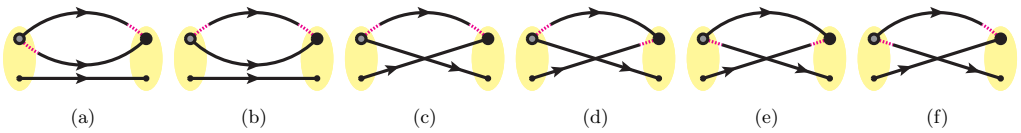

Figure 2.9 *All Feynman diagrams corresponding to the tree-level correlation function $\Gamma_\Omega(t)$. Points connecting two propagators are contractions of a diquark pair, and dashed magenta portions of a propagator indicate contraction with a transposed quark field.*

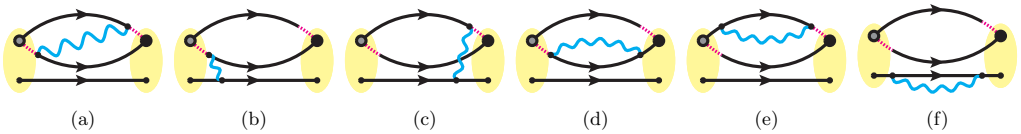

Figure 2.10 *All (connected) Feynman diagrams contributing to $\mathcal{R}^{em}_{\Omega}(t)$ originating from the tree-level contribution shown in fig. 2.9 (a). Similar diagrams exist for the other contributions.*

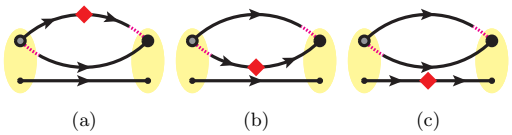

Figure 2.11 *All (connected) Feynman diagrams contributing to $\mathcal{R}^s_\Omega(t)$ originating from the tree-level contribution shown in fig. 2.9 (a). Similar diagrams exist for the other contributions.*

Numerical Results

We now present numerical results for these quantities on the close to physical point C0 and M0 ensembles from table 2.2. The data used on the C0 ensemble is the same as is used for QED scale setting in [29], however the analysis is independently performed by the author of this thesis. The results of these different analyses agree within statistical errors as expected.

Figures 2.12 and 2.13 show fits to the log effective mass

$$m_{\text{eff}}(t) = \ln\left(\frac{\Gamma_\Omega(t)}{\Gamma_\Omega(t+1)}\right), \tag{2.106}$$

the ratios $\mathcal{R}^{\text{em}}_\Omega(t)$ and $\mathcal{R}^{\text{s}}_\Omega(t)$, and its (second) derivative with respect to m_s and e

$$\delta_{m_s} m_{\text{eff}} = \frac{\partial m_{\text{eff}}(t)}{\partial m_s} = \mathcal{R}^s_\Omega(t) - \mathcal{R}^s_\Omega(t+1) \tag{2.107}$$

$$\delta_{\text{em}} m_{\text{eff}} = \frac{\partial^2 m_{\text{eff}}(t)}{\partial e^2} = \mathcal{R}^{\text{em}}_\Omega(t) - \mathcal{R}^{\text{em}}_\Omega(t+1) \tag{2.108}$$

for the C0 and M0 ensembles respectively. The fit values are given in tables 2.3 and 2.4, along with the two-tailed p-value which is the probability that the χ^2 test statistic would be more extreme than the observed value under the assumption that the fit describes the data. A 2-state fit ansatz is used for the simulation point Ω^- mass, while only a single state ansatz is used for the derivatives, due to a large number of additional undesired parameters destabilising the fits. The Ω^- mass in the absence of QED or strange quark retuning is consistent with those measured on these two ensembles in ref. [37].

On the C0 ensemble, these quantities are combined to give the full Ω^- mass in the presence of QED and with physical strange quark mass. It can be seen that the statistical error on this quantity is heavily dominated by that of the simulation point mass. A similar combined value is not given on the M0 ensemble since the strange quark mass retuning in the presence of isospin-breaking effects is not currently known on this ensemble.

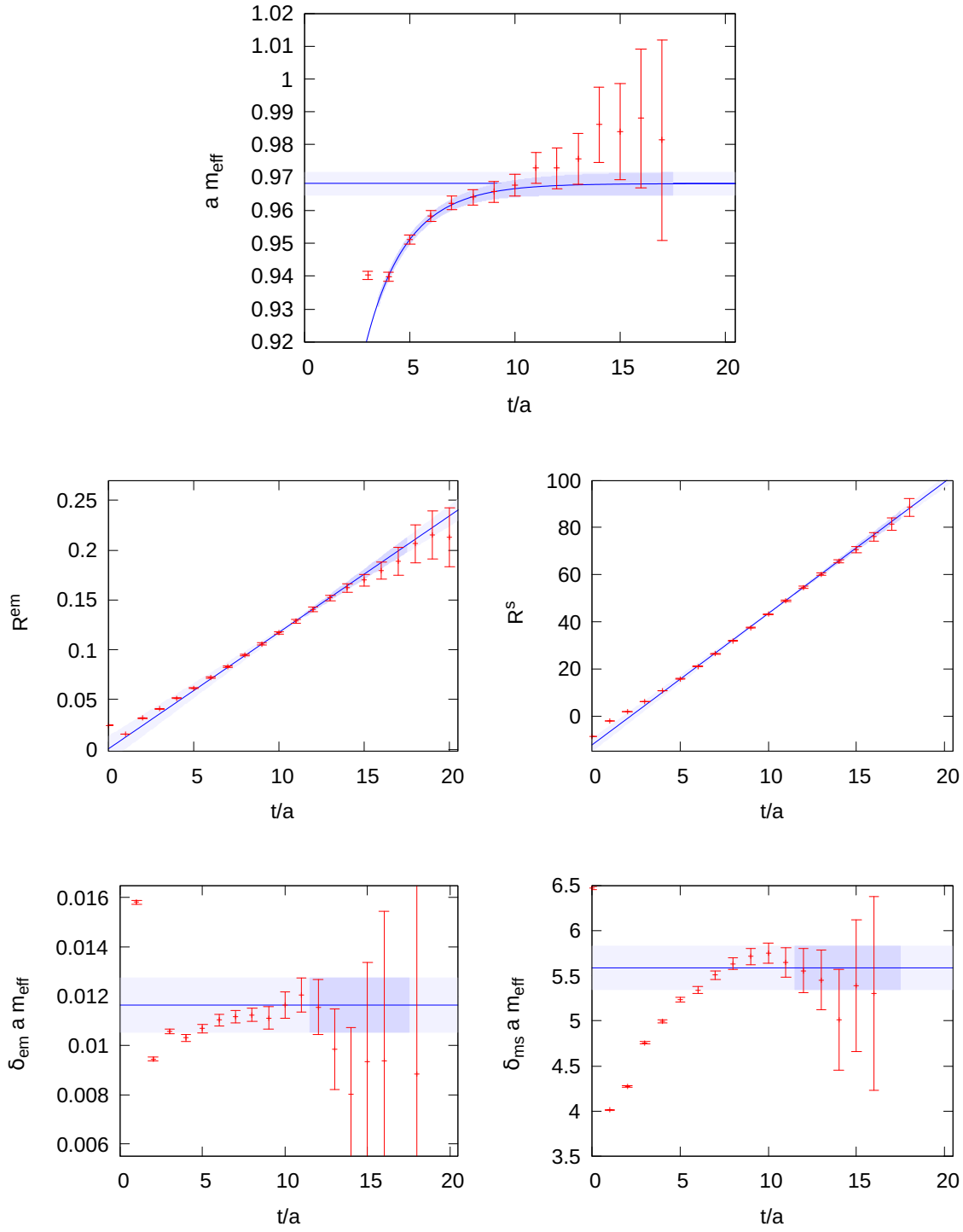

Figure 2.12 *Fits to the Ω^- baryon effective mass (top), the ratios of the corrections in the e.m. coupling (middle left) and bare strange quark mass (middle right) and their derivatives (bottom) on the C0 ensemble (see table 2.2).*

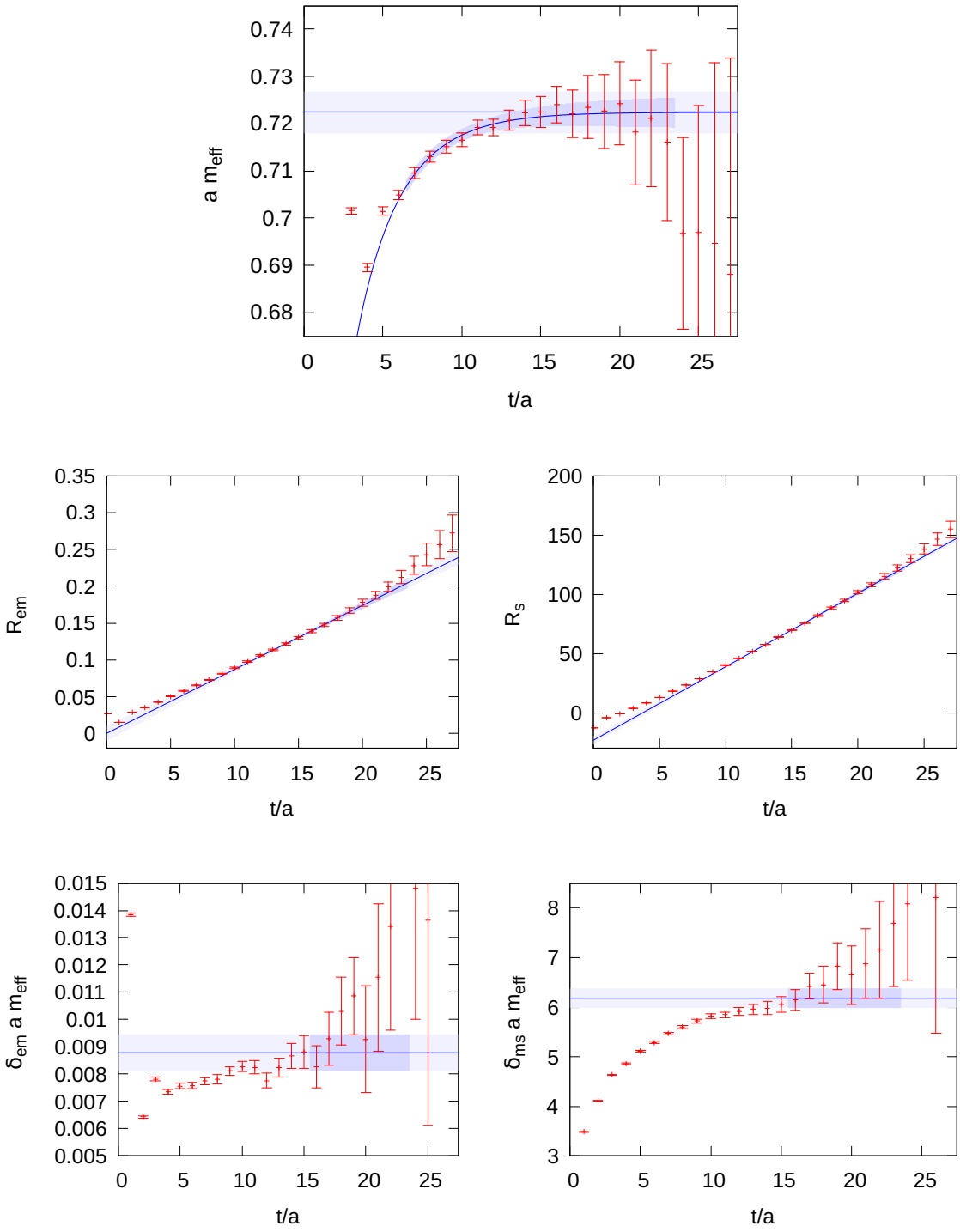

Figure 2.13 *Fits to the Ω^- baryon effective mass (top), the ratios of the corrections in the e.m. coupling (middle left) and bare strange quark mass (middle right) and their derivatives (bottom) on the M0 ensemble (see table 2.2).*

Observable	Value	p-value
am_Ω	0.9682(35)	0.351
$\frac{\partial^2 am_\Omega}{\partial e^2}$	$1.17(11) \times 10^{-2}$	0.972
$\frac{\partial am_\Omega}{\partial am_s}$	5.59(24)	0.707
am_Ω^{QED}	0.9637(35)	-

Table 2.3 *Fits results for the mass of the Ω^- baryon and its derivatives in the e.m. coupling and bare strange quark mass on the $C0$ ensemble. These are combined to give the lattice result for the QED value using $e^2 = \frac{4\pi}{137}$, and $\delta m_s = -0.0010(4)$ from [29].*

Observable	Value	p-value
am_Ω	0.7224(44)	0.141
$\frac{\partial^2 am_\Omega}{\partial e^2}$	$8.78(66) \times 10^{-3}$	0.408
$\frac{\partial am_\Omega}{\partial am_s}$	6.18(19)	0.902

Table 2.4 *Fits results for the mass of the Ω^- baryon and its derivatives in the e.m. coupling and bare strange quark mass on the $M0$ ensemble. These are not combined to give a final result since the strange quark mass shift is not yet known on this ensemble.*

M	x	b
$\gamma_5 D$	S	$\gamma_5 \eta$
$D\gamma_5$	$\gamma_5 S$	η
$D^\dagger D$	S	$D^\dagger \eta$
$DD^\dagger$	$(D^\dagger)^{-1} S$	η

Table 2.5 *Example choices for creating a hermitian linear system that is equivalent to eq. (2.109).*

2.4.2 Deflation

Generally, the most computationally expensive part of making measurements of fermionic quantities on the lattice is the (repeated) inversion of the Dirac operator on various sources, i.e. solving the equation

$$DS = \eta \,, \tag{2.109}$$

where S is the quark propagator sourced by η, and D is the Dirac operator. This is a very large, but sparse, linear system which is often well suited to CG type algorithms. However, since D is not a Hermitian operator, the linear system must be modified to contain a Hermitian operator

$$Mx = b \tag{2.110}$$

where $M = M^\dagger$. Some examples of M, x and b are listed in table 2.5, the first two of which require the Dirac operator to be γ_5-hermitian, $\gamma_5 D \gamma_5 = D^\dagger$.

A measure of the difficulty of solving this linear system is the condition number of the matrix M. If M has dimension N, then the eigenvalues can be labelled λ_i for $i = 1, 2, ..., N$, where they are ordered by their magnitude $|\lambda_1| \leq |\lambda_2| \leq ...|\lambda_N|$. The condition number is then given by

$$\kappa = \left| \frac{\lambda_N}{\lambda_1} \right| . \tag{2.111}$$

For a CG algorithm, once the initial transient behaviour has ended, each subsequent iteration improves the norm-squared error of the solution on average by a factor [40]

$$\Sigma = \frac{\sqrt{\kappa} - 1}{\sqrt{\kappa} + 1} \,. \tag{2.112}$$

For $\kappa \gg 1$, $\Sigma \simeq 1 - \frac{2}{\sqrt{\kappa}}$ showing that a larger condition number increases the number of iterations needed to achieve a given precision on the solution. While the matrix

to be inverted gives the general characteristics of the problem, the difficulty of the inversion process is also dependant on the source b. If b has no support from certain eigen-modes of M, then the corresponding eigen-directions will be trivially solved for by a zero starting guess, and therefore the effective condition number can be considered

$$\kappa_{\text{eff}} = \left| \frac{\lambda_{\max \in b}}{\lambda_{\min \in b}} \right| . \tag{2.113}$$

This effective condition number, and therefore the iteration count, can be reduced by constructing linear systems in which the source has no support in the high and/or low eigenspace of the matrix M.

Iterative algorithms like CG require an initial starting guess for the solution, x_0, that is commonly chosen to be a zero vector. If instead there exists a good approximation to the solution, this can be used as the initial guess. Writing the full solution as $x = x_0 + x'$ allows the linear equation to be rewritten as

$$Mx' = b' = b - Mx_0 \, . \tag{2.114}$$

This gives us freedom to modify the linear system to improve the effective condition number.

Low-mode deflation is a technique that utilises a precomputed set of the lowest n eigenvectors v_i and eigenvalues λ_i of the operator M. A guess for the CG is constructed specifically to remove support of the source on the lowest eigen-modes of M.

Since the inverse of the matrix M can be written

$$M^{-1} = \sum_{i=1}^{N} \frac{1}{\lambda_i} v_i v_i^\dagger \, , \tag{2.115}$$

this matrix can be inverted exactly on the low-mode subspace (using the $n < N$ lowest eigenvectors), giving the guess

$$x_0 = \sum_{i=1}^{n} \frac{1}{\lambda_i} \left(v_i, b \right) v_i \, , \tag{2.116}$$

where (a, b) is the inner product of the complex vectors a and b. The effective linear

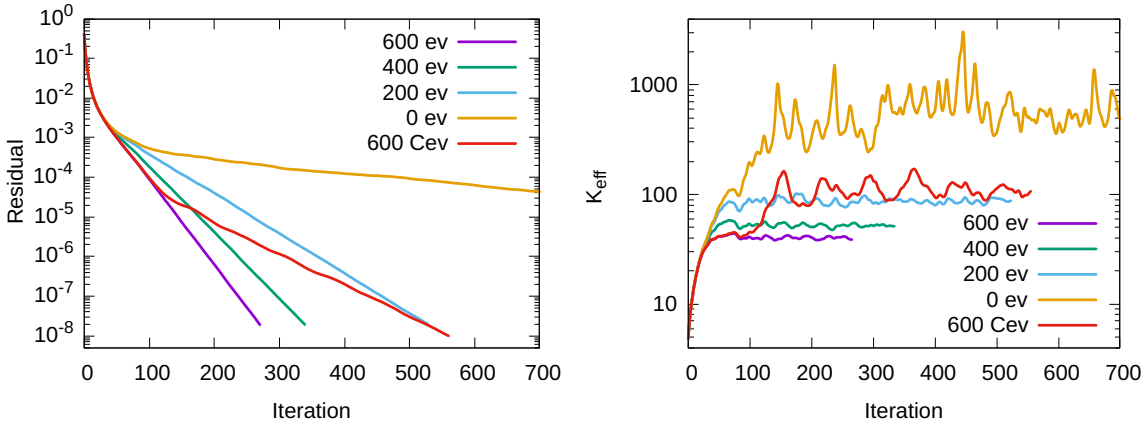

Figure 2.14 *Residual (left) and effective condition number (right) histories for deflation of the light quark on the C1 ensemble, with several numbers of exact eigenvectors, and 600 local-coherence compressed eigenvectors.*

system to solve is then given by

$$Mx' = b - Mx_0 = \sum_{i=n+1}^{N} b_i v_i \,, \tag{2.117}$$

which has an effective condition number

$$\kappa_{\text{eff}} = \left| \frac{\lambda_N}{\lambda_{n+1}} \right| \leq \left| \frac{\lambda_N}{\lambda_1} \right| \,. \tag{2.118}$$

This can significantly reduce the number of iterations to solution, depending on the number of eigenvectors used and the eigenvalue density of the low modes. Figure 2.14 shows the residual history and measured condition number for several numbers of low modes used to deflate a light quark on the C1 ensemble listed in table 2.2. It can be seen how the total number of iterations to solution, and the height of the κ_{eff} plateau, decrease with an increasing number of low-modes used in deflation.

Eigenvector Compression

Due to the fact that these eigenvectors are lattice sized objects, storing many of them on disk or in memory can become problematic as lattices get larger and/or finer. For this reason, it is hugely beneficial to compress these eigenvectors in some way.

The simplest approach is to reduce the numerical precision with which they are

stored, which can easily reduce the disk/memory footprint by a factor 2 when going from double to single precision floating point numbers. This is a form of lossy compression that has the advantage of only requiring the casting of fields to different precisions, which is a relatively fast operation on modern hardware. It does, however, throw away information about the physics indiscriminately, loosing information of both high and low value to the system being solved.

A more physically motivated approach introduced by Lüscher in ref. [41] utilises the local coherence of the low-mode eigenvectors to remove redundant information. This local-coherence deflation has previously been investigated on physical point lattice ensembles in ref. [42], where it has been seen to yield a compression of up to 90% for the eigenvectors of the red-black preconditioned 5D domain wall fermion Dirac operator.

Local coherence is the observation that two fields $\psi(x)$ and $\phi(x)$ can be orthogonal globally $(\phi, \psi) = \sum_{x\in\Lambda} \phi^\dagger(x)\psi(x) = 0$, but not orthogonal when restricted to only a local subvolume of the lattice Λ_a, $\sum_{x\in\Lambda_a} \phi^\dagger(x)\psi(x) \neq 0$. Splitting the full lattice Λ into several local sublattices $\Lambda = \Lambda_1 \cup \Lambda_2 ... \cup \Lambda_A$, fields can be restricted to a specific sublattice Λ_a as

$$\psi^a(x) = \begin{cases} \psi(x) & \text{for} \quad x \in \Lambda_a \\ 0 & \text{else} \end{cases} , \tag{2.119}$$

and an inner product on the sublattice Λ_a can be defined as

$$(\phi, \psi)_a = \sum_{x\in\Lambda_a} \phi^\dagger(x)\psi(x) = (\phi^a, \psi^a) \tag{2.120}$$

where it can be seen that $(\phi^a, \psi^b) \propto \delta^{ab}$ since the sublattices Λ_a and Λ_b share no sites if $a \neq b$. Taking the lowest n normalised eigenvectors of the operator M, the hermiticity of M guarantees these are globally orthogonal $(v_i, v_j) = \delta_{ij}$, however locally they may be coherent $(v_i, v_j)_a \neq 0$ for $i \neq j$. Defining a set of orthonormal basis vectors on the sublattice as u_k^a, such that $(u_k, u_{k'})_a = \delta_{kk'}$, the Dirac operator eigenvectors can be decomposed as

$$v_i^a = \sum_k (u_k, v_i)_a u_k^a \,. \tag{2.121}$$

By writing all fields in this local basis form, it can be seen that the exact deflation

of source b is equivalent to

$$x_0 = \sum_i \frac{1}{\lambda_i}(v_i, b)v_i = \sum_{a,k}\sum_i \frac{1}{\lambda_i}\left(\sum_{a',k'}(u_{k'}, v_i)^*_{a'}(u_{k'}, b)_{a'}\right)(u_k, v_i)_a u^a_k \,. \tag{2.122}$$

We can now associate the sublattice inner product of a field with a basis vector $(u^a_k, \psi^a)_a = \widetilde{\psi}_k(a)$ as a field in a new space where a behaves like a spatial position coordinate and k like some internal degrees of freedom. We refer to fields on the original lattice Λ as fine fields, while those on this new space as coarse fields, since each sublattice Λ^a corresponds to a single site of a coarsened lattice $\widetilde{\Lambda}$. The inner product on this new space is denoted as

$$\langle\widetilde{\phi}, \widetilde{\psi}\rangle = \sum_a \sum_k (\widetilde{\phi}_k(a))^* \widetilde{\psi}_k(a) \,. \tag{2.123}$$

In this new notation, the exact low mode deflation from eq. (2.122) has the form

$$x_0 = \sum_{a,k} \widetilde{x}_{0k}(a)\, u^a_k \qquad , \qquad \widetilde{x}_{0k}(a) = \left[\sum_i \frac{1}{\lambda_i}\langle\widetilde{v}_i, \widetilde{b}\rangle \widetilde{v}_{ik}(a)\right] . \tag{2.124}$$

This is exactly equivalent to using the basis vectors u^a_k to project the eigenvectors v_i and the source b into the coarse space, then doing an exact low-mode deflation with these fields to get $\widetilde{x}_{0k}(a)$, and finally promoting back to the fine space.

The only issue now is constructing the basis vectors u^a_k. Note that in practice the number of basis vectors in the complete set is larger than the number of low modes eigenvectors used, and therefore only span a subspace of the basis. The source b is arbitrary and therefore may span the whole basis, however, since the deflation only takes the projection on the low-mode subspace, this extra span is irrelevant. This allows for the basis to be truncated, while still being exact, to just the basis vectors that span the space of eigenvectors on the sublattice.

In order to guarantee the truncated basis captures the subspace spanned by the eigenvectors, it can be constructed from them via an orthonormalisation procedure on the local sublattice Λ_a, giving n basis vectors. Note however that with all n basis vectors, this procedure is equivalent to exact low-mode deflation. Since no information has been lost it is clear that no compression has taken place, and therefore the total memory/storage required has not improved.

The local coherence of the eigenvectors $(v_i, v_j)_a \neq 0$ for $i \neq j$ shows that the eigenvectors on each sublattice overlap with some common set of local basis vectors,

and have only small overlap with the rest. Therefore, we can truncate the basis vectors further to only include these major axes, rendering the deflation inexact, but also reducing the size of the basis that needs to be stored. This is done by constructing the basis vectors by block orthonormalising the $\widetilde{n} < n$ lowest eigenvectors.

Figure 2.14 shows the deflation of a light quark on the C1 ensemble with 600 local coherence compressed eigenvectors, using a basis size of $\widetilde{n} = 150$ and a local lattice size of $2^4 \times 16$ on a 5D lattice of global size $24^3 \times 64 \times 16$. This corresponds to a compression of 65%. It can be seen that the effective condition number initially plateaus to the same value as 600 exact eigenvalues, but later increases as the residual error reaches the level of the inexactness from the compression. This inexactness can be overcome using a restarting defect correction that redeflates at each step.

In the course of this project the local coherence deflation, as well as compression and decompression of the eigenvectors, has been implemented in the Grid and Hadrons libraries. This allows us to begin computing light quark observables on the M0 ensemble in table 2.2 with the Tursa supercomputer.

2.4.3 All-Mode-Averaging

When performing measurements on the lattice, the Dirac operator must be inverted many times, which is often of great computational cost. The number of iterations of a CG algorithm, and therefore the time to solution, is dependent on the stopping residual chosen. This must be chosen appropriately to minimise the cost on each inversion, but also achieve an accurate solve.

If a particular residual is deemed good enough to recover all the important properties of the observable in question, i.e. improving the residual has no noticeable effect on the observables, we call inversions to this residual "exact" solves.

Of course, solving to a worse residual will decrease the time-to-solution for an inversion, but will also have some effect on the observable in question, which is an artefact of the measurement and not the physics we wish to capture. We call this an "inexact" solve. In performing an inexact solve, a bias has been introduced into the measurement that must be corrected to get reliable results. This bias correction step to guarantee our results are free from statistically significant measurement artefacts, is known as the All Mode Averaging (AMA) procedure and was first described in [43].

Consider a general exact observable to measure on the lattice $\mathcal{O}_{\text{Ex}}$, and an inexact observable $\mathcal{O}_{\text{Inex}}$, that is some approximation of $\mathcal{O}_{\text{Ex}}$. The unbiased gauge average of this observable with N measurements is given by

$$\langle \mathcal{O}_{\text{Ex}} \rangle_N = \frac{1}{N} \sum_{i=1}^{N} [\mathcal{O}_{\text{Ex}}]_i \,, \tag{2.125}$$

where $[\mathcal{O}]_i$ indicates the measurement of the operator $\mathcal{O}$ on a single configuration i. This is equivalent to

$$\begin{aligned} \langle \mathcal{O}_{\text{Ex}} \rangle_N =& \langle \mathcal{O}_{\text{Inex}} \rangle_N + \langle \mathcal{O}_{\text{Ex}} - \mathcal{O}_{\text{Inex}} \rangle_N & (2.126) \\ \simeq& \langle \mathcal{O}_{\text{Inex}} \rangle_N + \langle \mathcal{O}_{\text{Ex}} - \mathcal{O}_{\text{Inex}} \rangle_{\widetilde{N}} \,, & (2.127) \end{aligned}$$

where we have approximated the second gauge average with one over fewer measurements $\widetilde{N} < N$. i.e. we are computing the biased estimator on the full statistics relatively cheaply, and computing the bias correction on smaller statistics. If the inexact operator is a sufficiently good approximation, then the bias correction will be small and will have little effect on the result. Alternatively, if the approximation is poor, the bias correction will be large and the statistical error

will be dominated by the lower statistics of $\widetilde{N}$ measurements. The final estimator will be unbiased to within statistical errors so long as N and $\widetilde{N}$ are large enough to get reliable error estimates for the gauge averages.

In practice, the correlation between the inexact measurement and the bias correction on a configuration-by-configuration level can be significant, and therefore it is beneficial to have the inexact and bias correction measurements on the exact same configurations. This can be achieved by computing the lower statistics of $\widetilde{N}$ as a smaller number of measurements per configuration.

For example, for a 2-point correlation function, the time translation symmetry can be used to make N_t measurements per configuration. If n_b of these are used for the bias correction, and the remaining $N_t - n_\mathrm{b}$ are used for the inexact calculation, a bias corrected observable can be constructed as

$$\widetilde{\mathcal{O}}(t) = \frac{1}{n_\mathrm{b}} \sum_{k=0}^{n_b-1} \left(\mathcal{O}_\mathrm{Ex}(t+t_k) - \mathcal{O}_\mathrm{Inex}(t+t_k)\right) + \frac{1}{N_t - n_\mathrm{b}} \sum_{k=n_b}^{N_t-1} \mathcal{O}_\mathrm{Inex}(t+t_k)\,, \quad (2.128)$$

that is an unbiased estimator, i.e.

$$\lim_{N\to\infty} \left(\langle \widetilde{\mathcal{O}}(t) \rangle_N - \langle \mathcal{O}_\mathrm{Ex}(t) \rangle_N \right) = 0\,. \quad (2.129)$$

The work presented in chapter 3 utilises the AMA procedure to correct for the bias in solving propagators to an inexact residual, as well as in approximating the 5D Möbius action with a zMöbius action with smaller L_s.

CHAPTER

THREE

THE RARE KAON DECAY $K^+ \to \pi^+\ell^+\ell^-$

There exists a variety of rare decays of the charged and neutral kaons that can be used as probes for new physics beyond the SM. Of particular interest are the $s \to d$ quark FCNC decays: $K \to \pi\ell^+\ell^-$ with the kinematically allowed charged leptons $\ell = e, \mu$; and $K \to \pi\nu\bar{\nu}$ where all generations of SM neutrinos contribute. This work shall focus on the decay with charged leptons in the final state, however, the neutrino modes are of great importance in their own right, and have been extensively studied from the theoretical perspective, with recent developments given in refs. [44, 45], and progress from the lattice community in refs. [46–48]. However, due to the experimental difficulties caused by the neutrinos, these decays are not as well measured experimentally as the charged lepton modes at the present time [6].

The charged lepton rare kaon decays have several channels corresponding to the charged hadrons $K^\pm \to \pi^\pm\ell^+\ell^-$, and the neutral hadrons $K^0_{\mathrm{S,L}} \to \pi^0\ell^+\ell^-$. The charged kaon decays are related to one another by Charge Parity (CP) symmetry, however the two neutral decays have a very different structure to one another. The K^0_{S} decay is dominated by the long distance virtual photon contribution since it has a large overlap with the CP even state K_1, while the K^0_{L} decay has this contribution suppressed due to its large overlap with the CP odd state K_2.

Tables 3.1 and 3.2 show the experimental measurements of the branching ratio for the charged kaon decay in the electronic and muonic decay modes respectively, where uncertainties at the level of a few percent are observed. Alternatively, the neutral kaon decays are much more difficult to measure experimentally. The current

Experiment		Value [$\times 10^{-7}$]
PDG Average	[6]	3.00(9)
NA48/2	[53]	3.11(4)(12)
E865	[54]	2.94(5)(14)
Alliegro et al.	[55]	2.75(23)(13)
Bloch et al.	[56]	2.7(5)

Table 3.1 *Experimental measurements of the branching fraction of the rare kaon decay in the electronic decay mode $\mathcal{B}(K^+ \to \pi^+ e^+ e^-)$. The first error is statistical and the second is systematic unless only one is given, in which case it combines the statistical and systematic error.*

Experiment		Value [$\times 10^{-8}$]
NA62*	[57]	9.15(8)
PDG Average	[6]	9.4(6)
NA48/2	[58]	9.62(21)(13)
Hyper CP	[59]	9.8 (1.0)(5)
E865	[60]	9.22(60)(49)
E787	[61]	5.0(4)(9)

Table 3.2 *Experimental measurements of the branching fraction of the rare kaon decay in the muonic decay mode $\mathcal{B}(K^+ \to \pi^+ \mu^+ \mu^-)$. The first error is statistical and the second is systematic unless only one is given, in which case it combines the statistical and systematic error.*
$*$ Result more recent than the PDG average.

most precise values for the K_S^0 are $\mathcal{B}(K_S^0 \to \pi^0 e^+ e^-) = 3.0^{+1.5}_{-1.2} \times 10^{-9}$ [49] and $\mathcal{B}(K_S^0 \to \pi^0 \mu^+ \mu^-) = 5.8^{+2.9}_{-2.4} \times 10^{-9}$ [50] from the NA48/1 experiment, while the K_L^0 decay only has limits set at $\mathcal{B}(K_L^0 \to \pi^0 e^+ e^-) < 2.8 \times 10^{-10}$ [51] and $\mathcal{B}(K_L^0 \to \pi^0 \mu^+ \mu^-) < 3.8 \times 10^{-10}$ [52]. The significantly lower precision of the neutral kaon channels limits their sensitivity to new physics compared to the charged kaon decays, and therefore we focus on the $K^+ \to \pi^+ \ell^+ \ell^-$ decay in this work.

3.1 Theoretical Background

It was shown in ref. [62], that the $K^+ \to \pi^+ \ell^+ \ell^-$ decay is dominated by the long distance contribution $K^+ \to \pi^+ \gamma^*$, $\gamma^* \to \ell^+ \ell^-$ where the di-lepton pair originate from a virtual intermediate photon. For this contribution first order in electromagnetism, the amplitude factorises into a leptonic and hadronic part. Due to the non-perturbative nature of QCD, the hadronic component gives rise to the theoretical difficulty of this decay process. Once the heavy degrees of freedom have been integrated out to give a Fermi effective theory, the hadronic amplitude is

obtained as the matrix element of a point-like effective flavour-changing operator, and a vector current that couples to the virtual photon, all between the initial and final state hadron states. This is given by

$$\mathcal{A}_\mu(q^2) = \int d^4x \, \left\langle \pi^+(\boldsymbol{p}) \right| T\{H_W(x) J_\mu(0)\} \left| K^+(\boldsymbol{k}) \right\rangle \,, \tag{3.1}$$

where $\boldsymbol{k}$ and $\boldsymbol{p}$ are the 3-momentum of the kaon and pion respectively, and $q = k - p$ is the 4-momentum transferred by the virtual photon. $J_\mu = \frac{2}{3}V_\mu^u - \frac{1}{3}V_\mu^d + \frac{2}{3}V_\mu^c - \frac{1}{3}V_\mu^s$ is the electromagnetic current, where V_μ^q is the conserved flavour-diagonal vector current for the quark q, and H_W is the $\Delta S = 1$ effective weak Hamiltonian given by [10, 63]

$$H_W = \frac{G_F}{\sqrt{2}} V_{us}^* V_{ud} \left[\sum_{i=1,2} C_i (Q_i^u - Q_i^c) + \sum_{i=3,..,10} C_i Q_i \right] + \text{h.c.} \tag{3.2}$$

where $V_{qq'}$ are the CKM matrix elements, and the Q_i are a set of known operators with corresponding Wilson coefficients C_i. This weak Hamiltonian accounts for the effects of the heavy degrees of freedom of the electroweak theory that are integrated out to get a low energy effective model. The dominant contributions for the long distance $s \to d\ell^+\ell^-$ transitions are the so-called "current-current" operators

$$Q_1^q = (\bar{s}_i \gamma_\mu^L q_j)(\bar{q}_j \gamma^{L\ \mu} d_i) \tag{3.3}$$

$$Q_2^q = (\bar{s}_i \gamma_\mu^L q_i)(\bar{q}_j \gamma^{L\ \mu} d_j) \,, \tag{3.4}$$

where i, j are summed colour indices and $\gamma_\mu^L = \gamma_\mu(1-\gamma_5)$. For a renormalisation scale above the charm quark mass, the Glashow–Iliopoulos–Maiani (GIM) mechanism is manifest as the difference of the up and charm quark contributions $Q_i^u - Q_i^c$. The operators $Q_{3\ldots6}$ are the QCD penguin operators

$$Q_3 = (\bar{s}_i \gamma_\mu^L d_i) \sum_q (\bar{q}_j \gamma^{L\ \mu} q_j) \quad , \quad Q_4 = (\bar{s}_i \gamma_\mu^L d_j) \sum_q (\bar{q}_j \gamma^{L\ \mu} q_i) \,, \tag{3.5}$$

$$Q_5 = (\bar{s}_i \gamma_\mu^L d_i) \sum_q (\bar{q}_j \gamma^{R\ \mu} q_j) \quad , \quad Q_6 = (\bar{s}_i \gamma_\mu^L d_j) \sum_q (\bar{q}_j \gamma^{R\ \mu} q_i) \,, \tag{3.6}$$

where the quarks q with electric charge e_q are from the set of active flavours at a chosen renormalisation scale, and $\gamma_\mu^R = \gamma_\mu(1+\gamma_5)$. Finally the electroweak penguin

operators $Q_{7...10}$ are given by

$$Q_7 = \frac{3}{2}(\bar{s}_i\gamma_\mu^L d_i)\sum_q e_q(\bar{q}_j\gamma^{R\ \mu}q_j) \quad , \quad Q_8 = \frac{3}{2}(\bar{s}_i\gamma_\mu^L d_j)\sum_q e_q(\bar{q}_j\gamma^{R\ \mu}q_i)\,, \tag{3.7}$$

$$Q_9 = \frac{3}{2}(\bar{s}_i\gamma_\mu^L d_i)\sum_q e_q(\bar{q}_j\gamma^{L\ \mu}q_j) \quad , \quad Q_{10} = \frac{3}{2}(\bar{s}_i\gamma_\mu^L d_j)\sum_q e_q(\bar{q}_j\gamma^{L\ \mu}q_i)\,. \tag{3.8}$$

The Wilson coefficients $C_{3...10}$ are suppressed by a factor $\frac{V_{ts}^*V_{td}}{V_{us}^*V_{ud}} \sim 10^{-3}$ relative to $C_{1,2}$, and therefore we are safe to ignore these penguin type operators at the current level of precision. A detailed description of the $\Delta S = 1$ effective weak Hamiltonian is given in ref. [64] in the context of the $K \to \pi\ell^+\ell^-$ and $K \to \pi\nu\bar{\nu}$ decays.

It is most convenient for us to use operators where the spinor and color indices are contracted within the same pairs of quarks. While the Q_2^q operator is already in this form, the Q_1^q operator must undergo a Fierz transformation, under which the $\gamma_\mu^L \otimes \gamma^{L\mu}$ structure is invariant, resulting in the operator

$$Q_1^q = (\bar{s}_i\gamma_\mu^L d_i)(\bar{q}_j\gamma^{L\ \mu}q_j)\,. \tag{3.9}$$

The amplitude (3.1) can be decomposed into a basis of all independent Lorentz structures in the decay, which when combined with the requirement that it must satisfy the Ward-Takahashi identity $q^\mu\mathcal{A}_\mu = 0$ from electromagnetic gauge invariance, can be expressed in terms of a single form factor $V(z = \frac{q^2}{m_K^2})$

$$\mathcal{A}_\mu = -\,i\frac{G_F}{(4\pi)^2}\,V(z)\left(q^2(k+p)_\mu - (m_K^2 - m_\pi^2)q_\mu\right)\,. \tag{3.10}$$

All of the hadronic information of this decay is contained in $V(z)$ and therefore this is the goal of any theoretical calculation of this decay. The form factor has previously been analysed using the methods of ChPT in ref. [65], and can be separated into the contributions

$$V(z) = a + bz + W^{\pi\pi}(z) \tag{3.11}$$

where the $W^{\pi\pi}$ comes from the $\pi\pi \to \gamma^*$ intermediate contribution, and the part linear in z absorbs all other contributions from higher mass intermediate states. It is known up to $O(p^4)$ in the chiral expansion that $W^{\pi\pi}(0) = 0$.

While we have focused on the charged kaon decay here, the K_S^0 decay amplitude has exactly the same form, and therefore results quoted in the literature are given a subscript $+$ or 0 to indicate the form factor contributions to the K^+ or K_S^0 decay.

Origin	ℓ	a	b
NA48/2 [53]	e	-0.578(16)	-0.779(66)
NA48/2 [58]	μ	-0.575(39)	-0.813(145)
NA62 [57]	μ	-0.575(13)	-0.722(43)
D'Ambrosio et al. [66]	-	-1.59(8)	-0.82 (6)

Table 3.3 *Experimental and theory results for the form factor coefficients of the* $K^+ \to \pi^+\ell^+\ell^-$ *decay.*

Table 3.3 gives the experimental measurements of the a and b coefficients in the form factor, as well as the existing theory result which utilises a two-loop low-energy expansion of $V(z)$ in three-flavor QCD, with phenomenological inputs for unknown quantities. It can be seen that the a and b coefficients are consistent between all the experiments, and while b is also consistent with the theory prediction, the a coefficient has a clear discrepancy between theory and experiment. Due to this discrepancy, it is important to produce an alternative SM prediction of this form factor in an *ab initio* manner, which currently can only be done using the methods of lattice QCD.

3.1.1 Lattice Theory

Ref [67] gives a detailed description of the methodology for extracting the $K \to \pi\ell^+\ell^-$ form factor from the lattice, which we summarise in this section.

The amplitude in eq. (3.1) can be written in spectral form as

$$\begin{aligned}\mathcal{A}_\mu =& i\int_0^\infty d\omega \left(\frac{\rho(\omega)}{E_K(\boldsymbol{k})-\omega-i\epsilon}-\frac{\sigma(\omega)}{\omega-E_\pi(\boldsymbol{p})+i\epsilon}\right) \\ =& -i\int_0^\infty d\omega \left(\frac{\rho(\omega)}{\omega-E_K(\boldsymbol{k})+i\epsilon}+\frac{\sigma(\omega)}{\omega-E_\pi(\boldsymbol{p})+i\epsilon}\right),\end{aligned} \tag{3.12}$$

the second line of which will be most convenient for comparison with lattice objects. The two spectral functions in eq. (3.12) are given by

$$\rho(\omega) = \sum\!\!\!\!\!\!\int_\alpha \frac{\delta(\omega-E_\alpha(\boldsymbol{k}))}{2E_\alpha(\boldsymbol{k})} \left\langle \pi^+(\boldsymbol{p})\right| J_\mu \left|\alpha(\boldsymbol{k})\right\rangle \left\langle \alpha(\boldsymbol{k})\right| H_W \left|K^+(\boldsymbol{k})\right\rangle \tag{3.13}$$

$$\sigma(\omega) = \sum\!\!\!\!\!\!\int_\beta \frac{\delta(\omega-E_\beta(\boldsymbol{p}))}{2E_\beta(\boldsymbol{p})} \left\langle \pi^+(\boldsymbol{p})\right| H_W \left|\beta(\boldsymbol{p})\right\rangle \left\langle \beta(\boldsymbol{p})\right| J_\mu \left|K^+(\boldsymbol{k})\right\rangle, \tag{3.14}$$

where the states that contribute to the $|\alpha(\boldsymbol{k})\rangle$ spectrum have strangeness $S=0$ and momentum $\boldsymbol{k}$ as the weak Hamiltonian operator does not impart any momentum.

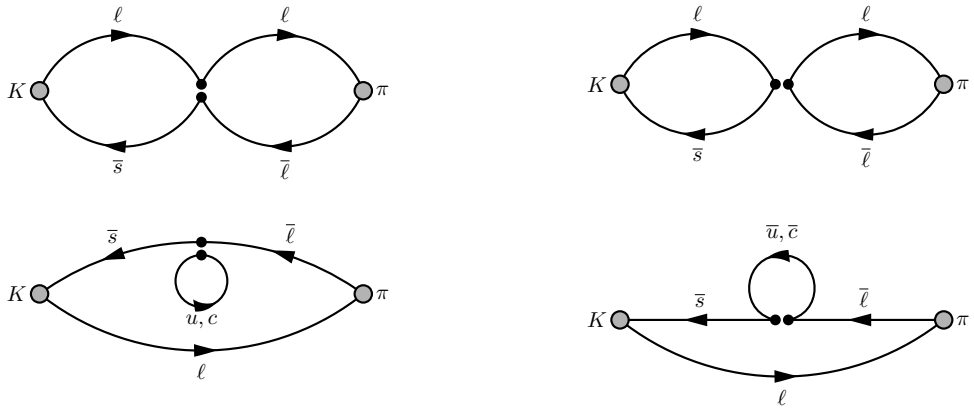

Figure 3.1 *Quark contraction topologies for the weak Hamiltonian 3-point function with kaon and pion external states. Topologies are given the names: Connected (top left); Wing (top right); Eye (bottom left); and Saucer (bottom left). The paired black dots represent the two $V - A$ quark currents that are located at the same space-time point.*

At the physical point, the lowest elements of this spectrum are the π, $\pi\pi$ and $\pi\pi\pi$ states. The states $|\beta(\boldsymbol{p})\rangle$ have $S = 1$, the lowest of which are the K, $K\pi$, $K\pi\pi$ states.

In order to compute this amplitude on the lattice, it must be obtained from discrete, finite-volume, Euclidean correlation functions. In the following discussion, we shall assume all objects are evaluated in the continuum.

The Euclidean analogue of the amplitude in 3.1 is the 4-point correlation function

$$\Gamma_{\mu}^{(4)}(t_H, t_J; \boldsymbol{k}, \boldsymbol{p}) = \int d^3\boldsymbol{x} \, \langle \phi_\pi(t_\pi, \boldsymbol{p}) \, J_\mu(0) H_W(t_H, \boldsymbol{x}) \, \phi_K^\dagger(t_K, \boldsymbol{k}) \rangle \tag{3.15}$$

where $\phi_P(t, \boldsymbol{p})$ is an interpolating operator for the pseudoscalar meson P in the time-momentum representation, and the operators J_μ and H_W are the electromagnetic current and weak Hamiltonian in position space representation. The quark contractions that are required for the computation of this weak Hamiltonian can be separated into 4 different topologies shown in fig. 3.1, corresponding to the contractions of the 3-point function $\langle \phi_\pi H_W \phi_K^\dagger \rangle$. The connected and eye diagrams stem from the Q_1 operator, while the wing and saucer diagrams stem from Q_2. For brevity, when referring to both the Eye and Saucer diagrams together, we shall use the term "eye-type" diagrams, and "non-eye" diagrams for the Connected and Wing diagrams. The full set of quark contractions for the 4-point function can be obtained from those of fig. 3.1 by the insertions of a vector current vertex on each of the quark legs, which are given in appendix A.

Assuming ground state dominance and the time ordering $t_K \ll 0, t_H \ll t_\pi$, this correlation function has the spectral representation

$$\Gamma_\mu^{(4)}(t_K, t_H, t_\pi; \boldsymbol{k}, \boldsymbol{p}) = \\ Z_{K\pi}(t_K, t_\pi; \boldsymbol{k}, \boldsymbol{p}) \int_0^\infty d\omega \begin{cases} \rho_L(\omega)\, e^{-(E_K(\boldsymbol{k})-\omega)t_H} & \text{for} \quad t_H < 0 \\ \sigma_L(\omega)\, e^{-(\omega - E_\pi(\boldsymbol{p}))t_H} & \text{for} \quad 0 < t_H \end{cases}, \tag{3.16}$$

where we have collected the creation, annihilation and propagation of the external states into the factor

$$Z_{K\pi}(t_K, t_\pi; \boldsymbol{k}, \boldsymbol{p}) = \frac{\langle 0|\, \phi_\pi(0, \boldsymbol{p})\, |\pi^+(\boldsymbol{p})\rangle\, \langle K^+(\boldsymbol{k})|\, \phi_K^\dagger(0, \boldsymbol{k})\, |0\rangle}{4E_K(\boldsymbol{k})E_\pi(\boldsymbol{p})}\, e^{E_K(\boldsymbol{k})t_K} e^{-E_\pi(\boldsymbol{p})t_\pi}\,, \tag{3.17}$$

and the two spectral functions ρ_L and σ_L are the finite volume equivalent of the spectral functions in eq. (3.13). Specifically, they run over the finite volume spectrum which is fully discrete, and the multi-particle energy levels that appear are heavily influenced by the size of the lattice.

We define the amputated 4-point function by removing this external state factor

$$\hat{\Gamma}_\mu^{(4)}(t_H; \boldsymbol{k}, \boldsymbol{p}) = \frac{\Gamma_\mu^{(4)}(t_K, t_H, t_\pi; \boldsymbol{k}, \boldsymbol{p})}{Z_{K\pi}(t_K, t_\pi; \boldsymbol{k}, \boldsymbol{p})}\,. \tag{3.18}$$

Then integrating the weak Hamiltonian in the window $t_H \in (-T_a, T_b)$ around the vector current (with $T_a, T_b > 0$), we get the integrated 4-point function

$$I_\mu(T_a, T_b; \boldsymbol{k}, \boldsymbol{p}) = \int_{-T_a}^{T_b} dt_H\, \hat{\Gamma}^{(4)}(t_H; \boldsymbol{k}, \boldsymbol{p}) \tag{3.19}$$

$$= \int_0^\infty d\omega \left(\rho_L(\omega) \frac{1 - e^{-(\omega - E_k(\boldsymbol{k}))T_a}}{\omega - E_K(\boldsymbol{k})} + \sigma_L(\omega) \frac{1 - e^{-(\omega - E_\pi(\boldsymbol{p}))T_b}}{\omega - E_\pi(\boldsymbol{p})} \right). \tag{3.20}$$

It can be seen that the contribution to the integrated 4-point function that is independent of T_a and T_b is exactly (up to a trivial factor or $-i$) the amplitude of interest eq. (3.12), with the infinite volume spectral functions replaced with their finite volume counterparts.

For the regions of the ω integral where $\omega > E_K(\boldsymbol{k})$ and $E_\pi(\boldsymbol{p})$, the additional contributions decay exponentially as $T_a, T_b \to \infty$. However, for regions of the spectrum where $\omega < E_K(\boldsymbol{k})$ the $T_a \to \infty$ limit blows up, and similarly for T_b when $\omega < E_\pi(\boldsymbol{p})$. At the physical point, there are no such states in which $\omega < E_\pi(\boldsymbol{p})$,

since the ground state of the $S = 1$ spectrum is heavier than the pion, and therefore the $T_b \to \infty$ limit can be taken without issue. However, for this same reason, there do exist states in the $S = 0$ spectrum for which $\omega < E_K(\boldsymbol{k})$. These exponentially growing intermediate states are the single pion state, the finite-volume $\pi\pi$ and $\pi\pi\pi$-like states below the threshold $E_K(\boldsymbol{k})$. These states must be accounted for prior to taking $T_a \to \infty$.

3.1.2 Growing exponential removal

As is proposed in [67], there are two methods for removing these exponentially growing intermediate state terms. The first is most general and can be applied to all problematic contributions, as well as for contributions above the threshold that only decay slowly as $T_a, T_b \to \infty$. The second method can only remove a single growing exponential, however it is generally simpler to implement and can be used in conjunction with method 1 for the rest of the states.

Explicit Construction

The first method, referred to as "Method 1" in [67–70], is where the exponentially growing contributions are constructed explicitly from measured energies and matrix elements, and removed from the integrated 4-point function. If we consider the contribution from an intermediate state $|\alpha\rangle$, the exponential term is

$$\Delta I_\mu^\alpha(T_a; \boldsymbol{k}, \boldsymbol{p}) = \frac{\langle \pi(\boldsymbol{p})| J_\mu |\alpha(\boldsymbol{k})\rangle \langle \alpha(\boldsymbol{k})| H_W |K(\boldsymbol{k})\rangle}{2E_\alpha(\boldsymbol{k})(E_\alpha(\boldsymbol{k}) - E_K(\boldsymbol{k}))} e^{-(E_\alpha(\boldsymbol{k}) - E_K(\boldsymbol{k}))T_a}, \tag{3.21}$$

and therefore a full reconstruction requires measurements of the matrix elements of the electromagnetic current and the weak Hamiltonian, as well as the energies of the initial, final and intermediate state. These can all be extracted from various 2- and 3-point functions.

Scalar Shift

The scalar shift method, referred to as "Method 2" in [67–70], modifies the weak Hamiltonian in such a way as to remove the contribution from a state of our choosing, while also leaving the total amplitude unchanged. There exists two operators with which we can shift the weak Hamiltonian in such a way, the scalar and pseudoscalar

$s \to d$ quark bilinears

$$H'_W = H_W - c_S\,\bar{s}d - c_P\,\bar{s}\gamma_5 d\,. \tag{3.22}$$

It is shown in [67] (and later in the context of the rare hyperon decay in chapter 5) that as a result of the chiral ward identities, the amplitude of the rare kaon and rare hyperon decays, as well as their finite-volume estimators, are unaffected by this shift for arbitrary values of c_S and c_P. We wish to choose these coefficients such that they cancel the matrix element of a problematic state, and therefore cancel the growing exponential associated with it.

For this application, the convenient choice of problematic intermediate state is the single pion state, and therefore we require

$$\langle \pi(\boldsymbol{k})|\, H'_W\, |K(\boldsymbol{k})\rangle = 0\,. \tag{3.23}$$

Since the weak Hamiltonian matrix element has only a single form factor that conserves the parity of the state, the pseudoscalar matrix element will identically vanish, and therefore the shifted matrix element can be cancelled with only the scalar operator. This fixes the coefficient of the shift to be

$$c_S = \frac{\langle \pi(\boldsymbol{k})|\, H_W\, |K(\boldsymbol{k})\rangle}{\langle \pi(\boldsymbol{k})|\, \bar{s}d\, |K(\boldsymbol{k})\rangle}\,, \tag{3.24}$$

which can be measured simply from a ratio of 3-point functions. Once c_S has been obtained, the shifted 4-point function can be constructed from the original 4-point function with H_W, and a second 4-point function with H_W replaced with this scalar bilinear. The integrated 4-point function obtained from this shifted 4-point function then has the same form as eq. (3.19), however, the single pion intermediate state does not contribute to the ρ spectrum, and therefore there is no growing exponential associated with this state.

3.1.3 Renormalisation

The renormalisation of the quantities relevant to the rare kaon decay come in two forms. The first is the renormalisation of the individual operators J_μ and H_W. The second is the renormalisation of divergences that can occur when the two operators make contact (i.e. $\lim_{x\to 0} J_\mu(0)H_W(x)$). These will be taken in turn.

When using the lattice conserved vector current for the electromagnetic current J_μ,

the associated ward identity ensures no renormalisation is required for this operator in isolation. This would not be true if the local vector current were used for example.

The operators entering the weak Hamiltonian are known and the corresponding Wilson coefficients have been computed at next-to-leading order in the $\overline{\text{MS}}$ renormalisation scheme in ref. [10]. Due to the perturbative nature of the $\overline{\text{MS}}$ scheme, it is not accessible via purely non-perturbative renormalisation. Instead, the Q_i^q operators can be renormalised non-perturbatively on the lattice with a scheme such as RI-MOM [71] or RI-SMOM [72]. The operators can then be matched between the two schemes using perturbation theory, so long as this is done at a high enough scale. If a chiral formulation of fermions is used, the left-handed operators Q_i are prevented from mixing with their right-handed counterparts. Finally, taking the linear combination

$$\widetilde{Q}_\pm = Q_1 \pm Q_2 \,, \tag{3.25}$$

it can be seen that these transform in the $(84, 1)$ and $(20, 1)$ representation of the $\text{SU}(4) \times \text{SU}(4)$ group respectively, and therefore they cannot mix with each other (or other operators from any other representations). A detailed description of this is given in ref. [73]. The mixing structure in the original operator basis is then given by

$$H_W = \sum_i C_i^{\overline{\text{MS}}} Q_i^{\overline{\text{MS}}} = \sum_i C_i^{\text{lat}} Q_i^{\text{lat}} \tag{3.26}$$

$$= \sum_{i,j,k} C_i^{\overline{\text{MS}}} \left(\mathbb{1} + \Delta r^{\text{RI}\to\overline{\text{MS}}} \right)_{ij} Z_{jk}^{\text{RI}} Q_k^{\text{lat}} \,, \tag{3.27}$$

where the operators Q_i^{lat} are the bare operators computed on the lattice. The lack of mixing of $\widetilde{Q}_\pm$ results in $\Delta r_{11}^{\text{RI}\to\overline{\text{MS}}} = \Delta r_{22}^{\text{RI}\to\overline{\text{MS}}}$ and $\Delta r_{12}^{\text{RI}\to\overline{\text{MS}}} = \Delta r_{21}^{\text{RI}\to\overline{\text{MS}}}$, as well as $Z_{11}^{\text{RI}} = Z_{22}^{\text{RI}}$ and $Z_{12}^{\text{RI}} = Z_{21}^{\text{RI}}$. The coefficients (at a renormalisation scale of 2.15 GeV) required to perform this calculation on the relevant $C0$, $C1$ and $C2$ ensembles are given in table 3.4.

The final type of divergence that must be accounted for comes from the contact of the two operators, which is discussed in detail in [63]. By power counting it can be seen that matrix elements of the operator

$$a^4 \sum_x Q_i(x) J_\mu(0) \tag{3.28}$$

can diverge at most quadratically ($\sim 1/a^2$). However, since the electromagnetic field

Coeff	Value	Ref.
$C_1^{\overline{\text{MS}}}$	-0.2967	[10]
$C_2^{\overline{\text{MS}}}$	1.1385	
$\Delta r_{11=22}^{\text{RI}\to\overline{\text{MS}}}$	-6.562×10^{-2}	[74]
$\Delta r_{12=21}^{\text{RI}\to\overline{\text{MS}}}$	7.521×10^{-3}	
$Z_{11=22}^{\text{RI}}$	0.5916	[75]
$Z_{12=21}^{\text{RI}}$	-0.05901	
C_1^{lat}	-0.2216	-
C_2^{lat}	0.6439	

Table 3.4 *Renormalisation factors and Wilson coefficients required for the four-quark operators Q_1 and Q_2 that contribute to the effective weak Hamiltonian eq. (3.2).*

couples to the lattice conserved vector current, the U(1) gauge invariance implies the presence of a transversality factor $q_\mu q_\nu - q^2\eta_{\mu\nu}$ which reduces the degree of divergence by two down to a logarithmic one, which would not be the case if the local vector current were to be used. The remaining logarithmic divergence is independent of the quark mass, and cancels when performing the GIM subtraction $Q_i^u - Q_i^c$. Therefore, in this case there are no divergences coming from the contact of the two operators.

3.1.4 Finite Volume Corrections

In a finite volume, on-shell intermediate multi-particle states introduce power-like volume corrections that should be corrected for when obtaining the amplitude in question. As has been discussed earlier, the multi-particle states that can go on shell in this case are the $\pi\pi$ and $\pi\pi\pi$ states.

The finite volume corrections to this process from the $\pi\pi$ state can in principle be calculated using the Lellouch-Lüscher finite volume formalism for matrix element calculations [76], and is described in the context of the $K_L - K_S$ mass splitting calculation [77], which has a very similar structure to the rare kaon decay calculation.

At the time of ref. [67], it was not yet known how to utilise the 3-particle formalism [78] to compute the $\pi\pi\pi$ finite volume effects to this decay. However, in the intervening years, theoretical progress has been made towards 3-particle transitions amplitudes [79] and the application to $K^0 - \bar{K}^0$ mixing [80].

3.2 Physical Point Calculation

The first proof-of-concept exploratory calculation of the rare kaon decay using the theoretical framework discussed in the previous section is given in ref. [70]. This was performed on the C2 ensemble in table 2.2, which importantly has an unphysically heavy pion of mass $m_\pi = 430\,\text{MeV}$, and it was demonstrated that the rare kaon decay amplitude can be extracted from lattice data in practice. The calculation benefited from the heavy pion in several ways: the heavier light quark reduces the cost of inverting the Dirac operator compared to a physical point simulation; with a close to physical kaon mass, the $\pi\pi$ and $\pi\pi\pi$ states lie above the E_K threshold and therefore do not contribute growing exponentials or power-like finite-volume effects; and finally, a smaller mass difference between the light and charm quarks provides better cancellation of the noise from the eye-type diagrams.

The natural continuation of this proof-of-concept study is to perform this calculation directly at the physical point in order to allow for a direct comparison with experimental measurements and phenomenological predictions. Work from this PhD has contributed to this physical point result presented below, and published in ref. [1]. This includes the implementation and tuning of the MADWF solver (see section 2.2.2) which reduces the inversion times for this calculation; assisting with running measurements for these Möbius solves; contributing to discussions during the data analysis; and contributing to the writing of the manuscript.

3.2.1 Computational Setup

This calculation was performed on the C0 ensemble listed in table 2.2, with near physical pion and kaon masses of $m_\pi = 139.2(2)\,\text{MeV}$ and $m_K = 499.2(2)\,\text{MeV}$ respectively. 87 statistically independent gauge configurations were used.

This ensemble utilises the scaled Shamir limit of the Möbius action, with $\alpha = 2$ and $L_s = 24$ for the sea quarks. Due to the large cost of inverting the light quark Dirac operator, the valence light quark is simulated with the zMöbius action with $L_s = 10$, and tuned to approximate the sea action. An AMA-style bias correction is then performed to correct for this mismatched action setup, as is described in section 2.4.3. In order to cancel the logarithmic UV divergence from the eye-type diagrams, the charm quark is also computed with the zMöbius action. Finally, the light quark inversions are further accelerated by the use of low-mode deflation described in section 2.4.2, with 2000 exact low modes used.

Since the domain wall formalism breaks down for physical mass charm quarks at this lattice spacing [81], the rare kaon decay amplitude is computed at 3 values of unphysically light charm quarks and extrapolated to the physical charm mass, set by an extrapolation of the η_c meson mass to its physical value. The simulated bare charm masses are $am_c = 0.25, 0.30, 0.35$ and the physical charm mass is found to be $am_c^{\text{phys}} = 0.51$.

The chosen kinematics are a stationary kaon, $\boldsymbol{k} = \mathbf{0}$, and a pion with 1 unit of lattice momentum corresponding to $|\boldsymbol{p}| = \frac{2\pi}{48a} = 226\,\text{MeV}$. With this kinematic setup, and the pseudoscalar masses on this ensemble, the momentum transfer is $q^2 = 0.0029\,\text{GeV}^2$ or $z = \frac{q^2}{m_K^2} = 0.012$. This is sufficiently close to the $z = 0$ limit that this measurement of the form factor can be taken as a good approximation of the a coefficient of the form factor in eq. (3.11)

Since this process is only governed by a single hadronic form factor, only one Lorentz component of the amplitude is required, which we choose as the temporal component $\mu = 0$.

The source and sink operator times have been chosen to be $t_K = 0$ and $t_\pi = 32$, and the electromagnetic current is inserted halfway between them at $t_J = 16$. This is to allow enough separation for ground state dominance of the external sates, while also remaining in the $t < T/2$ region to suppress around-the-world effects on our lattice with temporal extent $T = 96$.

3.2.2 Loop Propagators

The eye-type diagrams contain a quark loop, requiring a propagator from a position x to itself for all values of x on the lattice, i.e. $S(x|x)\,\forall x$. However, due to the fact that the Dirac operator gets inverted onto a fixed source, if performed exactly this would require a new inversion for each lattice site which is completely infeasible on modern lattices with $O(10^7)$ sites or more.

An alternative is to evaluate this loop propagator stochastically [82] by inverting the Dirac operator on a set of N noise "hits" $\eta_i(x)$ that come from a distribution

that satisfy

$$\lim_{N\to\infty} \sum_{i=1}^{N} \eta_i(x) = 0 \tag{3.29}$$

$$\lim_{N\to\infty} \frac{1}{N} \sum_{i=1}^{N} \eta_i(x)\eta_i^\dagger(y) = \delta_{xy}\,. \tag{3.30}$$

It can then be seen that a stochastic estimation of the loop propagator is obtained as

$$S(x|x) \simeq \frac{1}{N} \sum_{i=1}^{N} S(x|\eta_i)\eta_i^\dagger(x)\,, \tag{3.31}$$

where we have used the shorthand notation $S(x|\eta) = \sum_y S(x|y)\,\eta(y)$.

One very common choice of noise source is the full volume Z_2 noise source [83], where the value at each lattice site is chosen independently from the set $Z_2 \times Z_2 = \{\frac{1}{\sqrt{2}}(1+i), \frac{1}{\sqrt{2}}(1-i), \frac{1}{\sqrt{2}}(-1-i), \frac{1}{\sqrt{2}}(-1+i)\}$ with a uniform distribution.

Sparse Sources

In order to improve upon the full volume noise source, they can be "sparsened" in a way similar to that used in [84] where a type of spatial dilution is applied. Here the noise source is taken to only have support on sites that are separated by some integer n_s in all directions

$$\eta_i^{(1)}(x) = \begin{cases} \eta_i(x) & \text{for } x_\mu = 0 \,(\text{mod } n_s) \\ 0 & \text{else} \end{cases}\,. \tag{3.32}$$

To cover the full lattice with D dimensions, n_s^D sparse sources are required, which are obtained by translating $\eta_i^{(1)}$ into the missing positions. The loop propagator is then estimated as

$$S(x|x) \simeq \frac{1}{N} \sum_{i=1}^{N} \sum_{a=1}^{n_s^D} S\left(x|\eta_i^{(a)}\right)\left(\eta_i^{(a)}(x)\right)^\dagger\,. \tag{3.33}$$

The cost benefit analysis of this sparsening in the context of the rare kaon decay with $n_s = 2$, and therefore $2^4 = 16$ sources per noise hit, is given in the appendix of ref. [1]. It is observed that when normalised to equal cost, this sparsening gives approximately 2-3 times smaller statistical error than using full volume noise

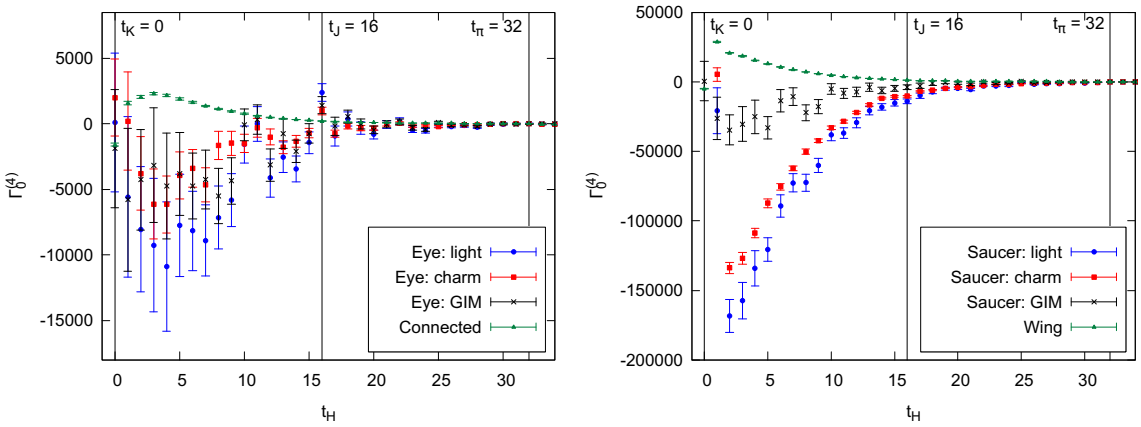

Figure 3.2 *4-point correlation function of the Q_1 (left) and Q_2 (right) operators broken down by diagram topology, and demonstrating the GIM subtraction of the eye-type diagrams for the lightest charm mass $am_c = 0.25$. Figure reproduced from [1].*

sources, and therefore this method of sparsening is chosen for the measurement of the eye-type diagrams in this analysis.

In order to increase the loop propagator statistics for a given cost, we again use the AMA procedure with 10 inexact hits inverted with a solver residual of 10^{-4}, the first of these is also solved with a tighter solver residual of 10^{-8} for light quarks, and 10^{-10}, 10^{-12}, 10^{-14} for the three charm quark masses simulated, which are used for the AMA bias correction.

3.2.3 Results

Figure 3.2 shows a breakdown of the contributions to the 4-point functions, separated into the Q_1 and Q_2 parts of the weak Hamiltonian operator (without Wilson coefficients applied). For the eye-type diagrams, the contributions are further broken down into the light and charm loop contributions, as well as the GIM subtracted contribution. It is clear that the eye-type diagrams dominate the statistical uncertainties, and that there is a large cancellation between the light and charm contributions in the GIM subtraction. In addition, there is a clear hierarchy in the size of the Q_1 and Q_2 contributions which was also observed in the previous unphysical calculation [70].

The removal of the single pion growing intermediate state is done via the scalar shift method for the final analysis, while the method of explicit construction and subtraction is also performed as a cross-check of the validity of the scalar shift.

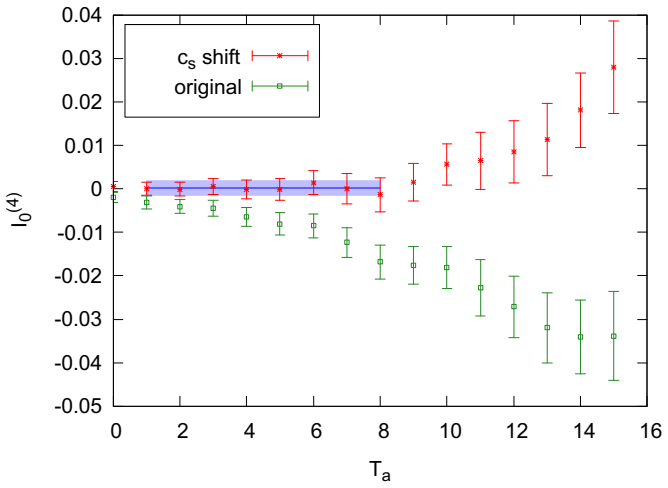

Figure 3.3 *Integrated 4-point correlation function with and without the scalar shift applied. Shown is the $T_b = 8$ slice as a function of T_a. The blue band indicates the fit to the scalar shifted correlator. Figure reproduced from [1].*

Both methods give consistent results to within statistical errors. Figure 3.3 shows the integrated 4-point correlator from eq. (3.19) for a fixed upper integration limit $T_b = 8$, before and after the application of the scalar shift method. It can clearly be seen that a significant part of the growing exponential is removed.

In addition to the single pion intermediate state, the finite volume $\pi\pi$ and $\pi\pi\pi$ states are also below the $E_K(\boldsymbol{k})$ threshold and therefore can in principle contribute additional growing exponentials that should be removed. As is discussed in ref. [67], the O(4) symmetry of Euclidean space-time requires that the $\pi\pi$ contributions to the amplitude vanish, and therefore no exponential growing term can stem from them. However, at finite lattice spacing this $O(4)$ symmetry is broken down to a hypercubic symmetry, allowing for a non-zero contribution from these states. These lattice artefacts must vanish in the continuum, however, due to the exponential growth multiplying their contribution, these effects can in principle become arbitrarily large in the integrated 4-point function. While these $\pi\pi$ states have yet to be included in this physical point analysis, studies from the similar calculation of the $K_L - K_S$ mass difference have been performed at the same lattice spacing [75, 85], and it is found that the lattice artefacts from these states have such a small contribution that these effects are estimated to be sub-percent contributions for all currently accessible values of T_a, and therefore these effects are neglected in this analysis.

The $\pi\pi\pi$ states have been estimated in ref. [67] to contribute with a factor $O(1/500)$ suppression relative to the $\pi\pi$ states due to having a smaller phase space. Since the

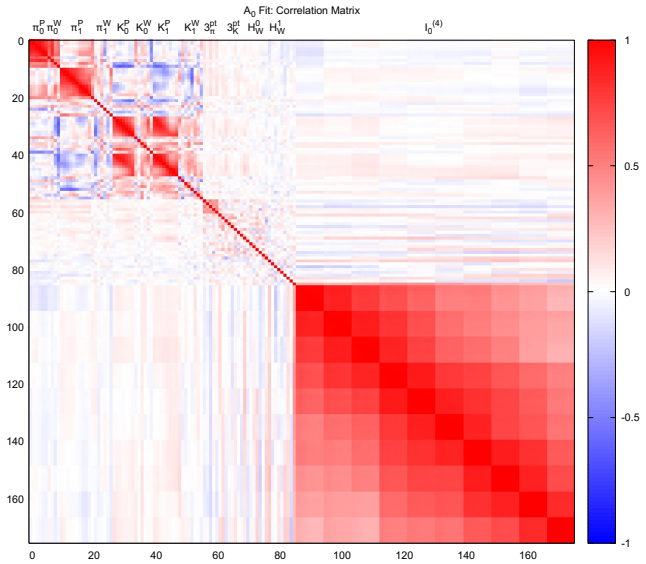

Figure 3.4 *Measured correlation matrix of the data-points used in the fit to the 2-, 3- and 4-point correlation functions. The pion and kaon 2-point functions are labelled with a subscript indicating* 0 *or* 1 *units of lattice momentum, and superscripts P or W indicating point or wall sinks (both with a wall source). The label* $3^{pt}_{\pi,K}$ *indicates the vector current 3-point function of the pion and kaon respectively. Figure from [1].*

$\pi\pi$ states are already very likely subdominant in this analysis, the $\pi\pi\pi$ states can be safely neglected as well.

Due to the suppression of these multi-particle states, the corresponding finite volume corrections are also suppressed in this calculation. Once sufficient precision is obtained for the rare kaon decay amplitude, these corrections should be taken into account. However, such a precision has not yet been achieved, so no finite volume correction is applied in this calculation.

With the growing intermediate states accounted for, a simultaneous fit is made to all relevant 2- and 3-point functions as well as the 2-dimensional integrated 4-point function. The correlation matrix of data points included in the fit is given in figure 3.4. Due to the high degree of correlation of the data points of the integrated 4-point function, and the large total number of data points within the combined fit, it is only possible to perform a semi-correlated fit in which the 2- and 3-point sectors are fully correlated, while the 4-point sector is uncorrelated.

Table 3.5 shows the results of the measurement of the temporal component of the amplitude (3.12) for the three values of the charm mass, as well as the value linearly extrapolated to the physical charm mass. The final results of the amplitude is found to be $\mathcal{A}_0 = 0.00035(180)$ which corresponds to a form factor

am_c	0.25	0.30	0.35	0.51_{phys}
$\mathcal{A}_0$	0.00022(172)	0.00024(173)	0.00027(174)	0.00035(180)

Table 3.5 *Measured amplitude $\mathcal{A}_0$ for the 3 simulated bare charm quark masses, and the linearly extrapolated value to physical charm mass.*

of $V(0.013(2)) = -0.87(4.44)$. If we consider the decomposition of the form factor from eq. (3.11), taking b to be $O(1)$, and estimate $W_{\pi\pi}(0.013) = -0.00076(73)$ following from the results of ref. [65], this allows us to neglect these contributions within our level uncertainty, and therefore our measurement of the parameter a is $a = -0.87(4.44)$.

Due to the very large uncertainty on this result, the lattice cannot currently discriminate between the experimental and phenomenological results. While the error on this result is approximately 8 times larger than the experimental values in table 3.3, it is only 3 times that of the current SM prediction, and therefore may be able to provide a competitive theoretical bound in the coming years with sufficient methodological improvements.

The large statistical uncertainty of this result is heavily dominated the eye-type diagrams. From fig. 3.2, we can see that while some of the individual flavor contributions are quite well estimated using the sparse noise approach, the GIM subtraction contains a large cancellation which leaves the uncertainty of the subtracted contribution heavily dependent on the correlation between the light and charm loops. Due to the two quarks having the same discretisation, the short distance behaviour of these loops is likely very similar, however, the long distance behaviour will be dominated by the quark mass which will decorrelate the loops as the two quarks approach their respective physical mass. This can be seen in figure 3.5 which shows the cross-correlation matrix between the light and charm loop eye diagrams for the previous unphysical calculation [70], and this physical point calculation. They key observation of this plot is that the diagonal for the unphysical calculation has a correlation very close to 1, but only $\sim 0.25 - 0.5$ in this calculation. Therefore calculations with heavier than physical light quarks and a lighter than physical charm quark have significantly higher correlation between the two diagrams, allowing for smaller uncertainties after the GIM subtraction.

There are several approaches to be explored that may allow for improvements in the calculation of the rare kaon decay amplitude on the lattice. The first is a method that integrates over the current time t_J at the time of measurement, allowing for significantly fewer inversions and reducing the cost for a given statistical precision.

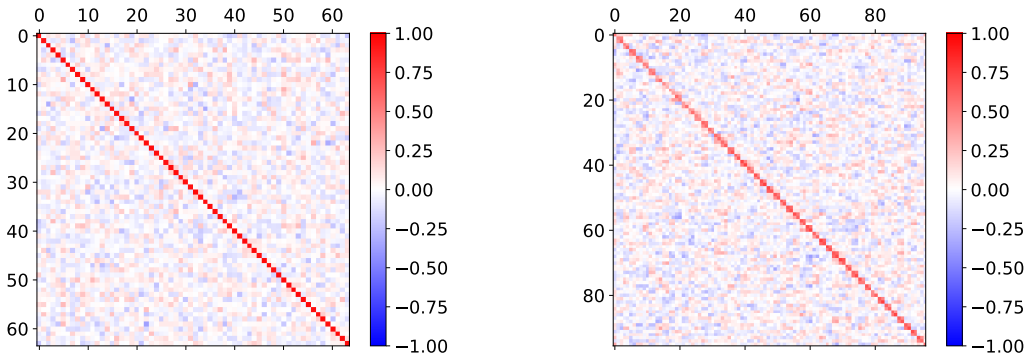

(a) (b)

Figure 3.5 *Measured cross-correlation matrix between the eye diagram with light and charm quark loops, on the unphysical C2 ensemble (left), and the physical point C0 ensemble (right). Figure reproduced from [1].*

This is investigated in section 4.

Other directions worth investigation are in improvements in the estimation of loop propagators, for example with the use of the frequency-splitting technique presented in [86] which has promisingly seen the cost of disconnected loop traces reduce by up to 2 orders of magnitude. It has recently been shown that this technique also applies for domain wall fermions in ref. [87], however it still has to be assessed whether this methodology can be applied to the eye-type diagrams in the rare kaon decay.

Finally, one could perform this calculation with the weak Hamiltonian renormalised at a different renormalisation scale, in such a way that there is a trade off between our existing statistical uncertainty and a systematic uncertainty from perturbation theory. Specifically, if one chooses a scale low enough for the charm quark to no longer be active, the rare kaon decay can be evaluated in a 3 flavour theory, that would remove the GIM subtraction that is the source of our uncertainty. This would also introduce additional issues that must be resolved, such as the introduction of the logarithmic divergence as the electromagnetic current and weak Hamiltonian approach one another. Also, with the charm quark integrated out and no longer dynamical, an additional systematic error is introduced, however, this is likely significantly smaller than the current statistical uncertainty and could therefore potentially allow for a great improvement on the precision of our result, although at the cost of not being systematically improvable.

CHAPTER

FOUR

THE SUMMED METHOD IN LATTICE SIMULATIONS

One method that may be able to reduce the cost of the rare kaon decay proposed in chapter 3 is the use of correlation functions in which the vector current is integrated over time (or summed in discrete time) directly during the measurement step. The use of such correlators in LQCD calculations is known as the "summed method" or "summation method" originally proposed in [88]. The summed method has been used in many calculations of matrix elements using 3-point functions with degenerate external states, and is very closely linked with the Feynman-Hellmann theorem which is discussed in detail in the context of lattice calculations in [89–94].

In this chapter, we investigate the use of this method for applications with non-degenerate external states, and 4-point functions in the specific context of the rare kaon decay. For simplicity, we make several assumptions that can be lifted at the cost of additional tedious bookkeeping, however, none of the conclusions made will be affected. These simplifications are the use of mesonic external states, as well as the use of an infinite continuous time variable.

4.1 3-point functions

Suppose we wish to compute the matrix element of an operator J between two arbitrary states $|i\rangle$ and $|f\rangle$. This matrix element is contained in the ground state

contribution to the 3-point correlation function

$$\Gamma^3(t, t_f) = \langle \phi_f(t_f)\, J(t)\, \phi_i^\dagger(0) \rangle \tag{4.1}$$

where ϕ_i and ϕ_f are interpolators for which the $|i\rangle$ and $|f\rangle$ states are the ground states. This 3-point function has the spectral representation, for a fixed source-sink separation $t_f > 0$, given by

$$\Gamma^3(t, t_f) = \begin{cases} \sum_{nm} [\phi_f]_{0m} [J]_{mn} [\phi_i^\dagger]_{n0}\ e^{-E_m t_f} e^{-(E_n - E_m)t} & \text{for} \quad 0 < t < t_f \\ \sum_{nl} [J]_{0l} [\phi_f]_{ln} [\phi_i^\dagger]_{n0} \quad e^{-(E_n - E_l)t_f} e^{-E_l t} & \text{for} \quad 0 < t_f < t \\ \sum_{km} [\phi_f]_{0m} [\phi_i^\dagger]_{mk} [J]_{k0}\ e^{-E_m t_f} e^{E_k t} & \text{for} \quad t < 0 < t_f \end{cases} , \tag{4.2}$$

where we have defined the compact notation $[A]_{mn} = \langle m |\, A(0)\, | n \rangle$, E_n is the energy of a state $|n\rangle$, and the sums run over the spectrum of states with appropriate quantum numbers. Specifically in this case, states $|n\rangle$ have the quantum numbers of ϕ_i, $|m\rangle$ those of ϕ_f, $|l\rangle$ those of J or equivalently $\phi_f^\dagger \phi_i$, and $|k\rangle$ those of $J^\dagger$ or $\phi_f \phi_i^\dagger$.

The most general method for extracting the matrix element $[J]_{fi}$ utilises the time ordering $0 < t < t_f$ in the limit $t \gg \frac{1}{\Delta E_i}$ and $t_f - t \gg \frac{1}{\Delta E_f}$, where the ΔE are the energy gaps between the ground and first excited states. In this regime, the 3-point function is approximately given by

$$\Gamma^3(t, t_f) \simeq [\phi_f]_{0f} [J]_{fi} [\phi_i^\dagger]_{i0}\, e^{-E_f(t_f - t)} e^{-E_i t} , \tag{4.3}$$

which can be fit to give the ground-to-ground state matrix element, up to the overlap factors $[\phi_i]_{0i}$ and $[\phi_f]_{0f}$. In practice however, this large time separation can be very difficult to achieve when performing calculations with a signal-to-noise problem, such as with baryonic correlation functions. It is therefore often necessary to include the effects of excited state contamination where a number of states above the ground state are also included in the fit

$$\Gamma^3(t, t_f) \simeq \sum_n^N \sum_m^M [\phi_f]_{0m} [J]_{mn} [\phi_i^\dagger]_{n0}\, e^{-E_m t_f} e^{-(E_n - E_m)t} . \tag{4.4}$$

Some simplifying assumptions may be made, for example certain excited-to-excited matrix elements may be set to zero, or certain energies may be constrained by 2-point correlation functions. It is clear, however, that the number of fit parameters grows quickly with the number of states included, causing fit stability to decrease and/or requiring additional data at multiple values of t_f to constrain the parameters. A rather extreme example of this is given in [93] where a 5-state fit is performed in the extraction of the nucleon axial charge. It can be seen that using this method,

the excited states become exponentially suppressed in the temporal distance from both of the interpolators $e^{\Delta E_f (t_f - t)}$ and $e^{-\Delta E_i t}$.

In the special case where the initial and final state spectra are degenerate, the summed method can be applied where the operator insertion is summed (or integrated in continuous time). This summation can be applied over just the source-sink window $0 < t < t_f$, or over the full temporal extent. Generally, the former is most desirable as it contains only contributions from the time ordering of interest, however, it can usually only be applied during the post-processing stage of a calculation. In contrast, the latter includes contributions from the other two time orderings, but can often be applied directly in the measurement step which may allow for a reduction in cost, for example via sequential inversions of the Dirac operator. For the purposes of this section, we shall consider the integral over all time.

Ref. [92] gives a detailed derivation of the summation of this 3-point function including the handling of a discrete and finite time, and special consideration for the contact terms where the operators coincide. In the continuum, it can be seen that the integrated 3-point function has the spectral representation

$$I^3(t_f) = \int_{-\infty}^{\infty} dt\, \Gamma^3(t, t_f) \tag{4.5}$$

$$= \sum_{nm} [\phi_f]_{0m} [J]_{mn} [\phi_i^\dagger]_{n0} \frac{e^{-E_m t_f} - e^{-E_n t_f}}{E_n - E_m} \tag{4.6}$$

$$+ \sum_{nl} [J]_{0l} [\phi_f]_{ln} [\phi_i^\dagger]_{n0} \frac{e^{-E_n t_f}}{E_l} + \sum_{km} [\phi_f]_{0m} [\phi_i^\dagger]_{mk} [J]_{k0} \frac{e^{-E_m t_f}}{E_k} \,,$$

where the last two terms come from the other time orderings $t < 0$ and $t > t_f$ which shall be referred to as the "Out-Of-Order" (O^3) terms. In the special case where the two spectra are degenerate, the equal energy "diagonal" terms ($n = m$) can be separated out to give

$$I^3(t_f) = \sum_{n} [\phi_f]_{0n} [J]_{nn} [\phi_i^\dagger]_{n0}\, t_f\, e^{-E_n t_f} \tag{4.7}$$

$$+ \sum_{n \neq m} [\phi_f]_{0m} [J]_{mn} [\phi_i^\dagger]_{n0} \frac{e^{-E_m t_f} - e^{-E_n t_f}}{E_n - E_m}$$

$$+ \sum_{nl} \left([J]_{0l} [\phi_f]_{ln} [\phi_i^\dagger]_{n0} + [\phi_f]_{0n} [\phi_i^\dagger]_{nl} [J]_{l0} \right) \frac{e^{-E_n t_f}}{E_l} \,.$$

We can see that these diagonal terms have a time dependence that is exponential times linear, while the off-diagonal terms come as the difference of two decaying

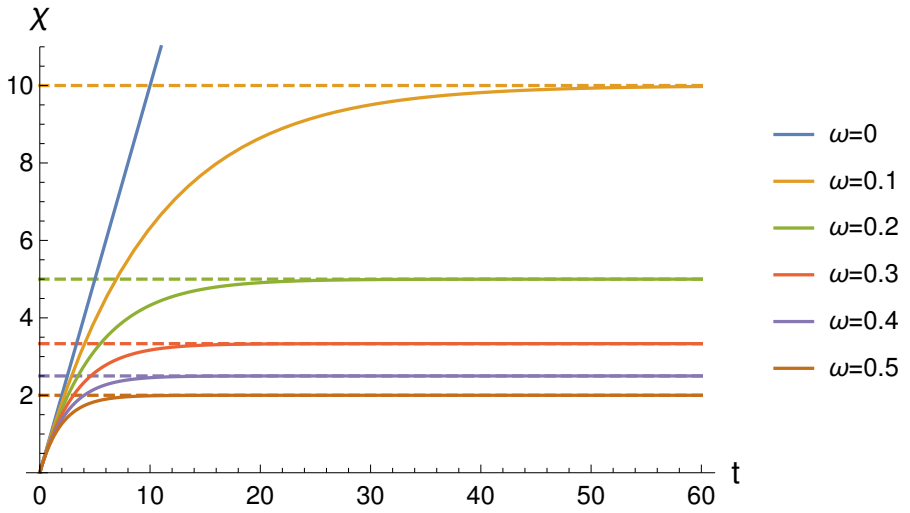

Figure 4.1 *Plot of $\chi(\omega, t)$ in eq. (4.8) for multiple values of ω. Dashed lines indicate the asymptotic value as $t \to \infty$.*

exponentials of different energy. Note that the O^3 terms also have a simple exponential time dependence decaying with energies of states that overlap with the interpolators, and not states that overlap with J or the pairs of interpolators.

One key advantage of this summed method is that, from eq. (4.7), it can be seen that the excited states are suppressed by $e^{-\Delta E t_f}$ and therefore ground state dominance is achieved when $t_f \gg \frac{1}{\Delta E}$. This is in contrast to the non-summed method in eq. (4.2) where both $t_f - t$ and $t \gg \frac{1}{\Delta E}$. Taking the point at $t = t_f/2$, this means that the non-summed method requires a source-sink separation about twice as large as with the summed method to achieve the same level of excited state suppression.

Examining the time dependence of the off-diagonal terms, we define the envelope function

$$\chi(\omega, t) = \frac{1 - e^{-\omega t}}{\omega}\,, \tag{4.8}$$

and therefore (assuming $E_n > E_m$) this time dependence is given by

$$\frac{e^{-E_m t_f} - e^{-E_n t_f}}{E_n - E_m} = \chi(E_n - E_m, t_f)\, e^{-E_m t_f}\,. \tag{4.9}$$

If instead $E_m > E_n$, this gives $\chi(E_m - E_n, t_f)\, e^{-E_n t_f}$, so the off-diagonal terms can always be expressed as the envelope with a positive energy argument and an exponential factor that goes with the smaller of the two energies. Figure 4.1 shows time the dependence of the envelope function χ.

It can be seen from the functional form that $\chi(\omega \to 0, t) \to t$ and therefore it

recovers the linear time dependence seen in the diagonal terms. In addition, the small time limit gives $\chi(\omega, t \ll 1/\omega) \simeq t$, and the large time limit at strictly positive ω is $\chi(\omega, t \to \infty) \to \frac{1}{\omega}$. Therefore the envelope has linear early time behaviour and constant large time behaviour, where the timescale of the transition between the two is $t \sim \frac{1}{\omega}$.

In the case of degenerate spectra in eq. (4.7) it can be seen that for large times $t \gg \frac{1}{\Delta E}$, the exponentials suppress the excited states leaving

$$\begin{aligned} I^3(t_f) \simeq \Big(& [\phi_f]_{01}[J]_{11}[\phi_i^\dagger]_{10}\, t_f \\ & + \sum_{m>1} \Big([\phi_f]_{0m}[J]_{m1}[\phi_i^\dagger]_{10} + [\phi_f]_{01}[J]_{1m}[\phi_i^\dagger]_{m0} \Big)\, \chi(E_m - E_1, t_f) \\ & + \sum_{l} \frac{[J]_{0l}[\phi_f]_{l1}[\phi_i^\dagger]_{10} + [\phi_f]_{01}[\phi_i^\dagger]_{1l}[J]_{l0}}{E_l} \Big)\, e^{-E_1 t_f} \,. \end{aligned} \tag{4.10}$$

Up to the overall external exponential that separates out the ground state, there are 3 types of time dependence: the linear component that has the ground-to-ground state matrix element as a prefactor; the χ terms that behave linearly at small times and constant at large times; and the constant O^3 terms. Therefore at large enough times, all unwanted components contribute to a constant term, and the matrix element is simply the gradient of the linear term. This degenerate case of the summed method has been successfully used in many calculations, for example various stationary charges of the baryon octet, including (but by no means limited to) the works [93, 95–97].

Non-Degenerate Case

We now investigate the behaviour of *eq.* (4.6) in the case of non-degenerate spectra. Writing the integrated 3-point function in terms of the envelope function and separating the sum over the two spectra into two energy ordered sums gives

$$\begin{aligned} I^3(t_f) = & \sum_m \left(\sum_{\substack{n \\ E_n \geq E_m}} [\phi_f]_{0m}[J]_{mn}[\phi_i^\dagger]_{n0}\, \chi(E_n - E_m, t_f) + \sum_k \frac{[\phi_f]_{0m}[\phi_i^\dagger]_{mk}[J]_{k0}}{E_k} \right) e^{-E_m t_f} \\ & + \sum_n \left(\sum_{\substack{m \\ E_m > E_n}} [\phi_f]_{0m}[J]_{mn}[\phi_i^\dagger]_{n0}\, \chi(E_m - E_n, t_f) + \sum_l \frac{[J]_{0l}[\phi_f]_{ln}[\phi_i^\dagger]_{n0}}{E_l} \right) e^{-E_n t_f} \,. \end{aligned} \tag{4.11}$$

It can be seen that, inside the brackets, the O^3 terms behave as a constant, while the correct time ordering terms contain matrix elements between states modulated by the envelope function. Terms with large energy separations plateau much earlier in time, while those that are minimally separated plateau much later. However, as $t \to \infty$, all contributions eventually tend to a constant. Therefore, at asymptotic times, the matrix element is no longer separable from the excited state and O^3 contamination. This is an important observation because it shows that for any arbitrarily small non-zero degeneracy breaking, the summed method must eventually break down for sufficiently large times.

In practice, however, with a finite temporal extent, T, we can never examine correlators at asymptotic time on the lattice. Therefore the the minimum scale of energy splitting for which the non-linearity can be reasonably resolved is $E_i - E_f \sim 1/T$. For energy splitting $E_i - E_f \lesssim 1/T$, the states will be practically degenerate. In the quasi-degenerate limit where the energy splitting is smaller than the energy gap to the excited states but still large enough to resolve the non-linearity, $1/T \lesssim E_i - E_f \ll \Delta E$, the matrix element can only be extracted at these intermediate times before the linear behaviour of the states of interest ends, but after the plateau of the excited states.

In the fully non-degenerate limit where this energy splitting hierarchy is inverted, i.e. $E_i - E_f \gtrsim \Delta E$, then the ground-to-excited (or excited-to-ground) state matrix element will be the latest contribution to plateau. In this scenario, it is practically impossible to extract the ground state matrix element using the summed method as given by eq. (4.5).

Ultimately, this behaviour stems from the fact that the unintegrated 3-point function (4.6) has non-constant t dependence coming from the initial-final state energy difference. This represents the fact that the operator must take away that amount of energy to conserve energy. In Minkowski time, this conservation requires that the operator come with an additional phase $e^{i(E_i - E_f)t}$. In Euclidean time, however, energy is not conserved, and therefore the equivalent factor $e^{(E_i - E_f)t}$ is not required for the integrated correlator to be non-zero. If this factor is manually included with the operator

$$\Gamma^3(t, t_f) = \langle \phi_f(t_f)\, J(t) e^{(E_i - E_f)t} \phi_i^\dagger(0) \rangle\,, \tag{4.12}$$

the problematic time dependence is removed, and the summed method can be applied just as in the energy degenerate case without issue. Of course, with a finite time extent, care must be taken to account for the periodicity of the lattice.

This energy correction is actually performed implicitly in many calculations where various ratios of 2- and 3-point functions are made to cancel the time dependence and the resulting correlator is summed, as was originally used in [98] and has been used in many subsequent calculations. Some examples include [99, 100]. The simplest such construction is

$$R(t_f) = \sum_{t=0}^{t_f} \frac{\Gamma^3(t, t_f)}{\Gamma_i^2(t)\Gamma_f^2(t_f - t)}\,, \tag{4.13}$$

although more complicated ratios are used in practice. These ratios are performed in the post-processing stage of a calculation, however, in the event the energies of the relevant states are already known, the additional exponential factor could in principal be included in the directly integrated correlation functions. The calculation of the real photon emission $P \to \ell\bar{\nu}\gamma$ presented in [101] requires the use of such an exponential factor to select the appropriate photon energy.

There has been recent work on the extension of the Feynman-Hellmann theorem to include quasi-degenerate external states in [94], however, it is still not known if this method can be extended to fully non-degenerate states. Since the summed method is closely linked to Feynman-Hellman theorem, further research is required into whether this breakdown of the summed method should also affect the non-degenerate Feynman-Hellmann theorem, or if it is protected from this behaviour and could therefore be used to navigate such issues with the summed method.

4.2 4-point functions and the rare kaon decay

While the summed method is most commonly used for extraction of matrix elements from 3-point functions, it is also possible to do the same with 4-point functions. This has been used in the case of degenerate initial and final state spectra and two insertions of the same operator in the calculation of the $K_L - K_S$ mass difference [75, 85], and using the Feynman-Hellmann theorem for the calculation of the Compton amplitude in [102]. In the $K_L - K_S$ mass difference calculation, both of the intermediate operators get integrated within a window $t_1, t_2 \in (t_a, t_b)$ where t_a and t_b are taken to be sufficiently far away from the initial and final state operators in order to project out the ground states.

The existing methodology of the rare kaon decay used in [1, 70], and chapter 3, uses a similar windowed integration for only the weak Hamiltonian, with the vector

Method	Light	Strange	Charm
Fixed t_J	$N_t(6+N_\eta)+N_\eta$	$3N_t$	$N_\eta(1+N_t)$
$N_\eta = 14,\ N_t = 12$	254	36	182
$N_\eta = 14,\ N_t = 32$	654	96	462
Summed t_J	$6N_t + 2N_\eta$	$3N_t$	$2N_\eta$
$N_\eta = 14,\ N_t = 12$	114	36	42
$N_\eta = 14,\ N_t = 32$	234	96	42

Table 4.1 *Number of light, strange and charm propagators to compute per configuration for the rare kaon decay calculation using the traditional fixed t_J method, and the summed t_J method. Numbers are shown for several numbers of time translations N_t and for $N_\eta = 14$ noise hits.*

current fixed at a specific time. The vector current is implemented via a sequential inversion of the quark propagator on which it is inserted. Since the current time t_J is fixed, multiple sets of sequential inversions must be performed if a time translation average is to be applied. This increases the cost of the calculation linearly with the number of translations, and the majority of these sequential inversions occur on the noise loops. Therefore one could get a substantial reduction in cost with a technique that does not require these new inversions for every translation.

This is the case if the summed method can be used on the vector current to integrate over t_J directly at the time of inversion. It should be noted that this reduction in number of inversions can only be obtained if the integration is performed over the entire temporal extent of the lattice and is independent of the other times in the problem (i.e. t_K, t_π and t_H). In that case a single sequential inversion of the noise loop propagator can be reused for all time translations.

Table 4.1 shows a comparison of the number of propagator inversions required per configuration for the rare kaon decay calculation, following the counting of [70], for a single pion momentum and charm mass, N_η noise sources and N_t time translations. It can be clearly seen that for simulations dominated by light and charm inversions, the summed method can be significantly faster for a fixed N_η and N_t.

As in the the previous section we assume an infinite continuum in the temporal direction for simplicity, however, similar results can be obtained for finite and discrete time. Extending the definition of the 4-point correlation function from

chapter 3 to allow for all 4 operators to have variable times,

$$\Gamma^4(t_i,t_H,t_J,t_f) = \langle \phi_f(t_f) H_W(t_H) J(t_J) \phi_i^\dagger(t_i)\rangle \tag{4.14}$$

$$= \sum_{nm} Z_{nm}(t_i,t_f) \int_0^\infty d\omega \begin{cases} \rho_{nm}(\omega)\, e^{-(E_n-\omega)t_H} e^{-(\omega-E_m)t_J} & \text{for} \quad t_i<t_H<t_J<t_f \\ \sigma_{nm}(\omega)\, e^{-(E_n-\omega)t_J} e^{-(\omega-E_m)t_H} & \text{for} \quad t_i<t_J<t_H<t_f \end{cases} \tag{4.15}$$

where we have left all momenta and the current index μ implicit. Since t_J will be integrated over, we no longer assume the ground state dominance of the external states at this point. This gives rise to the generalisation of the spectral densities

$$\rho_{nm}(\omega) = \sum\!\!\!\!\!\!\int_\alpha \frac{\delta(\omega-E_\alpha)}{2E_\alpha} \langle m|\, J_\mu\, |\alpha\rangle \langle \alpha|\, H_W\, |n\rangle \tag{4.16}$$

$$\sigma_{nm}(\omega) = \sum\!\!\!\!\!\!\int_\beta \frac{\delta(\omega-E_\beta)}{2E_\beta} \langle m|\, H_W\, |\beta\rangle \langle \beta|\, J_\mu\, |n\rangle \ , \tag{4.17}$$

and overlap factor

$$Z_{nm}(t_i,t_f) = \frac{[\phi_i]_{0m}[\phi_K^\dagger]_{n0}}{4E_nE_m} e^{E_n t_i} e^{-E_m t_f} \ , \tag{4.18}$$

with general external states n and m. Denoting the energy differences as $\Delta_{nm} = E_n - E_m$ and $\Delta_{n\omega} = E_n - \omega$, the 4-point function integrated over the current time is given by

$$I(t_i,t_H,t_f) = \int_{t_i}^{t_f} dt_J\, \Gamma^4(t_i,t_H,t_J,t_f) = \tag{4.19}$$

$$\sum_{nm} Z_{nm}(t_i-t_H,t_f-t_H) \int_0^\infty d\omega \left[\rho_{nm}(\omega)\frac{1-e^{\Delta_{\omega m}(t_f-t_H)}}{\Delta_{\omega m}} + \sigma_{nm}(\omega)\frac{1-e^{-\Delta_{\omega n}(t_H-t_i)}}{\Delta_{\omega n}}\right] , \tag{4.20}$$

where we have neglected the O^3 terms. The external ground states can be isolated simply by taking the separations $t_H - t_i$ and $t_f - t_H$ to be large, as in the case of the unintegrated 3-point function from the previous section. Amputating the external state propagation leaves just the spectral integral

$$\hat{I}(t_H) = \frac{I(t_i,t_H,t_f)}{Z_{if}(t_i-t_H,t_f-t_H)} \tag{4.21}$$

$$= \int_0^\infty d\omega \left[\rho_{if}(\omega)\frac{1-e^{-\Delta_{\omega f}(t_f-t_H)}}{\Delta_{\omega f}} + \sigma_{if}(\omega)\frac{1-e^{-\Delta_{\omega i}(t_H-t_i)}}{\Delta_{\omega i}}\right] . \tag{4.22}$$

This has a very similar structure to the amputated integrated 4-point function in

eq. (3.19), however, the temporally constant component does not give the amplitude of interest. Instead the energy differences in the denominator differ from (3.12), and instead the amplitude that would be extracted is

$$\mathcal{B}_\mu = \int d^4x \, \langle \pi(\boldsymbol{p}) | \, T\{H_W(0) J_\mu(x)\} \, | K(\boldsymbol{k}) \rangle \tag{4.23}$$

$$= -i \int_0^\infty d\omega \left(\frac{\rho(\omega)}{\omega - E_\pi(\boldsymbol{p}) + i\epsilon} + \frac{\sigma(\omega)}{\omega - E_K(\boldsymbol{k}) + i\epsilon} \right) , \tag{4.24}$$

which when applying translational invariance to change the integral to the other operator can be written

$$\mathcal{B}_\mu = \int d^4x \, e^{-i(k-p)\cdot x} \, \langle \pi(\boldsymbol{p}) | \, T\{H_W(x) J_\mu(0)\} \, | K(\boldsymbol{k}) \rangle \ . \tag{4.25}$$

Comparing this form to eq. (3.1), it can be seen that this amplitude differs by an additional phase factor within the integral. In exactly the same way as in the case of the 3-point function, the temporal part of this phase imposes that the weak Hamiltonian carry away the energy difference $E_i - E_f$ instead of the electromagnetic current. This of course corresponds to a completely different (and unphysical) process.

One method to correct for the effect of this additional phase in the lattice calculation is to include an exponential factor within the integral

$$I(t_i, t_H, t_f) = \int_{t_i}^{t_f} dt_J \, e^{(E_i - E_f) t_J} \Gamma^4(t_i, t_H, t_J, t_f) \tag{4.26}$$

$$\simeq Z_{if}(t_i - t_H, t_f - t_H) \int_0^\infty d\omega \left[\rho_{if}(\omega) \frac{1 - e^{\Delta_{\omega i}(t_f - t_H)}}{\Delta_{\omega i}} + \sigma_{if}(\omega) \frac{1 - e^{-\Delta_{\omega f}(t_H - t_i)}}{\Delta_{\omega f}} \right] . \tag{4.27}$$

After amputation, the correct amplitude can then be extracted as the t_H independent component in a method similar to that used in chapter 3. This however does not satisfy our conditions for reducing the cost of the rare kaon decay calculation as it would require a new shifted exponential factor for each time translation measured on the lattice.

A second method of extracting the amplitude is to integrate the 4-point function over both the vector current and the weak Hamiltonian. In the event we have access to the full range of t_H values (as is the case in chapter 3), this can be done in post-processing, allowing for the integration to be performed only within the window $t_H \in (t_i + \tau, t_f - \tau)$ where τ is a buffer to allow for saturation of the external ground

states. The doubly integrated 4-point function is then given by

$$I^{(2)}(t_i, t_f, \tau) = \int_{t_i+\tau}^{t_f-\tau} dt_H \int_{t_i}^{t_f} dt_J \, \Gamma^4(t_i, t_H, t_J, t_f) \tag{4.28}$$

$$\begin{aligned} &= Z_{if}(t_i, t_f) e^{-\Delta_{if}(t_i+\tau)} \int_0^\infty d\omega \left[\left(\frac{\rho_{if}(\omega)}{\Delta_{\omega i}} + \frac{\sigma_{if}(\omega)}{\Delta_{\omega f}} \right) \chi(\Delta_{if}, t_f - t_i - 2\tau) \right. \\ &+ \frac{\rho_{if}(\omega)}{\Delta_{\omega i}} \left(- \frac{1 - e^{-\Delta_{\omega f}(t_f - t_i - 2\tau)} e^{-\Delta_{if}(t_i+\tau)}}{\Delta_{\omega f}} + \frac{1 - e^{-\Delta_{\omega f}\tau}}{\Delta_{\omega f}} e^{-\Delta_{if}(t_f - t_i - 2\tau)} \right) \\ &\left. + \frac{\sigma_{if}(\omega)}{\Delta_{\omega f}} \left(+ \frac{1 - e^{\Delta_{i\omega}(t_f - t_i - 2\tau)} e^{\Delta_{i\omega}\tau}}{\Delta_{i\omega}} e^{-\Delta_{if}(t_f - t_i - 2\tau)} + \frac{1 - e^{-\Delta_{i\omega}\tau}}{\Delta_{i\omega}} \right) \right] . \end{aligned} \tag{4.29}$$

Importantly, this has a term corresponding to the amplitude of interest, up to the overlap factor and the time dependence $\chi(\Delta_{if}, t_f - t_i - 2\tau)$. It should be noted that for non-degenerate initial and final states, the asymptotic time behaviour no longer isolates the amplitude but instead it gets mixed with additional intermediate state contributions, analogous to the behavour observed in the 3-point functions. In the event the initial and final states are degenerate, however, this becomes

$$\begin{aligned} I^{(2)}(t_i, t_f, \tau) = Z_{if}(t_i, t_f) \int_0^\infty d\omega \left[\left(\frac{\rho_{if}(\omega)}{\Delta_{\omega i}} + \frac{\sigma_{if}(\omega)}{\Delta_{\omega f}} \right) (t_f - t_i - 2\tau) \right. \\ + \frac{\rho_{if}(\omega)}{\Delta_{\omega i}} \left(- \frac{1 - e^{-\Delta_{\omega f}(t_f - t_i - 2\tau)}}{\Delta_{\omega f}} + \frac{1 - e^{-\Delta_{\omega f}\tau}}{\Delta_{\omega f}} \right) \\ \left. + \frac{\sigma_{if}(\omega)}{\Delta_{\omega f}} \left(+ \frac{1 - e^{\Delta_{i\omega}(t_f - t_i - 2\tau)} e^{\Delta_{i\omega}\tau}}{\Delta_{i\omega}} + \frac{1 - e^{-\Delta_{i\omega}\tau}}{\Delta_{i\omega}} \right) \right] , \end{aligned} \tag{4.30}$$

the last two lines of which contain terms that at large times behave as constants so long as there are no intermediate states with energies sufficiently close to the initial or final states. If this the case, the finite volume estimator can be fit simply as the gradient of the linear time behaviour, as in the case of the 3-point summation method.

4.2.1 Numerical Results

In order to test this methodology, we reproduce the exploratory study of the rare kaon decay presented in [70]. This utilises the $C2$ ensemble listed in table 2.2 with a heavy pion mass $m_\pi \simeq 430\,\text{MeV}$. This ensemble has the advantage that for a single unit of lattice momentum, the initial-final state energy difference is $am_K - aE_\pi(\boldsymbol{p}) = 0.0047(21)$ and therefore the non-linear time behaviour only occurs on a timescale $t/a \sim 200$ which is much larger than the $T/a = 64$ temporal extend of this lattice.

If both the vector current and weak Hamiltonian are to be summed over the lattice, multiple source-sink separations t_f are required to extract the amplitude. Even though the times t_i and t_f are fixed at the time of the solves, when performing a time translation average over every N^{th} timeslice, we have access to the propagators necessary to obtain every N^{th} source-sink separation. For this study we use every 2^{nd} time translation which on this lattice corresponds to $N_t = 32$ in table 4.1.

In addition, in order to remove the problematic single pion intermediate state, we utilise the scalar shift method which, as in the original methodology, leaves the amplitude unaffected, while removing the problematic intermediate state from the additional exponentials. The non-eye and eye contributions to the shift coefficient are found to be $c_s^{\text{NE}} = 5.62(3) \times 10^{-4}$ and $c_s^{\text{Eye}} = -3.14(7) \times 10^{-4}$ respectively.

Figure 4.2 shows the fit to the non-eye and eye components to the doubly integrated amputated 4-point correlation functions given by

$$\hat{I}^{(2)}(t_f, \tau) = \sum_{t_H=\tau}^{t_f-\tau} \sum_{t_J=0}^{T} \frac{\Gamma^4(0, t_H, t_J, t_f)}{Z_{K\pi}(0, t_f)} \,. \tag{4.31}$$

In order to suppress excited state contributions, the value $\tau = 5$ is used. Due to the sufficiently small energy splitting, we take the fit ansatz to be the simple linear component of eq. (4.30) with the gradient giving the amplitude. The remaining terms are constants up to contributions suppressed by the buffer size τ. The non-

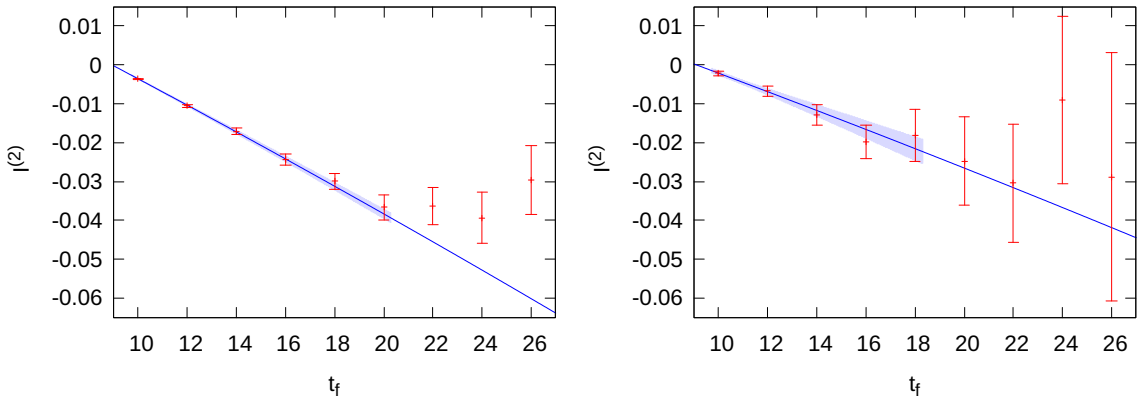

Figure 4.2 *Fits to the rare Kaon 4-point function summed over all t_J and $t_H \in [5, t_f - 5]$ as a function of t_f (with t_i fixed to 0). Shown are the non-eye (left) and eye-type (right) contributions.*

eye and eye contributions are found to be

$$\mathcal{A}_t^{\mathrm{NE}} = -1.68(5) \times 10^{-3} \qquad \text{and} \qquad \mathcal{A}_t^{\mathrm{Eye}} = -1.18(19) \times 10^{-3}\,, \tag{4.32}$$

which are in agreement within statistical errors to the results obtained in [70]. In addition, we have obtained approximately a factor 3 reduction in the statistical error on both the non-eye and eye contributions. Table 4.1 shows the number of light, strange and charm quark propagators required in each calculation (fixed t_J with $N_t = 12$ for [70], and summed t_J with $N_t = 32$ for this study). It can be seen that the number of light quark inversions is approximately equal, while more strange quark inversions are required. However, the saving is obtained in the number of charm quark inversions which are reduced by more than a factor 4 for a single charm mass. This saving then grows in proportion with the number of charm masses simulated for the extrapolation to physical charm quarks, and therefore could provide a massive cost saving with reduced error compared to the original method.

This study has shown that the summed method can be applied to applications involving 4-point functions such as the rare kaon and rare hyperon decays, and provide a signal-per-cost improvement. However, the methodology only allows for states that are sufficiently close to having degenerate initial and final states. Unfortunately, this limits the momentum transfer to only a single value that is in general away from the $q^2 = 0$ point of most interest to these calculations. Since this is a non-general methodology, in following chapters investigating the rare hyperon decay, we do not utilise the summed method in this way, but rather extend the existing methodology of [67].

CHAPTER

FIVE

PROSPECTS FOR THE RARE HYPERON DECAY $\Sigma^+ \to p\ell^+\ell^-$

This chapter is a reproduction of the open access published work [2], of which I am a co-author. I have made significant contributions to the content and writing of this work, except for section 5.3 to which I contributed by checking work performed by other co-authors.

5.0.1 Introduction

The transition of an s- to a d-quark ($s \to d$) requires a FCNC, which is only allowed through quantum corrections within the SM of particle physics. Consequently, processes involving such transitions are rare in the SM and could be enhanced by potential new physics that includes a flavour changing neutral current in its Lagrangian. An example for such a process is the rare semi-leptonic hyperon decay $\Sigma^+ \to p\ell^+\ell^-$, for which the muonic mode has been recently measured by the LHCb experiment [103] with a branching ratio of

$$\mathcal{B}(\Sigma^+ \to p\mu^+\mu^-) = (2.2^{+1.8}_{-1.3}) \times 10^{-8}\,. \tag{5.1}$$

Evidence for this decay had previously been found by the HyperCP collaboration [104] giving

$$\mathcal{B}(\Sigma^+ \to p\mu^+\mu^-) = (8.6^{+6.6}_{-5.4} \pm 5.5) \times 10^{-8}\,, \tag{5.2}$$

where the first uncertainties are statistical, and the second is systematic. This determination follows from three events, all at nearly the same invariant mass of the $\mu^+\mu^-$ pair. However, such a resonant structure in the $\mu^+\mu^-$ invariant mass could not be confirmed by the more recent LHCb measurement [103].

The current state-of-the-art SM theory predictions for this process [105–107] use a combination of dispersion relations, experimental input, various formulations of Baryon ChPT and model estimates (e.g. vector meson dominance) and arrive at a range of results [107]

$$1.6 \times 10^{-8} \leq \mathcal{B}\left(\Sigma^+ \to p\mu^+\mu^-\right) \leq 8.9 \times 10^{-8}\,. \tag{5.3}$$

More details on the phenomenological background of this decay can be found in section 5.1.

The rare hyperon decay $\Sigma^+ \to p\ell^+\ell^-$ can be viewed as the baryonic analogue of the rare kaon decay $K \to \pi\ell^+\ell^-$, which has been previously calculated from first principles using lattice simulations by the RBC-UKQCD collaboration, including recent results at physical quark masses [1, 67, 70]. Taking inspiration from this progress, in this paper we explore prospects for calculating the required form factors for the $\Sigma^+ \to p\ell^+\ell^-$ decay using LQCD. While other hyperon decays with much higher yields, such as $\Sigma^- \to n\ell^-\overline{\nu}_\ell$, can be used to make measurements of the CKM matrix element V_{us} in order to test for new physics that would break the CKM unitarity relations, this decay can be sensitive to new physics due to its rarity within the SM.

As already discussed in refs. [1, 67, 70, 77, 108], a key challenge in extracting decays such as $\Sigma^+ \to p\ell^+\ell^-$ and $K \to \pi\ell^+\ell^-$ from LQCD is that the physical observables (most directly defined in terms of infinite-volume Minkowski-signature correlation functions) contain on-shell intermediate states that can propagate between the weak Hamiltonian, effecting the $s \to d$ transition, and the electromagnetic current emitting the di-lepton pair. For the case of the rare hyperon decay in particular, intermediate $N\pi$ states contribute, where N represents the nucleon doublet and π the pion triplet. As we discuss in more detail in the following sections, in practice the states are projected to definite isospin as this is a good quantum number of the numerical calculation, provided the light quarks are degenerate and dynamical electromagnetism is not included, as we assume throughout. Fortunately, three-(or-more)-particle intermediate states are kinematically guaranteed to be off-shell and do not require special treatment.

Complications arise because numerical LQCD calculations only allow one to directly determine Euclidean correlation functions in a finite spacetime volume. Specifically, the finite-volume Euclidean correlator that most closely matches the rare hyperon decay is a four-point function, defined with operators to create the incoming Σ^+ and the outgoing p as well as the weak Hamiltonian and electromagnetic current. Careful examination of this correlator shows that the on-shell $N\pi$ intermediate states manifest in a number of ways, all of which complicate the calculation.

First, after the baryonic operators are used to project out the Σ^+ and p states, one finds that the on-shell intermediate states lead to exponentials that grow with the Euclidean-time separation between the weak Hamiltonian and the current [77]. In practice, the number of such exponentials is finite, dictated by the discrete finite-volume spectrum, and thus these states can be removed through various strategies that we detail in the following sections.

However, a consequence of discarding these terms is that the resulting finite-volume estimator has poles at the locations of all finite-volume energies with $N\pi$ quantum numbers. In addition, the resulting quantity is known to have power-like volume effects away from the poles, and to miss the imaginary part appearing in the physical amplitude due to the long-distance propagation of intermediate states. In short, removing growing exponentials defines a finite-volume object that *a priori* has no clear relation to the targeted amplitude. Fortunately, as we describe in section 5.3 following refs. [77, 108], the strategy to convert the finite-volume estimator to the physical observable (and thereby cancel the poles and include the imaginary contribution) is known and can be applied in this case.

The remainder of this paper is organized as follows: In section 5.1 we discuss the currently available phenomenological strategy and predictions to compute the $\Sigma^+ \to p\ell^+\ell^-$ branching ratio. Section 5.2 then outlines our strategy on the lattice, which aims to recover the $\Sigma^+ \to p\ell^+\ell^-$ amplitude via carefully chosen, numerically calculable Euclidean correlation functions. Here we discuss various strategies to remove the exponentially growing terms that will appear in the direct lattice result. In section 5.3 we discuss the removal of finite-volume singularities and make contact with the physical observable. In addition to translating the general formalism of refs. [77, 108] to our particular case, we also provide an explicit expression for an expansion that arises when the volume is tuned so that the mass of the Σ^+ coincides with one of the finite-volume $N\pi$ energies.

5.1 Phenomenological background

In the following, we will briefly review the phenomenological determination [105–107] of the branching ratio for $\Sigma^+ \to p\ell^+\ell^-$ leading to the result quoted in eq. (5.3). Short distance contributions to $\Sigma^+ \to p\ell^+\ell^-$ originate from penguin and box diagrams (cf. fig. 5.1) and are found to contribute only at the order of 10^{-12} [105] to the branching ratio of the muonic mode $\Sigma^+ \to p\mu^+\mu^-$, which is much smaller than the experimental measurements (eqs. (5.1) and (5.2)), indicating that this decay is long-distance dominated.

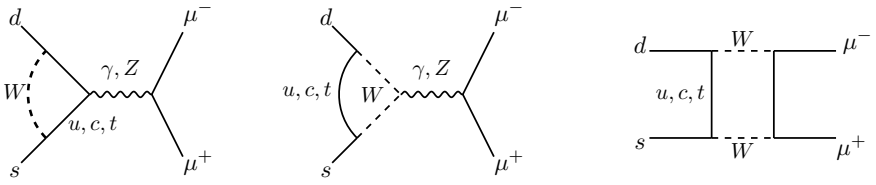

Figure 5.1 *Short-distance SM contributions to the $s \to d$ transition from penguin and box diagrams.*

The matrix element for the long-distance SM contribution to the $\Sigma^+ \to p\ell^+\ell^-$ decay can be written as [105, 109]

$$\begin{aligned}\mathcal{A}(\Sigma^+ \to p\ell^+\ell^-) = -e^2 G_F \times \overline{u}_\ell(\boldsymbol{p}_{\ell^-})\,\gamma^\nu\, v_\ell(\boldsymbol{p}_{\ell^+}) \\ \times \overline{u}_p(\boldsymbol{p})\left[\frac{i}{q^2}\left(a(q^2)+b(q^2)\gamma_5\right)\sigma_{\mu\nu}q^\mu + \gamma_\nu\left(c(q^2)+d(q^2)\gamma_5\right)\right] u_\Sigma(\boldsymbol{k})\,,\end{aligned} \tag{5.4}$$

in terms of the four form factors $a(q^2)$, $b(q^2)$, $c(q^2)$ and $d(q^2)$. Here γ^ν, γ_5 and $\sigma_{\mu\nu}$ are (combinations of) Minkowski gamma matrices, with conventions defined in appendix B of [2], and $u_\Sigma(\boldsymbol{k})$, $\overline{u}_p(\boldsymbol{p})$, $\overline{u}_\ell(\boldsymbol{p}_{\ell^-})$, and $v_\ell(\boldsymbol{p}_{\ell^+})$ are the usual Dirac spinors for the incoming Σ^+ and the outgoing proton, ℓ^-, and ℓ^+, respectively. The four-momentum transfer is $q = k - p$, where k and p are the on-shell four-momenta of the Σ^+ and proton, respectively.

Some information about the form factors a and b can be obtained from the decay

$\Sigma^+ \to p\gamma$ with a real photon. The respective decay rate[1] can be written as

$$\Gamma(\Sigma^+ \to p\gamma) = \frac{G_F^2 e^2}{\pi} |\boldsymbol{q}|^3 \left(|a(0)|^2 + |b(0)|^2\right) , \tag{5.5}$$

$$\frac{d\Gamma(\Sigma^+ \to p\gamma)}{d\cos\theta} \propto 1 + \alpha \cos\theta \qquad \text{with} \qquad \alpha = \frac{2\,\mathrm{Re}(a(0)b(0)^*)}{|a(0)|^2 + |b(0)|^2} , \tag{5.6}$$

where $|\boldsymbol{q}|$ is the energy of the photon and θ is the angle between the spin of the Σ^+ and the momentum of the proton.

The imaginary parts of the four form factors can be obtained from unitarity using amplitudes for $\Sigma \to N\pi$ and $N\pi \to N\gamma^*$. While the amplitude for $\Sigma \to N\pi$ is known from experimental measurements [110], the authors of ref. [105] calculate the amplitude $N\pi \to N\gamma^*$ from ChPT using either the relativistic baryon ChPT [111] or the heavy-baryon ChPT [112, 113] formulation. The momentum dependence of the imaginary parts of the form factors is found to be very mild. Once the imaginary parts of the form factors are known, information on the real parts of $a(q^2)$ and $b(q^2)$ at $q^2 = 0$ can be obtained from equations eq. (5.5) and eq. (5.6) and experimental data for the decay $\Sigma^+ \to p\gamma$. Since this decay only determines values for $|a(0)|^2 + |b(0)|^2$ and $\mathrm{Re}[a(0)b(0)^*]$, this leads to four possible solutions for $\big(\mathrm{Re}\big[a(0)\big], \mathrm{Re}\big[b(0)\big]\big)$. Motivated by the mild q^2-dependence of the imaginary parts of the form factors, the authors of ref. [105] assume that $\mathrm{Re}\big[a(q^2)\big] = \mathrm{Re}\big[a(0)\big]$ and $\mathrm{Re}\big[b(q^2)\big] = \mathrm{Re}\big[b(0)\big]$ for their prediction of $\mathcal{B}(\Sigma^+ \to p\ell^+\ell^-)$. The real parts of the $c(q^2)$ and $d(q^2)$ form factors are calculated assuming vector meson dominance in [105] and explicitly calculating vector meson pole contributions to the decay $\Sigma^+ \to p\ell^+\ell^-$. The q^2-dependence of $\mathrm{Re}\big[c(q^2)\big]$ and $\mathrm{Re}\big[d(q^2)\big]$ is found to be mild, just like in the imaginary parts.

Depending on the formulation of baryon ChPT used and the four possible solutions for $\mathrm{Re}\big[a(0)\big]$ and $\mathrm{Re}\big[b(0)\big]$ from $\Sigma^+ \to p\gamma$ decays, the authors of ref. [105] find the SM prediction for $\mathcal{B}(\Sigma^+ \to p\mu^+\mu^-)$ to be in the range

$$1.6 \times 10^{-8} \leq \mathcal{B}\left(\Sigma^+ \to p\mu^+\mu^-\right) \leq 9.0 \times 10^{-8} , \tag{5.7}$$

and very similar ranges are found in refs. [106, 107].

[1] The Particle Data Group [110] quotes $\mathcal{B}\left(\Sigma^+ \to p\gamma\right) = 1.23 \pm 0.05 \times 10^{-3}$ with $\tau_{\Sigma^+} = 0.8018 \pm 0.0026 \times 10^{-10}$ s, giving $\Gamma(\Sigma^+ \to p\gamma) = (10.1 \pm 0.4) \times 10^{-15}$ MeV and $\alpha = -0.76 \pm 0.08$.

5.2 Extracting the amplitude from Euclidean correlators

In this section and the next, we describe how to extract the $\Sigma^+ \to p\ell^+\ell^-$ amplitude from a numerical lattice calculation. The approach closely follows the methods of refs. [1, 67, 70, 77, 108], adjusted here to treat issues specific to this system. This section details the Euclidean two-, three-, and four-point correlation functions needed to construct a finite-volume estimator, denoted by $\widetilde{F}_\mu(\boldsymbol{k}, \boldsymbol{p})_L$. The following section describes how to relate this quantity to the physical rare hyperon amplitude.

5.2.1 Spectral representation

The determination of the long-distance contribution to $\Sigma^+ \to p\ell^+\ell^-$ requires a calculation of the $\Sigma^+ \to p\gamma^*$ amplitude, defined as

$$\mathcal{A}_\mu^{rs}(k,p) = \int d^4x \left\langle p(\boldsymbol{p}), r \middle| \mathrm{T}\left[\mathcal{H}_W(x)\, J_\mu(0)\right] \middle| \Sigma^+(\boldsymbol{k}), s \right\rangle , \tag{5.8}$$

with r and s labelling the azimuthal spin component of the state. Here we are assuming Minkowski-signature conventions and working in an infinite space-time volume. This amplitude can be re-expressed as a Dirac matrix, $\widetilde{\mathcal{A}}_\mu(k,p)$, using the relation

$$\mathcal{A}_\mu^{rs}(k,p) = \overline{u}_p^r(\boldsymbol{p})\, \widetilde{\mathcal{A}}_\mu(k,p)\, u_\Sigma^s(\boldsymbol{k}) , \tag{5.9}$$

with the spinors u_p and u_Σ of the proton and Σ^+, respectively.[2]

The effective weak Hamiltonian density of the $qs \to qd$ transition is given by [10]

$$\mathcal{H}_W(x) = \frac{G_F}{\sqrt{2}} V_{us} V_{ud}^* \left[C_1 \left(Q_1^u(x) - Q_1^c(x) \right) + C_2 \left(Q_2^u(x) - Q_2^c(x) \right) + \cdots \right] , \tag{5.10}$$

where the C_i are Wilson coefficients, the Q_i^q are four-quark operators, defined in terms of Dirac spinors for up, down, strange and charm quarks (respectively u, d, s and c) as

$$Q_1^q = (\overline{d}_i \gamma^{L\,\mu} s_i)(\overline{q}_j \gamma_\mu^L q_j) , \qquad Q_2^q = (\overline{d}_i \gamma^{L\,\mu} q_i)(\overline{q}_j \gamma_\mu^L s_j) . \tag{5.11}$$

Here i, j denote colour indices and we define $\gamma_\mu^L \equiv \gamma_\mu(1-\gamma_5)$. There are additional

[2] To avoid clutter in notation, we denote indices for the Σ^+ by Σ only. We still use Σ^+ where the charge is relevant, e.g. for creation and annihilation operators.

four-quark operators in eq. (5.10) with Wilson coefficients of order $|\frac{V_{ts}V_{td}}{V_{us}V_{ud}}| \simeq 0.00142$ which will be neglected in this work.

The electromagnetic current in eq. (5.8) is given by

$$J_\mu = \frac{2}{3}\overline{u}\gamma_\mu u - \frac{1}{3}\overline{d}\gamma_\mu d - \frac{1}{3}\overline{s}\gamma_\mu s + \frac{2}{3}\overline{c}\gamma_\mu c\,, \tag{5.12}$$

and we make use of translational invariance by fixing the position of the electromagnetic current to $y = 0$. Including an additional Fourier transform on the current would lead to an overall momentum-conserving Dirac delta function, to be removed at a later step, and we find it more convenient to follow the approach where this is never introduced.

The Hamiltonian density decomposes into a parity-positive and a parity-negative component

$$\mathcal{H}_W(x) = \mathcal{H}_W^+(x) + \mathcal{H}_W^-(x)\,, \tag{5.13}$$

defined via the parity operator $\hat{\mathcal{P}}$ according to

$$\hat{\mathcal{P}}\mathcal{H}_W^\pm(x)\hat{\mathcal{P}} = \pm\mathcal{H}_W^\pm(\mathcal{P}\cdot x)\,, \tag{5.14}$$

where $\mathcal{P}^\mu{}_\nu = \mathrm{diag}\big[1,-1,-1,-1\big]$ and $\hat{\mathcal{P}}$ is the Hilbert-space representation of the parity operator. Both parity sectors contribute to the amplitude we are evaluating.

Defining $\widetilde{\mathcal{A}}_\mu^\pm(k,p)$ as in eqs. (5.8) and (5.9), but with $\mathcal{H}_W(x)$ replaced by $\mathcal{H}_W^\pm(x)$, one can next decompose each definite-parity amplitude in terms of form factors as follows [105, 109]:

$$\widetilde{\mathcal{A}}_\mu^+(k,p) = i\sigma_{\nu\mu}q^\nu a(q^2) + \big(q^2\gamma_\mu - q_\mu \not{q}\big)\, c(q^2)\,, \tag{5.15}$$

$$\widetilde{\mathcal{A}}_\mu^-(k,p) = i\sigma_{\nu\mu}q^\nu\gamma_5 b(q^2) + \big(q^2\gamma_\mu - q_\mu \not{q}\big)\,\gamma_5 d(q^2)\,, \tag{5.16}$$

where we recall that $q = k - p$ is the four-momentum transfer of the virtual photon. This form-factor decomposition is derived in appendix B. Note also that, while the amplitude is a Dirac matrix and thus depends on individual components of the four-momenta, the form factors are Lorentz scalars and can therefore only depend on q^2.

We will see in the following that the amplitude, and thus also the form factors, are complex-valued due to on-shell intermediate $N\pi$ states. Since the Euclidean correlators are real-valued, this complexity already signals the fact that it is non-trivial to extract the amplitudes. This turns out to be closely related to the interplay

of the Euclidean signature and the finite volume. As we will show in the following, the quantum numbers of the contributing $N\pi$ states differ for $\widetilde{\mathcal{A}}_\mu^+$ and $\widetilde{\mathcal{A}}_\mu^-$, and thus the finite-volume formalism must be applied independently to the two quantities.

To explain this in more detail we return to eq. (5.8) and insert a complete set of states between the current and the weak Hamiltonian to write

$$\widetilde{\mathcal{A}}_\mu^\pm(k,p) = \int_0^\infty d\omega \left[\int_{-\infty}^0 dt\, \widetilde{\rho}_\mu^\pm(\omega)\, e^{-i(E_\Sigma(\boldsymbol{k})-\omega+i\epsilon)t} + \int_0^\infty dt\, \widetilde{\sigma}_\mu^\pm(\omega)\, e^{-i(\omega-E_p(\boldsymbol{p})-i\epsilon)t} \right], \tag{5.17}$$

where we have introduced the spectral functions, satisfying

$$\overline{u}_p^r(\boldsymbol{p})\, \widetilde{\rho}_\mu^\pm(\omega)\, u_\Sigma^s(\boldsymbol{k}) = \sum_\alpha \frac{\delta(\omega - E_\alpha(\boldsymbol{k}))}{2E_\alpha(\boldsymbol{k})} \left\langle p(\boldsymbol{p}), r \middle| J_\mu(0) \middle| E_\alpha, \boldsymbol{k} \right\rangle \left\langle E_\alpha, \boldsymbol{k} \middle| \mathcal{H}_W^\pm(0) \middle| \Sigma^+(\boldsymbol{k}), s \right\rangle, \tag{5.18}$$

$$\overline{u}_p^r(\boldsymbol{p})\, \widetilde{\sigma}_\mu^\pm(\omega)\, u_\Sigma^s(\boldsymbol{k}) = \sum_\beta \frac{\delta(\omega - E_\beta(\boldsymbol{p}))}{2E_\beta(\boldsymbol{p})} \left\langle p(\boldsymbol{p}), r \middle| \mathcal{H}_W^\pm(0) \middle| E_\beta, \boldsymbol{p} \right\rangle \left\langle E_\beta, \boldsymbol{p} \middle| J_\mu(0) \middle| \Sigma^+(\boldsymbol{k}), s \right\rangle. \tag{5.19}$$

Note that one must treat the two time orderings separately and this leads to two types of intermediate states encoded in $\widetilde{\rho}$ and $\widetilde{\sigma}$, which have strangeness $S = 0$ and $S = -1$ respectively. The sums over α and β represent both sums and phase-space integrals over the multi-particle QCD Fock space for all states that contribute. For example, the sum over α includes $N\pi$, $N\pi\pi$, $\Delta\pi$ and ΛK states.

Evaluating the time integrals then gives a compact result

$$\widetilde{\mathcal{A}}_\mu^\pm(k,p) = i \int_0^\infty d\omega\, \frac{\widetilde{\rho}_\mu^\pm(\omega)}{E_\Sigma(\boldsymbol{k}) - \omega + i\epsilon} - i \int_0^\infty d\omega\, \frac{\widetilde{\sigma}_\mu^\pm(\omega)}{\omega - E_p(\boldsymbol{p}) - i\epsilon}. \tag{5.20}$$

The aim of the following sections is to review how this amplitude can be extracted from finite-volume Euclidean-signature correlation functions.

5.2.2 Euclidean correlation functions

We now discuss how to extract a finite-volume estimator for the desired Minkowski-space amplitude eq. (5.20) from Euclidean correlation functions that can be calculated on the lattice. All quantities in this section (e.g. Dirac γ-matrices, four-vectors) are defined with Euclidean conventions detailed in Appendix B of [2].

Two-point functions

The two-point function of a baryon B can be written as

$$\Gamma_B^{(2)}(t,\boldsymbol{p})_{\alpha\beta} = \int d^3\boldsymbol{x}\, e^{-i\boldsymbol{p}\cdot\boldsymbol{x}} \left\langle \psi_\alpha^B(t,\boldsymbol{x})\, \overline{\psi}_\beta^B(0) \right\rangle , \tag{5.21}$$

where $\overline{\psi}_\beta^B(t,\boldsymbol{x})$ and $\psi_\alpha^B(t,\boldsymbol{x})$ create and annihilate, respectively, a baryon B and α and β are Dirac spinor indices. Examples for operators that have overlap with the proton p and Σ^+ are

$$\psi_\delta^p(t,\boldsymbol{x}) = \epsilon^{abc}\, (P^+\Gamma^A)_{\delta\gamma}\, u_{c,\gamma}(x)\, \left(u_{a,\alpha}(x)\, \Gamma^B_{\alpha\beta}\, d_{b,\beta}(x)\right) , \tag{5.22}$$

$$\psi_\delta^{\Sigma^+}(t,\boldsymbol{x}) = \epsilon^{abc}\, (P^+\Gamma^A)_{\delta\gamma}\, u_{c,\gamma}(x)\, \left(u_{a,\alpha}(x)\, \Gamma^B_{\alpha\beta}\, s_{b,\beta}(x)\right) , \tag{5.23}$$

with $\Gamma^A = \mathbb{1}$, $\Gamma^B = C\gamma_5$ for spin 1/2 particles and the charge conjugation operator defined by $C = \gamma_0\gamma_2$. $P^+ = \frac{1}{2}(1+\gamma_0)$ projects to the positive parity state. Here, and below, Roman and Greek indices refer to colour and Dirac indices, respectively.

For $t > 0$, the two-point function eq. (5.21) has the spectral representation

$$\Gamma_B^{(2)}(t,\boldsymbol{p}) = \sum_s \frac{|Z_B|^2 u_B^s \overline{u}_B^s}{2\, E_B(\boldsymbol{p})} e^{-tE_B(\boldsymbol{p})} = |Z_B|^2\, \frac{M_B}{E_B(\boldsymbol{p})}\, \mathbb{P}_B(\boldsymbol{p}) e^{-tE_B(\boldsymbol{p})} , \tag{5.24}$$

plus contributions from excited states, which are exponentially suppressed in t by their higher energies. The moving-frame energy of the baryon is given by $E_B(\boldsymbol{p}) = \sqrt{M_B^2 + \boldsymbol{p}^2}$ and the four-momentum vector is $p_B \equiv (iE_B(\boldsymbol{p}), \boldsymbol{p})$. We have introduced the projector

$$\mathbb{P}_B(\boldsymbol{p}) = \frac{1}{2M_B} \sum_r u_B^r(\boldsymbol{p}) \bar{u}_B^r(\boldsymbol{p}) = \frac{(-i\not{p}_B + M_B)}{2M_B} . \tag{5.25}$$

The overlap factor Z_B is defined by

$$\left\langle B(\boldsymbol{p}), s \middle| \overline{\psi}^B(0) \middle| 0 \right\rangle_\infty = Z_B^\dagger(\boldsymbol{p})\ \overline{u}_B^s(\boldsymbol{p}_B) , \qquad \left\langle 0 \middle| \psi^B(0) \middle| B(\boldsymbol{p}), s \right\rangle_\infty = Z_B(\boldsymbol{p})\ u_B^s(\boldsymbol{p}_B) . \tag{5.26}$$

Throughout this section and the next, we neglect the finite-volume effects on single-hadron energies and matrix elements. These are known to be exponentially suppressed, scaling as $e^{-M_\pi L}$. We also include the ∞ label on states that are normalized according to

$$\left\langle B(\boldsymbol{p'}), s' \middle| B(\boldsymbol{p}), s \right\rangle_\infty = 2E_B(\boldsymbol{p}) \delta_{s's} (2\pi)^3 \delta^3(\boldsymbol{p'} - \boldsymbol{p}) , \tag{5.27}$$

as this differs from the normalization of finite-volume states used below.

Three-point functions

We turn now to the three-point function of the effective weak Hamiltonian $\mathcal{H}_W$ between a Σ^+ and a p operator

$$\Gamma_H^{(3)}(t_H, t_p, t_\Sigma; \boldsymbol{p})_{\alpha\beta} = \int d^3\boldsymbol{x}_p d^3\boldsymbol{x}_\Sigma \, e^{-i\boldsymbol{p}\cdot(\boldsymbol{x}_p - \boldsymbol{x}_\Sigma)} \left\langle \psi_\alpha^p(t_p, \boldsymbol{x}_p) \; \mathcal{H}_W(t_H, \boldsymbol{0}) \; \overline{\psi}_\beta^{\Sigma^+}(t_\Sigma, \boldsymbol{x}_\Sigma) \right\rangle , \tag{5.28}$$

with the effective weak Hamiltonian density $\mathcal{H}_W$ given in eq. (5.10). We leave the parity labels implicit throughout this section unless stated explicitly.

Here the weak Hamiltonian is assumed to be appropriately renormalised. In the case of chirally symmetric fermion discretisations, the 4-quark operators in eq. (5.11) are protected from mixing with other dimension-6 operators, and as such the renormalisation comes purely in the determination of the Wilson coefficients C_1 and C_2. This process is described in detail for domain-wall-fermions in the calculation of the $K_L - K_S$ mass difference [75, 85].

The three-point function eq. (5.28) gives rise to four different topologies[3] for the Wick contractions, which are shown in Figure 5.2. The double point labelled with $\mathcal{H}_W$ shows the position of the weak Hamiltonian, and the points labelled Σ^+ and p are the positions of the Σ^+ and proton operator, respectively. The quark lines are labelled by their respective quark flavours. The two diagrams shown on the left-hand side of Figure 5.2 arise from contractions using the Q_1 operator in the weak Hamiltonian, the two diagrams on the right-hand side arise from contractions using the Q_2 operator.

The spectral representation of the Euclidean three-point function $\Gamma^{(3)}$ is given by

$$\Gamma_H^{(3)}(t_H, t_p, t_\Sigma; \boldsymbol{p}) = \sum_{r,s} \frac{Z_p(\boldsymbol{p}) \, Z_\Sigma^\dagger(\boldsymbol{p}) \; u_p^r(\boldsymbol{p}) \; \mathcal{A}_H^{rs} \; \overline{u}_\Sigma^s(\boldsymbol{p})}{4E_p(\boldsymbol{p})E_\Sigma(\boldsymbol{p})} \, e^{-E_p(\boldsymbol{p})\,(t_p - t_H)} \, e^{-E_\Sigma(\boldsymbol{p})\,(t_H - t_\Sigma)} , \tag{5.29}$$

for large time-separations $t_\Sigma \ll t_H$ and $t_H \ll t_p$, such that excited states are suppressed, with

$$\mathcal{A}_H^{rs} = \left\langle p(\boldsymbol{p}), r \middle| \mathcal{H}_W(0) \middle| \Sigma^+(\boldsymbol{p}), s \right\rangle_\infty \equiv \overline{u}_p^r(\boldsymbol{p}) \; \widetilde{\mathcal{A}}_H \; u_\Sigma^s(\boldsymbol{p}) , \tag{5.30}$$

where r and s are the spins of the proton and Σ^+, respectively. In the following it

[3] Naming conventions for the diagrams shown in Figure 5.2 are inspired by ref. [67].

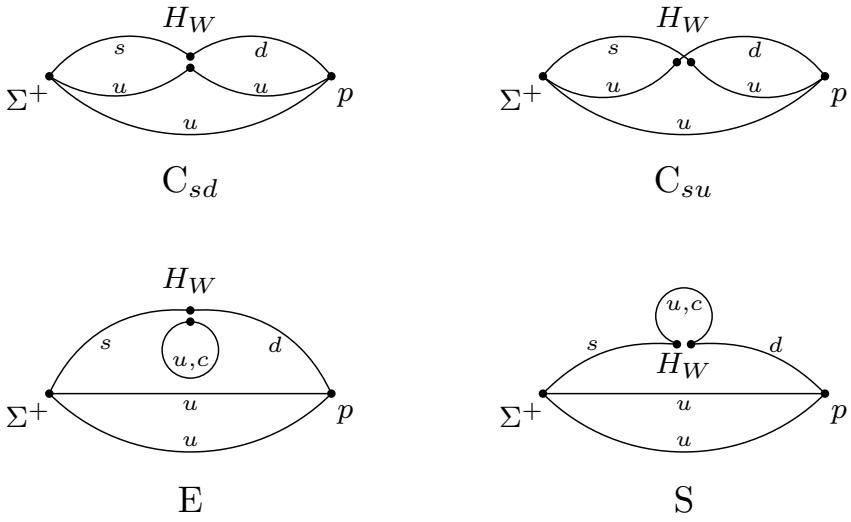

Figure 5.2 *The four different topologies for the Wick contractions of the three-point function eq. (5.28). Two fully connected contractions C_{sd} and C_{su} and two topologies (E and S) containing quark loops. The two diagrams on the left (C_{sd} and E) arise from contractions using the Q_1 operator, the two diagrams on the right (C_{su} and S) from Q_2.*

will be convenient to define the overall normalization factor

$$Z_{BB'}(t_B, t_{B'}; \boldsymbol{p}, \boldsymbol{k}) \equiv \frac{Z_B(\boldsymbol{p})\, Z^\dagger_{B'}(\boldsymbol{k}) M_B M_{B'}}{E_B(\boldsymbol{p}) E_{B'}(\boldsymbol{k})} e^{-E_B(\boldsymbol{p})\, t_B}\, e^{E_{B'}(\boldsymbol{k})\, t_{B'}}\,, \tag{5.31}$$

where $B, B' \in \{p, \Sigma\}$. This factor can be constructed using information extracted from Σ^+ and proton two-point functions (cf. eq. (5.24)). Completing the spin sum, the spectral representation eq. (5.29) can be written as

$$\Gamma^{(3)}_H(t_H, t_p, t_\Sigma; \boldsymbol{p}) = Z_{p\Sigma}(t_p, t_\Sigma; \boldsymbol{p}, \boldsymbol{p}) \mathbb{P}_p(\boldsymbol{p})\, \widetilde{\mathcal{A}}_H\, \mathbb{P}_\Sigma(\boldsymbol{p})\, e^{-t_H[(E_\Sigma(\boldsymbol{p}) - E_p(\boldsymbol{p})]}\,, \tag{5.32}$$

plus contributions from excited states. Similarly, one can define the three-point function for a baryon B (here $B \in \{p, \Sigma\}$) with an electromagnetic current J_μ

$$\Gamma^{(3)}_{\mu,B}(t_J, t_f, t_i; \boldsymbol{p}, \boldsymbol{k})_{\alpha\beta} = \int d^3\boldsymbol{x}_f d^3\boldsymbol{x}_i\, e^{-i(\boldsymbol{p}\cdot\boldsymbol{x}_f - \boldsymbol{k}\cdot\boldsymbol{x}_i)} \left\langle \psi^B_\alpha(t_f, \boldsymbol{x}_f)\; J_\mu(t_J, \boldsymbol{0})\; \overline{\psi}^B_\beta(t_i, \boldsymbol{x}_i) \right\rangle . \tag{5.33}$$

The spectral representation of such a three-point function is given by

$$\Gamma^{(3)}_{\mu,B}(t_J, t_f, t_i; \boldsymbol{p}, \boldsymbol{k}) = Z_{BB}(t_f, t_i; \boldsymbol{p}, \boldsymbol{k}) \mathbb{P}_B(\boldsymbol{p})\, \widetilde{\mathcal{A}}_{\mu,B}(\boldsymbol{q})\, \mathbb{P}_B(\boldsymbol{k}) e^{-t_J(E_B(\boldsymbol{k}) - E_B(\boldsymbol{p}))}\,, \tag{5.34}$$

with $\widetilde{\mathcal{A}}_{\mu,B}$ defined by

$$\mathcal{A}^{rs}_{\mu,B}(\boldsymbol{q}) = \left\langle B(\boldsymbol{p}), r \right| J_\mu(0) \left| B(\boldsymbol{k}), s \right\rangle_\infty \equiv \overline{u}^r_B(\boldsymbol{p})\ \widetilde{\mathcal{A}}_{\mu,B}(\boldsymbol{q})\ u^s_B(\boldsymbol{k})\,. \tag{5.35}$$

Just as with the weak Hamiltonian operator, the electromagnetic vector current is also assumed to be renormalised. If the conserved Noether current is used, then the vector Ward identity is exactly obeyed on the lattice and no renormalisation is necessary.

Here we have only considered three-point functions with single-hadron states. However, as discussed in the following subsection, to construct the target finite-volume estimator, one may also require matrix elements involving the finite-volume analogue of a multi-particle excited state. Many details of the construction of $\mathcal{A}^{rs}_H$ and $\mathcal{A}^{rs}_{\mu,B}(\boldsymbol{q})$ also apply for the excited-state analogues, but important differences arise which are described in appendix D of [2].

Finally, we define amputated versions of three-point functions with certain factors removed. For the vector current we take

$$\hat{\Gamma}^{(3)}_{\mu,p}(t_J;\boldsymbol{p},\boldsymbol{k}) \equiv \frac{\Gamma^{(3)}_{\mu,p}(t_J,t_f,t_i;\boldsymbol{p},\boldsymbol{k})}{Z_{pp}(t_i,t_f;\boldsymbol{p},\boldsymbol{k})} = \mathbb{P}_p(\boldsymbol{p})\left[\widetilde{\mathcal{A}}_{\mu,p}(\boldsymbol{q}) e^{-t_J(E_p(\boldsymbol{k})-E_p(\boldsymbol{p}))}\right]\mathbb{P}_p(\boldsymbol{k})\,, \tag{5.36}$$

and for the weak Hamiltonian

$$\hat{\Gamma}^{(3)}_{H}(t_H;\boldsymbol{k}) \equiv \frac{\Gamma^{(3)}_{H}(t_H,t_p,t_\Sigma;\boldsymbol{k})}{Z_{p\Sigma}(t_p,t_\Sigma;\boldsymbol{k},\boldsymbol{k})} = \mathbb{P}_p(\boldsymbol{k})\left[\widetilde{\mathcal{A}}_{H}\, e^{-t_H(E_\Sigma(\boldsymbol{k})-E_p(\boldsymbol{k}))}\right]\mathbb{P}_\Sigma(\boldsymbol{k})\,. \tag{5.37}$$

In both cases we drop time dependence which cancels in the limit that the ground-state dominates.

Four-point functions

We turn now to the four-point function of the time-ordered product of the weak-Hamiltonian density, $\mathcal{H}_W(x)$, and the electromagnetic current, $J_\mu(0)$, between a Σ^+ and a p state

$$\begin{aligned}\Gamma^{(4)}_{\mu,\alpha\beta}(t_H,t_p,t_\Sigma;\boldsymbol{p},\boldsymbol{k})_{L,T} = \int_L d^3\boldsymbol{x} d^3\boldsymbol{x}_p d^3\boldsymbol{x}_\Sigma\, e^{-i(\boldsymbol{x}_p\cdot\boldsymbol{p}-\boldsymbol{x}_\Sigma\cdot\boldsymbol{k})} \\ \times\left\langle \psi^p_\alpha(t_p,\boldsymbol{x}_p)\ \mathrm{T}\left[\mathcal{H}_W(t_H,\boldsymbol{x})\, J_\mu(0)\right]\ \overline{\psi}^{\Sigma^+}_\beta(t_\Sigma,\boldsymbol{x}_\Sigma)\right\rangle_{L,T}\,.\end{aligned} \tag{5.38}$$

Here the subscripts L, T indicate that the quantity is evaluated in a finite space-time volume. This is of particular importance for the four-point function, so we emphasize the fact with our notation. Note also that the lattice path integral will always give the time-ordered product of all four-fields. We restrict attention to the case of $t_\Sigma < 0, t_H < t_p$ so that the fields can be written as shown.

The weak-Hamiltonian and electromagnetic current operators should be renormalised in the same way as the relevant three-point functions above to remove divergences coming from the operators themselves. However, additional divergences can come from the contact of the two operators $x = (t_H, \boldsymbol{x}) \to 0$. The arguments for the cancellation of these divergences is given in chapter 3 in the context of the rare kaon decay. Since none of the arguments rely on the nature of the external states, no additional modifications are required for use in the baryonic decay $\Sigma^+ \to p\ell^+\ell^-$.

As with the Minkowski amplitude and the three-point function considered above, $\boldsymbol{q} = \boldsymbol{k} - \boldsymbol{p}$ denotes the momentum transfer at the electromagnetic vertex. From the four-point function, one obtains six Wick contractions for each of the four topologies (cf. Figure 5.2) of the three-point function with the weak Hamiltonian: the electromagnetic current J_μ can be inserted on any of the five quark lines or on a disconnected quark-loop. The diagrams corresponding to the in total 24 Wick contractions are shown in appendix A.

We next remove the overlap factor $Z_{p\Sigma}(t_p, t_\Sigma; \boldsymbol{p}, \boldsymbol{k})$, given in eq. (5.31), to define $\hat{\Gamma}^{(4)}_\mu$ as

$$\hat{\Gamma}^{(4)}_\mu(t_H; \boldsymbol{p}, \boldsymbol{k})_L = Z_{p\Sigma}(t_p, t_\Sigma; \boldsymbol{p}, \boldsymbol{k})^{-1}\, \Gamma^{(4)}_\mu(t_H, t_p, t_\Sigma; \boldsymbol{p}, \boldsymbol{k})_{L,T}\,. \tag{5.39}$$

We drop the dependence on T, t_p, and t_Σ in this quantity since the ratio is independent of these time coordinates as long as $T \gg t_p$, $T \gg |t_\Sigma| \gg 1/\Delta E_\Sigma$ and $|t_p| \gg 1/\Delta E_p$, where ΔE_Σ, ΔE_p are the gaps between the ground and first-excited states for the quantum numbers indicated by the subscript. We view it as a task of the numerical analysis to remove or quantify residual dependence on T, t_p, and $|t_\Sigma|$ and omit these coordinates for the remainder of this work.

The amputated four-point function is then equal to the matrix element

$$\hat{\Gamma}^{(4)}_\mu(t_H; \boldsymbol{p}, \boldsymbol{k})_L = \mathbb{P}_p(\boldsymbol{k})\, \widetilde{\mathcal{A}}_\mu(t_H; \boldsymbol{p}, \boldsymbol{k})_L\, \mathbb{P}_\Sigma(\boldsymbol{k})\,, \tag{5.40}$$

where $\widetilde{\mathcal{A}}_\mu(t_H; \boldsymbol{p}, \boldsymbol{k})_L$ is defined implicitly through

$$\mathcal{A}^{rs}_\mu(t_H; \boldsymbol{p}, \boldsymbol{k})_L \equiv \overline{u}^r_p(\boldsymbol{p})\; \widetilde{\mathcal{A}}_\mu(t_H; \boldsymbol{p}, \boldsymbol{k})_L\; u^s_\Sigma(\boldsymbol{p})\,, \tag{5.41}$$

where we have introduced the finite-volume, Euclidean-time-dependent analogue of eq. (5.8)

$$\mathcal{A}_\mu^{rs}(t_H;\boldsymbol{p},\boldsymbol{k})_L \equiv \int_L d^3\boldsymbol{x}\,\big\langle p(\boldsymbol{p}),r\big|\mathrm{T}\left[\mathcal{H}_W(t_H,\boldsymbol{x})J_\mu(0)\right]\big|\Sigma^+(\boldsymbol{k}),s\big\rangle_L\,. \tag{5.42}$$

Inserting a complete set of finite-volume states between the current and weak-Hamiltonian density, one can give a spectral representation of the four-point function in Euclidean space-time as

$$\hat{\Gamma}_\mu^{(4)}(t_H;\boldsymbol{p},\boldsymbol{k})_L = \begin{cases} \int_0^\infty d\omega\,\mathbb{P}_p(\boldsymbol{p})\,\widetilde{\sigma}_\mu(\omega)_L\,\mathbb{P}_\Sigma(\boldsymbol{k})\,e^{-t_H[\omega-E_p(\boldsymbol{p})]}\,, & \text{for } t_H>0 \\ \int_0^\infty d\omega\,\mathbb{P}_p(\boldsymbol{p})\,\widetilde{\rho}_\mu(\omega)_L\,\mathbb{P}_\Sigma(\boldsymbol{k})\,e^{-t_H[E_\Sigma(\boldsymbol{k})-\omega]} & \text{for } t_H<0 \end{cases}, \tag{5.43}$$

where $\widetilde{\rho}_\mu(\omega)_L$ and $\widetilde{\sigma}_\mu(\omega)_L$ are defined as in eqs. (5.18) and (5.19) above but here with the Euclidean conventions in the gamma matrices and with the sum now running over the discrete finite-volume spectrum. For example, $\widetilde{\rho}_\mu(\omega)_L$ can be written as

$$\widetilde{\rho}_\mu(\omega)_L = \sum_n \frac{\widetilde{C}_{n,\mu}(\boldsymbol{k})}{2E_n(\boldsymbol{k})}\,\delta\big(E_n(\boldsymbol{k})-\omega\big)\,, \tag{5.44}$$

where

$$\bar{u}_p^r(\boldsymbol{p})\,\widetilde{C}_{n,\mu}(\boldsymbol{k})\,u_\Sigma^s(\boldsymbol{k}) \equiv \big\langle p(\boldsymbol{p}),r\big|J_\mu(0)\big|E_n,\boldsymbol{k}\big\rangle_L\,\big\langle E_n,\boldsymbol{k}\big|\mathcal{H}_W(0)\big|\Sigma^+(\boldsymbol{k}),s\big\rangle_L\,, \tag{5.45}$$

and $\big|E_n,\boldsymbol{k}\big\rangle_L$ is the nth finite-volume state with the relevant quantum numbers to contribute, normalized as $\big\langle E_n,\boldsymbol{k}\big|E_n,\boldsymbol{k}\big\rangle_L = 2E_n(\boldsymbol{k})$.

5.2.3 Finite-volume estimator for the decay amplitude

Our aim now is to extract the infinite-volume, Minkowski-signature amplitude (with spectral representation given in eq. (5.20)) from the finite-volume Euclidean four-point function, decomposed above in eq. (5.43). To do so, one needs to separately treat the issues of Euclidean time and finite volume, and we find it most instructive to address the first point in this subsection and the second in the section following. To this end we define a physical-energy finite-volume estimator of eq. (5.20) as follows:

$$\widetilde{F}_\mu(\boldsymbol{k},\boldsymbol{p})_L \equiv i\int_0^\infty d\omega\,\frac{\widetilde{\rho}_\mu(\omega)_L}{E_\Sigma(\boldsymbol{k})-\omega} - i\int_0^\infty d\omega\,\frac{\widetilde{\sigma}_\mu(\omega)_L}{\omega-E_p(\boldsymbol{p})}\,. \tag{5.46}$$

This definition looks similar to eq. (5.20) but with the key difference that finite-

volume spectral functions have been substituted. As a result, the $i\epsilon$ pole prescription has also been discarded, since this has no effect in the finite volume. To see this more explicitly we write out the first term by substituting the definition of $\widetilde{\rho}_\mu(\omega)_L$

$$\int_0^\infty d\omega \, \frac{\widetilde{\rho}_\mu(\omega)_L}{E_\Sigma(\boldsymbol{k}) - \omega} = \sum_n \frac{\widetilde{C}_{n,\mu}(\boldsymbol{k})}{2E_n(\boldsymbol{k})\big(E_\Sigma(\boldsymbol{k}) - E_n(\boldsymbol{k})\big)} \,. \tag{5.47}$$

The sum over n runs over the discrete set of finite-volume states including the proton-like ground state and multi-hadron excited states that can be related to proton-pion and other scattering amplitudes. A subtlety of this analysis is that, for non-zero $\boldsymbol{k}$, parity is no longer a good quantum number for the finite-volume multi-particle states since $|E_n, \boldsymbol{k}\rangle$ and $|E_n, -\boldsymbol{k}\rangle$ are distinct states. We will avoid this issue by restricting attention to $\boldsymbol{k} = \boldsymbol{0}$ in the following section.

Various strategies are possible for extracting this finite-volume estimator from the amputated four-point function. One technical issue affecting all methods is that, because $\hat{\Gamma}^{(4)}_\mu(t_H; \boldsymbol{p}, \boldsymbol{k})_L$ only depends on the projected spectral functions, $\mathbb{P}_p(\boldsymbol{p})\, \widetilde{\sigma}_\mu(\omega)_L\, \mathbb{P}_\Sigma(\boldsymbol{k})$ and $\mathbb{P}_p(\boldsymbol{p})\, \widetilde{\rho}_\mu(\omega)_L\, \mathbb{P}_\Sigma(\boldsymbol{k})$, it is only possible to extract a similarly projected version of $\widetilde{F}_\mu(\boldsymbol{k}, \boldsymbol{p})_L$. Rather than carrying these projectors in all subsequent equations, we find it most convenient to change to spin indices at this stage, defining

$$F^{rs}_\mu(\boldsymbol{k}, \boldsymbol{p})_L = \bar{u}^r_p(\boldsymbol{p}) \widetilde{F}_\mu(\boldsymbol{k}, \boldsymbol{p})_L u^s_\Sigma(\boldsymbol{k}) \,, \tag{5.48}$$

$$\hat{\Gamma}^{(4)rs}_\mu(t_H; \boldsymbol{p}, \boldsymbol{k})_L = \bar{u}^r_p(\boldsymbol{p}) \hat{\Gamma}^{(4)}_\mu(t_H; \boldsymbol{p}, \boldsymbol{k})_L u^s_\Sigma(\boldsymbol{k}) \,, \tag{5.49}$$

and similar for all other quantities defined as Dirac matrices above.

To extract $F^{rs}_\mu(\boldsymbol{k}, \boldsymbol{p})_L$ from $\hat{\Gamma}^{(4)rs}_\mu(t_H; \boldsymbol{p}, \boldsymbol{k})_L$, a crucial issue that any method must address is that certain intermediate states lead to exponentially growing Euclidean time dependence. This arises because, in eq. (5.39), one is multiplying by growing exponentials depending on the energies of the incoming Σ^+ and outgoing proton. If the intermediate energies in the sum over n are sufficiently large, then these contribute decaying exponentials that outweigh the growth. However, due to low-lying finite-volume states, $\hat{\Gamma}^{(4)rs}_\mu(t_H; \boldsymbol{p}, \boldsymbol{k})_L$ can in principle diverge either for $t_H \to \infty$ or $t_H \to -\infty$.

To understand the point in more detail, we consider the unphysical quantity

$$-\int_{-\infty}^{\infty} dt_H\, e^{-\omega'|t_H|}\, \hat{\Gamma}_\mu^{(4)rs}(t_H;\boldsymbol{p},\boldsymbol{k})_L = \int_0^\infty d\omega\, \frac{\rho_\mu^{rs}(\omega)_L}{E_\Sigma(\boldsymbol{k})-\omega'-\omega} - \int_0^\infty d\omega\, \frac{\sigma_\mu^{rs}(\omega)_L}{\omega+\omega'-E_p(\boldsymbol{p})}\,. \quad (5.50)$$

Here ω' is chosen such that the integral over t_H is convergent, and one finds a result that is very similar to the targeted finite-volume estimator, $F_\mu^{rs}(\boldsymbol{k},\boldsymbol{p})_L$. In fact, the right-hand side gives this desired quantity in the $\omega' \to 0$ limit, but this is not useful as the integral on the left-hand side is divergent if evaluated at $\omega' = 0$. Physically, this expression corresponds to allowing the weak Hamiltonian to carry away energy from the system such that no on-shell intermediate states occur. It thus solves the problem of growing exponentials, but at the unacceptable cost of giving an unphysical quantity.

Two closely related options are available to reach the desired expression at $\omega' = 0$. The original proposal, introduced in refs. [67, 77], is to integrate t_H over a finite range of times, i.e. over the range $t_H \in [-T_a, T_b]$. One can then remove growing exponentials as a function of T_a and T_b in order to extract the desired finite-volume quantity. A closely related alternative, described in ref. [108], is to explicitly remove the exponentials as a function of t_H before integrating and then to re-introduce the missing poles in a second step.

Here we focus on the method of refs. [67, 77], defining

$$I_\mu^{rs}(T_a,T_b;\boldsymbol{p},\boldsymbol{k}) = (-i)\int_{-T_a}^{T_b} dt_H\; \hat{\Gamma}_\mu^{(4)rs}(t_H;\boldsymbol{p},\boldsymbol{k})\,, \quad (5.51)$$

with $-T_a < 0 < T_b$. The summed correlator has a spectral representation given by

$$I_\mu^{rs}(T_a,T_b;\boldsymbol{p},\boldsymbol{k}) = \int_0^\infty d\omega \left[i\rho_\mu^{rs}(\omega)_L\, \frac{1-e^{-(\omega-E_\Sigma(\boldsymbol{k}))T_a}}{E_\Sigma(\boldsymbol{k})-\omega} - i\sigma_\mu^{rs}(\omega)_L\, \frac{1-e^{-(\omega-E_p(\boldsymbol{p}))T_b}}{\omega-E_p(\boldsymbol{p})} \right], \quad (5.52)$$

in which the growing exponentials are displayed explicitly. From these expressions one sees that contributions growing as $T_a \to \infty$ will arise if $\rho_\mu^{rs}(\omega)_L$ includes finite-volume energies for which $E_n(\boldsymbol{k}) < E_\Sigma(\boldsymbol{k})$ and similarly contributions growing as $T_b \to \infty$ will arise if $\sigma_\mu^{rs}(\omega)_L$ includes finite-volume energies for which $E_n(\boldsymbol{p}) < E_p(\boldsymbol{p})$.

By studying the contributions in this specific system, we deduce that the limit $T_b \to \infty$ can be taken without any difficulties, since all possible baryonic intermediate

states with strangeness $S = -1$ and momentum $\boldsymbol{p}$ have energies $E_n(\boldsymbol{p}) > E_p(\boldsymbol{p})$. This will be true so long as the strange quark mass is greater than the down quark mass. As a result, the term with $e^{-T_b(\omega - E_p(\boldsymbol{p}))}$ is exponentially suppressed for large T_b. However, any intermediate state with $S = 0$ that has an energy smaller than the initial state energy $E_\Sigma(\boldsymbol{k})$ will lead to an exponentially growing term when $T_a \to \infty$. For simulations at physical or close-to-physical quark masses, such intermediate states can be either a single proton state with momentum $\boldsymbol{k}$ or a nucleon-pion state with total momentum $\boldsymbol{k}$ and an energy smaller than $E_\Sigma(\boldsymbol{k})$. For sufficiently large light-quark masses, the energy of the finite-volume nucleon-pion states will be greater than the Σ^+ energy and become decaying exponentials in T_a, leaving only the single proton state to grow as $T_a \to \infty$.

To extract $F_\mu^{rs}(\boldsymbol{k}, \boldsymbol{p})_L$ from $I_\mu^{rs}(T_a, T_b; \boldsymbol{p}, \boldsymbol{k})$, all growing terms need to be removed. It is additionally possible to remove decaying states such that the $T_a \to \infty$ limit is saturated for smaller values of T_a. The removal of slowly decaying states was already applied in ref. [70], in the context of rare kaon decays. To express this compactly, it is convenient to introduce a modification of ρ_μ^{rs} that is cut off to only include low-lying states

$$\rho_\mu^{[N]rs}(\omega)_L = \sum_{n=0}^{N-1} \delta(\omega - E_n(\boldsymbol{k})) \frac{C_{n,\mu}^{rs}(\boldsymbol{k})}{2E_n(\boldsymbol{k})}\,, \tag{5.53}$$

where $C_{n,\mu}(\boldsymbol{k})$ is defined in eq. (5.45) above, and N must satisfy the condition that $E_n(\boldsymbol{k}) > E_\Sigma(\boldsymbol{k})$ for $n \geq N$. We stress here that $n = 0$ refers to the finite-volume single-proton state. Then one can write

$$\overline{I}_\mu^{rs}(T_a, T_b; \boldsymbol{p}, \boldsymbol{k}) = I_\mu^{rs}(T_a, T_b;\, \boldsymbol{p}, \boldsymbol{k}) - \Delta I_\mu^{rs}(T_a; \boldsymbol{p}, \boldsymbol{k})\,, \tag{5.54}$$

$$\Delta I_\mu^{rs}(T_a; \boldsymbol{p}, \boldsymbol{k}) \equiv (-i) \int_0^\infty d\omega\, \rho_\mu^{[N]rs}(\omega)_L \frac{e^{-(\omega - E_\Sigma(\boldsymbol{k}))T_a}}{E_\Sigma(\boldsymbol{k}) - \omega}\,. \tag{5.55}$$

Note that $\overline{I}_\mu^{rs}(T_a, T_b; \boldsymbol{p}, \boldsymbol{k})$ then has the desired large $T_{a,b}$ limits

$$F_\mu^{rs}(\boldsymbol{k}, \boldsymbol{p})_L = \lim_{T_{a,b} \to \infty} \overline{I}_\mu^{rs}(T_a, T_b; \boldsymbol{p}, \boldsymbol{k})\,. \tag{5.56}$$

In contrast to I_μ^{rs}, the separate quantities $\overline{I}_\mu^{rs}$ and ΔI_μ^{rs}, as well as $F_\mu^{rs}(\boldsymbol{k}, \boldsymbol{p})_L$, have poles as a function of L for any fixed kinematics. The distinction arises because, in the original expression, $1 - e^{-(E_n(\boldsymbol{k}) - E_\Sigma(\boldsymbol{k}))T_a}$ vanishes whenever E_n and E_Σ coincide so that the combination has a finite limit

$$\lim_{E_n \to E_\Sigma} \frac{1 - e^{-(E_n(\boldsymbol{k}) - E_\Sigma(\boldsymbol{k}))T_a}}{E_\Sigma(\boldsymbol{k}) - E_n(\boldsymbol{k})} = T_a\,. \tag{5.57}$$

This must be the case since the manifestly finite correlator $\hat{\Gamma}_\mu^{(4)rs}$, integrated over a finite range of times, cannot diverge for any L. By contrast, ΔI_μ^{rs}, $\overline{I}_\mu^{rs}$ and F_μ^{rs} are divergent if $E_\Sigma(\boldsymbol{k})$ coincides with a finite-volume energy. We stress that there is no problem here, this is simply part of the correct definition of the finite-volume estimator. These poles will be removed in the final relation between F_μ^{rs} and the infinite-volume Minkowski amplitude $\mathcal{A}_\mu^{rs}$.

A slight variation in extracting $F_\mu^{rs}(\boldsymbol{k},\boldsymbol{p})_L$, discussed in ref. [108], is to remove the growing exponentials before integrating. In the present context it leads one to define

$$I_\mu^{\geq N,rs}(T_a,T_b;\boldsymbol{p},\boldsymbol{k}) \equiv (-i)\int_{-T_a}^{T_b} dt_H \Bigg[\hat{\Gamma}_\mu^{(4)rs}(t_H;\boldsymbol{p},\boldsymbol{k}) - \Theta(-t_H)\int_0^\infty d\omega\, \rho_\mu^{[N]rs}(\omega)_L\, e^{-t_H[E_\Sigma(\boldsymbol{k})-\omega]}\Bigg]. \quad (5.58)$$

This object now has a well-defined $T_{a,b}\to\infty$ limit, but it is not the desired estimator as the poles from the subtracted states are completely absent. These are then re-introduced by the relation

$$F_\mu^{rs}(\boldsymbol{k},\boldsymbol{p})_L = \lim_{T_{a,b}\to\infty} I_\mu^{\geq N,rs}(T_a,T_b;\boldsymbol{p},\boldsymbol{k}) + F_\mu^{[N]rs}(\boldsymbol{k},\boldsymbol{p})_L\,, \quad (5.59)$$

where we have introduced

$$F_\mu^{[N]rs}(\boldsymbol{k},\boldsymbol{p})_L \equiv i\int_0^\infty d\omega\, \frac{\rho_\mu^{[N]rs}(\omega)_L}{E_\Sigma(\boldsymbol{k})-\omega} = i\sum_{n=0}^{N-1}\frac{C_{n,\mu}^{rs}(\boldsymbol{k})}{2E_n(\boldsymbol{k})\big(E_\Sigma(\boldsymbol{k})-E_n(\boldsymbol{k})\big)}\,. \quad (5.60)$$

This method is analogous to the approach of using low-lying states to estimate the $T\to\infty$ integral for the hadronic-vacuum-polarization contribution to the magnetic moment of the muon [114].

Whether the removal of growing (and slowly decaying) exponentials is performed before or after t_H integration, it requires determination of the overlaps $C_{n,\mu}^{rs}(\boldsymbol{k})$ and energies $E_n(\boldsymbol{k})$ of all states to be removed. We discuss the detailed approach for determining this information in the following subsections. Having completed this, it is equally important to understand how to relate $F_\mu^{rs}(\boldsymbol{k},\boldsymbol{p})_L$ to the physical amplitude $\mathcal{A}_\mu^{rs}(k,p)$. This requires treating the multi-hadron finite-volume effects and understanding how to include the $N\pi$ branch cut that is part of the physical amplitude's definition. The method is discussed in detail in section 5.3. In addition, the general method for extracting the form factors from the physical amplitude $\mathcal{A}_\mu^{rs}(k,p)$ is given in appendix C, as well as an example for a specific kinematic setup.

Removal of the single-proton state

In this subsection, we describe two methods for removing the growing exponential arising from the single-proton state. Recalling the definitions

$$\left\langle p(\boldsymbol{p}), r \middle| J_\mu(0) \middle| p(\boldsymbol{k}), r' \right\rangle_\infty \equiv \bar{u}_p^r(\boldsymbol{p})\, \widetilde{\mathcal{A}}_{\mu,p}(\boldsymbol{q})\, u_p^{r'}(\boldsymbol{k})\,, \tag{5.61}$$

$$\left\langle p(\boldsymbol{k}), r' \middle| \mathcal{H}_W(0) \middle| \Sigma^+(\boldsymbol{k}), s \right\rangle_\infty \equiv \bar{u}_p^{r'}(\boldsymbol{k})\, \widetilde{\mathcal{A}}_H\, u_\Sigma^s(\boldsymbol{k})\,, \tag{5.62}$$

denoting the single-proton state with a p subscript (i.e. $C^{rs}_{p,\mu}(\boldsymbol{k}) = C^{rs}_{n=0,\mu}(\boldsymbol{k})$) one can show

$$C^{rs}_{p,\mu}(\boldsymbol{k}) \equiv \sum_{r'} \left\langle p(\boldsymbol{p}), r \middle| J_\mu(0) \middle| p(\boldsymbol{k}), r' \right\rangle \left\langle p(\boldsymbol{k}), r' \middle| \mathcal{H}_W(0) \middle| \Sigma^+(\boldsymbol{k}), s \right\rangle, \tag{5.63}$$

$$= 2M_p\, \bar{u}_p^r(\boldsymbol{p})\, \widetilde{\mathcal{A}}_{\mu,p}(\boldsymbol{q})\, \mathbb{P}_p(\boldsymbol{k})\, \widetilde{\mathcal{A}}_H\, u_\Sigma^s(\boldsymbol{k})\,, \tag{5.64}$$

$$= 2M_p\, \bar{u}_p^r(\boldsymbol{p}) \cdot \hat{\Gamma}^{(3)}_{\mu,p}(0; \boldsymbol{p}, \boldsymbol{k}) \cdot \hat{\Gamma}^{(3)}_H(t_H; \boldsymbol{k}) \cdot u_\Sigma^s(\boldsymbol{k}) e^{t_H[E_\Sigma(\boldsymbol{k}) - E_p(\boldsymbol{k})]}\,, \tag{5.65}$$

where in the last line we have used the hatted three-point functions defined in eqs. (5.36) and (5.37) and have also applied the identity $\mathbb{P}_p(\boldsymbol{p})^2 = \mathbb{P}_p(\boldsymbol{p})$. This expression for $C^{rs}_{p,\mu}(\boldsymbol{k})$ can then be used to remove the single-particle state. One can define

$$\Delta I^{(p)rs}_\mu(T_a; \boldsymbol{p}, \boldsymbol{k}) \equiv (-i)\, \frac{C^{rs}_{p,\mu}(\boldsymbol{k})}{2E_p(\boldsymbol{k})}\, \frac{e^{-(E_p(\boldsymbol{k}) - E_\Sigma(\boldsymbol{k}))T_a}}{E_\Sigma(\boldsymbol{k}) - E_p(\boldsymbol{k})}\,, \tag{5.66}$$

as the single-proton contribution to $\Delta I^{rs}_\mu(T_a; \boldsymbol{p}, \boldsymbol{k})$, defined in eq. (5.55).

In fact, it is instructive here to consider the case where only the single proton leads to a growing exponential, as would be the case for sufficiently large pion mass calculations. Then the method for extracting $F^{rs}_\mu(\boldsymbol{p}, \boldsymbol{k})_L$, with the proton removed after summation, can be summarized succinctly via

$$F^{rs}_\mu(\boldsymbol{p}, \boldsymbol{k})_L = i \frac{C^{rs}_{p,\mu}(\boldsymbol{k})}{2E_p(\boldsymbol{k})}\, \frac{e^{T_a(E_\Sigma(\boldsymbol{k}) - E_p(\boldsymbol{k}))}}{E_\Sigma(\boldsymbol{k}) - E_p(\boldsymbol{k})} - i \int_{-T_a}^{\infty} dt_H\, \hat{\Gamma}^{(4)rs}_\mu(t_H; \boldsymbol{p}, \boldsymbol{k})\,. \tag{5.67}$$

The estimator with the proton removed before summation instead gives

$$F^{rs}_\mu(\boldsymbol{p}, \boldsymbol{k})_L = i\, \frac{C^{rs}_{p,\mu}(\boldsymbol{k})}{2E_p(\boldsymbol{k})}\, \frac{1}{E_\Sigma(\boldsymbol{k}) - E_p(\boldsymbol{k})} - i \int_{-\infty}^{\infty} dt_H \left[\hat{\Gamma}^{(4)rs}_\mu(t_H; \boldsymbol{p}, \boldsymbol{k}) - \Theta(-t_H) \frac{C^{rs}_{p,\mu}(\boldsymbol{k})\, e^{-t_H[E_\Sigma(\boldsymbol{k}) - E_p(\boldsymbol{k})]}}{2E_p(\boldsymbol{k})} \right], \tag{5.68}$$

where one can directly make use of the time-dependence arising within eq. (5.37)

$$C^{rs}_{p,\mu}(\boldsymbol{k})\, e^{-t_H[E_\Sigma(\boldsymbol{k})-E_p(\boldsymbol{k})]} = 2M_p\, \bar{u}^r_p(\boldsymbol{p}) \cdot \hat{\Gamma}^{(3)}_{\mu,p}(0;\boldsymbol{p},\boldsymbol{k}) \cdot \hat{\Gamma}^{(3)}_{H}(t_H;\boldsymbol{k}) \cdot u^s_\Sigma(\boldsymbol{k})\,. \tag{5.69}$$

One can readily show that these two expressions are mathematically equivalent. They may, however, lead to statistical differences depending on how exactly the first term in eq. (5.67) and the first and last terms in eq. (5.68) are estimated.

Note also that it follows from eqs. (5.67) and (5.68) that, in the case where $C^{rs}_{p,\mu}(\boldsymbol{k}) = 0$, there is no need to explicitly treat the single-proton state. As was shown in refs. [1, 67, 70] for the single pion intermediate state in $K \to \pi\ell^+\ell^-$, it is in fact possible to define a modified weak Hamiltonian, denoted $\mathcal{H}'_W(0)$, such that $F^{rs}_\mu(\boldsymbol{p},\boldsymbol{k})_L$ is invariant under $\mathcal{H}_W \to \mathcal{H}'_W$, but

$$\langle p(\boldsymbol{k}), r|\, \mathcal{H}'_W(0)\, \big|\Sigma^+(\boldsymbol{k}), s\big\rangle = 0 \quad \Longrightarrow \quad C'^{rs}_{p,\mu}(\boldsymbol{k}) = 0\,, \tag{5.70}$$

where the prime on $C^{rs}_{p,\mu}$ indicates the $\mathcal{H}_W \to \mathcal{H}'_W$ replacement. The redefined Hamiltonian density is given explicitly by

$$\mathcal{H}'_W(x) = \mathcal{H}_W(x) - c_S \mathcal{S}^{\bar{d}s}(x) - c_P \mathcal{P}^{\bar{d}s}(x)\,, \tag{5.71}$$

where c_S and c_P are constants to be determined and

$$\mathcal{S}^{\bar{q}'q}(x) = \bar{q}'(x)q(x)\,, \qquad \mathcal{P}^{\bar{q}'q}(x) = \bar{q}'(x)\gamma_5 q(x)\,, \tag{5.72}$$

are flavour non-singlet scalar and pseudo-scalar densities. In the following we first prove that $F^{rs}_\mu(\boldsymbol{p},\boldsymbol{k})_L$ is invariant under $\mathcal{H}_W \to \mathcal{H}'_W$ and then explain how one fixes c_S and c_P to set the single-proton contribution to vanish.

Begin by recalling that the conserved and partially conserved vector and axial currents, $V^{\bar{q}'q}_\mu$ and $A^{\bar{q}'q}_\mu$ respectively, exactly satisfy the chiral Ward identities:

$$\partial^\mu V^{\bar{q}'q}_\mu(x) = i(m'-m)\mathcal{S}^{\bar{q}'q}(x)\,, \qquad \partial^\mu A^{\bar{q}'q}_\mu(x) = i(m'+m)\mathcal{P}^{\bar{q}'q}(x)\,. \tag{5.73}$$

Thus, inserting the scalar and pseudo-scalar densities between generic final and initial states with matching momenta, $\langle E_f,\boldsymbol{k}|_L$ and $|E_i,\boldsymbol{k}\rangle_L$ respectively, one finds

$$\langle E_f,\boldsymbol{k}|\, \mathcal{S}^{\bar{q}'q}(x)\, |E_i,\boldsymbol{k}\rangle_L = i\frac{E_i-E_f}{m'-m}\, \langle E_f,\boldsymbol{k}|\, V^{\bar{q}'q}_0(x)\, |E_i,\boldsymbol{k}\rangle_L\,, \tag{5.74}$$

$$\langle E_f,\boldsymbol{k}|\, \mathcal{P}^{\bar{q}'q}(x)\, |E_i,\boldsymbol{k}\rangle_L = i\frac{E_i-E_f}{m'+m}\, \langle E_f,\boldsymbol{k}|\, A^{\bar{q}'q}_0(x)\, |E_i,\boldsymbol{k}\rangle_L\,. \tag{5.75}$$

The crucial point is that $\mathcal{S}^{\bar{d}s}(x)$ and $\mathcal{P}^{\bar{d}s}(x)$ have no effect on $F_\mu^{rs}(\boldsymbol{p},\boldsymbol{k})_L$. To demonstrate this we define $F_\mu'^{rs}(\boldsymbol{p},\boldsymbol{k})_L$ as the result of replacing $\mathcal{H}_W \to \mathcal{H}'_W$ in F_μ^{rs}, and then use the c_S and c_P dependence to unambiguously decompose as

$$F_\mu'^{rs}(\boldsymbol{p},\boldsymbol{k})_L = F_\mu^{rs}(\boldsymbol{p},\boldsymbol{k})_L - c_S S_\mu^{rs}(\boldsymbol{p},\boldsymbol{k})_L - c_P P_\mu^{rs}(\boldsymbol{p},\boldsymbol{k})_L\,, \tag{5.76}$$

thereby defining $S_\mu^{rs}(\boldsymbol{p},\boldsymbol{k})_L$ and $P_\mu^{rs}(\boldsymbol{p},\boldsymbol{k})_L$. Taking the scalar for concreteness note that this can then be written explicitly as

$$\begin{aligned} S_\mu^{rs}(\boldsymbol{p},\boldsymbol{k})_L = \; & i\sum_{n'} \frac{1}{2E_{n'}(\boldsymbol{k})} \frac{\langle p(\boldsymbol{p}),r|\, J_\mu\, |E_{n'},\boldsymbol{k}\rangle_L \,\langle E_{n'},\boldsymbol{k}|\, \mathcal{S}^{\bar{d}s}\, |\Sigma^+(\boldsymbol{k}),s\rangle_L}{E_\Sigma(\boldsymbol{k}) - E_{n'}(\boldsymbol{k})} \\ & - i\sum_{n} \frac{1}{2E_n(\boldsymbol{p})} \frac{\langle p(\boldsymbol{p}),r|\, \mathcal{S}^{\bar{d}s}\, |E_n,\boldsymbol{p}\rangle_L \,\langle E_n,\boldsymbol{p}|\, J_\mu\, |\Sigma^+(\boldsymbol{k}),s\rangle_L}{E_n(\boldsymbol{p}) - E_p(\boldsymbol{p})}\,, \end{aligned} \tag{5.77}$$

where the sum over n' runs over finite-volume states with proton quantum numbers and that over n runs over states with strangeness $S=-1$. Using eq. (5.74) then gives

$$\begin{aligned} S_\mu^{rs}(\boldsymbol{p},\boldsymbol{k})_L = \; & \frac{1}{m_s - m_d}\left(\sum_{n'} \frac{1}{2E_{n'}(\boldsymbol{k})} \langle p(\boldsymbol{p}),r|\, J_\mu\, |E_{n'},\boldsymbol{k}\rangle_L \,\langle E_{n'},\boldsymbol{k}|\, V_0^{\bar{d}s}\, \big|\Sigma^+(\boldsymbol{k}),s\big\rangle_L \right. \\ & \left. - \sum_{n} \frac{1}{2E_n(\boldsymbol{p})} \langle p(\boldsymbol{p}),r|\, V_0^{\bar{d}s}\, |E_n,\boldsymbol{p}\rangle_L \,\langle E_n,\boldsymbol{p}|\, J_\mu\, \big|\Sigma^+(\boldsymbol{k}),s\big\rangle_L \right)\,, \end{aligned} \tag{5.78}$$

where the energy differences in the chiral Ward identity have cancelled the poles. As a result each term now contains an insertion of the identity that can be collapsed to reach

$$S_\mu^{rs}(\boldsymbol{p},\boldsymbol{k})_L = \frac{\langle p(\boldsymbol{p}),r|\, [J_\mu, V_0^{\bar{d}s}]\, |\Sigma^+(\boldsymbol{k}),s\rangle}{m_s - m_d}\,. \tag{5.79}$$

Similarly, for the pseudoscalar one finds

$$P_\mu^{rs}(\boldsymbol{p},\boldsymbol{k})_L = \frac{\langle p(\boldsymbol{p}),r|\, [J_\mu, A_0^{\bar{d}s}]\, |\Sigma^+(\boldsymbol{k}),s\rangle}{m_s + m_d}\,. \tag{5.80}$$

Since the electromagnetic current J_μ is a singlet in flavour space and the flavour changing axial and vector currents are not, they will commute causing the shifts to the estimator to vanish. We can therefore shift the weak Hamiltonian by any amount of the scalar and pseudoscalar operators without affecting the value of the

estimator:

$$S_\mu^{rs}(\boldsymbol{p},\boldsymbol{k})_L = 0\,, \quad P_\mu^{rs}(\boldsymbol{p},\boldsymbol{k})_L = 0 \qquad \Longrightarrow \qquad F_\mu'^{rs}(\boldsymbol{p},\boldsymbol{k})_L = F_\mu^{rs}(\boldsymbol{p},\boldsymbol{k})_L\,. \tag{5.81}$$

It remains only to fix the values of c_S and c_P. This can be achieved by demanding

$$\langle p(\boldsymbol{k}), r|\, \mathcal{H}_W'^{\pm}\, |\Sigma^+(\boldsymbol{k}), s\rangle = 0\,, \tag{5.82}$$

where we have restored the $\pm$ superscript as it is relevant here that one can study the definite parity sectors separately. As shown in appendix B, a generic Lorentz (pseudo)scalar operator $\mathcal{O}$ can be decomposed into scalar and pseudoscalar form factors $a_\mathcal{O}$ and $b_\mathcal{O}$ respectively, giving the decompositions

$$\langle p(\boldsymbol{k}), r|\, \mathcal{H}_W'^{+}\, |\Sigma^+(\boldsymbol{k}), s\rangle = \bar{u}_p^r(\boldsymbol{k})\,(a_H - c_S\, a_S)\, u_\Sigma^s(\boldsymbol{k})\,, \tag{5.83}$$

$$\langle p(\boldsymbol{k}), r|\, \mathcal{H}_W'^{-}\, |\Sigma^+(\boldsymbol{k}), s\rangle = \bar{u}_p^r(\boldsymbol{k})\,(b_H - c_P\, b_P)\,\gamma_5\, u_\Sigma^s(\boldsymbol{k})\,, \tag{5.84}$$

where we have used that only $\mathcal{S}^{\bar{d}s}$ contributes to $\mathcal{H}_W^+$ (and only $\mathcal{P}^{\bar{d}s}$ to $\mathcal{H}_W^-$). We deduce $c_S = \frac{a_H}{a_S}$ and $c_P = \frac{b_H}{b_P}$ are required for the single proton intermediate state to vanish.

Comparing this to the scalar shift in the rare kaon decay [67], we note that due to the additional spin degree of freedom, there is an additional pseudoscalar form factor describing the weak Hamiltonian matrix element. In general, it is therefore not sufficient to perform only a scalar shift to remove the single proton intermediate state from both parity sectors. There is however a kinematic point where the pseudoscalar shift is no longer required. This is when the spinor contraction $\bar{u}_p^r(\boldsymbol{k})\gamma_5 u_\Sigma^s(\boldsymbol{k})$ vanishes at $\boldsymbol{k} = \boldsymbol{0}$, corresponding to the Σ^+ at rest.

Removal of multi-hadron states

At close-to-physical quark masses, the other growing exponentials come from the lowest-lying $N\pi$ states, which have energy smaller than the mass of the Σ^+. Because these are excited states, their subtraction is more involved. In general, all lattice interpolating operators with the correct quantum numbers will overlap the states of interest, but in practice one can only reliably extract excited state energies and matrix elements by solving a generalized eigenvalue problem (GEVP) with a diverse set of multi-hadron operators. In the present case, the low-lying states are expected to be $N\pi$-like states together with resonances. Therefore, operators built from a

nucleon and pion that are individually momentum projected are required to reliably determine the excited spectrum. Depending on the finite-volume box size, three-particle states could also become important, requiring an even more complicated operator basis.

It is also important to break up the intermediate excited states according to irreducible representations (irreps) of the octahedral symmetry group (including parity) or, in the case that the Σ^+ baryon has non-zero spatial momentum $\boldsymbol{k}$, to a little group that leaves the latter invariant. The GEVP analysis is then performed separately within each irrep and the final result is constructed from the separately determined spectra. Details are given in appendix D of [2].

Once an optimized operator for a given excited state is determined, the removal of that state proceeds as in eq. (5.45) for the single proton. The energy $E_n(\boldsymbol{k})$ is extracted from the two-point function and the product of matrix elements

$$C^{rs}_{n,\mu}(\boldsymbol{k}) \equiv \sum_{r'} \left\langle p(\boldsymbol{p}), r \middle| J_\mu(0) \middle| E_n, \boldsymbol{k}, r' \right\rangle_L \left\langle E_n, \boldsymbol{k}, r' \middle| \mathcal{H}_W(0) \middle| \Sigma^+(\boldsymbol{k}), s \right\rangle_L , \tag{5.85}$$

from the three-point functions. It should be noted that this procedure can be applied to remove the exponentials associated with arbitrarily many intermediate states (whether growing or decaying), and for states with higher numbers of hadrons, so long as a sufficient operator basis can be obtained.

This completes our discussion of the construction of $F^{rs}_\mu(\boldsymbol{k}, \boldsymbol{p})_L$. We now turn to the formalism required to relate this object to the physical amplitude for the weak decay $\Sigma^+ \to p\ell^+\ell^-$.

5.3 Finite-volume effects

For calculations with sufficiently heavy pions, the energy of the lowest $N\pi$ states will lie above the $E_\Sigma(\mathbf{k})$ threshold, and therefore only exponentially suppressed finite volume effects will be present. At the physical point however, the low-lying $N\pi$ states will be below this threshold, inducing additional power-like finite volume effects.

In this section, we detail the correction of these power-like finite volume effects from such $N\pi$ states which can be accounted for via a simple additive term, denoted by $\Delta F^{rs}_\mu(\boldsymbol{k}, \boldsymbol{p})_L$. This allows one to determine the physical amplitude, up to

exponentially suppressed L effects, using the relation

$$\mathcal{A}_\mu^{rs}(k,p) = F_\mu^{rs}(\boldsymbol{k},\boldsymbol{p})_L + \Delta F_\mu^{rs}(\boldsymbol{k},\boldsymbol{p})_L\,. \tag{5.86}$$

At this stage, we also switch from labelling states by definite individual quark flavour content (e.g. p and Σ^+) to isospin state labels (N for the neutron-proton doublet and $N\pi$ for two-particle states with possible isospin values $I = 1/2, 3/2$). This is necessary to introduce the finite-volume formalism for multi-particle states below.

Since $\mathcal{A}_\mu^{rs}(k,p)$ does not contain poles associated with the finite-volume $N\pi$ intermediate states, these must cancel between the two terms on the right-hand side. As discussed in detail in ref. [108], this means that the numerical steps that introduce poles in $F_\mu^{rs}(\boldsymbol{k},\boldsymbol{p})_L$ must match those in the construction of $\Delta F_\mu^{rs}(\boldsymbol{k},\boldsymbol{p})_L$, such that the singularities exactly cancel. To keep track of this, it is useful to group the cancelling poles via the definitions

$$\mathcal{A}_\mu^{rs}(k,p) = \lim_{T_{a,b}\to\infty}\left[I_\mu^{rs}(T_a,T_b;\,\boldsymbol{p},\boldsymbol{k}) + \delta\overline{F}_\mu^{rs}(T_a;\boldsymbol{k},\boldsymbol{p})_L\right], \tag{5.87}$$

$$\delta\overline{F}_\mu^{rs}(T_a;\boldsymbol{k},\boldsymbol{p})_L = -\Delta I_\mu^{rs}(T_a;\boldsymbol{p},\boldsymbol{k}) + \Delta F_\mu^{rs}(\boldsymbol{k},\boldsymbol{p})_L\,. \tag{5.88}$$

An important subtlety here is that $I_\mu^{rs}(T_a,T_b;\,\boldsymbol{p},\boldsymbol{k})$ and $\delta\overline{F}_\mu^{rs}(T_a;\boldsymbol{k},\boldsymbol{p})_L$ each diverge as $T_a\to\infty$, in such a way that the combination in eq. (5.87) remains finite.

An alternative to eq. (5.87) can be written by directly using the quantity $I_\mu^{\geq N,rs}(T_a,T_b;\boldsymbol{p},\boldsymbol{k})$, defined in eq. (5.58). In particular, combining the various definitions given above, one finds

$$\mathcal{A}_\mu^{rs}(k,p) = \lim_{T_{a,b}\to\infty} I_\mu^{\geq N,rs}(T_a,T_b;\boldsymbol{p},\boldsymbol{k}) + \delta F_\mu^{rs}(\boldsymbol{k},\boldsymbol{p})_L\,, \tag{5.89}$$

where we have introduced a T_a-independent analogue of $\delta\overline{F}_\mu^{rs}(T_a;\boldsymbol{k},\boldsymbol{p})_L$, defined as

$$\delta F_\mu^{rs}(\boldsymbol{k},\boldsymbol{p})_L = \delta\overline{F}_\mu^{rs}(T_a;\boldsymbol{k},\boldsymbol{p})_L - i\sum_{n=0}^{N-1}\frac{C_{n,\mu}^{rs}(\boldsymbol{k})[e^{-(E_n(\boldsymbol{k})-E_\Sigma(\boldsymbol{k}))T_a}-1]}{2E_n(\boldsymbol{k})(E_\Sigma(\boldsymbol{k})-E_n(\boldsymbol{k}))}\,, \tag{5.90}$$

This is the unique combination in this work that is (i) T_a-independent, (ii) free of finite-volume singularities, and (iii) depends only on the states explicitly removed and not on the full sum over all states in the spectral decomposition. For this reason it will be useful in our detailed discussion of the single-channel case below.

We are now ready to give the full definition for $\Delta F_\mu^{rs}(\boldsymbol{k},\boldsymbol{p})_L$. The finite-volume

correction can be written as [67, 108, 115]

$$\Delta F_\mu^{rs}(\boldsymbol{k},\boldsymbol{p})_L = i\mathcal{A}^r_{J_\mu}(E_\Sigma(\boldsymbol{k}),\boldsymbol{k},\boldsymbol{p})\cdot\mathcal{F}\big(E_\Sigma(\boldsymbol{k}),\boldsymbol{k},L\big)\cdot\mathcal{A}^s_{H_W}(E_\Sigma(\boldsymbol{k}),\boldsymbol{k})\,, \tag{5.91}$$

where we have introduced

$$\mathcal{A}^r_{J_\mu}(E_\Sigma(\boldsymbol{k}),\boldsymbol{k},\boldsymbol{p}) = \big\langle N(\boldsymbol{p}),r\big|J_\mu(0)\big|E,(N\pi)^{\text{in}}(\boldsymbol{k})\big\rangle\,, \tag{5.92}$$

$$\mathcal{A}^s_{H_W}(E_\Sigma(\boldsymbol{k}),\boldsymbol{k}) = \big\langle E,(N\pi)^{\text{out}}(\boldsymbol{k})\big|\mathcal{H}_W(0)\big|\Sigma(\boldsymbol{k}),s\big\rangle\,, \tag{5.93}$$

$$\mathcal{F}(E,\boldsymbol{P},L) = \frac{1}{F(E,\boldsymbol{P},L)^{-1}+\mathcal{M}(E_{\mathsf{cm}})}\,. \tag{5.94}$$

Here $F(E,\boldsymbol{P},L)$ is a known geometric function, reviewed in this work in the following paragraphs, and $\mathcal{A}^r_{J_\mu}(\boldsymbol{k},\boldsymbol{p})$, $\mathcal{A}^s_{H_W}(\boldsymbol{k})$, and $\mathcal{M}(E_{\mathsf{cm}})$ are three types of infinite-volume amplitudes, each involving $N\pi$ states.

This construction and the following discussion is similar to that given in refs. [77, 116], in that case of $\pi\pi$ intermediate states in $K-\bar{K}$ mixing and the decay $K\to\pi\bar{\nu}\nu$. The formalism of that work was generalized to particles with any spin, including the present case, in ref. [108]. The purpose of the following is to explain the relevant formalism in the specific context of $N\pi$ states, including the role of parity, spin and non-degenerate masses. The formalism for long-range matrix elements also draws on that used for scattering and transition amplitudes [76, 115, 117–121].

We begin by specifying the index space used in the definition of $\Delta F_\mu^{rs}(\boldsymbol{k},\boldsymbol{p})_L$. The product on the right-hand side of eq. (5.91) is understood as a matrix ($\mathcal{F}$) contracted with two vectors ($\mathcal{A}^r_{J_\mu}$ and $\mathcal{A}^s_{H_W}$) such that no hanging indices remain. The index space of this contraction is also required for the exact definitions of $F(E,\boldsymbol{P},L)$ and the other quantities appearing above. The space is denoted by J,ℓ,μ, referring to the total angular momentum J, orbital angular momentum, ℓ, total spin (in this case fixed to 1/2), and azimuthal component of total angular momentum m_J. For example,

$$\mathcal{A}^r_{J_\mu}(E,\boldsymbol{k},\boldsymbol{p})_{J,\ell,m_J} = \big\langle N(\boldsymbol{p}),r\big|J_\mu(0)\big|E,(N\pi)^{\text{in}}(\boldsymbol{k}),J,\ell,m_J\big\rangle\,, \tag{5.95}$$

$$\mathcal{A}^s_{H_W}(E,\boldsymbol{k})_{J,\ell,m_J} = \big\langle E,(N\pi)^{\text{out}}(\boldsymbol{k}),J,\ell,m_J\,\big|\mathcal{H}_W(0)\big|\Sigma(\boldsymbol{k}),s\big\rangle\,, \tag{5.96}$$

and the combined labels of total energy E, total momentum $\boldsymbol{k}$, and J,ℓ,m_J are both necessary and sufficient to exactly specify the $N\pi$ state.

We define the geometric matrix, $F(E,\boldsymbol{P},L)$, for the $N\pi$ system, by first considering the quantity for two non-identical scalar particles with masses M_π, M_N [122].

Focusing on the $\boldsymbol{P} = \boldsymbol{0}$ case, the definition reads

$$F_{\ell' m';\ell m}(E, \boldsymbol{0}, L) = \lim_{\alpha \to 0^+} \left[\frac{1}{L^3} \sum_{\boldsymbol{k}} - \int \frac{\mathrm{d}^3 \boldsymbol{k}}{(2\pi)^3} \right] \frac{4\pi Y^*_{\ell' m'}(\hat{\boldsymbol{k}}) Y_{\ell m}(\hat{\boldsymbol{k}}) e^{-\alpha(\boldsymbol{k}^2 - p^2)}}{2\omega_\pi 2\omega_N (E - \omega_\pi - \omega_N + i\epsilon)} \left(\frac{|\boldsymbol{k}|}{p} \right)^{\ell + \ell'} , \tag{5.97}$$

with $\hat{\boldsymbol{k}} = \boldsymbol{k}/|\boldsymbol{k}|$, $\omega_\pi = \sqrt{M_\pi^2 + \boldsymbol{k}^2}$, $\omega_N = \sqrt{M_N^2 + \boldsymbol{k}^2}$. We have also introduced p as the magnitude of back-to-back momentum, satisfying

$$E = E_{\mathsf{cm}} = \sqrt{M_\pi^2 + p^2} + \sqrt{M_N^2 + p^2} \, . \tag{5.98}$$

As discussed in Refs. [115, 117], ultraviolet divergences in the sum-integral difference cancel so that any smooth regulator can be used in the evaluation of each. The explicit exponential included gives one option that is also convenient for numerical evaluation. As discussed in ref. [120], a straightforward combination of Clebsch-Gordon coefficients can then be used to promote this scalar version to the final F function on the full space for particles with spin:

$$F_{J' \ell' \mu', J \ell m_J}(E, \boldsymbol{P}, L) = \sum_{m, \sigma, m'} \langle \ell m; \frac{1}{2} \sigma | J m_J \rangle \langle \ell' m'; \frac{1}{2} \sigma | J' m'_J \rangle F_{\ell' m'; \ell m}(E, \boldsymbol{P}, L) \, . \tag{5.99}$$

This is the quantity entering the definition of $\mathcal{F}$ in eq. (5.94).

The second matrix entering the $\mathcal{F}$ matrix is the $N\pi \to N\pi$ scattering amplitude, denoted $\mathcal{M}$. This can be represented on the $J\ell\mu$ index space via

$$\mathcal{M}_{J' \ell' m'_J; J \ell m_J}(E_{\mathsf{cm}}) = \delta_{J' J} \delta_{l' l} \delta_{m'_J m_J} \frac{8\pi E_{\mathsf{cm}}}{p \cot \delta_{J,\ell}(p) - ip} \, , \tag{5.100}$$

where

$$E_{\mathsf{cm}}^2 = E^2 - \boldsymbol{P}^2 \, , \tag{5.101}$$

defines the centre-of-mass energy and $\delta_{J,\ell}(p)$ is the scattering phase shift with quantum numbers as indicated.

This concludes our explanation of all quantities entering $\Delta F_\mu^{rs}(\boldsymbol{k}, \boldsymbol{p})_L$. The content of eq. (5.91) can be summarized as follows: By combining a determination of the $N\pi \to N\pi$ scattering amplitude with the $\Sigma \xrightarrow{H_W} N\pi$ and $N\pi \xrightarrow{J_\mu} N$ transition amplitudes, one can calculate the correction that relates the finite-volume estimator $F_\mu^{rs}(\boldsymbol{k}, \boldsymbol{p})_L$ to the amplitude $\mathcal{A}_\mu^{rs}(k, p)$.

5.3.1 Determining $\mathcal{M}$, $\mathcal{A}^s_{H_W}$ and $\mathcal{A}^r_{J_\mu}$

So far we have made reference to poles cancelling between $F^{rs}_\mu(\boldsymbol{k},\boldsymbol{p})_L$ and $\Delta F^{rs}_\mu(\boldsymbol{k},\boldsymbol{p})_L$, but without explicitly explaining why the poles are the same between the two terms. This follows from the observation that the condition that $\mathcal{F}(E,\boldsymbol{P},L)$ diverges is equivalent to the Lüscher quantization condition [115, 117]

$$\det\left[\mathcal{M}^{-1}(E^{\mathsf{cm}}_n)+F(E_n,\boldsymbol{P},L)\right]=0\,, \tag{5.102}$$

where

$$E^{\mathsf{cm}}_n=\sqrt{E_n^2-\boldsymbol{P}^2}\,. \tag{5.103}$$

This relation allows one to constrain the amplitude $\mathcal{M}(E^{\mathsf{cm}})$ from a numerical lattice calculation by computing many finite-volume energies.

The energies, E_n, directly correspond to the poles in $\Delta F^{rs}_\mu(\boldsymbol{k},\boldsymbol{p})_L$, as can be readily seen from its definition in eq. (5.91). In the limit of infinite statistics, the formalism guarantees a perfect cancellation between the poles in $F^{rs}_\mu(\boldsymbol{k},\boldsymbol{p})_L$ and those in $\Delta F^{rs}_\mu(\boldsymbol{k},\boldsymbol{p})_L$. However, for realistic data, with statistical uncertainties, care must be taken. In particular, given the best fit for the lattice energies $E_n(L)$ from Euclidean correlators, one can use a given parametrization in the quantization condition to determine the best fit for $\mathcal{M}(E^{\mathsf{cm}})$. If the lattice energies are used to construct $F^{rs}_\mu(\boldsymbol{k},\boldsymbol{p})_L$ rather than the best-fit quantization energies (those predicted by the quantisation condition given a best-fit for the phase shift), the singularities will fail to exactly cancel in the amplitude. As discussed in ref. [108], the most straightforward solution here is to directly use the best-fit quantization energies everywhere.

The Lellouch-Lüscher formalism [76] and its extensions can be used to determine the remaining amplitudes $\mathcal{A}^s_{H_W}$ and $\mathcal{A}^r_{J_\mu}$. This follows from the eigenvectors of the quantization condition matrix which is known to be rank one near the finite-volume energy

$$\lim_{E\to E_n(L)}\big(E-E_n(L)\big)\frac{1}{\mathcal{M}(E^{\mathsf{cm}}_n)+F^{-1}(E_n,\boldsymbol{P},L)}=\mathcal{E}^{(n),\mathsf{in}}\otimes\mathcal{E}^{(n),\mathsf{out}}\,, \tag{5.104}$$

where the $\otimes$ indicates an outer-product in the same index space, so that $\mathcal{E}^{(n),\mathsf{in}}$ and $\mathcal{E}^{(n),\mathsf{out}}$ each carry the J,ℓ,μ indices. Then the amplitudes are related to finite-volume

matrix elements via

$$\left\langle E_n, \boldsymbol{k} \middle| \mathcal{H}_W(0) \middle| \Sigma(\boldsymbol{k}), s \right\rangle_L = \mathcal{E}^{(n),\mathsf{out}} \cdot \mathcal{A}^s_{H_W}(E, \boldsymbol{k}) \,, \tag{5.105}$$

$$\left\langle N(\boldsymbol{p}), r \middle| J_\mu(0) \middle| E_n, \boldsymbol{k} \right\rangle_L = \mathcal{A}^r_{J_\mu}(E, \boldsymbol{k}, \boldsymbol{p}) \cdot \mathcal{E}^{(n),\mathsf{in}} \,, \tag{5.106}$$

up to an inherent phase ambiguity that will cancel between $\mathcal{E}^{(n),\mathsf{out}}$ and $\mathcal{E}^{(n),\mathsf{in}}$ in the full finite-volume correction.

An in depth example of the use of this finite-volume formalism has been given in ref. [2] for the case of a single channel contributing to the process. The expansion about the pole is also derived allowing for the correction of any mistuning that would inevitably occur in real simulations with finite statistics, and allows errors to be propagated effectively.

CHAPTER

SIX

EXPLORATORY CALCULATION OF THE RARE HYPERON DECAY

With the theoretical framework for extracting the rare hyperon decay from the lattice known, it is in principle possible to produce all four form factors over the entire momentum transfer range required $(2m_\ell)^2 \leq q^2 \leq (m_\Sigma - m_p)^2$. This would remove all input from the $\Sigma^+ \to p\gamma$ decay, and the use of ChPT, giving a fully lattice SM prediction. While this should be the long term goal for this decay, improvements to the existing prediction can be made incrementally by incorporating lattice results into the existing work of [105, 106].

The main source of the large variation in the branching fraction in eq. (5.3) is the lack of constraint on $\mathrm{Re}\, a$ and $\mathrm{Re}\, b$ from the $\Sigma^+ \to p\gamma$ real photon emission decay. Figure 6.1 (reproduced from the work [106]) shows the value of the branching ratio sampled over the experimental uncertainty of the real photon emission measurement, along with the 4-fold ambiguity in these ill-constrained form factors. It is clear from this plot that even an unambiguous determination of the sign of $\mathrm{Re}\, a$ or $\mathrm{Re}\, b$ at $q^2 = 0$ could provide significant improvements to the theory prediction of the branching ratio, with a precise numerical value improving it further.

A lattice determination of $\mathrm{Re}\, a$ and $\mathrm{Re}\, b$ is of particular importance due to the recent measurement of the branching fraction $\mathcal{B}(\Sigma^+ \to p\gamma)$ from the BESIII collaboration [123]. They report a 4.2σ discrepancy with the PDG average value [6]. Using the BESIII results changes the value of the form factors by about $8 - 30\%$, which does not significantly alter the rare hyperon decay prediction, however, it is undesirable

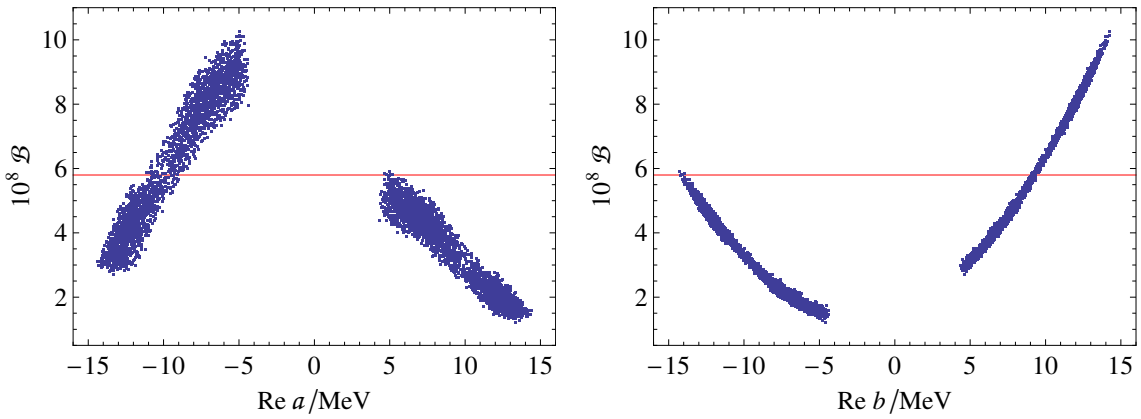

Figure 6.1 *Rare hyperon decay branching fraction sampled from experimental constraints on* Re a *and* Re b *form factors from the* $\Sigma^+ \to p\gamma$ *decay. Horizontal line marks the* 2σ *upper-limit of the LHCb measurement [103]. Figure reproduced from open access publication [106].*

to rely on these measurements while an unexplained discrepancy is observed.

We now go on to investigate the practicality of the framework of extracting the rare hyperon decay form factors from LQCD by performing an exploratory calculation at unphysical pion mass. For this we used the C1 ensemble listed in table 2.2. Additional important quantities for this simulation are the Nucleon and Sigma baryon masses on this ensemble, which have been measured to be $m_N \simeq 1200\text{MeV}$ and $m_\Sigma \simeq 1370\text{MeV}$. These are roughly 30% and 15% heavier than their physical values respectively. This ensemble has been chosen for several reasons:

- Heavier light quarks and smaller lattice volumes significantly reduce the cost of inverting the Dirac operator.
- Domain wall fermions posses an approximate chiral symmetry, preventing additional mixing of the 4-quark operators.
- With heavier pions, the energies of the $N\pi$ states are above the m_Σ threshold.

While all points above are important for the details of the calculation, the final point is most important for the physics in the Euclidean finite volume. With the $N\pi$ states above the m_Σ threshold, it is clear from the previous chapter that there will be no exponentially growing $N\pi$ intermediate states (leaving only the single proton intermediate state); and there will be no power-like finite-volume effects resulting from these states. This drastically simplifies the calculation to be performed. One additional consequence having $m_{N\pi} > m_\Sigma$ is that, by the optical theorem, there must be no imaginary component to the amplitude.

Of course, once it has been demonstrated that this calculation can be performed, when moving to the physical point the effects of having on-shell intermediate states must be taken into account. While the formalism to perform the finite-volume study of the $N\pi$ system and the decays $\Sigma \to N\pi$, $N\pi \to p\gamma^*$ is known [124, 125], there will of course be difficulties in performing these calculations in practice that must be overcome, resulting from the baryonic signal-to-noise problem.

6.1 Measurement Setup

Since this exploratory calculation is being performed away from the physical point, we are not able to make a direct comparison to the form factors obtained in [105, 106]. It is therefore not required to tune the kinematics to the $q^2 = 0$ point. It is however, worthwhile to have a setup that is not significantly different from a future physical point calculation. This means having the initial Σ^+ baryon at rest ($\boldsymbol{k} = 0$), as this drastically simplifies the finite-volume formalism once that becomes relevant. On this ensemble we use $\boldsymbol{k} = \boldsymbol{0}$ for the Σ^+, and one unit of lattice momentum in the x-direction $\boldsymbol{p} = (\frac{2\pi}{24a}, 0, 0)$ for the proton. This corresponds to $|\boldsymbol{p}| \simeq 470\,\text{MeV}$ and a momentum transfer of $q^2 \simeq -0.2\,\text{GeV}^2$.

6.1.1 Source-Sink Sampling

In order to project a lattice operator to a definite spatial momentum, a sum over all spatial lattice sites, Λ_3, with a momentum phase is required

$$\mathcal{O}(t, \boldsymbol{p}) = \sum_{\boldsymbol{x} \in \Lambda_3} \mathcal{O}(t, \boldsymbol{x}) e^{i\boldsymbol{p}\cdot\boldsymbol{x}} \,. \tag{6.1}$$

Due to our contraction method we are able to perform this full sum for both the weak Hamiltonian, H_W, and the vector current, J_μ. However, performing this sum exactly for the interpolators would require new inversions at every spatial lattice site. On this lattice that corresponds to $O(10^4)$ inversions, which is completely infeasible, and therefore a different approach is needed.

A method of sparsening was investigated in ref. [126] in which the full volume sum is replaced by a sum over a subset of sites that are arranged in a grid corresponding

to a coarser lattice with site separated by Na for some integer N,

$$\mathcal{O}(t, \boldsymbol{p}) \simeq \sum_{\boldsymbol{x} \in \widetilde{\Lambda}_3^{\mathrm{mod}N}} \mathcal{O}(t, \boldsymbol{x}) e^{i\boldsymbol{p}\cdot\boldsymbol{x}} \,, \tag{6.2}$$

$$\widetilde{\Lambda}_3^{\mathrm{mod}N} = \{(n_1, n_2, n_3) \,|\, 0 \leq n_i < L;\; n_i = 0 \,(\mathrm{mod}\; N)\} \,. \tag{6.3}$$

This approximation reduces the number of points in the sum by a factor N^3 which can provide a huge reduction in cost. By a simple Fourier analysis in 1 dimension, it can be seen that

$$\frac{1}{|\widetilde{\Lambda}_1^{\mathrm{mod}N}|} \sum_{\boldsymbol{x} \in \widetilde{\Lambda}_1^{\mathrm{mod}N}} e^{ipx} = \sum_{n=0}^{N-1} \delta_{p, \frac{2\pi n}{N}} \,, \tag{6.4}$$

while the full sum would give simply $\delta_{p,0}$. This shows that the sparse momentum projection does not project just a single momentum mode, but additional modes leak in. This is further investigated in ref. [127] where it is observed that the effective mass of the pion and nucleon acquire a statistically significant higher momentum contamination when using this fixed grid sparsening with an aggressive $N \simeq 10$.

In order to avoid this higher momentum contamination, they propose a stochastic sparsening in which the sum is performed over a randomly selected set of lattice sites. Compared to the fixed grid sparsening, the stochastic sparsening with an equal number of sites reduces the contamination to a statistically insignificant level. In addition, the stochastic sampling allows for a flexible number of sites to be selected rather than a fixed amount.

It is also seen in ref. [127] that the amount of sampling necessary is dependent on the type of source used. When using a point source, many samples must be used in order to get a reliable estimation of the sum, when using smeared sources however, the number of samples can be greatly reduced. This is due to the fact that with a smearing radius $\sigma \gg a$, sources with neighbouring centre points contain almost the same information. It therefore requires many fewer samples to effectively cover the entire lattice. In the extreme case where $\sigma \to \infty$, the smearing results in a wall source which is independent of position, and has an exact momentum projection with only a single sample.

It is also observed that the increase in sampling improves the statistical precision of the results. This is similar to making additional measurements per configuration, where the optimal scaling of the error is $1/\sqrt{N}$, when the results from each sample are completely independent.

In practice, an independent set of random sites is selected on every configuration, and every timeslice. This allows the gauge average and average over time translations to increase the effective number of samples measured.

It should be noted that momentum conservation (after the gauge average) implies that any n-point function only requires $n-1$ operators to be projected exactly for all states to have a definite momentum. The projection of the final operator is redundant and simply gives an additional factor of the volume. However, in the case where at least one of these projections is inexact, this redundancy can be utilised to improve the inexact projection. When applied to to both the source and the sink interpolators, we refer to this stochastic sampling as the source-sink sampling method.

As an example, consider a baryon 2-point function with position space interpolator $\psi^{\sigma,\boldsymbol{p}}(t,\boldsymbol{x})$ that has a smearing radius σ, and a momentum phase $\boldsymbol{p}$. The application of source-sink sampling with N samples gives a 2-point function of the form

$$\Gamma(t,\boldsymbol{p}) = \frac{1}{N_t}\sum_{t_i}\left\langle \Psi_k^{\sigma}(t+t_i,\boldsymbol{p})\bar{\Psi}_k^{\sigma}(t_i,\boldsymbol{p})\right\rangle_k \tag{6.5}$$

$$\Psi_k^{\sigma}(t,\boldsymbol{p}) = \frac{1}{N}\sum_{\boldsymbol{x}\in\widetilde{\Lambda}_3^k(t)} \psi^{\sigma,\boldsymbol{p}}(t,\boldsymbol{x})e^{i\boldsymbol{p}\cdot\boldsymbol{x}}\,, \tag{6.6}$$

where $\langle\cdot\rangle_k$ represents the average over gauge configurations with label k. The randomly sampled lattice sites are then

$$\widetilde{\Lambda}_3^k(t) = \{(n_1,n_2,n_3)\,|\,0\le n_i < L;\ n_i \text{ are uniform random integers}\}\,, \tag{6.7}$$

where the label k and argument t indicates that independent random samples are to be selected on each configuration and for each timeslice.

We have performed an investigation into the benefits of source-sink sampling in the specific context of the rare hyperon decay calculation. The non-eye contribution to the weak Hamiltonian 3-point function at zero momentum was chosen for this study since it is much more precise than the eye-type contribution, and the measurements of the 3-point functions are significantly less costly than the full 4-point function. This source-sink sampled 3-point function has the form

$$\Gamma^{(3)}(t,\Delta t) = \left\langle \frac{1}{N_t}\sum_{t_i}\Psi_k^{\sigma}(t_i+\Delta t,\boldsymbol{0})\,H_W^{(\mathrm{NE})}(t_i+t)\,\bar{\Psi}_k^{\sigma}(t_i,\boldsymbol{0})\right\rangle_k . \tag{6.8}$$

We use 2 different smearing widths $\sigma = 4, 9$ in lattice units, and a number of samples

up to $N = 8$. Figure 6.2 shows how the error on the correlation function scales with the number of samples used for a fixed source-sink separation of $\Delta t = 8$. The errors are normalised to the error when using only a single sample ($N = 1$). Also shown are the curves $1/N$ and $1/\sqrt{N}$ for reference. Note that $1/N$ is the optimal scaling when sampling on both the source and the sink independently.

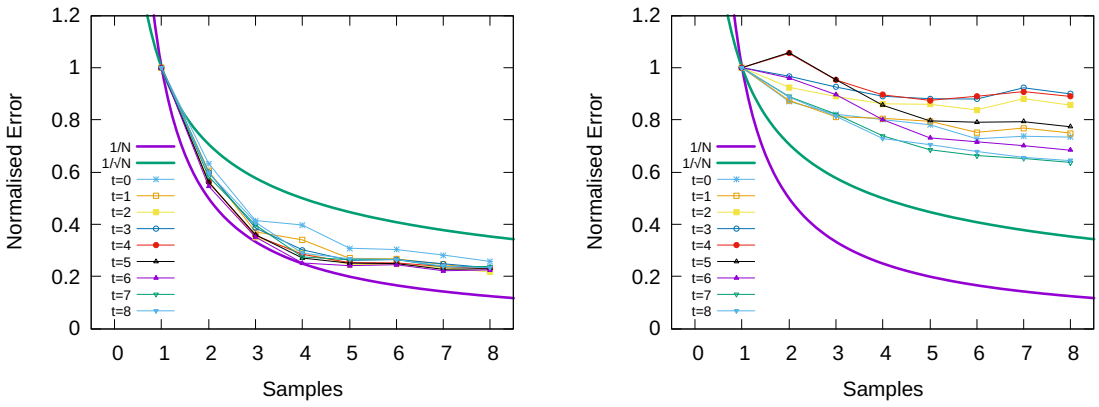

Figure 6.2 *Error of the weak Hamiltonian (non-eye) 3-point function for $\Delta t = 8$, scaling with number of source-sink samples. Gaussian smeared sources/sinks are used with a smearing width of $\sigma = 4$ (left) and $\sigma = 9$ (right). Values shown are normalised to the $N = 1$ error.*

It is clear that the smaller width source scales almost as $1/N$ and therefore initially benefits heavily from additional sources. Alternatively, the larger width source scales significantly less with increasing samples, making only small improvement for a factor 8 additional cost. This is a clear manifestation of the additional samples providing less independent information as the smearing increases.

Figure 6.3 shows the scaling of the value of the baryon masses and $H_W^{(\mathrm{NE})}$ matrix element measured from the 2- and 3-point functions. Only the smearing radius $\sigma = 4$ is shown as $\sigma = 9$ doesn't see significant benefits from additional sources. It is clear that the Σ and nucleon masses and the weak Hamiltonian matrix element do not observe any statistically significant contamination from higher momentum modes as the number of samples decreases.

From the error scaling, it can be seen that the error no longer behaves cleanly like $1/N$ once it has gone through the fitting procedure. In this case it looks as though it is more closely related to a $1/\sqrt{N}$ type scaling which is suboptimal, but still gives good statistical improvement.

From this small study, we confirm the conclusions of [127] for the case of our measurement setup, i.e. that there is little to no significant higher momentum

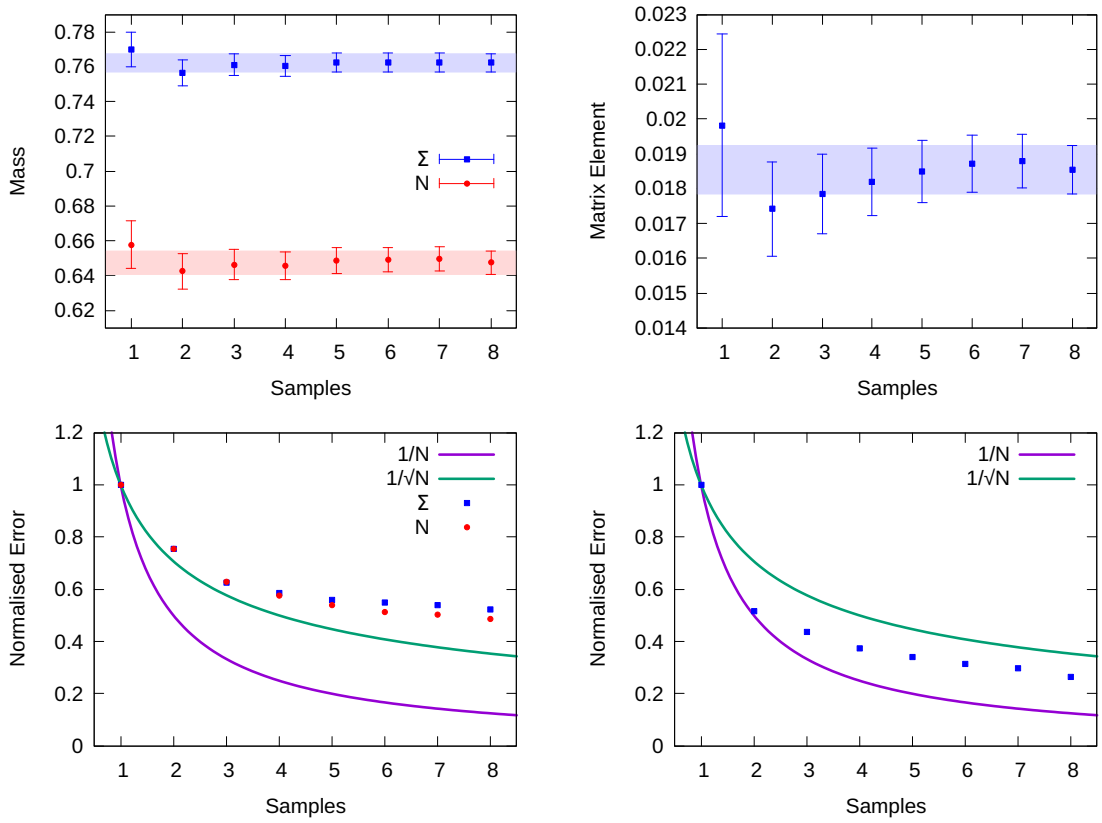

Figure 6.3 *Fit results (top) and error (bottom) for the mass of the* Σ *and nucleon (left), and the matrix element* $\langle p| H_W^{(N.E.)} |\Sigma\rangle$ *(right), scaling with number of source-sink samples. Gaussian smeared sources/sinks of width* $\sigma = 4$ *are used.*

mode contamination when applying the random source-sink sampling, and that for smaller smearing widths there is some statistical benefit to increasing the number of samples. It is observed however, that most of the statistical improvements have been made once $N = 8$ samples have been used, at a smearing of $\sigma = 4$.

6.1.2 2-point Functions

With the benefits of the source-sink sampling method evaluated for use in this specific calculation, we go on to describe the correlation functions measured. Measurements for all correlation functions are taken on a total of 70 decorrelated gauge configurations, with multiple measurements made per configuration by averaging over time translations.

The 2-point correlation functions measured for the baryons $B = p, \Sigma$ have the form

$$\Gamma^{2,B}(t_f, \boldsymbol{p}) = \frac{1}{N_t} \sum_{t_i} \sum_{\boldsymbol{x}} e^{i\boldsymbol{p}\cdot\boldsymbol{x}} \langle \psi_B^{\sigma,\boldsymbol{p}}(t_f + t_i, \boldsymbol{x})\, \bar{\Psi}_B^{\sigma}(t_i, \boldsymbol{k}) \rangle \,, \tag{6.9}$$

where the stochastic sampling with $N = 8$ samples is applied only at the source, since the sink can be projected exactly with a sum over all spatial positions. The average over initial time, t_i, is performed with $N_t = 32$ time translations $t_i \in \{0, 2, ..., 62\}$.

The initial/final baryon states are created/destroyed with the interpolators

$$\psi_B^{\sigma,\boldsymbol{p}}(x) = \epsilon^{abc} \left(\widetilde{q}_1^{\sigma,\boldsymbol{0}}(x)\right)^a \left[\left(\widetilde{q}_2^{\sigma,\boldsymbol{0}}(x)^{\mathrm{T}}\right)^b \Gamma \left(\widetilde{q}_3^{\sigma,\boldsymbol{p}}(x)\right)^c \right] , \tag{6.10}$$

where the quark fields are spatially smeared by a Gaussian kernel, and include a momentum phase

$$\widetilde{q}^{\sigma,\boldsymbol{p}}(t, \boldsymbol{x}) = \frac{1}{(2\pi\sigma^2)^{3/2}} \sum_{\boldsymbol{y}} e^{-\frac{(\boldsymbol{x}-\boldsymbol{y})^2}{2\sigma^2}} e^{i\boldsymbol{p}\cdot\boldsymbol{x}}\, q(t, \boldsymbol{y}) \,. \tag{6.11}$$

The momentum phase is placed on the quark q_3 since this is of a distinct flavour in the Σ and p interpolators, which simplifies our contraction setup. However, the momentum can in principle be placed on any one of the quarks or shared amongst them. Since the Gaussian smearing applied here is not gauge covariant, the measurements must be taken on gauge fixed configurations, for which we use the Coulomb gauge.

All interpolators use a smearing radius $\sigma = 6$ in lattice units (corresponding to roughly 0.66 fm) in order to reduce the overlap with excited states, as well as to not diminish the improvement obtained by the source-sink sampling.

6.1.3 3-point Functions

The relevant 3-point correlation functions measured for this analysis are those of the weak Hamiltonian and the $s \to d$ flavour changing scalar current $\mathcal{S} = \bar{d}s$,

$$\Gamma^{3,H_W}(t, t_f, \boldsymbol{p}) = \frac{1}{N_t} \sum_{t_i} \langle \Psi_p^{\sigma}(t_f + t_i, \boldsymbol{p})\, H_W(t_i + t)\, \bar{\Psi}_{\Sigma}^{\sigma}(t_i, \boldsymbol{p}) \rangle \tag{6.12}$$

$$\Gamma^{3,\mathcal{S}}(t, t_f, \boldsymbol{p}) = \frac{1}{N_t} \sum_{t_i} \langle \Psi_p^{\sigma}(t_f + t_i, \boldsymbol{p})\, \mathcal{S}(t_i + t)\, \bar{\Psi}_{\Sigma}^{\sigma}(t_i, \boldsymbol{p}) \rangle \,, \tag{6.13}$$

where $H_W(t)$ and $\mathcal{S}(t)$ are projected exactly to zero momentum transfer. The weak Hamiltonian can also be separated into contractions with only the non-eye or eye diagrams, H_W^{NE} and H_W^{Eye} respectively.

The non-eye diagrams are measured with source-sink separation $t_f = 12, 16$, $N_t = 32$ time translations are used, and the source sink-sampling is performed in 2 sets of $N = 4$ samples (with no cross-terms between the sets). The eye diagrams are measured with only $t_f = 16$ and on $N_t = 16$ time translation, with a single batch of $N = 4$ source-sink samples. In addition the quark loop in the eye diagrams are computed with a single hit of sparse noise sources, with a sparsening of 2 in each dimension (corresponding to 16 noise sources per hit).

As is described in chapter 5, the weak Hamiltonian operator can be separated into a parity conserving, and parity changing component. The Q_1 and Q_2 operators are the product of two bilinear currents with $V-A$ Dirac structure, and it can therefore be seen that the parity conserving component of the $(V-A)\otimes(V-A)$ structure is $V\otimes V + A\otimes A$, and the parity violating part is $-(V\otimes A + A\otimes V)$. These parity components give rise to the definite parity 4-quark operators

$$Q^+ = \sum_\mu \left([\bar{d}\gamma_\mu s][\bar{q}\gamma_\mu q] + [\bar{d}\gamma_\mu\gamma_5 s][\bar{q}\gamma_\mu\gamma_5 q] \right) , \tag{6.14}$$

$$Q^- = \sum_\mu \left([\bar{d}\gamma_\mu s][\bar{q}\gamma_\mu\gamma_5 q] + [\bar{d}\gamma_\mu\gamma_5 s][\bar{q}\gamma_\mu q] \right) , \tag{6.15}$$

where we have suppressed the color indices that distinguish Q_1 and Q_2. The full 4-quark operator is then given by $Q = Q^+ - Q^-$.

While data has been collected for both parity components, no signal is observed at the correlator level for the negative parity component, and therefore in this analysis we only investigate the positive parity weak Hamiltonian. Since the positive parity form factor a is ill-constrained by experiment, a lattice calculation of just this form factor would already be of phenomenological interest.

6.1.4 4-point Functions

The 4-point functions used in our analysis are defined by

$$\Gamma_{\mu}^{4,H_W}(t_J, t_H, t_f, \boldsymbol{k}, \boldsymbol{p}) = \frac{1}{N_t} \sum_{t_i} \langle \Psi_p^{\sigma}(t_f + t_i, \boldsymbol{p})\, H_W(t_H + t_i)\, \mathcal{J}_{\mu}(t_J + t_i, \boldsymbol{k} - \boldsymbol{p})\, \bar{\Psi}_{\Sigma}^{\sigma}(t_i, \boldsymbol{k}) \rangle \tag{6.16}$$

$$\Gamma_{\mu}^{4,\mathcal{S}}(t_J, t_S, t_f, \boldsymbol{k}, \boldsymbol{p}) = \frac{1}{N_t} \sum_{t_i} \langle \Psi_p^{\sigma}(t_f + t_i, \boldsymbol{p})\, \mathcal{S}(t_S + t_i)\, \mathcal{J}_{\mu}(t_J + t_i, \boldsymbol{k} - \boldsymbol{p})\, \bar{\Psi}_{\Sigma}^{\sigma}(t_i, \boldsymbol{k}) \rangle \,, \tag{6.17}$$

where $\mathcal{J}_{\mu}(t, \boldsymbol{q})$ is the conserved vector current with momentum transfer $\boldsymbol{q}$.

The values of t_f, N_t and N are the same as for the corresponding 3-point functions, and the vector current is inserted midway between the source and sink at $t_J = t_f/2$. In order to isolate the two positive parity form factors, two values of the vector current index μ are required. For this we use $\mu = t, z$.

In order to extract the rare hyperon decay amplitudes, we follow the method presented in chapter 5 of amputating the 4-point correlation functions and integrating the weak Hamiltonian around the vector current. As has been discussed, this only provides a measure of the finite-volume estimator, which is in general distinct from the amplitude. However, with our use of sufficiently heavy pions, there are no power-like finite volume effects, and therefore the amplitude and finite-volume estimator are equivalent up to exponentially suppressed finite volume effects that we ignore on this lattice with $m_{\pi} L \simeq 4.5$.

When constructing the integrated 4-point function, instead of integrating from $t_J - T_a$ to $t_J + T_b$, giving an object with a 2-dimensional time dependence, we separate the integral into two parts $\int_{t_J - T_a}^{t_J} dt_H$ and $\int_{t_J}^{t_J + T_b} dt_H$. This separates the two time orderings, and therefore gives access to the ρ and σ spectral integrals separately, which affords multiple benefits compared to the traditional strategy used in the rare kaon decay analysis in chapter 3.

The most important of these benefits is that since this clean separation is possible, the non-separated integrated correlator contains redundant information, which in turn gives rise to very large correlations that can be seen in fig. 3.4 for the rare kaon decay calculation. With this separation made, however, it is possible to fit the two time orderings separately, and combine their results. This removes the redundancy, and its corresponding correlation, as well as reducing the complexity

of each individual fit.

Taking into account the finite lattice spacing, the integrals become sums, and one must be careful not to double count the shared point at $t_H = t_J$. This is accounted for by including only half of this point in each sum. The amputated integrated 4-point functions are then defined as

$$\hat{I}^{\rho}_{\mu}(T_a) = \frac{1}{\zeta_{\mu,\gamma}\, Z_{\Sigma p}(t_J, t_f)} \left(\frac{1}{2} \operatorname{tr}\left[\Gamma^{(4)}_{\mu}(t_J, t_J, t_f) P^{+}\gamma\right] + \sum_{t_H = t_J - T_a}^{t_J - 1} \operatorname{tr}\left[\Gamma^{(4)}_{\mu}(t_H, t_J, t_f) P^{+}\gamma\right] \right) \tag{6.18}$$

$$\hat{I}^{\sigma}_{\mu}(T_b) = \frac{1}{\zeta_{\mu,\gamma}\, Z_{\Sigma p}(t_J, t_f)} \left(\frac{1}{2} \operatorname{tr}\left[\Gamma^{(4)}_{\mu}(t_J, t_J, t_f) P^{+}\gamma\right] + \sum_{t_H = t_J + 1}^{t_J + T_b} \operatorname{tr}\left[\Gamma^{(4)}_{\mu}(t_H, t_J, t_f) P^{+}\gamma\right] \right), \tag{6.19}$$

where we have suppressed the additional momentum arguments. The creation, propagation, and annihilation of the external states are amputated with the factor (5.31) appropriately shifted to $t_J \neq 0$ and $t_\Sigma = 0$

$$Z_{\Sigma p}(t_J, t_f) = \frac{Z_p(\boldsymbol{p}) Z^{*}_{\Sigma}(\boldsymbol{k}) m_\Sigma m_p}{E_\Sigma(\boldsymbol{k}) E_p(\boldsymbol{p})} e^{-E_\Sigma(\boldsymbol{k}) t_J} e^{-E_p(\boldsymbol{p})(t_f - t_J)} \,. \tag{6.20}$$

Since the correlator is spin matrix valued, the trace is taken with an arbitrary Dirac matrix γ and the positive parity projector, P^{+}, which projects the stationary Σ baryon to definite parity.

Finally, we have include an extra factor $\zeta_{\mu,\gamma}$ in the amputation, which is done to remove the artificial γ dependence from the traced correlator. It can be seen from appendix C, that with our kinematic setup $\boldsymbol{k} = \boldsymbol{0}$ and $\boldsymbol{p} = (p_x, 0, 0)$, the traced amplitudes can be written in the form

$$\operatorname{tr}\left[\mathbb{P}_p(\boldsymbol{p}) \widetilde{\mathcal{A}}_{\mu} \mathbb{P}_\Sigma(\boldsymbol{k}) P^{+}\gamma\right] = \zeta_{\mu,\gamma} f_\mu \,, \tag{6.21}$$

where f_μ is a linear combination of the form factors. For $\mu = t, z$ this can be written as the matrix equation

$$\begin{pmatrix} f_t \\ f_z \end{pmatrix} = \begin{pmatrix} 1 & m_\Sigma + m_p \\ m_\Sigma + m_p & q^2 \end{pmatrix} \begin{pmatrix} a \\ c \end{pmatrix} . \tag{6.22}$$

The relevant non-zero coefficients, $\zeta_{\mu,\gamma}$, are given by

$$\begin{aligned} \zeta_{t,\mathbb{1}} &= -\frac{p_x^2}{m_p} \quad , \quad \zeta_{t,\gamma x} = i\frac{p_x}{m_p}(E_p - m_p)\,, \\ \zeta_{z,\gamma_z} &= -\frac{E_p - m_p}{m_p} \quad , \quad \zeta_{z,\gamma_y\gamma_5} = i\frac{p_x}{m_p} \quad . \end{aligned} \tag{6.23}$$

Some interesting observations are that: for the positive parity coefficients above $\zeta_{\mu,\gamma} \to 0$ as $p_x \to 0$ and therefore the correlators vanish and the form factors become inaccessible at zero spatial momentum transfer; and at the $q^2 = 0$ point f_z contains only the a form factor, and therefore at this kinematic point a could be extracted from a single vector current component $\mu = z$.

With the amputation of this additional factor $\zeta_{\mu,\gamma}$, it can be seen that instead of measuring the amplitude directly, we are measuring the form factor combinations f_μ. The matrix eq. (6.22) can then be inverted using the measured masses from the 2-point functions to give the form factors a and c.

Using the information above, and the spectral decomposition of the 4-point function in eq. (5.43), the amputated integrated 4-point functions from eqs. (6.18) and (6.19) are given by

$$\hat{I}^\rho_\mu(T_a) = f^\rho_\mu - \int_0^\infty d\omega \, \frac{\mathrm{tr}[\mathbb{P}_p \widetilde{\rho}_\mu(\omega) \mathbb{P}_\Sigma P^+ \gamma]}{\zeta_{\mu,\gamma}} \, \frac{e^{-(\omega - m_\Sigma)T_a}}{e^{\omega - m_\Sigma} - 1} \tag{6.24}$$

$$\hat{I}^\sigma_\mu(T_b) = f^\sigma_\mu - \int_0^\infty d\omega \, \frac{\mathrm{tr}[\mathbb{P}_p \widetilde{\sigma}_\mu(\omega) \mathbb{P}_\Sigma P^+ \gamma]}{\zeta_{\mu,\gamma}} \, \frac{e^{-(\omega - m_p)T_b}}{e^{\omega - m_p} - 1}\,, \tag{6.25}$$

where f^X_μ represents the $X = \rho, \sigma$ spectral contribution to the form factor combination f_μ at finite lattice spacing

$$f^X_\mu = \int_0^\infty d\omega \, \frac{\mathrm{tr}\left[\mathbb{P}_p \widetilde{X}_\mu(\omega) \mathbb{P}_\Sigma P^+ \gamma\right]}{\zeta_{\mu,\gamma}} \, \frac{1 + e^{-(\omega - \omega_X)}}{2(1 - e^{-(\omega - \omega_X)})}\,, \tag{6.26}$$

with $\omega_\rho = m_\Sigma$ and $\omega_\sigma = m_p$. The full form factor combination is then obtained as

$$f_\mu = f^\rho_\mu + f^\sigma_\mu\,. \tag{6.27}$$

Since the energies in eq. (6.26) are in lattice units, it can be seen that as the lattice spacing goes to zero, the energies must also go to zero to maintain their physical value (up to vanishing lattice artefacts). Therefore as the continuum limit is taken,

the second factor becomes

$$\frac{1+e^{-(\omega-\omega_X)}}{2(1-e^{-(\omega-\omega_X)})} \to \frac{1}{\omega-\omega_X} \tag{6.28}$$

which recovers the continuum spectral integration kernel in eq. (5.20), and therefore gives f_μ^X the correct continuum limit.

6.2 Numerical Results

6.2.1 Fit Strategy

In order to extract physical observables from the lattice data described in the previous section, the correlators must be fit with a functional form containing the appropriate parameters. Since there are parameters shared between many correlators, e.g. baryon masses, it would be advantageous to perform a combined fit of all correlators together, where all fit parameters are determined simultaneously. This has the advantage of allowing every correlator to influence all relevant parameters, giving the maximum constraint on their values.

However, due to the large number of correlators involved in this analysis, such a fitting method results in highly unstable fits that often fail to converge on a minimum of the correlated χ^2 function. In addition, correlated fits require the estimation and inversion of the correlation matrix, which can easily break down for sufficiently large datasets. Some correlators may also be more constraining for certain parameters than others. For example, the 2-point functions are able to constrain the masses very well, however, the 4-point functions have much larger statistical errors, and more complicated functional dependence on the masses. Therefore the 4-point functions will likely not improve the measurements of these masses very significantly.

For these reasons, we decide to perform a hierarchy of fits, with the parameters of the earlier fits being given as fixed inputs to later fits. We use a bootstrap resampling method for the error estimation [128], allowing the earlier fit parameters to be passed sample-per-sample to later fits, in order to correctly maintain correlations.

We first fit the 2-point functions as two independent fits, one for each baryon, which are themselves combined fits to correlators with different momentum. Since the analytic form of the baryon lattice dispersion relation is not known, we impose the continuum dispersion relation on the energies, leaving only the baryon mass and

overlap factors as fit parameters. This is a reasonable assumption to our level of precision as we only consider a single unit of lattice momentum, and corrections to the dispersion relation are most relevant for large momenta.

These masses and overlap factors are then used to amputate the integrated 4-point functions, and are given to the corresponding 4-point function fits as constants. Since the 4-point functions only share these previously fixed constants, there are no longer any fit parameter in common between the different vector current components μ, and time orderings, and therefore these 4-point functions can be separated into independent fits.

For the 2-point function fits, we find the best fit in a systematic way by scanning over fit ranges and assigning each a score according to some criteria. For this we use a weight related to the Akaike Information Criterion (AIC) [129] which in this context is evaluated as

$$w = e^{-\frac{1}{2}(\chi^2 - 2n_{\text{dof}})}, \tag{6.29}$$

as is used in [29]. Maximising this weight favours lower χ^2 values, but in addition tries to maximise the number of degrees of freedom n_{dof}. The fit range with the maximum weight is then selected to define the central value and statistical error of the parameters. The fit systematic error on these parameters is then taken to be half of the spread of central values within the top 10 fits, ranked by w.

The 4-point functions do not undergo a similar scanning process as there is only a small set of fit ranges available, resulting from the relatively short source-sink separations for which we obtain a signal. Instead, the range is selected by hand, and the stability of this range is determined by varying the range by ± 1 timeslice. This variation is then propagated to the form factors by completing the analysis for each fit range and taking half the spread as the systematic error.

Finally, in order to evaluate the systematic error on the form factors due to the 2-point functions fits, the fit parameters from the top 10 fits of each 2-point function are used to reperform the analysis with the chosen 4-point function fit ranges. Again half the range of the resulting form factors is used to determine this component of the systematic error. The full fit systematics are then taken to be the quadrature sum of the variation from the 2- and 4-point fit ranges.

6.2.2 2-point Functions

The 2-point functions constructed in eq. (6.9) are fit to the single state functional form

$$\Gamma^{2,B}(t,\boldsymbol{p}) = L^3|Z_B(\boldsymbol{p})|^2\left(1+\frac{m_B}{E_B(\boldsymbol{p})}\right)e^{-E_B(\boldsymbol{p})t}, \tag{6.30}$$

with the fit parameters m_B and $Z_B(\boldsymbol{p})$, and the dispersion relation $E_B(\boldsymbol{p}) = \sqrt{m_B^2+\boldsymbol{p}^2}$ imposed. Figure 6.4 shows the $\boldsymbol{p}=\boldsymbol{0}$ effective masses of the p and Σ 2-point functions. The results of the combined fits to each baryon, with both momenta $\boldsymbol{p}=\boldsymbol{0}$ and $\boldsymbol{p}=(\frac{2\pi}{L},0,0)$, are shown in table 6.1. Figures 6.5 and 6.6 show the variation of the fit parameters over the 10 best scoring fits.

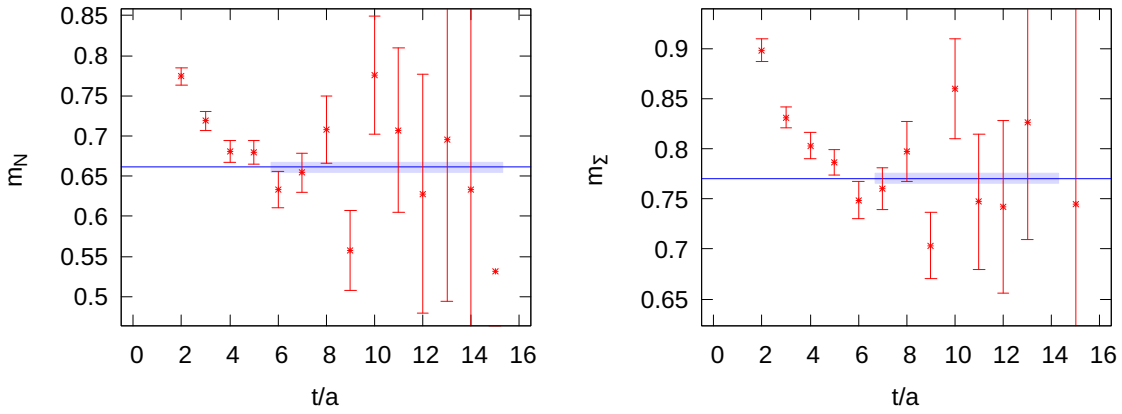

Figure 6.4 *Effective mass of the p (left) and Σ (right) baryon 2-point functions. Band indicates the mass parameter from the resulting fits. Note this is a visualisation of the fit result. The fit is not performed to the effective mass directly, but to the 2-point functions.*

Baryon	$\lvert\boldsymbol{p}\rvert$	Fit Range	Mass	$\lvert Z(\boldsymbol{p})\rvert$ [$\times 10^{-7}$]	P-value
p	0	$[6,15]$	$0.6611(66)(67)$	$4.94(11)(14)$	0.97
	$\frac{2\pi}{24}$	$[6,11]$		$3.67(7)(10)$	
Σ	0	$[7,14]$	$0.7703(49)(52)$	$4.90(8)(17)$	0.98
	$\frac{2\pi}{24}$	$[6,15]$		$3.86(6)(7)$	

Table 6.1 *Results of fits to 2-point functions of the p and Σ baryons. The first errors are statistical and the second are systematic resulting from fit range variation.*

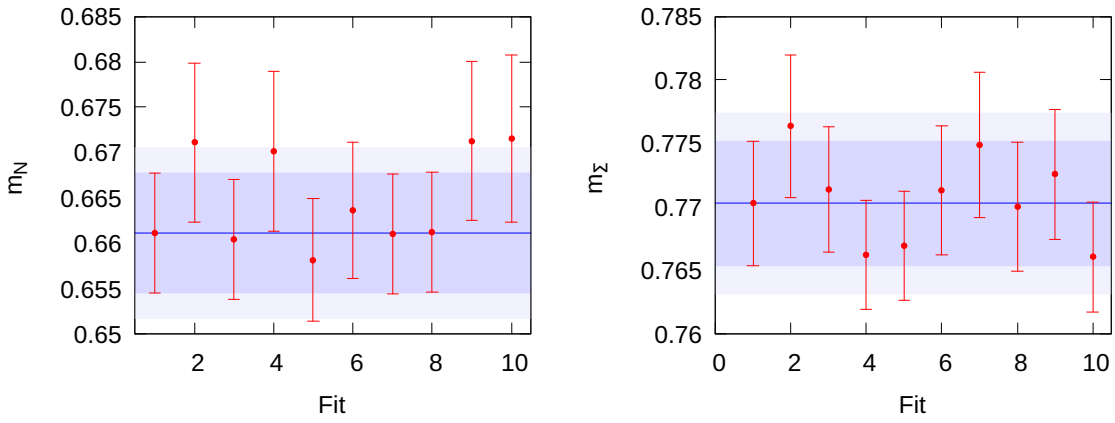

Figure 6.5 *Variation of the mass of the p (left) and Σ (right) for the top 10 scoring fits. Fits are ordered by weight (6.29), with Fit 1 defining the central value (blue line) and statistical error (dark band). The total error combining the statistical and systematic error in quadrature is given by the light band.*

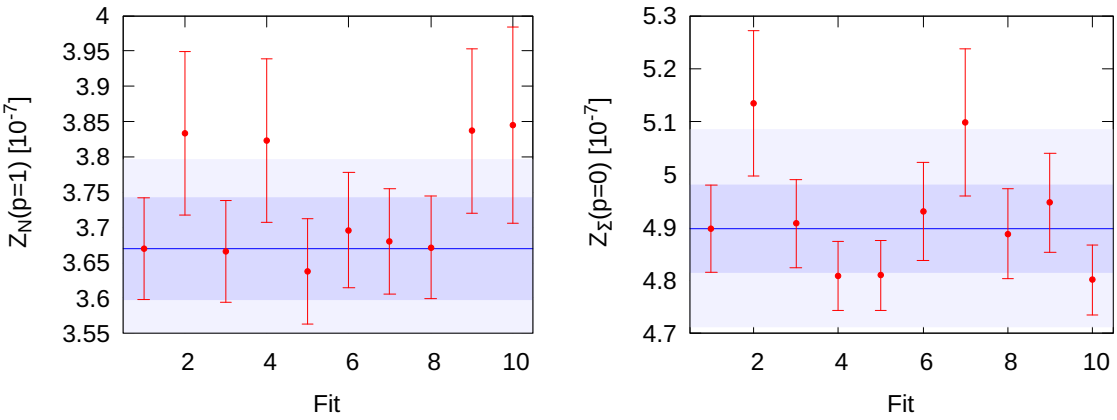

Figure 6.6 *Variation of the overlap factors $Z_p(\boldsymbol{p})$ (left) and $Z_\Sigma(\boldsymbol{k})$ (right) for the top 10 scoring fits. Fits are ordered by weight (6.29), with Fit 1 defining the central value (blue line) and statistical error (dark band). The total error combining the statistical and systematic error in quadrature is given by the light band.*

6.2.3 Scalar Shift Method

Due to the heavy pion mass used in this calculation, the only intermediate state with an exponentially growing contribution in the integrated 4-point function is the single proton state at rest. Therefore, the problem of growing contributions can in principle be resolved using only the scalar shift method discussed in section 5.2.

In order to construct the 4-point function with the shifted weak Hamiltonian

$H'_W = H_W - c_s\mathcal{S}$, the value of c_s must be determined such that the matrix element $\langle p(\mathbf{0}), r|\, H'_W\, |\Sigma(\mathbf{0}), s\rangle = 0$, and therefore

$$c_s = \frac{\langle p(\mathbf{0}), r|\, H_W\, |\Sigma(\mathbf{0}), s\rangle}{\langle p(\mathbf{0}), r|\, \mathcal{S}\, |\Sigma(\mathbf{0}), s\rangle}\,, \tag{6.31}$$

which can be measured by fitting a constant to the ratio of 3-point functions

$$R_s(t, t_f, \mathbf{0}) = \frac{\Gamma^{3,H_W}(t, t_f, \mathbf{0})}{\Gamma^{3,\mathcal{S}}(t, t_f, \mathbf{0})}\,. \tag{6.32}$$

Figure 6.7 shows a fit of this constant for $t_f = 12$ using only the non-eye contribution to the weak Hamiltonian which gives the result $c_s^{\mathrm{NE}} = -4.88(40) \times 10^{-3}$. Figure 6.8 then shows a comparison of the non-eye weak Hamiltonian and scalar 4-point correlation functions $\Gamma_t^{4,H_W^{\mathrm{NE}}}$ and $c_s^{\mathrm{NE}}\Gamma_t^{4\mathcal{S}}$. It is clear that the the latter has significantly larger errors than the former, to such an extent that when taking the difference no signal is observed. It is therefore clear that with the current level of statistics, we are unable to apply the scalar shift method to remove the growing single proton intermediate state, and therefore it must be handled by other means.

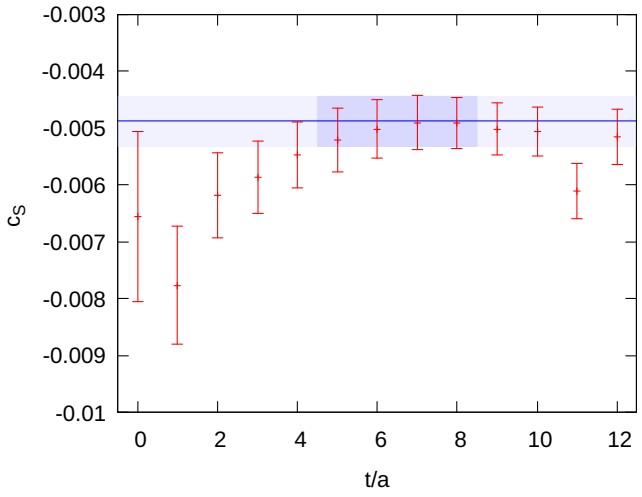

Figure 6.7 *Fit to the ratio $R_s(t, t_f, \mathbf{0})$ of the (non-eye) weak Hamiltonian and the scalar current 3-point functions in eq. (6.32), with a source-sink separation $t_f = 12$.*

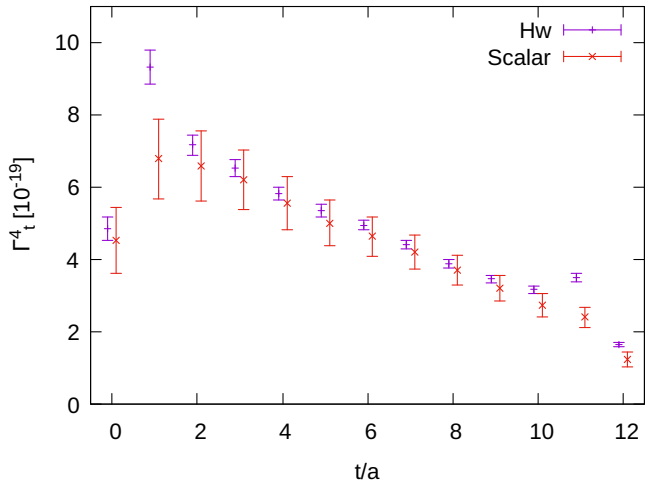

Figure 6.8 *4-point correlation functions* $\Gamma_\mu^{4,H_W^{NE}}$ *and* $c_S^{NE}\Gamma_\mu^{4,\mathcal{S}}$ *for the temporal current* $\mu = t$ *and source sink separation* $t_f = 12$*. Points are offset on the x-axis for clarity.*

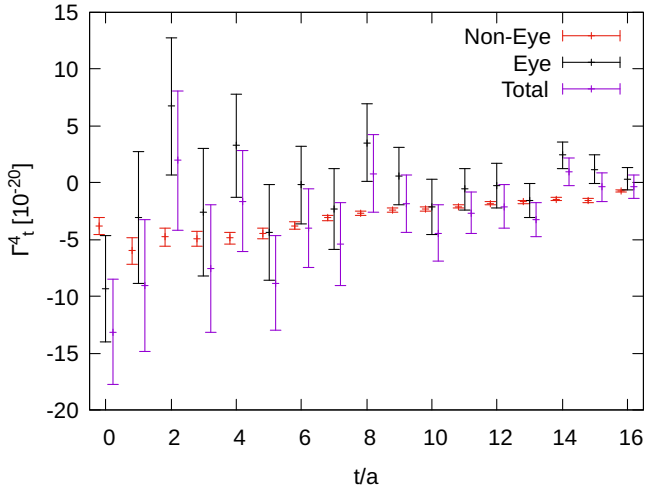

Figure 6.9 *Breakdown of the 4-point correlation function Γ^{4,H_W} into non-eye, eye and total contributions. The source-sink separation is $t_f = 16$, the current is located at $t_J = 8$ and the current component is $\mu = t$. Points are offset on the x-axis for clarity.*

6.2.4 4-point Functions

The breakdown of the temporal component of the weak Hamiltonian 4-point function into non-eye and eye components is given in fig. 6.9. It is clear that the non-eye diagrams can be significantly resolved, while the eye diagrams have large statistical errors coming from the stochastic estimation of the quark loop. Due to these large errors, the total 4-point function is then dominated by the eye type diagrams. Similarly, fig. 6.10 shows the amputated-integrated 4-point function for each of these components. While for a fixed t_H the central value and error of the eye diagrams dominates those of the total, when integrated the non-eye diagrams contribute the most to the central value, although the error is still dominated by the eye-diagrams. This is likely due to the cancellation of the eye diagrams between neighbouring times during the integral. This suggests (although more statistics are needed to confirm) that the eye contribution to the amplitude may be subdominant compared to the non-eye contribution.

Instead of directly constructing the exponential T_a and T_b dependence in eq. (6.24) from the 2- and 3-point functions explicitly, we opt to fix the energy of the leading exponential from the known masses, and leave the coefficient as a fittable parameter. This is chosen since the explicit construction method introduces additional statistical error from the measurement of the matrix elements, and therefore gives less precise

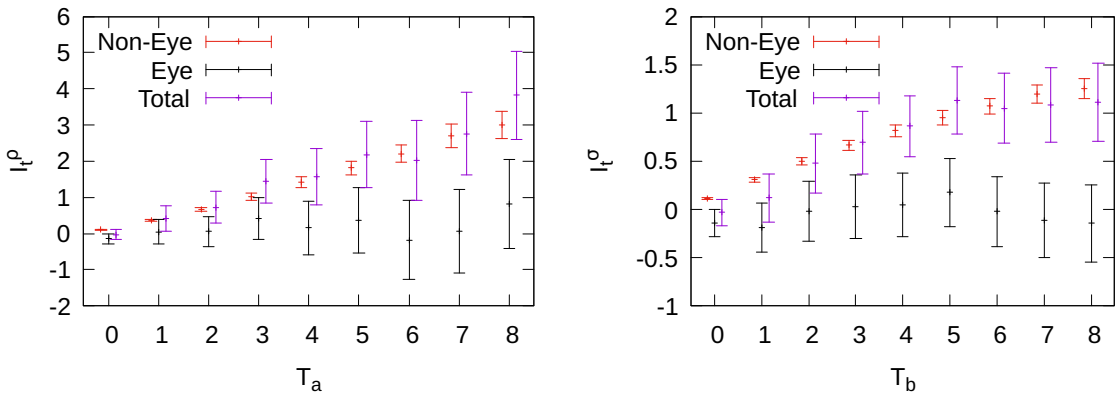

Figure 6.10 *Breakdown of the integrated and amputated 4-point correlation functions $\hat{I}^\rho(T_a)$ (left) and $\hat{I}^\sigma(T_b)$ (right) into non-eye, eye and total contributions. The source-sink separation is $t_f = 16$, the current is located at $t_J = 8$ and the current component is $\mu = t$. Points are offset on the x-axis for clarity.*

results. The fit ansätze used are therefore given by

$$\hat{I}^\rho_\mu(T_a) = f^\rho_\mu + \alpha^\rho_\mu \, e^{(m_\Sigma - m_p)T_a} \quad , \tag{6.33}$$

$$\hat{I}^\sigma_\mu(T_b) = f^\sigma_\mu + \alpha^\sigma_\mu \, e^{-(E_\Sigma(\boldsymbol{p}) - E_p(\boldsymbol{p}))T_b} \, . \tag{6.34}$$

The fit to the non-eye contribution for both time orderings is shown in fig. 6.11. The fit range for the correlator with source sink separation t_f and current insertion at $t_J = t_f/2$, is taken to be $T_a, T_b \in [1, t_J/2]$. This is chosen to balance maximising the number of fit points, with minimising the contamination from external excited states. The excited state problem, however, is a very challenging issue to overcome with such small source-sink separations for which we observe a signal. For reference, with $t_f = 16$ and $t_J = 8$, the $T_a, T_b = 4$ point is a physical distance of 0.44 fm from the source/sink. The issue of this contamination must therefore be resolved once a sufficient precision is attained.

Tables 6.2 and 6.3 give the fit results for f^X_μ defined by eq. (6.26), when fitting to only the non-eye or eye contributions separately, as well as to the total data. In addition, the sum of the fit results for the two types of diagrams separately is given. It can be seen from these results that the eye-type contributions are dominated by $> 100\%$ errors, as would be expected from the large stochastic noise observed in the correlators. The non-eye contributions, however, have significantly better errors at the level of $10 - 15\%$ when considering the two time orderings separately. It is therefore unfortunate that these two time orderings have opposite sign and

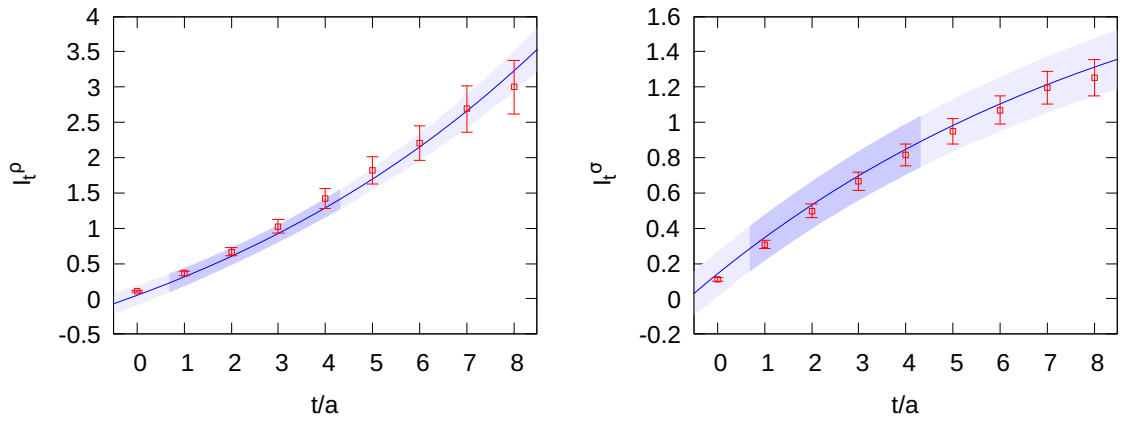

Figure 6.11 *Fits to the non-eye contribution to the integrated-amputated 4-point function $\hat{I}^\rho(T_a)$ (left) and $\hat{I}^\sigma(T_b)$ (right). The source sink separation is $t_f = 16$ and the vector current is at $t_J = 8$.*

almost equal magnitude, resulting in a large cancellation when combined together. This gives a value f_μ^{NE} consistent with zero even though its constituent parts are individually well resolved.

Parameter	Result	p-value	$f_t = f_t^\rho + f_t^\sigma$
$f_t^{\rho,\mathrm{NE}}$	2.16(31)	0.70	$-4.7(21.8) \times 10^{-2}$
$f_t^{\sigma,\mathrm{NE}}$	−2.21(21)	0.40	
$f_t^{\rho,\mathrm{Eye}}$	0.20(1.03)	0.72	−0.37(1.21)
$f_t^{\sigma,\mathrm{Eye}}$	−0.57(71)	0.32	
$f_t^{\mathrm{NE}} + f_t^{\mathrm{Eye}}$	-	-	−0.42(1.21)
f_t^ρ	2.52(1.62)	0.69	−0.25(1.75)
f_t^σ	−2.78(92)	0.34	

Table 6.2 *Fit results for the combined form factor f_t from the non-eye and eye diagrams, as well as all diagrams. In addition the sum of the non-eye and eye fit values is given. Errors are purely statistical.*

Parameter	Result	p-value	$f_z = f_z^\rho + f_z^\sigma$
$f_z^{\rho,\mathrm{NE}}$	−0.25(6)	0.96	$-2.2(5.8) \times 10^{-2}$
$f_z^{\sigma,\mathrm{NE}}$	0.23(4)	0.54	
$f_z^{\rho,\mathrm{Eye}}$	0.16(28)	0.43	0.20(36)
$f_z^{\sigma,\mathrm{Eye}}$	0.04(20)	0.86	
$f_z^{\mathrm{NE}} + f_z^{\mathrm{Eye}}$	-	-	0.18(36)
f_z^ρ	−0.08(28)	0.46	0.19(40)
f_z^σ	0.27(27)	0.85	

Table 6.3 *Fit results for the combined form factor f_z from the non-eye and eye diagrams, as well as all diagrams. In addition the sum of the non-eye and eye fit values is given. Errors are purely statistical.*

Table 6.4 shows the values of the form factors along with their systematic error. The various results come from inverting eq. (6.22) onto the values given in tables 6.2 and 6.3. Results are given restricted to the non-eye or eye diagrams only, as well as the sum of the two, and the form factors evaluated from the fits to the sum of all diagrams.

Figures 6.12 and 6.13 show the variation resulting from the scan over the 2-point function fits for the non-eye and eye determinations of the a and c form factors respectively. Figures 6.14 and 6.15 show the stability of the form factors with respect to the ± 1 fit range variation of the two time orderings of the integrated 4-point functions. Fit 1 in all figures corresponds to the one chosen for the central value and statistical error. The total systematic error resulting from the fitting procedure is determined by adding the systematic from these two sources in quadrature.

Form Factor	Value	(Stat)	(Sys)	
a^{NE}	5	(16)	(7)	MeV
c^{NE}	0.009	(30)	(15)	
a^{Eye}	-58	(100)	(56)	MeV
c^{Eye}	0.034	(173)	(79)	
$a^{\mathrm{NE}} + a^{\mathrm{Eye}}$	-53	(100)	(56)	MeV
$c^{\mathrm{NE}} + c^{\mathrm{Eye}}$	0.043	(174)	(79)	
a	-53	(114)	(97)	MeV
c	0.018	(249)	(98)	

Table 6.4 *Results for the positive parity form factors a and c obtained from the non-eye and eye diagrams separately, as well as the total of these results, and the form factors extracted from the fit to all diagrams. Fits utilise only a single source-sink separation $t_f = 16$.*

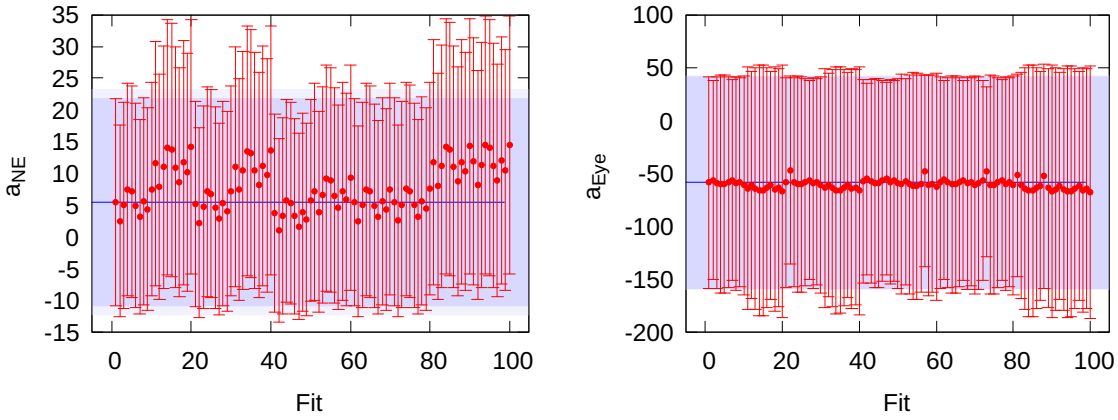

Figure 6.12 *Variation of the non-eye (left) and eye (right) contributions to the form factor a, due to the change of input values from the 10 best fits to each of the 2-point functions. Fit 1 corresponds to the result with the best 2-point function fits.*

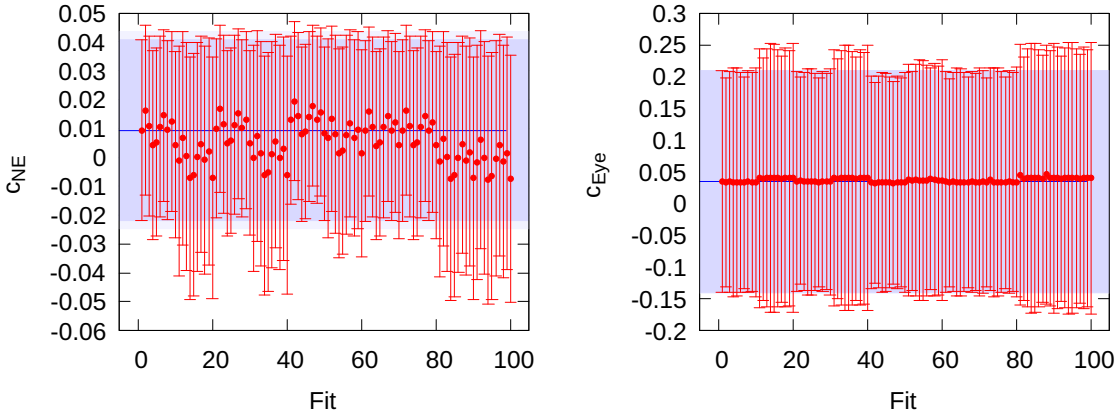

Figure 6.13 *Variation of the non-eye (left) and eye (right) contributions to the form factor c, due to the change of input values from the 10 best fits to each of the 2-point functions. Fit 1 corresponds to the result with the best 2-point function fits.*

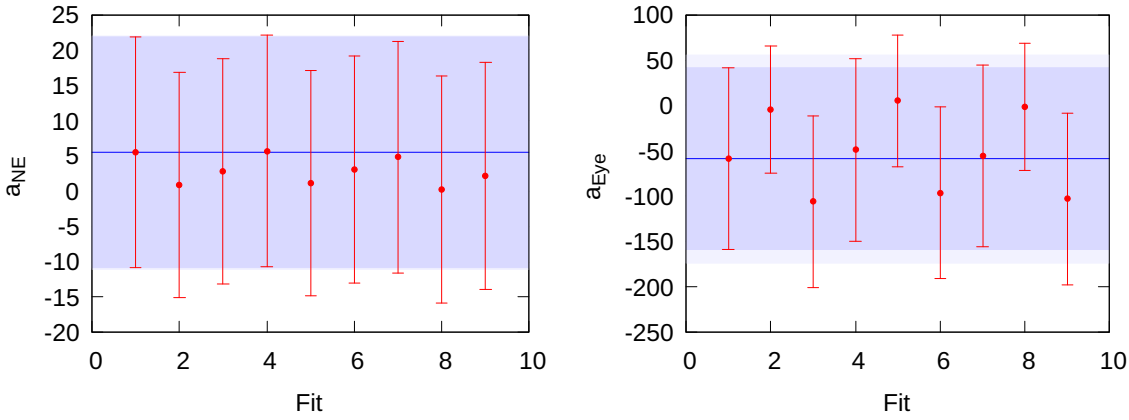

Figure 6.14 *Variation of the non-eye (left) and eye (right) contributions to the form factor a, due to ± 1 change to the fit range for each of the contributing 4-point functions. Fit 1 corresponds to the chosen fit range.*

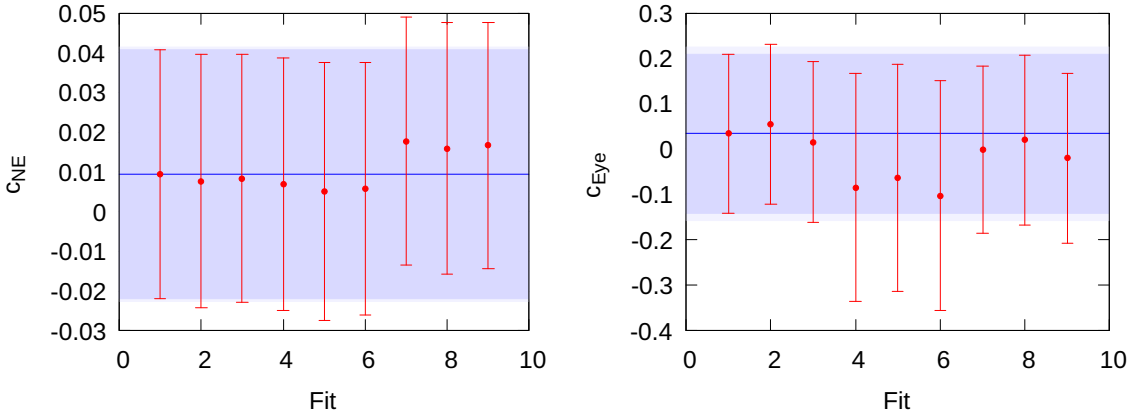

Figure 6.15 *Variation of the non-eye (left) and eye (right) contributions to the form factor c, due to ± 1 change to the fit range for each of the contributing 4-point functions. Fit 1 corresponds to the chosen fit range.*

6.3 Discussion

It is clear from the results in table 6.4, that the form factors extracted in this analysis are heavily dominated by statistical errors. This results from two important observations. First, the noise generated by the quark loops in the eye diagrams dominates the error at the level of the integrated 4-point correlation functions, and therefore also dominates in the fit results. From fig. 6.10 we can see that the non-eye diagrams have the largest contribution to the central value, and it may therefore be the case that with an increased number of noise hits, the error on the eye diagrams is reduced to the level that they are either resolved from zero, or that they are negligible compared to the non-eye contribution. Of course, this remains to be verified once extra statistics are available. These additional noise hits can be obtained at reduced cost by using the AMA approach (see section 2.4.3) to reduce the solver tolerance on the loop propagators, as was done in chapter 3.

The second observation is that, for the non-eye contribution, there is a large cancellation between the two time orderings of the spectrum f_μ^ρ and f_μ^σ. As a result, a reasonable statistical error on each part individually translates into no signal on their total. While this cancellation is observed at the level of the integrated spectral function,

$$\int_0^\infty d\omega \, \frac{\mathbb{P}_p \widetilde{\rho}_\mu(\omega) \mathbb{P}_\Sigma}{\omega - E_\Sigma} \simeq - \int_0^\infty d\omega \, \frac{\mathbb{P}_p \widetilde{\sigma}_\mu(\omega) \mathbb{P}_\Sigma}{\omega - E_p} \,, \tag{6.35}$$

it is currently unknown if there is also a cancellation directly at the level of the spectral functions, i.e.

$$\frac{\mathbb{P}_p \widetilde{\rho}_\mu(\omega) \mathbb{P}_\Sigma}{\omega - E_\Sigma} \simeq - \frac{\mathbb{P}_p \widetilde{\sigma}_\mu(\omega) \mathbb{P}_\Sigma}{\omega - E_p} \,, \tag{6.36}$$

which may be the result of some approximate symmetry (for example $\mathrm{SU}(3)_F$ or $\boldsymbol{p} = \boldsymbol{k}$ symmetry). With investigation into the mechanism of this cancellation, it may be possible to produce an improved approach to the form factor extraction that avoid such cancellations.

As a result of this large cancellation, it is clear that even with improvements on the estimation of the eye diagrams, the non-eye contribution also requires improvements. Under the assumption that they eye diagrams give a small contribution that can be well resolved in the near future, the non-eye diagrams have an error not far from the value of the form factors from [105], $\mathrm{Re}\, a \sim 10\,\mathrm{MeV}$ and

$\mathrm{Re}\, b \sim 10^{-2}$. It may be therefore be possible to achieve a non-zero result on this ensemble simply from the $1/\sqrt{N}$ scaling of additional statistics. However, this will likely be prohibitorily expensive to simulate directly at the physical point without methodological improvement. This process will therefore heavily benefit from research into overcoming signal-to-noise problems with variance reduction techniques, such as multilevel algorithms [130]. Currently it is not known how to apply multilevel algorithms to higher point correlation functions that are not trivially factorisable, and it is not known if the technique is applicable to domain wall fermions, both of which are required in order for this technique to be applied to this decay.

Finally, once a significant signal is observed for the form factors, it is clear that excited state contamination must be taken into account. In this study, we have a minimum separation between the operators and the external state interpolators of 0.44 fm which will not be enough to reliably isolate the ground state, even with interpolators tuned to suppress excited states. This contamination could be assessed and/or removed by using larger time separations, and by incorporating excited states into the fit ansatz. Both of these methods require additional data points that are affected by the exponential signal-to-noise loss, and therefore this must be accompanied by variance reduction techniques, and/or alternate measurements strategies that are of lower cost.

CHAPTER

SEVEN

CONCLUSIONS AND OUTLOOK

In this thesis, we have presented the latest work towards calculating the form factors of the rare kaon and rare hyperon decays, $K^+ \to \pi^+\ell^+\ell^-$ and $\Sigma^+ \to p\ell^+\ell^-$ respectively, on the lattice. This includes the first calculation of the rare kaon decay at the physical point; an investigation into methodological improvements for the rare kaon decay; the extension of the lattice framework to the rare hyperon decay; and the first exploratory calculation of the rare hyperon decay.

The calculation of rare kaon decay directly at physical pion mass utilises a variety of techniques to accelerate the measurement process, including low-mode deflation and the zMöbius action for the light quarks, as well as sparsened noise quark loop estimation with an AMA bias correction. The resulting measurement of the form factor parameter is $a = -0.87(4.44)$. The large error of this result is found to stem from the GIM subtraction of the light and charm loops in the eye-type diagrams.

While the lattice result is currently highly statistics dominated, with an error approximately 8 times larger than the experimentally measured value, it is only 3 times larger than the existing SM prediction, which is highly discrepant with the experimental value. It may therefore be possible to achieve a bound comparable to, or better than, the existing SM prediction in the near future simply via the $1/\sqrt{N}$ scaling of additional statistics. However, in order to achieve a result with significantly improved errors without extremely high cost, new methodologies must be investigated. Some promising directions include: cost reduction via direct summation of the vector current; improvements of quark loop estimation such as

frequency splitting techniques; and performing the calculation in a 3 flavour theory in which the GIM cancellation is removed.

We have proceeded to investigate the first of these approaches, in which the time coordinate of the vector current is summed over the entire lattice directly during the measurement process, which has been shown to reduce the cost of the calculation. This is closely linked with the summed method used in many LQCD calculations of 3-point functions with degenerate initial and final states. We have discussed the issues associated with breaking this degeneracy in the context of summed 3-point functions, and shown that the 4-point summed method can in principle be used to calculate the rare kaon decay, however, only reliably in the degenerate limit. This significantly restricts the kinematic setups available, and therefore cannot be used as a general method of computing the rare kaon decay without further modifications.

In addition to the calculation of the rare kaon decay, the original theoretical framework has been extended to allow for the baryonic equivalent, the rare hyperon decay, to be calculated on the lattice. This includes the handling of the additional spin degrees of freedom; the identification and handling of the exponentially growing intermediate state contributions; the extension of the scalar shift method to baryonic states; and the correction of the power-like finite volume effects brought about by on-shell multiparticle finite-volume states.

Finally, this framework is applied in an exploratory calculation of the rare hyperon decay with an unphysical pion mass $m_\pi = 340\,\mathrm{MeV}$. In this calculation, the finite-volume $N\pi$ states are above the m_Σ threshold, and therefore do not contribute the finite-volume corrections or growing intermediate states. This leaves only the problematic single proton state to be accounted for.

In the positive parity sector, the non-eye diagrams are observed to have a clear signal at the correlator level, while the eye-type diagrams are error dominated due to the noisy loop estimation. It is however, observed that the error from the eye diagrams contributes to the integrated correlator at a level below the central value of the non-eye diagrams. This suggests that with additional statistics on the loop estimators, the eye diagrams may only give a small contribution to the total. However, this remains to be seen once additional statistics are available.

Finally, it is observed that with the form factors separated into contributions from the two time orderings, each ordering contributes to amplitude with approximately equal magnitude and opposite sign. Therefore, even with a $10 - 15\%$ error on each contribution, the total non-eye amplitude is not significantly different from

zero. The errors on the non-eye contributions are, however, of the order of the phenomenological values, and therefore additional statistics may allow for a non-zero result to be observed in the near future. Once this level of precision is reached, the effects of excited state contamination must be taken into account, due to the short source-sink separations utilised in this analysis.

Of course, with the added difficulty of the baryonic signal-to-noise problem, it is unlikely a physical point calculation of the rare hyperon decay can be performed in the near future without methodological improvements. While this decay will benefit from improvements in the rare kaon decay calculation, investigation into variance reduction techniques will be required to tackle this exponential degradation of signal. One such method is the multi-level algorithm, although it is not yet known if this technique is applicable to processes of this type.

APPENDIX

A

WICK CONTRACTIONS

Rare Kaon

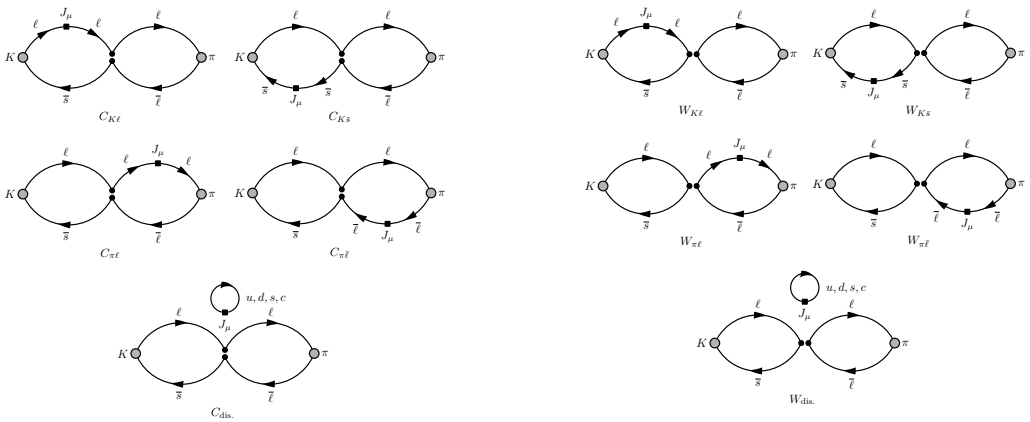

Figure A.1 *Diagrams contributing to the rare kaon 4-point correlation function (3.15) from the Connected (left) and Wing (right) topologies.*

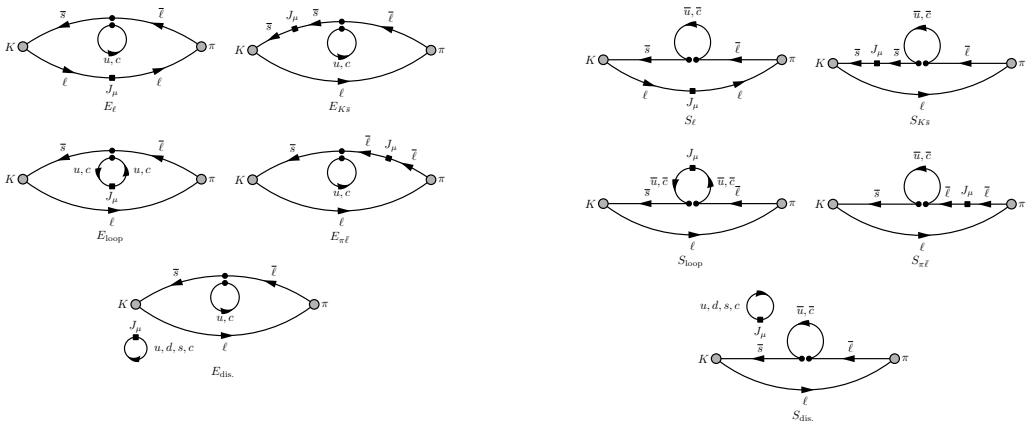

Figure A.2 *Diagrams contributing to the rare kaon 4-point correlation function* (3.15) *from the Eye (left) and Saucer (right) topologies.*

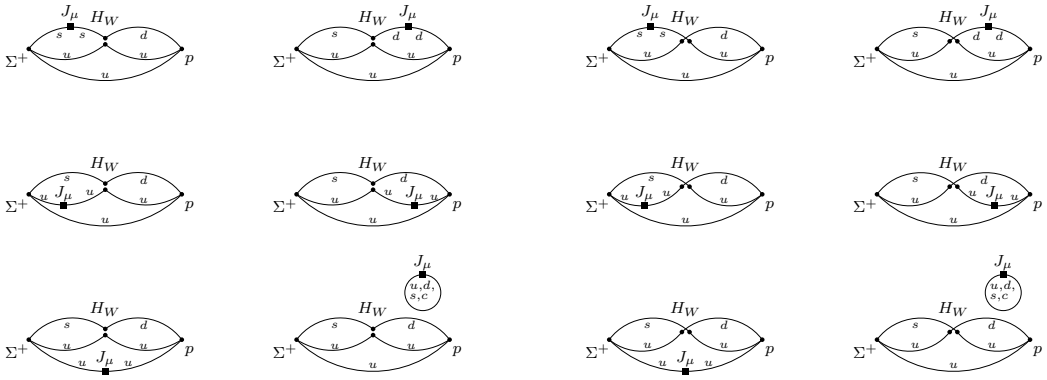

Figure A.3 *Diagrams contributing to the rare kaon 4-point correlation function (5.38) from the Connected (left) and Cross-Connected (right) topologies.*

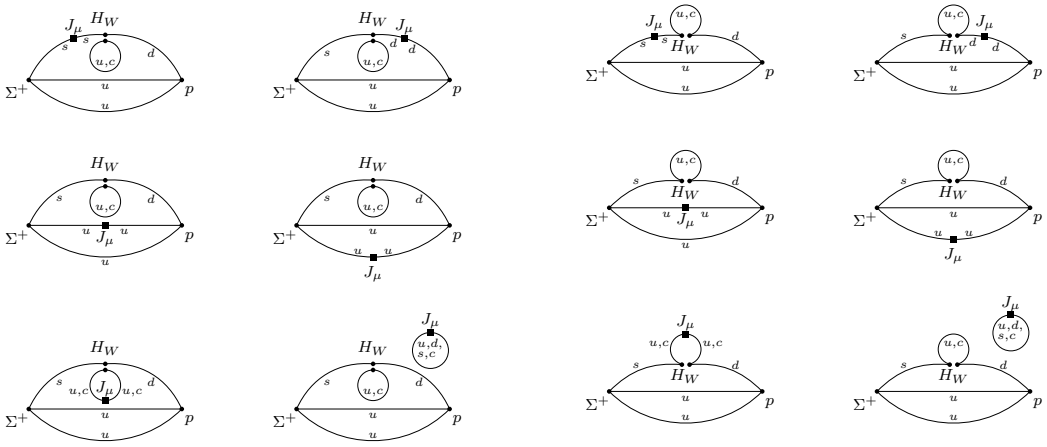

Figure A.4 *Diagrams contributing to the rare kaon 4-point correlation function (5.38) from the Eye (left) and Saucer (right) topologies.*

APPENDIX

B

FORM FACTORS

Generally the matrix element of an operator $\mathcal{O}$ between two baryonic states $|B(\boldsymbol{p}), s\rangle$ and $|B'(\boldsymbol{p}'), r\rangle$ with momenta $\boldsymbol{p}$ and $\boldsymbol{p}'$ and spin projections s and r can be split into the external spinors u and a 4×4 Dirac-matrix amplitude $\widetilde{\mathcal{A}}$

$$\mathcal{A}^{rs}(p, p') = \langle B'(\boldsymbol{p}'), r| \mathcal{O} |B(\boldsymbol{p}), s\rangle = \bar{u}^r_{B'}(\boldsymbol{p}')\widetilde{\mathcal{A}}(q, k)u^s_B(\boldsymbol{p}) \,, \tag{B.1}$$

where we now parametrize in terms of the 4-momenta $q = p - p'$ and $k = p + p'$. We then write $\widetilde{\mathcal{A}}$ in terms of all of the available Dirac-matrix structures $\Gamma \in \{1, \gamma_5, \gamma_\mu, \gamma_\mu\gamma_5, \sigma_{\mu\nu}\}$ in such a way as the Lorentz structure of the matrix element is recovered. These terms are associated with a form factor which is a scalar coefficient, and can only be a function of the Lorentz and spin scalar objects q^2 and k^2. However, $k^2 = 2m^2 + 2m'^2 - q^2$ and therefore k^2 and q^2 are not independent, so the form factors can be written as only a function of q^2.

The base set of Dirac-matrix Lorentz (pseudo-)scalar objects is:

$$\{1, \gamma_5, \not{q}, \not{q}\gamma_5, \not{k}, \not{k}\gamma_5, \sigma_{\mu\nu}q^\mu k^\nu, \sigma_{\mu\nu}q^\mu k^\nu\gamma_5\} \,. \tag{B.2}$$

The full list of structures is the infinite set of all combinations of these base elements. These additional structures can always be decomposed into a linear combination of the base elements using $\not{p}\not{p} = p^2$ and $\not{p}\not{p}' = 2p \cdot p' - \not{p}'\not{p}$ for any p, p'.

The base set of spin-matrix Lorentz (axial-)vectors objects is:

$$\{q_\mu, q_\mu\gamma_5, k_\mu, k_\mu\gamma_5, \gamma_\mu, \gamma_\mu\gamma_5, \sigma_{\mu\nu}q^\nu, \sigma_{\mu\nu}q^\nu\gamma_5, \sigma_{\mu\nu}k^\nu, \sigma_{\mu\nu}k^\nu\gamma_5\}\,, \tag{B.3}$$

where again the infinite combinations can be decomposed in terms of the base set.

B.0.1 Explicit form-factor decompositions

Using the base set for a generic Lorentz (pseudo-)scalar operator $\mathcal{S}$ as given above yields the form factor decomposition

$$\begin{aligned}\mathcal{A}^{rs}(p,p') &= \langle B'(\boldsymbol{p}'), r|\,\mathcal{S}\,|B(\boldsymbol{p}), s\rangle &\text{(B.4)}\\ &= \bar{u}^r_{B'}(\boldsymbol{p}')\left[a(q^2) + b(q^2)\gamma_5\right] u^s_B(\boldsymbol{p})\,, &\text{(B.5)}\end{aligned}$$

which is relevant for the matrix element of the weak Hamiltonian in the rare hyperon decay. Analogously, using the base set for a generic Lorentz (axial-)vector operator $\mathcal{J}_\mu$ one obtains

$$\begin{aligned}\mathcal{A}^{rs}_\mu(p,p') &= \langle B'(\boldsymbol{p}'), r|\,\mathcal{J}_\mu\,|B(\boldsymbol{p}), s\rangle &\text{(B.6)}\\ &= \bar{u}^r_{B'}(\boldsymbol{p}')\left[f_1(q^2)\gamma_\mu + f_2(q^2)\sigma_{\mu\nu}q^\nu + f_3(q^2)q_\mu\right. &\text{(B.7)}\\ &\quad \left. + g_1(q^2)\gamma_\mu\gamma_5 + g_2(q^2)\sigma_{\mu\nu}q^\nu\gamma_5 + g_3(q^2)q_\mu\gamma_5\right] u^s_B(\boldsymbol{p})\,,\end{aligned}$$

where we have used the generalisations of the Gordon decomposition identity with initial and final states of different mass

$$\begin{aligned}\bar{u}'\sigma_{\mu\nu}k^\nu u &= i(m-m')\bar{u}'\gamma_\mu u - iq_\mu\bar{u}'u &\text{(B.8)}\\ \bar{u}'\sigma_{\mu\nu}q^\nu u &= i(m+m')\bar{u}'\gamma_\mu u - ik_\mu\bar{u}'u &\text{(B.9)}\\ \bar{u}'\sigma_{\mu\nu}k^\nu\gamma_5 u &= -i(m+m')\bar{u}'\gamma_\mu\gamma_5 u - iq_\mu\bar{u}'\gamma_5 u &\text{(B.10)}\\ \bar{u}'\sigma_{\mu\nu}\gamma_5 q^\nu u &= -i(m-m')\bar{u}'\gamma_\mu\gamma_5 u - ik_\mu\bar{u}'\gamma_5 u\,. &\text{(B.11)}\end{aligned}$$

Finally, the relevant amplitude for the rare hyperon decay $\Sigma^+ \to p\ell^+\ell^-$ decomposes like

$$\begin{aligned}\mathcal{A}^{rs}_\mu(p,p') &= \langle p(\boldsymbol{p}'), r|\,\mathcal{H}_W J_\mu\,\big|\Sigma^+(\boldsymbol{p}), s\big\rangle &\text{(B.12)}\\ &= \bar{u}^r_p(\boldsymbol{p}')\left[(q^2\gamma_\mu - \not{q}q_\mu)(a(q^2) + b(q^2)\gamma_5) + (c(q^2) + d(q^2)\gamma_5)\sigma_{\mu\nu}q^\nu\right] u^s_\Sigma(\boldsymbol{p}) &\text{(B.13)}\end{aligned}$$

where we have used the Ward-Takahashi identity $q^\mu \mathcal{A}_\mu^{rs} = 0$. Note the different definitions of momenta in this appendix and in the main text, where the p carries momentum $\boldsymbol{p}$ and the Σ^+ carries momentum $\boldsymbol{k}$.

APPENDIX

C

RARE HYPERON FORM FACTOR TRACES

All quantities in this section are understood to be using the Euclidean definitions.

The form factor decomposition of the rare hyperon decay amplitude is given by

$$\tilde{\mathcal{A}}_\mu = \sigma_{\nu\mu} q^\nu \left[a - \gamma_5 b\right] + \left(-q^2 \gamma_\mu + q_\mu \not{q}\right) \left[c - \gamma_5 d\right] , \tag{C.1}$$

where the form factors a, b, c and d are all functions of the momentum transfer q^2. The object that is accessible on the lattice is the projected spin-matrix amplitude

$$\mathbb{P}_p(\boldsymbol{p}) \tilde{\mathcal{A}}_\mu \mathbb{P}_\Sigma(\boldsymbol{k}) , \tag{C.2}$$

where the projectors are defined by

$$\mathbb{P}_B(\boldsymbol{p}) = \frac{-i\not{p} + m_B}{2m_B} . \tag{C.3}$$

We define the trace of this object with different gamma structures as

$$\mathrm{tr}_\mu^{\gamma,\pm} \equiv \mathrm{Tr}\left[\mathbb{P}_p(\boldsymbol{p}) \tilde{\mathcal{A}}_\mu^{\pm} \mathbb{P}_\Sigma(\boldsymbol{k}) \gamma\right] \tag{C.4}$$

where the superscript $\pm$ indicates the separation between the positive and negative parity contributions, which can be obtained using either the $VV + AA$ or $VA + AV$ structures in the 4-quark operators. The goal is to find a complete set of traces and μ values that give access to all form factors.

We evaluate these traces for the kinematic point where the Σ^+ is at rest $\boldsymbol{k} = 0$ and the proton is moving along the x-direction $\boldsymbol{p} = (p_p, 0, 0)$. For the positive parity sector

$$\mathrm{tr}_0^{\mathbb{1},+} = \mathrm{tr}_0^{\gamma_0,+} = -\frac{p_p^2}{m_p}(a + c(m_p + m_\Sigma)) \tag{C.5}$$

$$\mathrm{tr}_0^{\gamma_1,+} = \mathrm{tr}_0^{\gamma_1\gamma_0,+} = i\frac{p_p(E_p - m_p)}{m_p}(a + c(m_p + m_\Sigma)) \tag{C.6}$$

$$\mathrm{tr}_2^{\gamma_2,+} = \mathrm{tr}_2^{\gamma_2\gamma_0,+} = -\frac{(E_p - m_p)}{m_p}\left[a(m_p + m_{\Sigma^+}) + c((E_p - m_{\Sigma^+})^2 - p_p^2)\right] \tag{C.7}$$

$$\mathrm{tr}_2^{\gamma_3\gamma_5,+} = \mathrm{tr}_2^{\gamma_1\gamma_2,+} = i\frac{p_p}{m_p}\left[a(m_p + m_{\Sigma^+}) + c((E_p - m_{\Sigma^+})^2 - p_p^2)\right], \tag{C.8}$$

and for the negative parity sector

$$\mathrm{tr}_0^{\gamma_5,-} = \mathrm{tr}_0^{\gamma_0\gamma_5,-} = -\frac{p_p^2}{m_p}(b + d(m_p - m_{\Sigma^+})) \tag{C.9}$$

$$\mathrm{tr}_0^{\gamma_1\gamma_5,-} = \mathrm{tr}_0^{\gamma_0\gamma_1,-} = i\frac{p_p(m_p + E_p)}{m_p}(b + d(m_p - m_{\Sigma^+})) \tag{C.10}$$

$$\mathrm{tr}_2^{\gamma_3,-} = \mathrm{tr}_2^{\gamma_3\gamma_0,-} = -i\frac{p_p}{m_p}\left[b(m_p - m_{\Sigma^+}) + d((E_p - m_{\Sigma^+})^2 - p_p^2)\right] \tag{C.11}$$

$$\mathrm{tr}_2^{\gamma_2\gamma_5,-} = -\mathrm{tr}_2^{\gamma_1\gamma_3,-} = \frac{(E_p + m_p)}{m_p}\left[b(m_p - m_{\Sigma^+}) + d((E_p - m_{\Sigma^+})^2 - p_p^2)\right]. \tag{C.12}$$

Traces with all other gamma matrices vanish identically, and similar relations can be obtained for the 2 remaining $\mu = 1, 3$. It can be seen that these results can be separated into a prefactor that depends on the value of μ and the gamma structure, and a combination of form factors that is only dependent on μ

$$\mathrm{tr}_\mu^{\gamma,\pm} = \zeta_\mu^{\gamma,\pm} f_\mu^\pm . \tag{C.13}$$

With $f_0^\pm$ and $f_2^\pm$, the form factors can then be isolated by inverting the linear systems

$$\begin{pmatrix} f_0^+ \\ f_2^+ \end{pmatrix} = \begin{pmatrix} 1 & m_p + m_\Sigma \\ m_p + m_\Sigma & q^2 \end{pmatrix} \begin{pmatrix} a \\ c \end{pmatrix} \tag{C.14}$$

$$\begin{pmatrix} f_0^- \\ f_2^- \end{pmatrix} = \begin{pmatrix} 1 & m_p - m_\Sigma \\ m_p - m_\Sigma & q^2 \end{pmatrix} \begin{pmatrix} b \\ d \end{pmatrix}, \tag{C.15}$$

where we have identified $q^2 = (E_p - m_{\Sigma^+})^2 - p_p^2$ as the momentum transfer.

APPENDIX

D

SPIN 3/2

Rarita-Schwinger equation of motion for massive spin-$\frac{3}{2}$ fermions is given by

$$\left[\epsilon^{\mu\nu\rho\sigma}\gamma_5\gamma_\rho\partial_\sigma - im\sigma^{\mu\nu}\right]\psi_\nu(x) = 0\,, \tag{D.1}$$

which can be equivalently decomposed into 4 equations [39]

$$\left[\partial_\nu\partial^\nu + m^2\right]\psi_\mu(x) = 0 \tag{D.2}$$

$$\left[i\partial\!\!\!/ - m\right]\psi_\mu(x) = 0 \tag{D.3}$$

$$\partial^\mu\psi_\mu(x) = 0 \tag{D.4}$$

$$\gamma^\mu\psi_\mu(x) = 0\,. \tag{D.5}$$

The first and second are the Klein-Gordon and Dirac equations that are satisfied for each μ component separately, and the third and fourth are the additional constraints specific for spin-$\frac{3}{2}$ particles.

As shown in [39], the positive and negative energy spinor solutions can be written as

$$u_s^\mu(\boldsymbol{p}) = \sum_{\lambda=-1}^{1}\sum_{m=-1/2}^{1/2} C_{s\lambda m}\,\epsilon_\lambda^\mu(\boldsymbol{p})\,u_m(\boldsymbol{p})\,\delta_{\lambda+m,s} \tag{D.6}$$

$$v_s^\mu(\boldsymbol{p}) = \sum_{\lambda=-1}^{1}\sum_{m=-1/2}^{1/2} C_{s\lambda m}\,\epsilon_\lambda^{\mu*}(\boldsymbol{p})\,v_m(\boldsymbol{p})\,\delta_{\lambda+m,s}\,. \tag{D.7}$$

Here $s \in \{\pm\frac{3}{2}, \pm\frac{1}{2}\}$, and the spinors u and v without the Lorentz index μ are the spin-$\frac{1}{2}$ solutions to the Dirac equation. ϵ is the spin-1 solution to the Proca equation, and $C_{s\lambda m}$ the Clebsch-Gordan coefficients

$$C_{s\lambda m} = \sqrt{\frac{(3/2+s)!(3/2-m)!}{3(1+\lambda)!(1-\lambda)!(1/2+m)!(1/2-m)!}}\,. \tag{D.8}$$

From [131], it can be seen that the positive energy solutions satisfy the orthogonality relation

$$\bar{u}^{\mu}(\boldsymbol{p}, s)u_{\mu}(\boldsymbol{p}, s') = -2m\delta_{ss'} \tag{D.9}$$

and the completeness relation

$$\Pi_{\mu\nu}(\boldsymbol{p}) = \sum_{s=-3/2}^{3/2} u_{\mu}(\boldsymbol{p}, s)\bar{u}_{\nu}(\boldsymbol{p}, s) \tag{D.10}$$

$$= -\left(\not{p} + m\right)\left(\eta_{\mu\nu} - \frac{p_\mu p_\nu}{m^2}\right) - \frac{1}{3}\left(\gamma_\mu + \frac{p_\mu}{m}\right)\left(\not{p} - m\right)\left(\gamma_\nu + \frac{p_\nu}{m}\right) \tag{D.11}$$

The stationary solution with $\boldsymbol{p} = \boldsymbol{0}$ is the special case relevant in this work. In this limit, the completeness relation becomes

$$\Pi_{\mu\nu}(\boldsymbol{0}) = -2mP^{+}\left(\eta_{\mu\nu} - \delta_{0\mu}\delta_{0\nu}\right) + \frac{2m}{3}\left(\gamma_\mu + \delta_{0\mu}\right)P^{-}\left(\gamma_\nu + \delta_{0\nu}\right) \tag{D.12}$$

where $P^{\pm} = \frac{1}{2}(1 \pm \gamma_t)$ are the parity projectors. The only non-zero components are the spatial ones

$$\Pi_{ij}(\boldsymbol{0}) = 2mP^{+}(\delta_{ij} + \frac{1}{3}\gamma_i\gamma_j)\,. \tag{D.13}$$

which written in Euclidean form is equivalent to that given in [132]

$$\Pi^{E}_{ij}(\boldsymbol{0}) = 2mP^{+}(\delta_{ij} - \frac{1}{3}\gamma^{E}_i\gamma^{E}_j)\,. \tag{D.14}$$

BIBLIOGRAPHY

[1] P. A. Boyle, F. Erben, J. M. Flynn, V. Gülpers, R. C. Hill, R. Hodgson, A. Jüttner, F. Ó. hÓgáin, A. Portelli, and C. T. Sachrajda. Simulating rare kaon decays K+→π+ℓ+ℓ- using domain wall lattice QCD with physical light quark masses. *Phys. Rev. D*, 107(1):L011503, 2023.

[2] Felix Erben, Vera Gülpers, Maxwell T. Hansen, Raoul Hodgson, and Antonin Portelli. Prospects for a lattice calculation of the rare decay $\Sigma^+ \to \mathrm{p}\ell^+\ell^-$. *JHEP*, 04:108, 2023.

[3] R. L. Workman et al. Review of Particle Physics. *PTEP*, 2022:083C01, 2022.

[4] Jeffrey Goldstone, Abdus Salam, and Steven Weinberg. Broken Symmetries. *Phys. Rev.*, 127:965–970, 1962.

[5] C. Vafa and E. Witten. Restrictions on symmetry breaking in vector-like gauge theories. *Nuclear Physics B*, 234(1):173–188, 1984.

[6] P. A. Zyla et al. Review of Particle Physics. *PTEP*, 2020(8):083C01, 2020.

[7] Leonardo Giusti, F. Rapuano, M. Talevi, and A. Vladikas. The QCD chiral condensate from the lattice. *Nucl. Phys. B*, 538:249–277, 1999.

[8] F. Englert and R. Brout. Broken symmetry and the mass of gauge vector mesons. *Phys. Rev. Lett.*, 13:321–323, Aug 1964.

[9] Peter W. Higgs. Broken symmetries and the masses of gauge bosons. *Phys. Rev. Lett.*, 13:508–509, Oct 1964.

[10] Gerhard Buchalla, Andrzej J. Buras, and Markus E. Lautenbacher. Weak decays beyond leading logarithms. *Rev. Mod. Phys.*, 68:1125–1144, 1996.

[11] Kenneth G. Wilson. Confinement of Quarks. *Phys. Rev. D*, 10:2445–2459, 1974.

[12] Holger Bech Nielsen and M. Ninomiya. No Go Theorem for Regularizing Chiral Fermions. *Phys. Lett. B*, 105:219–223, 1981.

[13] B. Sheikholeslami and R. Wohlert. Improved Continuum Limit Lattice Action for QCD with Wilson Fermions. *Nucl. Phys. B*, 259:572, 1985.

[14] Anthony Francis, Patrick Fritzsch, Martin Lüscher, and Antonio Rago. Master-field simulations of O(a)-improved lattice QCD: Algorithms, stability and exactness. *Comput. Phys. Commun.*, 255:107355, 2020.

[15] Wolfgang Bietenholz and U. J. Wiese. Perfect lattice actions for quarks and gluons. *Nucl. Phys. B*, 464:319–352, 1996.

[16] John B. Kogut and Leonard Susskind. Hamiltonian Formulation of Wilson's Lattice Gauge Theories. *Phys. Rev. D*, 11:395–408, 1975.

[17] Paul H. Ginsparg and Kenneth G. Wilson. A Remnant of Chiral Symmetry on the Lattice. *Phys. Rev. D*, 25:2649, 1982.

[18] Martin Luscher. Exact chiral symmetry on the lattice and the Ginsparg-Wilson relation. *Phys. Lett. B*, 428:342–345, 1998.

[19] David B. Kaplan. A Method for simulating chiral fermions on the lattice. *Phys. Lett. B*, 288:342–347, 1992.

[20] Yigal Shamir. Chiral fermions from lattice boundaries. *Nucl. Phys. B*, 406:90–106, 1993.

[21] Vadim Furman and Yigal Shamir. Axial symmetries in lattice QCD with Kaplan fermions. *Nucl. Phys. B*, 439:54–78, 1995.

[22] Yoshio Kikukawa and Tatsuya Noguchi. Low-energy effective action of domain wall fermion and the Ginsparg-Wilson relation. *Nucl. Phys. B Proc. Suppl.*, 83:630–632, 2000.

[23] Richard C. Brower, Harmut Neff, and Kostas Orginos. The Möbius domain wall fermion algorithm. *Comput. Phys. Commun.*, 220:1–19, 2017.

[24] Richard C. Brower, Hartmut Neff, and Kostas Orginos. Möbius fermions: Improved domain wall chiral fermions. *Nuclear Physics B - Proceedings Supplements*, 140:686–688, 2005. LATTICE 2004.

[25] R.C. Brower, H. Neff, and K. Orginos. Möbius fermions. *Nuclear Physics B - Proceedings Supplements*, 153(1):191–198, 2006. Proceedings of the Workshop on Computational Hadron Physics.

[26] Greg Mcglynn. Algorithmic improvements for weak coupling simulations of domain wall fermions. *PoS*, LATTICE2015:019, 2016.

[27] Hantao Yin and Robert D. Mawhinney. Improving DWF Simulations: the Force Gradient Integrator and the Möbius Accelerated DWF Solver. *PoS*, LATTICE2011:051, 2011.

[28] Antonin Portelli, Ryan Abott, Nils Asmussen, Alessandro Barone, Peter A Boyle, Felix Erben, Nelson Lachini, Michael Marshall, Vera Gülpers, Ryan C Hill, Raoul Hodgson, Fabian Joswig, Fionn Ó hÓgáin, and James P Richings. aportelli/hadrons: Hadrons v1.3, March 2022.

[29] Peter Boyle et al. Isospin-breaking corrections to light-meson leptonic decays from lattice simulations at physical quark masses. *JHEP*, 02:242, 2023.

[30] Sergey Syritsyn and John W. Negele. Oscillatory terms in the domain wall transfer matrix. *PoS*, LATTICE2007:078, 2007.

[31] Masaaki Tomii. Unphysical poles and dispersion relations for Möbius domain-wall fermions in free field theory at finite L_s. *Phys. Rev. D*, 96(7):074504, 2017.

[32] Giorgio Parisi. The strategy for computing the hadronic mass spectrum. *Physics Reports*, 103(1):203–211, 1984.

[33] G. Peter Lepage. The Analysis of Algorithms for Lattice Field Theory. In *Theoretical Advanced Study Institute in Elementary Particle Physics*, 6 1989.

[34] Peter Boyle, Azusa Yamaguchi, Guido Cossu, and Antonin Portelli. Grid: A next generation data parallel C++ QCD library. 12 2015.

[35] Azusa Yamaguchi, Peter Boyle, Guido Cossu, Gianluca Filaci, Christoph Lehner, and Antonin Portelli. Grid: OneCode and FourAPIs. *PoS*, LATTICE2021:035, 2022.

[36] Y. Iwasaki and T. Yoshie. Renormalization Group Improved Action for SU(3) Lattice Gauge Theory and the String Tension. *Phys. Lett. B*, 143:449–452, 1984.

[37] T. Blum et al. Domain wall QCD with physical quark masses. *Phys. Rev. D*, 93(7):074505, 2016.

[38] Y. Aoki et al. Continuum Limit Physics from 2+1 Flavor Domain Wall QCD. *Phys. Rev. D*, 83:074508, 2011.

[39] H. Shi-Zhong, R. Tu-Nan, W. Ning, and Z. Zhi-Peng. Solution to the Rarita-Schwinger equations. *The European Physical Journal C - Particles and Fields*, 26(1):609–623, 2003.

[40] Boris Polyak. *Introduction to Optimization*. Optimization Software, 1987.

[41] Martin Luscher. Local coherence and deflation of the low quark modes in lattice QCD. *JHEP*, 07:081, 2007.

[42] M. A. Clark, Chulwoo Jung, and Christoph Lehner. Multi-Grid Lanczos. *EPJ Web Conf.*, 175:14023, 2018.

[43] Eigo Shintani, Rudy Arthur, Thomas Blum, Taku Izubuchi, Chulwoo Jung, and Christoph Lehner. Covariant approximation averaging. *Phys. Rev. D*, 91(11):114511, 2015.

[44] Andrzej J. Buras and Elena Venturini. Searching for New Physics in Rare K and B Decays without $|V_{cb}|$ and $|V_{ub}|$ Uncertainties. *Acta Phys. Polon. B*, 53(6):A1, 9 2021.

[45] Andrzej J. Buras and Elena Venturini. The exclusive vision of rare K and B decays and of the quark mixing in the standard model. *Eur. Phys. J. C*, 82(7):615, 2022.

[46] Ziyuan Bai, Norman H. Christ, Xu Feng, Andrew Lawson, Antonin Portelli, and Christopher T. Sachrajda. Exploratory Lattice QCD Study of the Rare Kaon Decay $K^+ \to \pi^+ \nu\bar{\nu}$. *Phys. Rev. Lett.*, 118(25):252001, 2017.

[47] Ziyuan Bai, Norman H. Christ, Xu Feng, Andrew Lawson, Antonin Portelli, and Christopher T. Sachrajda. $K^+ \to \pi^+ \nu\bar{\nu}$ decay amplitude from lattice QCD. *Phys. Rev. D*, 98(7):074509, 2018.

[48] Norman H. Christ, Xu Feng, Antonin Portelli, and Christopher T. Sachrajda. Lattice QCD study of the rare kaon decay $K^+ \to \pi^+ \nu\bar{\nu}$ at a near-physical pion mass. *Phys. Rev. D*, 100(11):114506, 2019.

[49] J. R. Batley et al. Observation of the rare decay K(S) —> pi0 e+ e-. *Phys. Lett. B*, 576:43–54, 2003.

[50] J. R. Batley et al. Observation of the rare decay K(S) —> pi0 mu+ mu-. *Phys. Lett. B*, 599:197–211, 2004.

[51] A. Alavi-Harati et al. Search for the rare decay K(L) —> pi0 e+ e-. *Phys. Rev. Lett.*, 93:021805, 2004.

[52] A. Alavi-Harati et al. Search for the Decay $K_L \to \pi^0 \mu^+ \mu^-$. *Phys. Rev. Lett.*, 84:5279–5282, 2000.

[53] J. R. Batley et al. Precise measurement of the K+- —> pi+-e+e- decay. *Phys. Lett. B*, 677:246–254, 2009.

[54] R. Appel et al. A New measurement of the properties of the rare decay K+ —> pi+ e+ e-. *Phys. Rev. Lett.*, 83:4482–4485, 1999.

[55] C. Alliegro et al. Study of the decay K+ —> pi+ e+ e-. *Phys. Rev. Lett.*, 68:278–281, 1992.

[56] P. Bloch et al. Observation of the $K^+ \to \pi^+ e^+ e^-$ decay. *Phys. Lett. B*, 56:201, 1975.

[57] Eduardo Cortina Gil et al. A measurement of the $K^+ \to \pi^+ \mu^+ \mu^-$ decay. *JHEP*, 11:011, 2022.

[58] J. R. Batley et al. New measurement of the K+- –> pi+-mu+mu- decay. *Phys. Lett. B*, 697:107–115, 2011.

[59] H. K. Park et al. Observation of the Decay $K^- \to \pi^- \mu^+ \mu^-$ and Measurements of the Branching Ratios for $K^\pm \to \pi^\pm \mu^+ \mu^-$. *Phys. Rev. Lett.*, 88:111801, 2002.

[60] H. Ma et al. A New measurement of the rare decay K+ —> pi+ mu+ mu-. *Phys. Rev. Lett.*, 84:2580–2583, 2000.

[61] S. Adler et al. Observation of the decay K+ —> pi+ mu+ mu-. *Phys. Rev. Lett.*, 79:4756–4759, 1997.

[62] Gerhard Ecker, Antonio Pich, and Eduardo de Rafael. K —> pi Lepton+ Lepton- Decays in the Effective Chiral Lagrangian of the Standard Model. *Nucl. Phys. B*, 291:692–719, 1987.

[63] Gino Isidori, Guido Martinelli, and Paolo Turchetti. Rare kaon decays on the lattice. *Phys. Lett. B*, 633:75–83, 2006.

[64] Andrew J. Lawson. *Exploratory lattice QCD studies of rare kaon decays*. PhD thesis, Southampton U., 2017.

[65] G. D'Ambrosio, G. Ecker, G. Isidori, and J. Portoles. The Decays K —> pi l+ l- beyond leading order in the chiral expansion. *JHEP*, 08:004, 1998.

[66] Giancarlo D'Ambrosio, David Greynat, and Marc Knecht. Matching long and short distances at order $\mathcal{O}(\alpha_s)$ in the form factors for $K \to \pi\ell^+\ell^-$. *Phys. Lett. B*, 797:134891, 2019.

[67] N. H. Christ, X. Feng, A. Portelli, and C. T. Sachrajda. Prospects for a lattice computation of rare kaon decay amplitudes: $K \to \pi\ell^+\ell^-$ decays. *Phys. Rev.*, D92(9):094512, 2015.

[68] Norman Christ, Xu Feng, Andreas Juttner, Andrew Lawson, Antonin Portelli, and Christopher Sachrajda. Long distance contributions to the rare kaon decay $K \to \pi\ell^+\ell^-$. *PoS*, LATTICE2015:340, 2016.

[69] Andrew Lawson, Norman H. Christ, Xu Feng, Andreas Jüttner, Antonin Portelli, and Christopher Sachrajda. Progress in the exploratory calculation of the rare kaon decays $K \to \pi\ell^+\ell^-$. *PoS*, LATTICE2016:303, 2017.

[70] Norman H. Christ, Xu Feng, Andreas Jüttner, Andrew Lawson, Antonin Portelli, and Christopher T. Sachrajda. First exploratory calculation of the long-distance contributions to the rare kaon decays $K \to \pi\ell^+\ell^-$. *Phys. Rev.*, D94(11):114516, 2016.

[71] G. Martinelli, C. Pittori, Christopher T. Sachrajda, M. Testa, and A. Vladikas. A General method for nonperturbative renormalization of lattice operators. *Nucl. Phys. B*, 445:81–108, 1995.

[72] C. Sturm, Y. Aoki, N. H. Christ, T. Izubuchi, C. T. C. Sachrajda, and A. Soni. Renormalization of quark bilinear operators in a momentum-subtraction scheme with a nonexceptional subtraction point. *Phys. Rev. D*, 80:014501, 2009.

[73] Leonardo Giusti, P. Hernandez, M. Laine, P. Weisz, and H. Wittig. A Strategy to study the role of the charm quark in explaining the Delta I = 1/2 rule. *JHEP*, 11:016, 2004.

[74] Christoph Lehner and Christian Sturm. Matching factors for Delta S=1 four-quark operators in RI/SMOM schemes. *Phys. Rev. D*, 84:014001, 2011.

[75] N. H. Christ, T. Izubuchi, C. T. Sachrajda, A. Soni, and J. Yu. Long distance contribution to the KL-KS mass difference. *Phys. Rev. D*, 88:014508, 2013.

[76] Laurent Lellouch and Martin Luscher. Weak transition matrix elements from finite volume correlation functions. *Commun. Math. Phys.*, 219:31–44, 2001.

[77] Norman H. Christ, Xu Feng, Guido Martinelli, and Christopher T. Sachrajda. Effects of finite volume on the K_L-K_S mass difference. *Phys. Rev. D*, 91(11):114510, 2015.

[78] Maxwell T. Hansen and Stephen R. Sharpe. Relativistic, model-independent, three-particle quantization condition. *Phys. Rev. D*, 90(11):116003, 2014.

[79] Maxwell T. Hansen, Fernando Romero-López, and Stephen R. Sharpe. Decay amplitudes to three hadrons from finite-volume matrix elements. *JHEP*, 04:113, 2021.

[80] Andrew W. Jackura, Raúl A. Briceño, and Maxwell T. Hansen. Three-pion effects in $K^0 - \bar{K}^0$ mixing. *PoS*, LATTICE2022:062, 2023.

[81] Peter Boyle, Andreas Juttner, Marina Krstic Marinkovic, Francesco Sanfilippo, Matthew Spraggs, and Justus Tobias Tsang. An exploratory study of heavy domain wall fermions on the lattice. *JHEP*, 04:037, 2016.

[82] K. Bitar, A. D. Kennedy, R. Horsley, S. Meyer, and P. Rossi. The QCD Finite Temperature Transition and Hybrid Monte Carlo. *Nucl. Phys. B*, 313:348–376, 1989.

[83] Shao-Jing Dong and Keh-Fei Liu. Stochastic estimation with Z(2) noise. *Phys. Lett. B*, 328:130–136, 1994.

[84] T. Blum, P. A. Boyle, T. Izubuchi, L. Jin, A. Jüttner, C. Lehner, K. Maltman, M. Marinkovic, A. Portelli, and M. Spraggs. Calculation of the hadronic vacuum polarization disconnected contribution to the muon anomalous magnetic moment. *Phys. Rev. Lett.*, 116(23):232002, 2016.

[85] Z. Bai, N. H. Christ, T. Izubuchi, C. T. Sachrajda, A. Soni, and J. Yu. $K_L - K_S$ Mass Difference from Lattice QCD. *Phys. Rev. Lett.*, 113:112003, 2014.

[86] Leonardo Giusti, Tim Harris, Alessandro Nada, and Stefan Schaefer. Frequency-splitting estimators of single-propagator traces. *PoS*, LATTICE2019:157, 2020.

[87] Tim Harris, Vera Gülpers, Antonin Portelli, and James Richings. Efficiently unquenching QCD+QED at O(α). *PoS*, LATTICE2022:013, 2023.

[88] L. Maiani, G. Martinelli, M. L. Paciello, and B. Taglienti. Scalar Densities and Baryon Mass Differences in Lattice QCD With Wilson Fermions. *Nucl. Phys. B*, 293:420, 1987.

[89] R. Horsley, R. Millo, Y. Nakamura, H. Perlt, D. Pleiter, P. E. L. Rakow, G. Schierholz, A. Schiller, F. Winter, and J. M. Zanotti. A Lattice Study of the Glue in the Nucleon. *Phys. Lett. B*, 714:312–316, 2012.

[90] A. J. Chambers et al. Feynman-Hellmann approach to the spin structure of hadrons. *Phys. Rev. D*, 90(1):014510, 2014.

[91] A. J. Chambers et al. Disconnected contributions to the spin of the nucleon. *Phys. Rev. D*, 92(11):114517, 2015.

[92] Chris Bouchard, Chia Cheng Chang, Thorsten Kurth, Kostas Orginos, and Andre Walker-Loud. On the Feynman-Hellmann Theorem in Quantum Field Theory and the Calculation of Matrix Elements. *Phys. Rev. D*, 96(1):014504, 2017.

[93] Jinchen He et al. Detailed analysis of excited-state systematics in a lattice QCD calculation of gA. *Phys. Rev. C*, 105(6):065203, 2022.

[94] M. Batelaan, K. U. Can, R. Horsley, Y. Nakamura, P. E. L. Rakow, G. Schierholz, H. Stüben, R. D. Young, and J. M. Zanotti. Feynman–Hellmann approach to transition matrix elements and quasi-degenerate energy states. 5 2023.

[95] S. Capitani, M. Della Morte, G. von Hippel, B. Jager, A. Juttner, B. Knippschild, H. B. Meyer, and H. Wittig. The nucleon axial charge from lattice QCD with controlled errors. *Phys. Rev. D*, 86:074502, 2012.

[96] C. Alexandrou, S. Bacchio, M. Constantinou, J. Finkenrath, K. Hadjiyiannakou, K. Jansen, G. Koutsou, and A. Vaquero Aviles-Casco. Nucleon axial, tensor, and scalar charges and σ-terms in lattice QCD. *Phys. Rev. D*, 102(5):054517, 2020.

[97] Tim Harris, Georg von Hippel, Parikshit Junnarkar, Harvey B. Meyer, Konstantin Ottnad, Jonas Wilhelm, Hartmut Wittig, and Linus Wrang. Nucleon isovector charges and twist-2 matrix elements with $N_f = 2 + 1$ dynamical Wilson quarks. *Phys. Rev. D*, 100(3):034513, 2019.

[98] John Bulava, Michael Donnellan, and Rainer Sommer. On the computation of hadron-to-hadron transition matrix elements in lattice QCD. *JHEP*, 01:140, 2012.

[99] C. Alexandrou et al. Nucleon axial and pseudoscalar form factors from lattice QCD at the physical point. *Phys. Rev. D*, 103(3):034509, 2021.

[100] D. Djukanovic, T. Harris, G. von Hippel, P. M. Junnarkar, H. B. Meyer, D. Mohler, K. Ottnad, T. Schulz, J. Wilhelm, and H. Wittig. Isovector electromagnetic form factors of the nucleon from lattice QCD and the proton radius puzzle. *Phys. Rev. D*, 103(9):094522, 2021.

[101] A. Desiderio et al. First lattice calculation of radiative leptonic decay rates of pseudoscalar mesons. *Phys. Rev. D*, 103(1):014502, 2021.

[102] K. U. Can et al. The Compton Amplitude, lattice QCD and the Feynman-Hellmann approach. *SciPost Phys. Proc.*, 6:003, 2022.

[103] Roel Aaij et al. Evidence for the rare decay $\Sigma^+ \to p\mu^+\mu^-$. *Phys. Rev. Lett.*, 120(22):221803, 2018.

[104] HyangKyu Park et al. Evidence for the decay Sigma+ → p mu+ mu-. *Phys. Rev. Lett.*, 94:021801, 2005.

[105] Xiao-Gang He, Jusak Tandean, and G. Valencia. The Decay Sigma+ → p l+ l- within the standard model. *Phys. Rev.*, D72:074003, 2005.

[106] Xiao-Gang He, Jusak Tandean, and German Valencia. Decay rate and asymmetries of $\Sigma^+ \to p\mu^+\mu^-$. *JHEP*, 10:040, 2018.

[107] Li-Sheng Geng, Jorge Martin Camalich, and Rui-Xiang Shi. New physics in s → d semileptonic transitions: rare hyperon vs. kaon decays. *JHEP*, 02:178, 2022.

[108] Raúl A. Briceño, Zohreh Davoudi, Maxwell T. Hansen, Matthias R. Schindler, and Alessandro Baroni. Long-range electroweak amplitudes of single hadrons from Euclidean finite-volume correlation functions. *Phys. Rev. D*, 101(1):014509, 2020.

[109] Lars Bergstrom, Rafi Safadi, and Paul Singer. Phenomenology of $\Sigma^+ \to p\ell^+\ell^-$ and the Structure of the Weak Nonleptonic Hamiltonian. *Z. Phys.*, C37:281, 1988.

[110] M. Tanabashi et al. Review of Particle Physics. *Phys. Rev.*, D98(3):030001, 2018.

[111] J. Bijnens, H. Sonoda, and Mark B. Wise. On the Validity of Chiral Perturbation Theory for Weak Hyperon Decays. *Nucl. Phys.*, B261:185–198, 1985.

[112] Elizabeth Ellen Jenkins and Aneesh V. Manohar. Baryon chiral perturbation theory using a heavy fermion Lagrangian. *Phys. Lett.*, B255:558–562, 1991.

[113] Elizabeth Ellen Jenkins, Michael E. Luke, Aneesh V. Manohar, and Martin J. Savage. Weak radiative hyperon decays in chiral perturbation theory. *Nucl. Phys.*, B397:84–104, 1993.

[114] David Bernecker and Harvey B. Meyer. Vector Correlators in Lattice QCD: Methods and applications. *Eur. Phys. J. A*, 47:148, 2011.

[115] C. h. Kim, C. T. Sachrajda, and Stephen R. Sharpe. Finite-volume effects for two-hadron states in moving frames. *Nucl. Phys. B*, 727:218–243, 2005.

[116] Norman H. Christ, Xu Feng, Antonin Portelli, and Christopher T. Sachrajda. Prospects for a lattice computation of rare kaon decay amplitudes II $K \to \pi\nu\bar{\nu}$ decays. *Phys. Rev. D*, 93(11):114517, 2016.

[117] M. Lüscher. Volume Dependence of the Energy Spectrum in Massive Quantum Field Theories. 2. Scattering States. *Commun. Math. Phys.*, 105:153–188, 1986.

[118] Martin Lüscher. Two particle states on a torus and their relation to the scattering matrix. *Nucl. Phys. B*, 354:531–578, 1991.

[119] K. Rummukainen and Steven A. Gottlieb. Resonance scattering phase shifts on a nonrest frame lattice. *Nucl. Phys. B*, 450:397–436, 1995.

[120] Raul A. Briceño. Two-particle multichannel systems in a finite volume with arbitrary spin. *Phys. Rev. D*, 89(7):074507, 2014.

[121] Maxwell T. Hansen and Stephen R. Sharpe. Multiple-channel generalization of Lellouch-Lüscher formula. *Phys. Rev. D*, 86:016007, 2012.

[122] Maxwell T. Hansen and Harvey B. Meyer. On the effect of excited states in lattice calculations of the nucleon axial charge. *Nucl. Phys. B*, 923:558–587, 2017.

[123] M. Ablikim et al. Precision Measurement of the Decay $\Sigma^+ \to p\gamma$ in the Process $J/\psi \to \Sigma^+\bar{\Sigma}^-$. 2 2023.

[124] Raúl A. Briceño, Maxwell T. Hansen, and André Walker-Loud. Multichannel $1 \to 2$ transition amplitudes in a finite volume. *Phys. Rev. D*, 91(3):034501, 2015.

[125] Raúl A. Briceño and Maxwell T. Hansen. Multichannel $0 \to 2$ and $1 \to 2$ transition amplitudes for arbitrary spin particles in a finite volume. *Phys. Rev. D*, 92(7):074509, 2015.

[126] W. Detmold, D. J. Murphy, A. V. Pochinsky, M. J. Savage, P. E. Shanahan, and M. L. Wagman. Sparsening algorithm for multihadron lattice QCD correlation functions. *Phys. Rev. D*, 104(3):034502, 2021.

[127] Yuan Li, Shi-Cheng Xia, Xu Feng, Lu-Chang Jin, and Chuan Liu. Field sparsening for the construction of the correlation functions in lattice QCD. *Phys. Rev. D*, 103(1):014514, 2021.

[128] B. Efron. Bootstrap Methods: Another Look at the Jackknife. *The Annals of Statistics*, 7(1):1 – 26, 1979.

[129] H. Akaike. A new look at the statistical model identification. *IEEE Transactions on Automatic Control*, 19(6):716–723, 1974.

[130] Martin Luscher and Peter Weisz. Locality and exponential error reduction in numerical lattice gauge theory. *JHEP*, 09:010, 2001.

[131] Vyacheslav S. Rychkov and Alessandro Strumia. Thermal production of gravitinos. *Phys. Rev. D*, 75:075011, 2007.

[132] Steven Weinberg. *The quantum theory of fields. Vol. 3: Supersymmetry.* Cambridge University Press, 6 2013.